FLEXSense: Technical Assistance for Airborne Measurements during the FLEX Sentinel Tandem Experiment

ESA Contract No. 4000125402/18/NL/NA

CCN 1 – Campaign 2019

Final Report – Final Version

Deliverable D3

by

Uwe Rascher, Stephani Baum, Bastian Siegmann, Jim Buffat, Andreas Burkart, Sergio Cogliati, Roberto Colombo, Alexander Damm, Lorenzo Genesio, Jan Hanus, David Herrera, Tommaso Julitta, Oliver Knopf, Franco Miglietta, Onno Muller, Juan Quiros

March 24, 2022

TABLE OF CONTENTS

ABBREVIATIONS AND ACRONYMS

BRDF	Bidirectional Reflectance
Cal/Val	Calibration and Validation
CEST	Central European Summer Time
CKA	Campus Klein-Altendorf
DEM	Digital Elevation Model
DSM	Digital Surface Model
EC	Eddy Covariance
ESA	European Space Agency
FLEX	Earth Explorer 8 FLuorescence EXplorer
FWHM	Full Width at Half Maximum
GLT	Geometric Look-up Table
GPP	Gross Primary Production
H	Sensible Heat
ICOS	Integrated Carbon Observation System
iFLD	Improved Fraunhofer Line Depth
LAI	Leaf Area Index
LE	Latent Heat
LFRP	Large Fluorescence Reference Panel
LLL	Land-Leaving Radiance
LST	Land Surface Temperature
MMD	Maximum-Minimum Difference
NDVI	Normalized Difference Vegetation Index
NEE	Net Ecosystem Exchange
PAR	Photosynthetically Active Radiation
PC	Principal Components
PCA	Principal Components Analysis

PRISMA	Hyperspectral Precursor of the Application Mission
PSF	Point Spread Function
RT	Radiative Transfer
RTE	Radiative Transfer Equation
SFM	Spectral Fitting Method
SIF	Solar-Induced Fluorescence
SNR	Signal-to-Noise Ratio
SVD	Singular Vector Decomposition
SZA	Solar Zenith Angle
TOC	Top-of-Canopy
TR32	Transregional Collaborative Research Centre 32
UAV	Unmanned Aerial Vehicle
VHR	Very High Resolution
VZA	View Zenith Angle

Applicable Documents

SOW FLEXSense 2018

CIP FLEXSense 2019 (CCN1)

DAR FLEXSense 2019 (CCN1)

Reference Documents

[RD-01] FLEX Sentinel Tandem Campaign: Technical Assistance for Airborne measurements during the FLEX Sentinel Tandem Experiment 2018, CIP: Campaign Implementation Report, ESA Contr. No. 4000125402/18/NL/NA

[RD-02] FLEX Sentinel Tandem Campaign: Technical Assistance for Airborne measurements during the FLEX Sentinel Tandem Experiment 2018, DAR: Data Acquisition Report, ESA Contr. No. 4000125402/18/NL/NA

[RD-03] FLEX Sentinel Tandem Campaign: Technical Assistance for Airborne measurements during the FLEX Sentinel Tandem Experiment 2018, FR: Final Report, ESA Contr. No. 4000125402/18/NL/NA

[RD-04] Technical Note: Data Organization for FLEXSense 2018 campaign

[RD-05] ATMOFLEX: Technical Assistance for the Deployment of Ground-based Instruments for term measurements of Red and Far-red Sun-Induced Fluorescence (ATMOFLEX), Final report, ESA Contr. No. 4000122454/17/NL/FF/mg

[RD-06] NET-Sense 2019 Campaign: NASA-ESA Temperature Sensing Experiment (NET-Sense), Data Acquisition Report

[RD-07] SARSense: Technical Assistance for Airborne Measurements during the SAR Sentinel Experiment, CIP & DAR & FR, ESA Contr. No. 4000125444/18/NL/LF

[RD-08] Preliminary guidelines for Cal/Val activities in the context of the FLEX mission. Prepared by R. Colombo, U. Rascher & G. Mohammed; discussed in the FLEX MAG in 2017.

[RD-09] Photoproxy: Technical Assistance for the Photosynthetic-Proxy Experiment, Final Photosynthesis Report, ESA Contr. No. 4000125731/19/NL/LF

[RD-10] Deliverable D-2 of *HyPlant* Processing Experiment (HYPER): Documentation of Calibration Algorithms of *HyPlant*

1 SUMMARY OF MAIN FINDINGS

In the 2019 Fluorescence Explorer Sense (FLEXSense) campaign, the 2018 campaign activities were continued in order to address some specific, yet still outstanding, issues as well as expand upon the data sets of previous, synergistic FLEX campaign activities. The three-week campaign activities were undertaken in Germany and Italy with the goal of providing a complete set of high-resolution experimental data, including all relevant elements required for the preparation of the FLEX satellite mission. The main outcomes and findings of this activity are structured in several sections and can be summarized as follows:

Extended *HyPlant* data with uncertainty information (sections 3, 5, 6 & 8): During the FLEXSense 2018 campaign, several data quality measures and additional data layers giving first estimates of the uncertainty of *HyPlant* data were introduced. These new quality metrices and layers were operationally determined for all *HyPlant* flight lines recorded during the 2019 FlexSense campaign and the results are delivered as additional data layers attached to the SFM SIF maps. Additionally, we calculated errors and uncertainties on various *HyPlant* data products and provide quantitative data on radiometric calibration coefficients, detector uncertainties, at-sensor radiance and SIF products. This will facilitate the better integration of *HyPlant* data in future Cal/Val concepts of the FLEX satellite mission in which uncertainty estimates and error propagation need to be included. A detailed description and update on these new quality criteria and data layers which are used for the first time in the operational *HyPlant* processing chain are presented in sections 3.1.1, 5, 6.4, 8.2.4 & 8.3.1.

Evaluation of active and passive reference targets (section 6): We already employed active and passive reference targets during the 2018 campaign activity. However, only conceptual and technical tests with these novel reference targets were possible. We thus conducted an extensive laboratory and field evaluation of these reference targets within the scope of this activity, which are presented in this report:

- Both concepts tested as FLEX reference targets provide good data to compare and validate ground-based and airborne SIF reference values. Both concepts could be used in the field with sufficiently large dimensions to serve as reference points for airborne data. Both targets were successfully used under realistic field conditions.
- The passive reference targets proved to be very sensitive to short wavelength radiation and the panels showed a substantial degradation of the fluorescence signal during the field campaign. We were able to better understand the decay process and the half times of the SIF dye and give recommendations for the technical improvement of the passive reference targets.
- The active reference panels worked fine in the field set-up and the SIF-mimicking LEDs could be powered appropriately, giving a well-defined SIF-like signal. This signal was correctly measured by ground-based systems and the airborne imager *HyPlant*. These data were used to compare the airborne SIF products with the expected SIF measures on the ground, thus enabling us to further constrain the uncertainty of current *HyPlant* SIF products. We confirmed that there is no substantial error (bias) in *HyPlant* SIF retrievals and the uncertainty of the *HyPlant* SIF products were in the range of 0.1-0.5 mW $m^{-2}s^{-1}sr^{-1}$.
- Based on these results, we give a recommendation on how these novel SIF reference panels can be included in the FLEX Cal/Val concept (section 7.1).

Summarizing and integrating *HyPlant* and other uncertainties from the calibration to the fluorescence products (sections 3.1.1, 5.1, 6.4 & 8.3.1): Within this activity, we have collected information associated with *HyPlant* fluorescence products and integrated this formerly scattered information into a single result file. We have revisited the uncertainty that is associated with the current operational calibration of *HyPlant* at the SPECIM calibration facilities (sections 3.1.1). Furthermore, we have evaluated and discussed the uncertainty layers of *HyPlant* in a diurnal data set from Campus Klein-Altendorf (section 8.3), and we have statistically compared the fluorescence products of *HyPlant* with the predicted fluorescence values of the active and passive reference targets (section 6.4). Finally, we present an updated concept for the FLEX Cal/Val activities that integrates reference targets as well as ground, unmanned aerial vehicle (UAV), and airborne measurements (section 7.1). Results and gaps in these data are finally discussed for their potential use within a FLEX Cal/Val concept (section 7). For the definition of uncertainties, we have used the concept developed by Povey and Grainger (2015), and have aimed to provide quantitative values of the measurement error and uncertainty for the different steps used to calculate the FloX and *HyPlant* SIF products.

Potential of SIF to detect early signs of drought stress (section 8.2.2): We successfully conducted a drought stress experiment in Italy in which we exposed a corn field to a controlled drought treatment by turning off artificial watering. This experiment was conducted as a highly controlled field experiment with an adjacent well-watered control plot and a complete monitoring of all relevant soil, leaf and canopy parameters. We could show that drought affects actual photosynthesis of corn plants within a few days and that this drought-induced limitation of photosynthesis was readily visible in the SIF signal just three days after the start of the experiment. No other remote sensing parameter was able to detect these early signs of drought. Vegetation indices and thermal data reacted at the earliest six days after the start of the experiment. We could thus show that SIF detects drought approximately 50% faster than reflectance-based methods. Our quantitative analysis of SIF, vegetation reflectance and thermal data additionally furnishes a good basis for the potential development of an 'early drought stress product' for the FLEX satellite mission. The data from this experiment have already been submitted for publication to *Remote Sensing of Environment*; a copy of the scientific article is attached to this report (appendix 13.1).

Potential to improve fire detection by exploiting high-resolution FLEX data (section 8.2.3): We successfully conducted a controlled burn in Italy and managed to overfly the fire and the fire plume several times with the airborne sensor *HyPlant*. We could show that this fire and the potassium in the fire plume could be detected in the absorption bands that are normally used for fluorescence retrieval. Therefore, the very fine spectral resolution of FLEX in the red and near-infrared spectral region has the potential for use to detect fires, thus presenting a new area of application for the FLEX satellite system.

2 OVERVIEW OF THE CAMPAIGN CONCEPT

2.1 BACKGROUND

Within the framework of its Earth Observation Envelope Program, the European Space Agency (ESA) carries out a number of different activities to support geophysical algorithm development, calibration, validation, and the simulation of future space-borne earth observation missions.

The overall goals are derived from the general scientific objectives of several upcoming missions in the context of future Earth Observation (EO) programs and their users. Furthermore, the objectives are relevant for validation campaigns, which are prepared and conducted as part of the current missions in orbit or under development. The special focus of these campaign activities is on supporting the upcoming Earth Explorer 8 FLuorescence EXplorer (FLEX) satellite mission, which comprises a tandem mission between the newly developed FLEX satellite instrument (also referred to as FLORIS) and the operational Sentinel-3 satellite mission. The FLEX mission will be the first mission designed to monitor the photosynthetic activity of terrestrial vegetation by using a novel technique to measure the chlorophyll fluorescence signal that originates from the core of the photosynthetic machinery. This will open up new possibilities for assessing the dynamics of photosynthesis using solar-induced fluorescence (SIF), which represents a great advancement compared with current conventional land surface monitoring satellites, which can only detect the potential photosynthesis derived from passive reflectance measurements. The objective of the FLEX satellite mission is to provide global maps of actual photosynthesis and plant health status by measuring the fluorescence signal at a 300 m x 300 m resolution and global revisiting time of 10–25 days.

2.2 Specific Campaign Objectives

The basic setup of the FLEXSense 2019 campaign activities focused on collecting relevant airborne data over representative monitoring sites, concurrent with ground-based measurements for time intervals compatible with the FLEX/Sentinel-3 space-borne mission. In order to study the dynamic nature of solar-induced fluorescence and to explore synergies between different ground and airborne approaches, high-frequency sampling was conducted during intensive observation periods (IOP). Strong collaboration was sought among different communities to build on the experience from previously planned activities in the context of mission development as well as calibration and validation (Cal/Val) activities for the existing Sentinel-2 and Sentinel-3, and the future FLEX mission.

The overall aim of this activity was to complement the transdisciplinary database with a creative approach towards the alignment of national programs and the input of multiple actors and stakeholders. Although a focus placed was on vegetation components (e.g. fluorescence, land surface temperature [LST], chlorophyll content, and others), the data will also prove useful for other coastal and atmospheric related applications. During this campaign, several airborne and ground actions in combination with the relevant data processing, scientific data analysis, data storage, and dissemination activities were conducted during the 2019 vegetation period, covering two sites in Germany and one site in Italy. It is anticipated that the collected data will provide a solid basis for future activities in preparation for the FLEX satellite mission.

In the 2019 FLEXSense campaign, our aims during data acquisition and ongoing analysis were as follows:

- Complement and extend the high-quality reference real world data set covering the spatial scales from (i) ground leaf and canopy SIF estimates, selected biophysical vegetation parameters, and quantitative measurements of vegetation functioning and (ii) high-resolution airborne surface reflectance and SIF measurements. Special focus was put on (a) evaluating the potential of SIF to detect early signs of drought, (b) the potential of spectrally high-resolution measurements in the red and near-infrared region to detect potassium in fire plumes and (c) to characterize the concepts of passive and active reference targets for future FLEX Cal/Val concepts. To this end, flight lines from Germany and Italy were recorded during a 3-week campaign window in summer 2019.

- Currently, three different retrieval schemes are available to retrieve SIF from *HyPlant* data (Siegmann et al. 2019). In this activity, we operationally used the spectral fitting method (SFM), which is also the nominal retrieval method for the FLEX satellite mission. While we extended the SFM retrieval for *HyPlant* imagery during the 2018 campaign activity, we for the first time aimed to include quantitative uncertainty estimates (as developed in 2018) operationally in the processing of *HyPlant* data. We aimed to process all technically well-recorded flight lines with the new version of the SFM and also deliver the uncertainty layers. For those flight lines where, for example, insufficient atmospheric parameters or non-vegetated reference pixels are available, we will use the singular vector decomposition (SVD) as a fallback solution.
- Test and validate the different data products across the spatial scales using various data collected during this campaign. We aimed to qualitatively assess the quality of the *HyPlant* imagery, including sensor stability, uncertainties during the instrument calibration, retrieval errors, and errors that are a result of the atmospheric correction. We focused our work on the comparison between FloX and *HyPlant* SIF products as well as on the active and passive reference targets.
- Currently, the level 2 product retrieval schemes for the future FLEX satellite mission are being developed within the level 2 (lvl-2) study and to date mainly modeled data from the E2E simulator are used. In the next steps, the campaign data from this activity will form the basis to test and evaluate the level 2 retrievals based on real world data. To support this, we have delivered maps of top-of-canopy (TOC) radiance and reflectance, F_{687}, F_{760} and F_{tot}.
- Complement existing long time series of selected FLEX core sites in Germany (Selhausen, Transregional Collaborative Research Centre 32 [TR32], and CKA) and Italy (Grosseto), which are currently also under evaluation to become future Cal/Val super sites in ESA's Cal/Val activities.

2.3 SYNERGISTIC CAMPAIGN ACTIVITIES

The FLEXSense 2019 campaign took place in close coordination with (i) the Net-Sense campaign [RD-06], (ii) the ATMOFLEX campaign [RD-05], and (iii) the SARSense campaign activities of ESA [RD-07]. By synchronizing the campaign windows and by using overlapping campaign study sites and flight patterns, data from these three campaign activities can be combined, thus generating various synergies.

ATMOFLEX campaign
During the campaign window, continuous instrumentation that was developed during the ATMOFLEX campaign was operational at the study sites and time series from these instruments complement airborne measurements bridging the spatial and temporal support scales of the satellite and ground-based measurements. The measurements will eventually help to define the Cal/Val strategy for the future FLEX core validation sites.

NET-Sense campaign
During the campaign window, a high-performance thermal sensor developed by NASA (HyTES) was available. The flights during the Net-Sense campaign took place in Italy during June 17–19 and June 21–24, 2019 ([RD-06]). There were no flyovers with the HyTES sensor in Germany.
HyTES was available onboard a British aircraft and was co-mounted with an AisaFENIX sensor. This sensor package was employed over the same study sites in Italy in synchrony with the *HyPlant*/TASI/LiDAR sensor package of this campaign. Flight operations were adjusted for the following purposes:

- To study the impact of the revisit period and the overpath time for specific priority applications, including the accuracy of daily evapotranspiration under partly cloudy and sunny conditions.
- To study the impact of different numbers of bands and the related impact on thermal product accuracy.
- To provide data on daily evapotranspiration and remotely sensed evaporation, to demonstrate how the accuracy decreases beyond acceptable levels, and to evaluate the foreseen error limits per pixel, per land use class and per field.

The HyTES flyovers took place in synchrony with *HyPlant* in Italy (Table 1). The overall objectives of the Net-Sense campaign are derived from the objectives of the land surface temperature mission (LSTM), which aims to address water, agriculture and food security issues by monitoring the variability of LST, and hence evapotranspiration, at the European field scale. During the 2019 campaign, airborne data were acquired by the HyTES airborne sensor and complemented by ground-based in-situ data that were collected close to the flyovers. These in-situ data are surface spectral reflectance, surface spectral emissivity, radiometrically derived surface temperatures, contact surface temperatures, evapotranspiration, and atmospheric parameters, including downwelling radiation and aerosol optical depth. These data are described in detail in the NET-Sense campaign report [RD-06]. Flights of the airborne package of this campaign (*HyPlant*, TASI and Rigel LiDAR) were synchronized with the NET-Sense flyovers in Italy and we were able to record six synchronous flyovers with the two sensor packages (Table 1).

Table 1 Dates of total flyovers with the HyTES and the *HyPlant* sensor in Italy during the 2019 campaign. In brackets, the actual flight time and data acquisition is given in local time.

Date	***HyPlant* flyovers**	**HyTES flyovers**
June 16, 2019	12 (11:53 h – 11:41 h), (14:11 h – 14:24 h)	
June 17, 2019	4 (11:20 h – 11:33 h)	7 (10:02 – 12:15)
June 18, 2019	10 (11:13 h – 11:33 h), (14:11 h – 14:37 h)	11 (10:01 – 12:15)
June 19, 2019	27 (10:16 – 10:38 h), (13:15 h – 13:47 h), (16:11 h – 16:41 h)	12 (10:40 – 12:01)
June 20, 2019	4 (14:12 – 14:25)	20 (09:00 – 10:15), (13:35 – 14:20), (15:51 – 16:30)
June 23, 2019	4 (11:09 h – 11:28 h)	24 (08:56 – 10:10), (11:18 – 12:44), (15:25 – 16:08)
June 24, 2019	14 (11:13 – 11:17 h)	12 (09:22 – 11:21)

SARSense campaign

During the campaign window, the L-band and C-band SAR sensor operated by MetaSensing was available. This sensor package was employed over the same study sites in Germany in synchrony with the *HyPlant*/TASI/LiDAR sensor package of this campaign. The flyovers of the MetaSensing sensor took place on June 25 and 27, 2019. Flight operations were adjusted to generate reference L-band

and C-band datasets to support study of the joint use of EUROS-L and Sentinel-1 data for specific priority applications, including land cover/soil moisture mapping. In addition to the radar measurements for soil moisture, plant samples were taken for the analysis of biomass, carotenoid content and leaf area index (LAI) on June 25, 2019.

3 AIRBORNE INSTRUMENTATION

In order to bridge the gap between point-scale ground-based measurements and the satellite measurements representing 300 m x 300 m, various airborne measurements with the FLEX airborne demonstrator *HyPlant* were performed. Airborne data acquisition was optimized (i) to represent the nominal flyover time of the FLEX satellite mission and (ii) to be in synchrony with Sentinel-2 and Sentinel-3 data. In addition to the optical data from *HyPlant*, thermal data from the TASI imager and 3D surface data from the Riegl LiDAR instrument were recorded and processed. The three sensors were co-mounted and optically aligned within a CzechGlobe aircraft and we recorded data from all three sensors in each flight line.

3.1 HyPlant

The *HyPlant* sensor is a high-performance airborne instrument consisting of two sensor modules: The DUAL module that contains two push-broom imaging line scanners, providing spectral information from 380 nm to 2500 nm, and the FLUO module, which produces data at high spectral resolution (0.25 nm) in the spectral region between 670 nm and 780 nm. Both modules are connected to an Oxford 3052 GPS/INS unit, which provides, synchronously with the image data, aircraft position and orientation information for image rectification and geo-referencing. Both imagers (the DUAL and FLUO modules) are mounted on a single platform with the mechanical capability to align the field of view (FOV) (see Siegmann et al. 2019 for a detailed technical description of the *HyPlant* sensor).

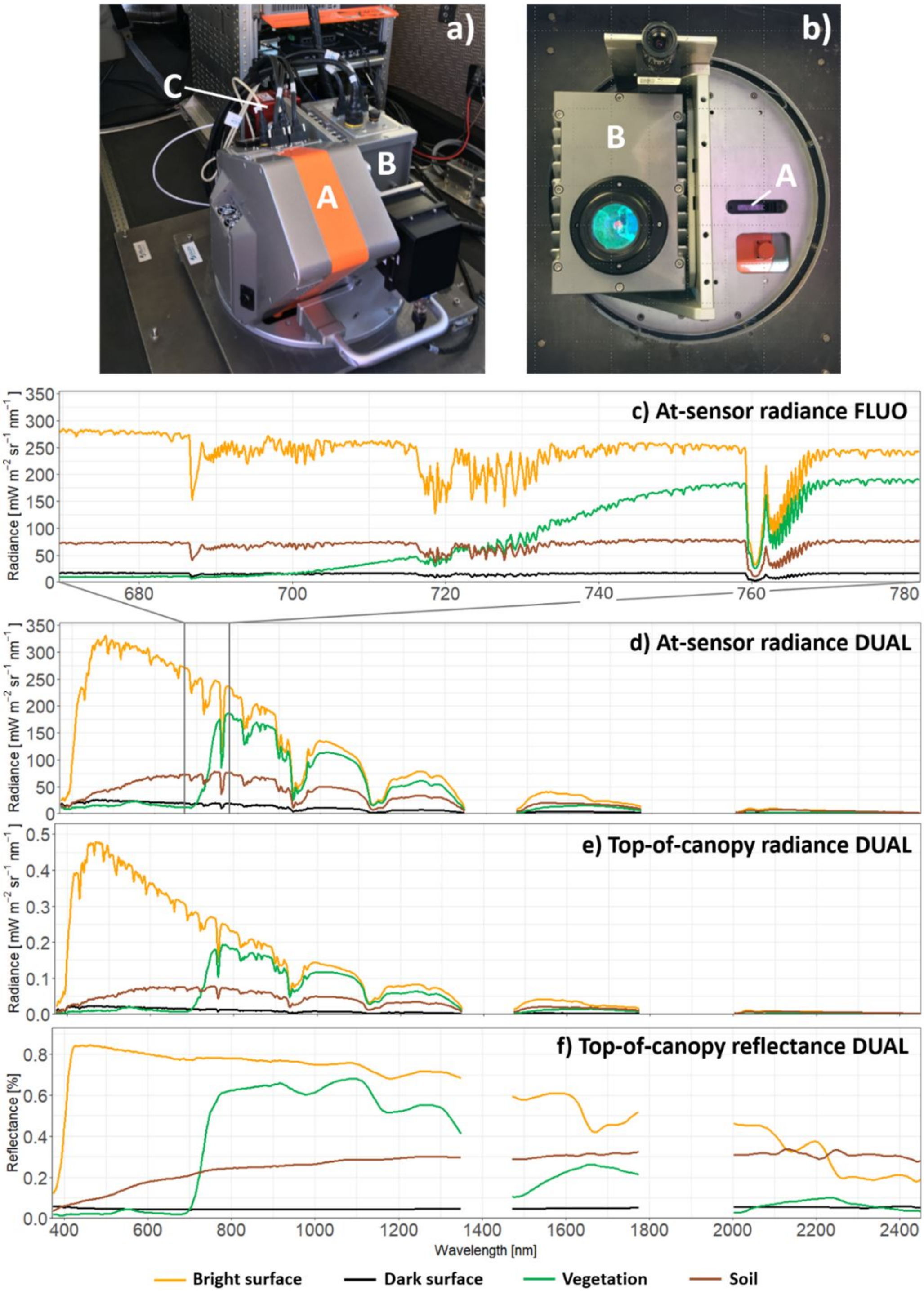

Figure 1 *HyPlant* airborne imaging spectrometer: a) installation of the sensor system in the aircraft, consisting of the broadband DUAL module (A), high-resolution FLUO module (B) and GPS/ INS unit (C); b) *HyPlant* DUAL (A) and FLUO (B) modules installed in the hatch of the aircraft (image taken from below the aircraft); c) *HyPlant* FLUO at-sensor radiance; d) *HyPlant* DUAL at-sensor radiance; e) *HyPlant* DUAL TOC radiance; and f) *HyPlant* DUAL TOC reflectance of selected surfaces (picture taken from Siegmann et al. 2019).

The *HyPlant* airborne imaging spectrometer was developed as a cooperative endeavor between Forschungszentrum Jülich, Germany and the Finnish company SPECIM. As the core reference and demonstration instrument for the FLEX satellite mission, *HyPlant* was the first airborne sensor optically optimized to retrieve the fluorescence full-spectrum, taking advantage of the oxygen absorption and fluorescence near 687 nm and 760 nm. Since the initial testing in 2012, research has confirmed the possibility to retrieve SIF in the O_2-A and O_2-B bands (Rascher et al. 2015, Rossini et al. 2015, Simmer et al. 2015). Since then, *HyPlant* data have been used in various activities and to date 24 scientific publications that use *HyPlant* fluorescence products have been released (Rascher et al. 2015, Rossini et al. 2015, Simmer et al. 2015, Wieneke et al. 2016, Drusch et al. 2017, Middleton et al. 2017, Colombo et al. 2018, Gerhards et al. 2018, von Hebel et al. 2018, Bandopadhyay et al. 2019, Gamon et al. 2019, Liu et al. 2019, Siegmann et al. 2019, Tagliabue et al. 2019, Yang et al. 2019, Pinto et al. 2020, Tagliabue et al. 2020, Vila-Guerau de Arellan et al. 2020, Hornero et al. 2021, Bandopadhyay et al. 2021, Porcar-Castell et al. 2021, Scharr et al. 2021, Siegmann et al. 2021, and Zeng et al. 2021).

The first *HyPlant* system has been continuously updated and the optical path, detector unit and read-out electronics have been continuously improved. Since the 2018 FLEXSense campaign activities, the *HyPlant* sensor has reached a consolidated status and the system is now labeled *HyPlant* 3. *HyPlant* 3 is annually calibrated and calibration data have shown a stable and comparable performance of the sensor since 2018. No sensor or data artifact is known from the laboratory calibration and we thus assume that the currently used *HyPlant* 3 sensor version is a consolidated airborne sensor for optical reflectance and fluorescence measurements that provides radiometrically stable and reproducible data with a geo-accuracy of one pixel (Siegmann et al. 2019).

3.1.1 Calibration

The *HyPlant* sensor is calibrated annually at the Specim calibration facility (Oulu, Finland). The calibration consists of radiometric and spectral calibration. Both calibration steps are done with an integration sphere (Gigahertz UPK190-S, manufactured by Gigahertz-Optics, Türkenfeld, Germany), which is equipped with Ar and Ne(Hg) spectral calibration lamps. Both modules (DUAL and FLUO) are calibrated separately. The calibration is repeated over the winter months and calibration files and traceability documents, calibration results and calibration parameters are available for 06/2012, 04/2013, 03/2014, 02/2015, 05/2017, 05/2018, 03/2019, 01/2020 and 01/2021.

In the following, we analyze the calibration results of the FLUO module that were performed in March 2019 (with some additional data that were obtained in January 2021) with the goal of providing a quantitative estimate of the calibration uncertainty. These estimates of sensor and calibration uncertainties are essential for calculating the overall error and uncertainty of *HyPlant* SIF products (see 6.1). Similar data are also available for the *HyPlant* DUAL module, and thus similar analysis were also performed for *HyPlant* broad band spectrometer data.

Radiometric calibration

For the radiometric calibration, the two *HyPlant* modules are placed in front of the calibration sphere and 100 images are acquired with the calibration sphere either being turned off or on. These 100 ‘dark images’ and 100 ‘light images’ are then averaged to two single calibration images, which are subtracted from each other (dark image subtraction). This produces a single image file that contains the radiometric correction parameters for every pixel of the detector (see Figure 2 for the radiometric correction parameters for the 2019 campaign). These radiometric parameters are comparable across different years and the spatial effects that are seen in Figure 2 are also visible in data from other years. In these data some optical artifacts are visible, which are typical for any imaging spectrometer, such as a gradient towards the edge of the detector or the vertical split of the detector. It is clearly visible that these artifacts are related to the read-out electronics of *HyPlant.*[1] After comparing the calibration results from the different years, we concluded that no aging or degradation of the detector in the FLUO module was apparent, even though we did see some variations in the annual calibration files, which presumably are associated with the uncertainty in the calibration units at SPECIM (see below).

To get an understanding of the uncertainty that may be associated with this radiometric calibration procedure, we requested from SPECIM the single measurements of the 100 dark and 100 light images. Although we were only able to receive these 'raw' data from the 2020/2021 calibration, we can assume that there is no major difference between the uncertainty in 2018/2019 and 2020/2021. From the 100 single measures, we calculated the uncertainty of the radiometric calibration procedure per se, by calculating the error propagation that is needed to account for uncertainties in the dark and light image acquisition.

The radiometric correction coefficients (*g*) are calculated according to eq. 1 from a series of line acquisitions $DN_{li}^{i}(x,\lambda)$ of a spectrally and radiometrically invariant light source (calibration lamp) *L* and a series of dark acquisitions $DN_{da}^{i}(x,\lambda)$

$$g = \frac{L}{\mu(DN_{li}^{i}) - \mu(DN_{da}^{i})} \qquad \text{eq. 1}$$

Then, under the assumption of normal and uncorrelated error distributions of *L* and *DN*, we can approximate the uncertainty on the gain measurement *g* as

$$\sigma_g^2 = \frac{\sigma_L^2}{DN^2} + \frac{\sigma_{DN}^2 L^2}{DN^4}, \text{ with } \sigma_{DN}^2 = \sigma_{DN_{li}}^2 + \sigma_{DN_{da}}^2 \qquad \text{eq. 2}$$

The error of the calibration unit of SPECIM (deviation of the true radiance values of the integrating sphere) was provided by the manufacturer, and we thus assume that for the FLUO module, the error that results from the calibration unit (r_L) to be equal 0.03 (Table 2). Even though the calibration is done in the optical laboratory of the manufacturer, the calibration unit is only of medium quality and the reliability of the calibration facility is limited.

Table 2 Error of the calibration unit (Gigahertz integrating sphere) as it is used at the SPECIM calibration facility. The numbers are based on the information from the manufacturer.

Wavelength nm	**Relative error % (k=2)**
400 to 420, steps 10 nm	± 6.0
430 to 450, steps 10 nm	± 4.0
460 to 490, steps 10 nm	± 3.5
500 to 990, steps 10 nm	± 3.0
1000 to 1100, steps 10 nm	± 4.0

[1] See the results from the HYPER project ([RD-10]) for further details.

1150 to 1700, steps 50 nm	± 4.5
1750 to 1950, steps 50 nm	± 6.5
2000 to 2150, steps 50 nm	± 6.5
2200 to 2400, steps 50 nm	± 8.5
2450 to 2500, steps 50 nm	± 9.0

With eq. 3

$$r_L(\lambda) = \frac{\sigma_{L(\lambda)}}{L(\lambda)} \qquad \text{eq. 3}$$

We can derive eq. 4

$$\sigma_L^2 = r_L^2\, L^2 = r_L^2\, g^2\, \left(\mu(DN_{li}^i) - \mu(DN_{da}^i)\right)^2 \qquad \text{eq. 4}$$

Taking the provided radiometric correction coefficients into account, this can be translated into a mean relative uncertainty of the raw digital numbers according to eq. 5. See also Figure 2 for a spatial and spectral representation of the uncertainties of the *HyPlant* FLUO module.

$$r_{DN} = \mu\left(\frac{\sigma_{DN}(x,\lambda)}{DN(x,\lambda)}\right) = 0.003 \qquad \text{eq. 5}$$

Thus, the relative uncertainty that is associated with the calibration routine and the instability of the detector itself is by a factor 10 smaller than the uncertainty that is associated with the calibration unit (we calculate a mean relative uncertainty on the DN measurements of r_{DN} = 0.003 compared to the manufacturer provided r_L = 0.03). Accordingly, to improve the future accuracy of *HyPlant* data, we strongly recommend developing a better calibration option for the *HyPlant* sensor. The most straight forward option would be a better absolute calibration or upgrade of the integrating sphere at SPECIM.

Using the calculations above, we now can also provide an analysis of the radiometric correction coefficients (g) and their uncertainties ($\boldsymbol{\sigma}^2_g$) across the 2-dimensional detector of the *HyPlant* sensor (Figure 2, Figure 3, and eq. 6).

$$\sigma_g^2 = \frac{\sigma_L^2}{DN^2} + \frac{L^2\sigma_{DN}^2}{DN^4} \equiv \Omega_L^2 + \Omega_{DN}^2 \qquad \text{eq. 6}$$

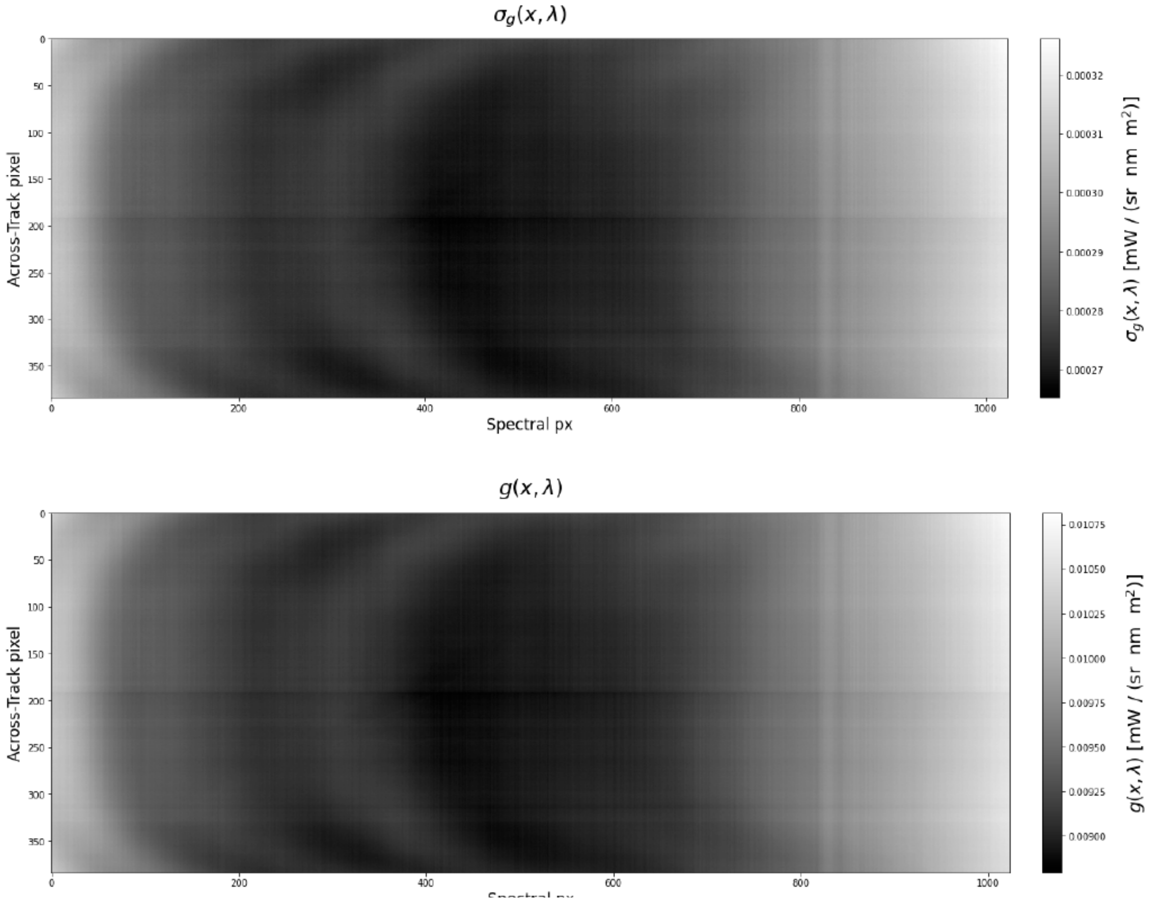

Figure 2 Radiometric calibration coefficients and their 'total error' (i.e. error from the offset of the calibration lamp plus the uncertainty of the detector) calculated from the 2021 laboratory calibration files from the calibration facility at SPECIM. The lower panel shows the radiometric calibration coefficients that are used to translate the raw DN measurements of every detector element into physically correct units. The upper panel is the combined error and uncertainty of these calibration coefficients derived from 100 single measurements by *HyPlant* in front of the calibration sphere. It has to be noted that the error of the calibration lamp strongly contributes to the total error, while the uncertainty of the detector is comparably smaller (c.f. Figure 4).

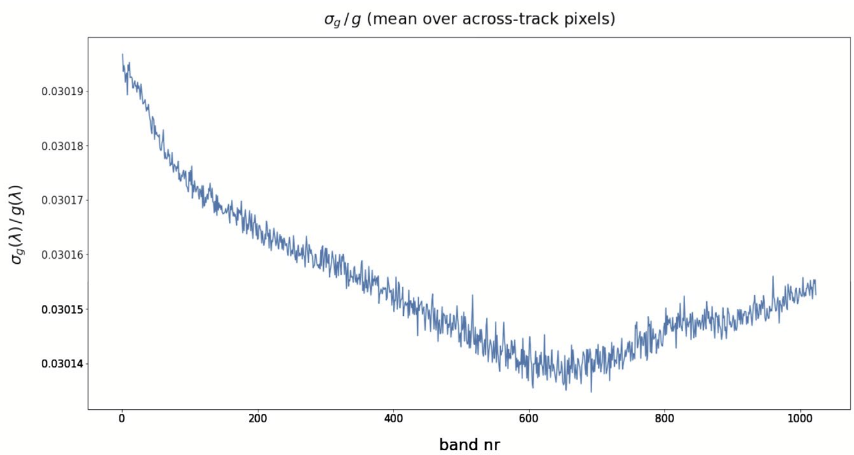

Figure 3 Relative uncertainty (σ_g/g) across the spectral dimension (spectral bands) of the FLUO module of *HyPlant* as derived from the calibration data given in Figure 2.

It is obvious that the uncertainty follows the values of g, which is explained by the comparably large uncertainty of the calibration unit (σ_L^2) (Figure 4). From the actual numbers it becomes clear that by far the greatest proportion of the absolute uncertainties are introduced by the calibration facility and only a minor share of the uncertainty can be traced to the detector and the radiometric correction coefficient.

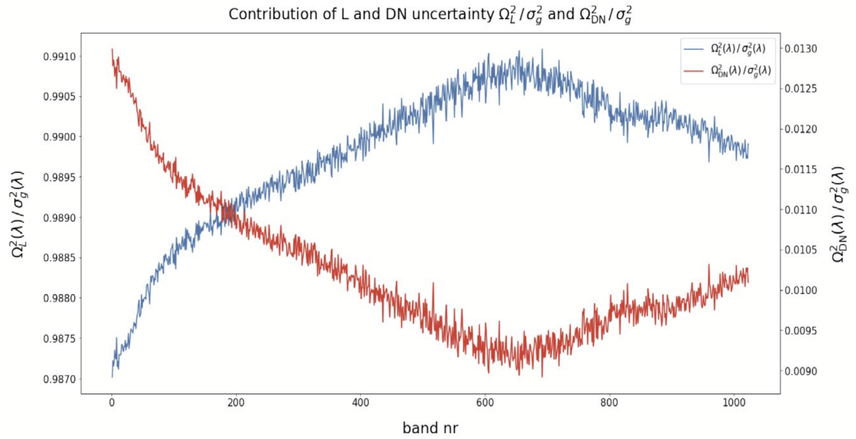

Figure 4 Relative contribution of uncertainties that are introduced by the calibration unit (L) and those uncertainties introduced by the detector (DN) to the variance of the radiometric correction coefficients (g). Here it become obvious that the error that is introduced by the offset of the calibration lamp is by far the largest source of uncertainty, greatly exceeding the uncertainty of the radiometric correction factors.

To visualize the uncertainty and their spatial contribution during the pre-processing steps, we have selected one representative flight line from Grosseto, which we also use for further analysis in chapter 8.2.4. We chose the flight line that was recorded at 10:35 as this is closest to the nominal overpass time of the FLEX satellite mission and present raw digital numbers as recorded by the detector of *HyPlant* (Figure 5, upper panels), the radiometrically corrected at-sensor radiance data (Figure 5, second row of panels), the estimated uncertainty of the detector element (Figure 5, third row of panels), and the absolute (or total) error of the at-sensor radiance data (Figure 5, lower panels). As outlined above highest uncertainty during preprocessing derives from the poor absolute accuracy of the calibration facility (Table 2). The uncertainty that is related to the noise of the detector and to the uncertainty of the calibration coefficients is comparably small (only approximately 10% of the total error). Thus, we here present both uncertainty estimates that are associated with preprocessing. Firstly, the estimated uncertainty that is related to the detector element only (Figure 5, third row of panels), which present the minimal error that is inherent in the *HyPlant* system and which would also be present if *HyPlant* was calibrated in a higher performance (or 'perfect') calibration facility. Secondly, the actual total uncertainty that is present in current *HyPlant* data and which is mainly related to an off-set of the true radiance value because of the error of the calibration lamp (Figure 5, lower panels). To illustrate the magnitude and spatial distribution of the uncertainty of at-sensor radiance, we chose four relevant spectral bands of the FLUO module, namely the two bands at the center of the oxygen absorption features (687.5 and 760.2 nm) as well as two bands at the shoulders of the oxygen absorption features (680 and 750 nm) (Figure 5).
For realistic illumination conditions, the uncertainty that is related to the detector itself is smaller than 0.6 $mWm^{-2}nm^{-1}sr^{-1}$ throughout the spectral and spatial domain of the detector (using the full resolution of the detector). Within the oxygen absorption features, where photon fluxes are generally lower, this uncertainty is smaller than 0.2 $mWm^{-2}nm^{-1}sr^{-1}$. As expected, highest absolute

uncertainties were found at bright surfaces. Absolute error in the at-sensor-radiance data however are considerably larger and are caused by the offset of the calibration lamp (Figure 5, lower panels). This large error could be directly reduced by using a better calibration lamp and it has to be noted that for fluorescence retrieval the uncertainty of the detector element is of importance. Most retrieval approaches exploit the relative band depth of the absorption features and thus the additive offset that is caused by the calibration lamp is not affecting the SIF products. Thus, for future error estimates and future calculation of error budgets, we recommend to use the estimated uncertainty of the detector element, the absolute at-sensor error shall however be used when comparing radiance values.

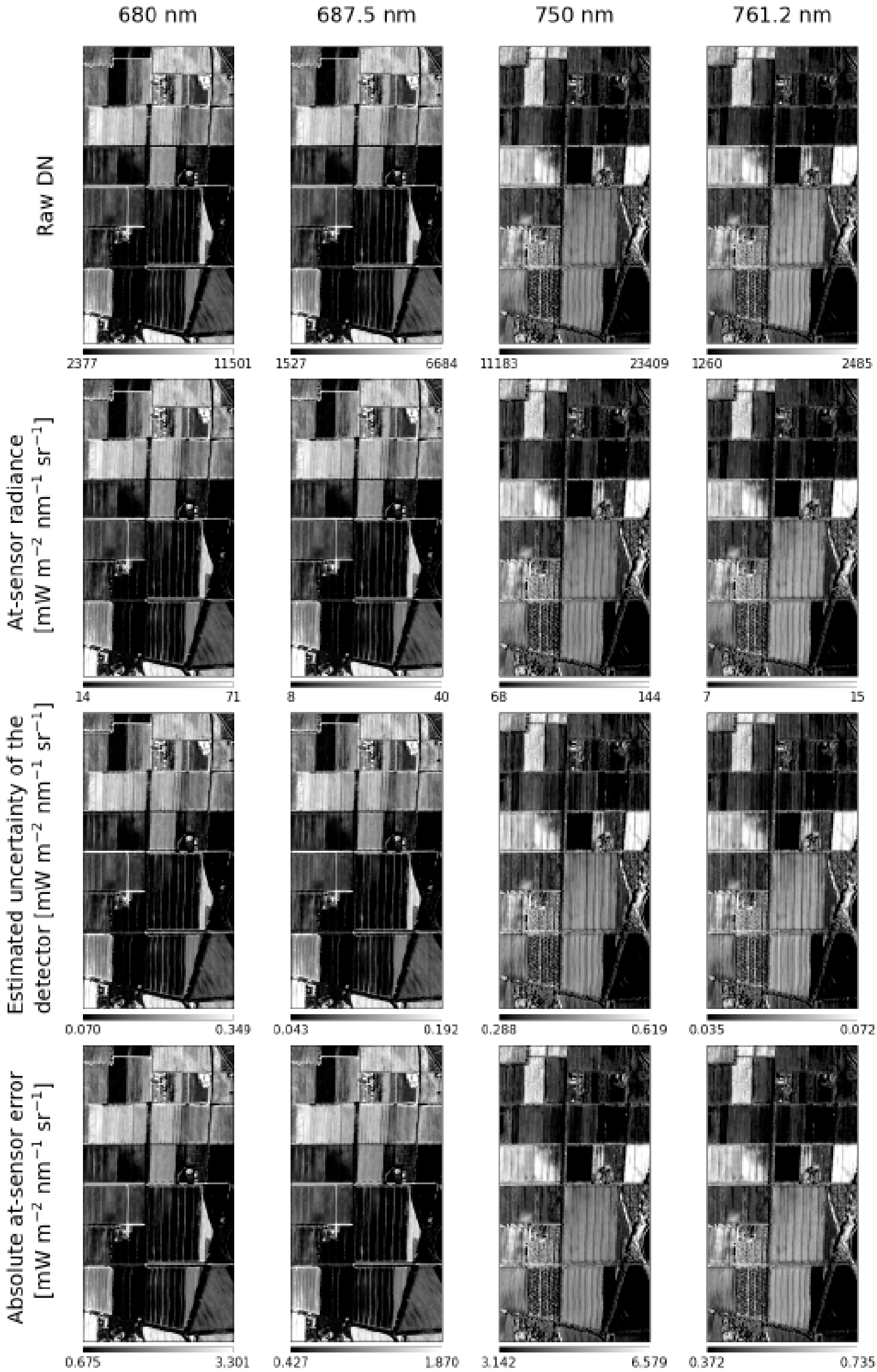

Figure 5 Uncertainty and error estimates that are associated with the laboratory calibration and pre-processing of the data of the FLUO module of *HyPlant* exemplified at the representative flight line that was recorded at 10:35 in Grosseto (see chapter 8.2.4 for more details on this flight line). Upper panels: raw digital numbers as recorded by the FLUO module of *HyPlant*; second row: radiometrically corrected at-sensor radiance; third row: estimated uncertainty of the detector; lower row: absolute error of the at-sensor radiance data. Uncertainties and errors were calculated as outlined in this chapter and the color bars were chosen to show the 98% data range, thus to present the full range of possible uncertainties in that flight line.

Spectral calibration

The *HyPlant* modules were taken out of the baseplate and were mounted in front of the Lot-Oriel monochromator in such a way that the exit slit of the monochromator is perpendicular to the exit slit of the spectrograph. Monochromator wavelength was scanned over the wavelength range of the spectrograph with 0.02 nm steps. Fifteen frames were collected, averaged and dark-frame corrected at each step. At each spectral band, a Gaussian function was fitted to the data. Full width at half maximum (FWHM) of the band was obtained from the fitted data. The final FWHM at each band was calculated as an average of 10 adjacent bands. Based on the 2019 calibration files, the FWHM was determined to be between 0.33 and 0.35, with only minor changes across the spectral window. This is consistent previously reported (Siegmann et al. 2019) and we can thus assume that the FWHM of the *HyPlant* sensor has remained stable over its years of operation. We, however, want to point out that the monochromator of the SPECIM calibration unit is not accurate enough to provide the FWHM with high accuracy or to calculate a spectral response function. In previous studies (HYPER project [RD-10] and Scharr et al. 2021), we evaluated different options for gaining a better characterization of the spectral response characteristics of *HyPlant*. The calibration units listed below could be modified and used for a highly accurate characterization of the spectral response of *HyPlant*. However, this would require substantial effort and was clearly beyond the scope of these campaign activities. Nevertheless, we recommend re-evaluating these options for future Cal/Val activities, as *HyPlant* may become an integrated component.

According to our knowledge, the following calibration facilities could provide high-resolution spectral calibration data for *HyPlant* with adaptations to associated optical requirements:[2]

- Calibration Homebase at DLR, Oberpfaffenhofen, Germany (Gege et al. 2009, Brachmann et al. 2016).
- Calibration facility at the National Physics Laboratory, Teddington, UK (Origo et al. 2020)
- Calibration facility at the Physikalisch-Technische Bundesanstalt, Braunschweig, Germany
- Calibration facility of the National Institute for Laser Plasma and Radiation Physics (PhIL) of the CETAL-INFLPR, Romania (Mihai et al. 2018)
- Calibration facility GLAMR, which is NASA Goddard Space Flight Center's portable version of the National Institute of Standards and Technology (NIST) Spectral Irradiance and Radiance responsivity Calibrations using Universal Sources (SIRCUS) (Brown et al. 2006, Paynter et al. 2020)

Characterization of the point spread function (PSF)

The PSF of *HyPlant* was characterized in the Specim calibration facility in 05/2017 and 05/2018 (Figure 5 in Siegmann et al. 2019). The PSF proved to be stable between the two characterizations and we then used this PSF to develop deconvolution methods that can optionally be used during the pre-processing of *HyPlant* data.[3] Details on the process for acquiring the PSF in the calibration facility, on the path to spectrally sharpen the PSF, and to finally use the PSF for data deconvolution is presented in detail in Scharr et al. (2021).

[2] The following information is based on various bilateral discussions with the operators of the calibration facilities. Substantial technical adjustments would be needed at all calibration facilities before *HyPlant* could be used with the large foreoptics.

[3] Currently, one method is included in the operational processing chain at Forschungszentrum Jülich; further methods are evaluated and described in Scharr et al. (2021).

Thus, all information on the influence of the PSF and its optional deconvolution during preprocessing is available. The deconvolution process involves nonlinear data transformation. Calculating an error propagation for the deconvolution is mathematically complex and could not be done within the scope of this activity.

Summary of uncertainties during *HyPlant* calibration

Based on the considerations given in this section, we can conclude that (i) the *HyPlant* sensor has provided stable radiometric performance since its technical refinement in winter 2014/2015 (i.e. *HyPlant 2* & *HyPlant 3*, cf. Siegmann et al. 2019), (ii) all elements for a full error propagation of *HyPlant* calibration and pre-processing is available, (iii) the main source of error is associated with the radiometric and spectral inaccuracy of the SPECIM calibration facility. The error that results from these inaccuracies in the calibration facility by far exceeds *HyPlant's* native measurement uncertainty. Based on our assumptions and findings from this section, the error introduced by calibration facility is larger than the uncertainty in the sensor itself by a factor of approximately 10. We thus can conclude that the long-term accuracy of *HyPlant* data at all levels can be substantially increased by using a better calibration facility for future Cal/Val activities. These better calibration data can then be used to calculate a full error budget for the sensor uncertainty of *HyPlant's* FLUO module.

3.1.2 Processing

The *HyPlant* processing chain gives an overview of the single processing steps of the DUAL and FLUO modules, from raw data to final products, such as TOC radiance, TOC reflectance, vegetation indices and fluorescence maps (Figure 6). The processing chain consists of four parts: the first part describes the transfer of raw data, associated navigation and header files, and calibration data of the two separate processing lines for the DUAL and FLUO modules. The second part explains the processing of the DUAL data, while the third and fourth parts deal with the processing of the FLUO data and the usage of different SIF-retrieval methods (Figure 6).

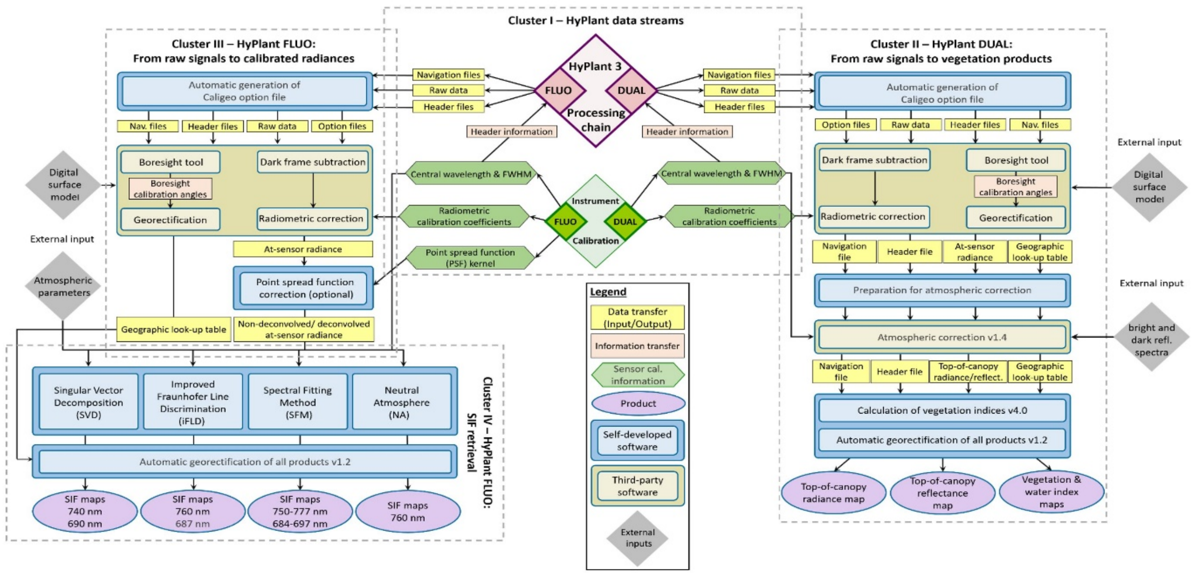

Figure 6 Overview of the *HyPlant* processing chain consisting of the four processing clusters. Picture taken from Siegmann et al. 2019.

The following paragraphs provide a more detailed overview of the processing of the DUAL and FLUO data (further details can be found in Siegmann et al. 2019).

DUAL module

Raw data from the *HyPlant* DUAL module are processed to at-sensor radiance using the software CaliGeoPRO and the most recent radiometric calibration provided by Specim. Furthermore, geometric look-up tables (GLT) and MapLoc files of the georectification were produced with CaliGeo and stored. Atmospheric correction was performed with the commercial software Atmospheric & Topographic Correction algorithm (ATCOR). Generated TOC reflectance and radiance data were georectified using the stored GLT files.

Vegetation indices that are related to chlorophyll content, water content, LAI, photosynthesis and non-photochemical quenching are calculated from the TOC reflectance data by default from *HyPlant* DUAL data (Siegmann et al. 2019).

FLUO module

Another part of the *HyPlant* processing chain describes the procedure of converting FLUO raw data to at-sensor radiance (Figure 6). For this purpose, the CaliGeoPro software is used with the most recent radiometric calibration data that are provided by Specim within the framework of the annual calibration procedure. As the result of this pre-processing, the user receives the at-sensor radiance and the GLT file in a similar manner to the DUAL processing. In contrast to the DUAL module, the radiometric correction of the FLUO module can optionally be extended by the application of a custom-made point spread function (PSF) deconvolution procedure. Ideally, an imaging spectrometer looking at a monochromatic point source should produce a single pixel response. In real systems, however, this is not the case, and the resulting signal spreads in the sensor matrix around this pixel. This distribution of light across the sensor is called instantaneous PSF and in the case of fluorescence retrieval may substantially affect the magnitude of the fluorescence signal. The sensitivity of the retrieved fluorescence products to an imperfect PSF was first described by Alonso et al. (2008) and then further evaluated by Scharr et al. (2021). Now it is established that the PSF should be minimized or corrected during preprocessing. In *HyPlant* 3, the PSF is optimized and *HyPlant* 3 operates with a greatly improved PSF. Based on some forward studies, we know that the impact of the PSF on fluorescence products is less than 20% for normal measurement settings, but nevertheless we have implemented a deconvolution routine that follows the van Cittert approach (Jähne 2005), which can be switched on or off by the user (Siegmann et al. 2019). The impact of the PSF on the fluorescence retrieval and the performance of the different point-spread function deconvolution routines were recently evaluated in detail and can be found in Scharr et al. (2021).

The main processing steps are labeled in the file name of the flight line (Table 3). Each file name contains the acquisition date, area and local time of the data acquisition, as well as information about the flight altitude from which the ground pixel size can be concluded. The basic information recorded was the name of the flight line, the heading of the aircraft during data acquisition and which module (DUAL or FLUO) the flight line was recorded with. After the radiometric and wavelength calibration, the label ‘radiance’ is added. *HyPlant* DUAL TOC radiance files are stored with the ‘img_surfrad’ label. The TOC reflectance files are additionally spectral polished and smile corrections are applied (these files are labeled with ‘img_atm_polish_smcorr’ in the file name). From TOC reflectance, vegetation indices are calculated and vegetation index files are labeled with ‘indices_up’.

For the FLUO module, the label 'deconv_i1' indicates that the deconvolution was applied using the PSF. The label 'Fs_linear_v2' indicates that the fluorescence maps were calculated with the SVD method. The label 'FIXDEM_V5' shows that the maps were calculated with the improved Fraunhofer line depth (iFLD) method. The fluorescence maps calculated with the SFM are stored in files, marked with the label 'SFM_ALL_noborder'. The suffix 'rect' indicates *HyPlant* flight lines for which the calculated product was georectified.

Table 3 The file names for the different *HyPlant* products using data acquired at the Selhausen test site in Germany as an example. Final products are marked bold.

Acquisition date	**Acquisition area**	**Recording time (local)**	**Flight altitude**	**Module of the sensor**	**Processing steps DUAL**	**Processing steps FLUO**
YYYYMMDD	-SEL (Selhausen)	-hh:mm	-0600 (1 m x 1 m pixel)	-FLUO	-radiance (radiometric calibration file of SPECIM was applied)	-radiance (radiometric calibration file of SPECIM was applied)
				-DUAL	**-img_surfrad (atmospherically corrected radiance data)**	-deconv_i1 (deconvolution of the spectra to correct the point spread function)
					-img_atm_polish_smcorr (atmospherically corrected reflectance data, with applied spectral polishing and smile correction)	**-FIXDEM_V5 (fluorescence maps calculated with brightness correction of the iFLD method)**
					-indices_up (calculation of selected vegetation indices)	**-Fs_linear_v2 (fluorescence maps calculated with the SVD method)**
					-rect (georectification using the GLT file)	**-SFM_ALL_noborder (fluorescence maps calculated with the SFM)**
						-rect (georectification using the GLT file)

Three different fluorescence retrieval methods have been implemented in the *HyPlant* processing chain since 2012: iFLD, SVD and SFM. During the 2019 campaign, all methods were applied to all flight lines.

SIF retrieval according to the SVD

The SVD retrieval method is a form of spectral fitting method for fluorescence retrieval (Guanter et al. 2012, Joiner et al. 2013). It also represents the at-sensor radiance as the sum of the radiance reflected by the surface and the fluorescence contribution. The reflected radiance is constructed as the product of a spectrally smooth surface reflectance (modeled as a polynomial in wavelength) and the atmospheric absorption. However, instead of using explicit radiative transfer modeling to calculate atmospheric absorption along the spectral fitting window, this is modeled as a linear combination of orthogonal spectral functions derived from the data through singular vector decomposition (similar to principal component analysis, PCA) (Siegmann et al. 2019). The SVD method for *HyPlant* imagery was established in 2014 and has been used since then for retrieving SIF from the FLUO data.

SIF retrieval using the iFLD method

The iFLD method used in the *HyPlant* processing chain is based on the iFLD method initially proposed by Alonso et al. (2008), which was adapted to allow SIF retrievals from the FLUO module of *HyPlant* (Rascher et al. 2015). The SIF signal is retrieved at two wavelengths: the oxygen absorption band at 687 nm (O_2-B) and 760 nm (O_2-A).

All required atmospheric transfer functions are obtained from MODTRAN5 (Berk et al. 2005) simulations, in combination with the MODTRAN5 interrogation technique (Damm et al. 2015; Verhoef et al. 2003, 2003a, 2007). For the airborne data, an empirical constraint based on non-vegetated reference surfaces is additionally implemented to account for uncertainties in the characterization of the atmosphere and remaining sensor artifacts (i.e. spectral shifts and detector miscalibration). Details on this approach can be found in Damm et al. (2014). The iFLD method can only be applied with sufficient non-vegetated reference pixels across track along the whole flight line (Siegmann et al. 2019).

SIF retrieval algorithm with soil correction

Airborne fluorescence retrieval based on the SFM (Cogliati et al. 2018) is aimed at quantifying the filling-in of canopy fluorescence within the O_2 absorption bands (Cogliati et al. 2015). The red and far-red fluorescence peaks are retrieved from *HyPlant* data by analyzing narrow spectral windows centered at the two O_2-B and O_2-A bands, respectively. The algorithm simulates the at-sensor radiance spectra at the O_2-A absorption band by means of a coupled surface/atmospheric radiation transfer equation (RTE), as described in Cogliati et al. (2015) and Verhoef et al. (2018). The atmospheric transmittance, path radiance and spherical albedo are simulated by the MODTRAN5 model (Berk et al. 2005). SIF and reflectance are modeled by using simple mathematical functions (piecewise spline and Gaussian-like functions) within the spectral window at the O_2 absorption bands. The retrieval algorithm simulates at-sensor radiance based on the forward model and optimizes SIF and reflectance until the best match with *HyPlant* FLUO radiance spectra is obtained.

The spectral fitting methodology that was developed during the 2018 FLEXSense campaign for *HyPlant* imagery uses an image-based technique to obtain a simplified and more robust characterization of the atmospheric variables, by exploiting the spectral information from non-vegetated pixels within the O_2 absorption bands. Specifically, the methodology aims at estimating the 'effective surface-sensor distance', i.e. the actual geometric distance that reproduces the O_2 absorption observed on non-vegetated surfaces (hereafter, the 'H1' parameter in accordance with MODTRAN). The approach allows the effect of atmospheric pressure to be included indirectly within MODTRAN5, resulting in more accurate modeling of the spectra in the range of the O_2 absorption bands. In practice, the method consists of the following steps that are systematically and automatically applied to the images: i) identifying non-fluorescence pixels (normalized difference vegetation index (NDVI) <= 0.1) at nadir; ii) estimating the effective surface-sensor path length on the basis of a MODTRAN look-up-table (LUT, diverse surface-sensor distances) and retrieval of SIF over non-fluorescence pixels assuming zero value; iii) decoupling SIF and reflectance by means of the SFM.

The recent developments mainly involved the design and implementation of operational quality flags related with the *HyPlant* at-sensor radiance spectra and the estimation of uncertainty related to the fluorescence/reflectance retrieval.

Figure 7 *HyPlant* processing steps including quality flags, uncertainty and a final reformatting of the output SIF map product.

Level 1 Quality Flags for SIF retrieval

Quality flags provide information about the instrument and data acquisition conditions, such as solar zenith angle (SZA), view zenith angle (VZA), surface topography, cloud cover, the availability of non-fluorescence reference surfaces and signal-to-noise ratio (SNR). Some quality flags have a general meaning (SZA, VZA, SNR), while surface topography and non-fluorescence pixels are intended to be used in SIF retrievals. For further information, see the FLEXSense 2018 final report ([RD-03]).

- Solar zenith angle (SZA)
- View zenith angle (VZA)
- Surface topography
- Cloud mask
- Non-fluorescence reference surface (nadir +/- 30 pixels)
- Signal-to-noise ratio (SNR)

Per-pixel SIF retrieval uncertainty

The fluorescence retrieval uncertainty (1σ) is estimated according to the standard rules for non-linear least square problems. Notably, the SFM retrieval module is based on a non-linear function minimization that finds the optimal set of parameters (fluorescence and reflectance) values that minimize a cost function (least-squares) between the *HyPlant* at-sensor radiance and the modeled spectrum computed by the retrieval model. The asymptotic normal distribution for the parameter estimate is a standard method to estimate uncertainty from non-linear least square fit. The confidence interval of the estimated parameters assumes that the Jacobian matrix (*K*) of the least-squares curve fitting is obtained at the solution point. *K* is defined as the partial derivatives of the cost function *f* with respect the free parameters around the final solution:

$$K = \begin{matrix} \frac{\partial f_1}{\partial x_1} & \cdots & \frac{\partial f_1}{\partial x_M} \\ \vdots & \ddots & \vdots \\ \frac{\partial f_N}{\partial x_1} & \cdots & \frac{\partial f_N}{\partial x_M} \end{matrix} \qquad \text{eq. 7}$$

The uncertainty for each of the retrieved parameters is given by the following equation, where *b* is the coefficient estimated by the numerical optimization and *t* is a factor that depends on the confidence level (fixed to 95%) computed using the inverse of Student's *t* cumulative distribution function (Abramovitz & Stegun 1964).

$$C = b \pm t\sqrt{(S)} \qquad \text{eq. 8}$$

S is a vector of the diagonal elements from the covariance matrix of the estimated coefficients, δ is the mean squared error of the residuals for all the spectral channels and υ the degrees of freedom.

$$s^2 = \frac{1}{\sqrt{\upsilon}} \sum_{i=1}^{N} \delta_i^2 \qquad \text{eq. 9}$$

The uncertainty value estimated within the SFM includes the contributions from different error sources along the data processing chain, also including some uncertainties propagated from the level 1 processing. Giving the nature of the retrieval algorithm in which image-based techniques are employed to refine the radiative transfer (RT) model atmospheric simulations (MODTRAN), the uncertainties can be addressed to: i) forward model assumptions (i.e., shape of fluorescence/ reflectance), ii) numerical optimization process (i.e., iterative search of the best forward model parameters), iii) atmospheric modeling, iv) instrumental random noise. However, a more comprehensive study should consider the more complex and full propagation of the uncertainties from the level 1 at-sensor data processor to the outputs of the level 2 SFM fluorescence retrieval.

3.1.3 *HyPlant* FLUO detector split

In a few *HyPlant* SIF maps, an artifact is visible in form of a vertical split in the middle of the map (corresponding to the middle of the FLUO detector). Such SIF maps are characterized by lower SIF values on the left and higher SIF values on the right side or the other way around. This artifact is referred to as 'detector split' in this section. Figure 8 shows example SIF_{687} and SIF_{760} maps of the nursery near Grosseto recorded on June 19, 2019 at 13:27 local time, in which the detector split is visible in the middle of the map.

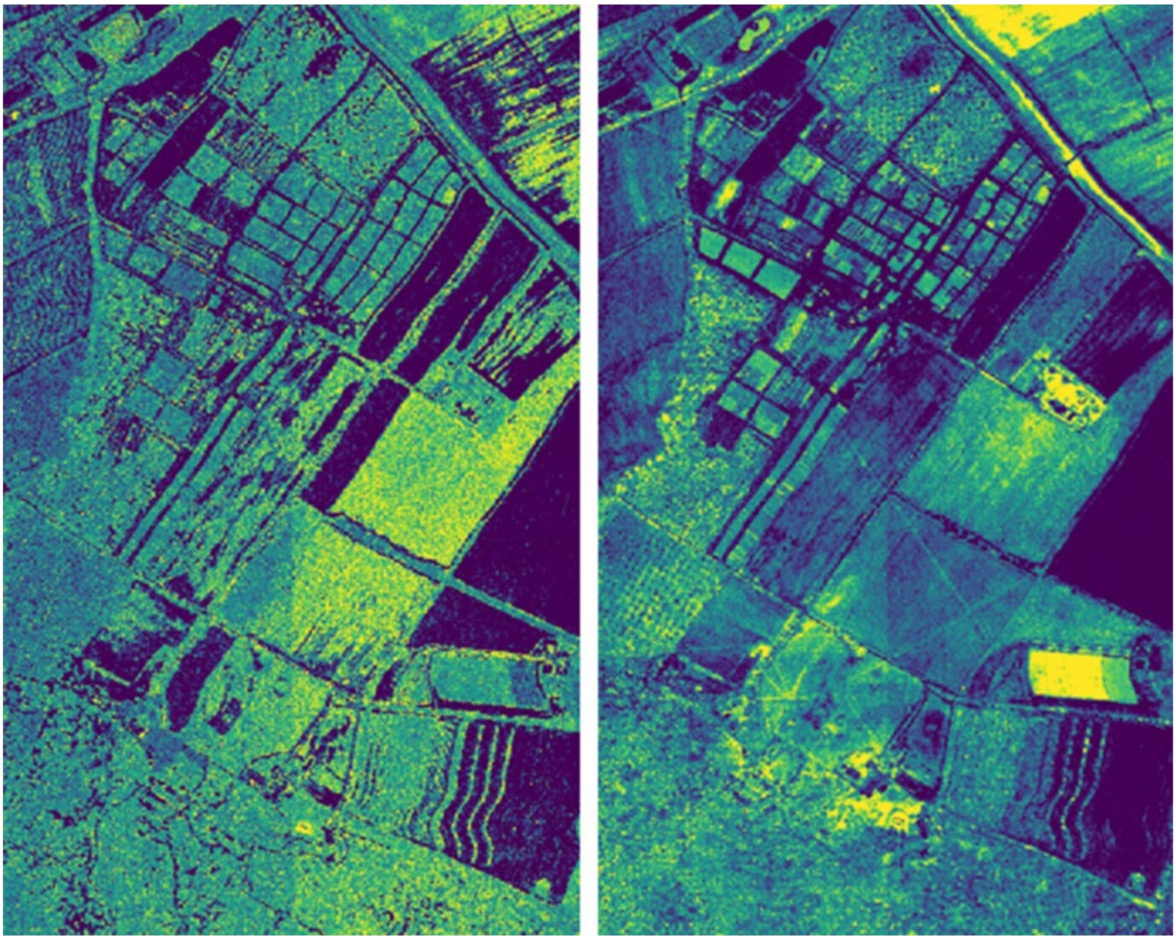

Figure 8 Subsets of *HyPlant* SFM SIF_{687} and SIF_{760} maps of the nursery near Grosseto recorded on June 19, 2019 at 13:27 local time. Both SIF maps are characterized by a lower SIF values on the left and higher SIF values on the right side divided by a border in the middle of the detector.

The aim of this analysis was to find the origin of this artifact in order to understand better if it is related to SIF retrieval, the pre-processing of *HyPlant* FLUO data, or if it is already included in the raw data. During a first visible inspection of the raw and at-sensor radiance data of the flight line presented in Figure 8, the artifact was not visible. Therefore, a PCA was applied to the 1024 spectral bands of the raw and at-sensor radiance data to convert each to 20 principal components (PCs). The aim of a PCA is to convert high-dimensional (e.g., hyperspectral) image data to a different feature space, in which the image is represented by a distinctly lower number of PCs that are ordered by the amount of image variance they explain. Normally, the first PCs contain most of the image variance, while the lower order PCs contribute a distinctly lower amount of variance. In the case of the analyzed example flight line, the detector split was firstly visible in PC 7 of the raw and PC 8 of the at-sensor radiance data. Both PCs are illustrated in Figure 9.

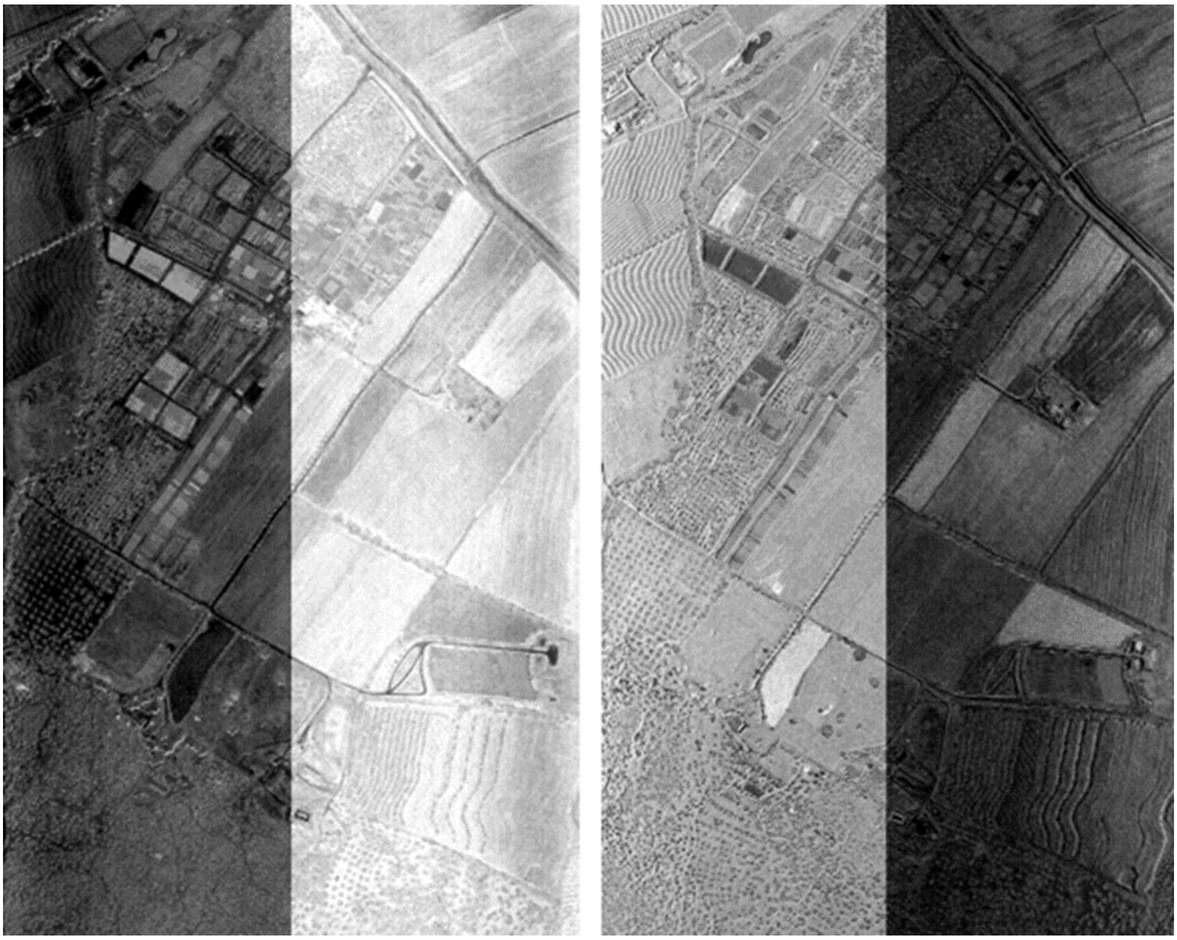

Figure 9 PC 7of the raw (left) and PC 8 of the at-sensor radiance (right) of the investigated *HyPlant* flight line of the nursery recorded on June 19, 2019.

Since the detector split is clearly visible in PC 7 of the raw data, we can exclude the SIF retrieval as the source of the artifact. It seems that the detector split is caused by the sensor readout, which happens from the middle of the detector to both sides with a small delay in time. We reported this artifact to the sensor manufacturer SPECIM and they will investigate the problem during the annual calibration of the sensor to prevent it in the future. For data recorded in the past, a different solution needs to be found. First, we investigated the eigenvalues of the PCA applied to the raw and at-sensor radiance data of the example flight line. The eigenvalue of a PC represents its variance contribution to the entire image. The eigenvalues of the PCs of both images are displayed in Figure 10 and Figure 11. In both cases, the first two PCs explain almost 100% of the image variance, while the remaining PCs have relative eigenvalues lower than 1%. PC 7 of the raw data explains 0.008% of the variance, while the explained variance of PC 8 of the at-sensor radiance is slightly lower at 0.004%. Since the variance is smaller in the at-sensor radiance and the detector split is in a PC of higher order, it seems that the artifact is partly removed by the radiometric calibration. The illustration of the radiometric calibration coefficients shown in Figure 2 can be used as an indicator for this assumption because the detector split in the middle of the image is clearly visible. Nevertheless, the radiometric calibration could obviously not fully account for the artifact. Although the detector split in PC 8 of the at-sensor radiance explains a very low amount of the entire image variance, it seems to influence the SIF retrieval. For this reason, an adjustment of the grey values of both detector sides to each other in the PC of flight lines affected by the artifact could be a possible solution to remove the detector split. Subsequently, an inverse PCA including the modified PC can be conducted before the SIF retrieval is applied. The development of an automated procedure to correct for the detector split is not straight forward because PCs are unique for every image and therefore a method to automatically find the detector split in the PCs of a flight line needs to be developed.

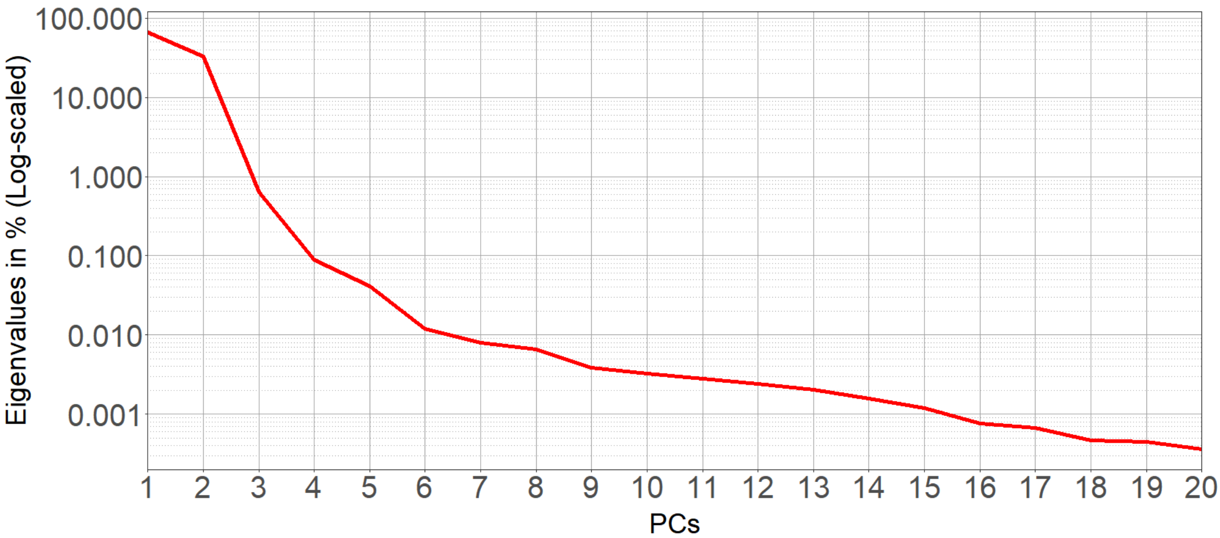

Figure 10 Log-scaled relative eigenvalues of the 20 PCs of the raw data of the *HyPlant* FLUO subset of the nursery near Grosseto recorded on June 19, 2019.

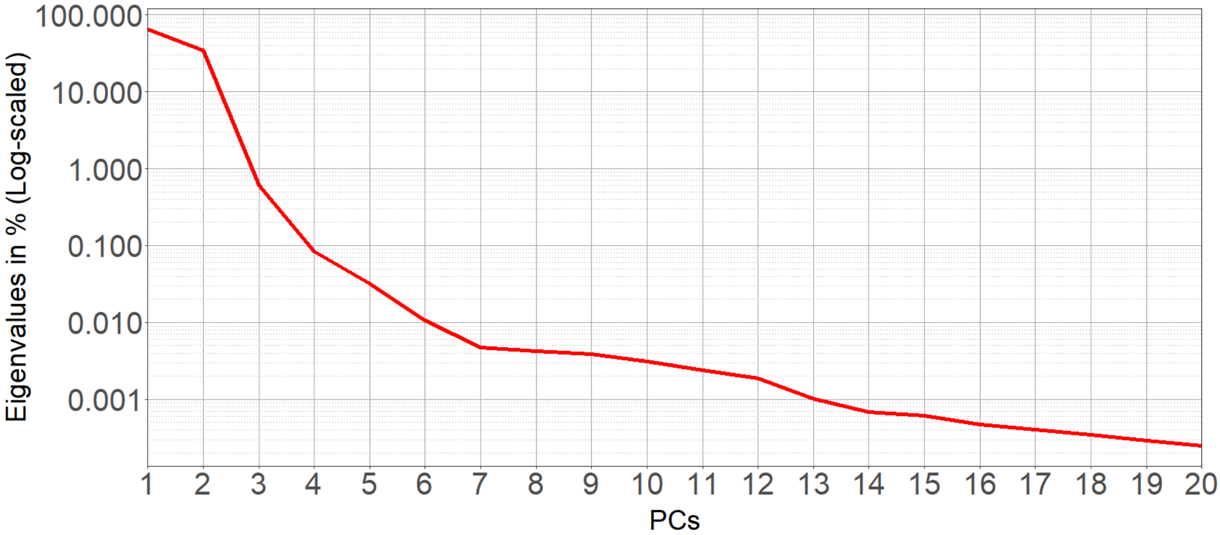

Figure 11 Log-scaled relative eigenvalues of the 20 PCs of the at-sensor radiance data of the *HyPlant* FLUO subset of the nursery near Grosseto recorded on June 19, 2019.

3.2 TASI

TASI-600 is a push broom hyperspectral thermal sensor system designed specifically for airborne use by the Canadian company ITRES (Figure 12). The TASI is sensitive to wavelengths in the long-wave infrared (LWIR) part of the electromagnetic spectrum. This instrument measures the intensity of emitted radiance from the imaged target across 32 spectral bands in the range of 8 to 11.5 microns. The TASI-600 collects an image swath of 600 pixels ‘across track’ by 1 pixel ‘along track’. The raw imagery from the TASI has a data depth of 14-bits (0–16,383). The TASI used in this study is equipped through onboard dual black body calibration, which allows radiometric calibration to be performed for each flight line during the flight and the radiometric accuracy to be improved. As a thermal sensor, TASI can be used for a number of applications, i.e. forest or agriculture ecosystem monitoring, as well as for archaeological or urban heat island detection.

3.2.1 Processing

Several methods exist for the retrieval of LST from thermal infrared (TIR) remote sensed data. In this section, LST and land surface emissivity (LSE) are obtained by using the temperature and emissivity separation (TES) algorithm (Gillespie et al. 1998), which requires at least four or five thermal bands.

TES algorithm

The TES algorithm was developed by Gillespie et al. (1998) and is used to produce the standard products of LST and LSE from the advanced spaceborne thermal emission and reflection radiometer (ASTER) data. The TES algorithm simultaneously provides LST and emissivity data, and requires at least four or five TIR bands. As inputs, it uses land-leaving radiances (LLL) and downwelling atmospheric radiance, and it is composed of three different modules: normalized emissivity method (NEM), RATIO, and maximum-minimum difference (MMD). The NEM module provides a first estimate of the surface temperature and emissivity using an iterative procedure. The RATIO module normalizes the surface emissivity, providing the so-called beta spectrum, and the MMD module recovers the final surface emissivity and temperature using a semi-empirical relationship between minimum emissivity (e_{min}) and spectral contrast (MMD), e_{min}=a+b·MMD^c. The TES algorithm was adapted to TASI characteristics (a = 0.9994; b = 0.7427; c = 0.7617).

Radiometric corrections

Radiometric corrections of measured data were carried out in the RadCorr program (ITRES Ltd.). For the radiometric calibration of the TASI-600 data, calibration coefficients derived from two calibration black bodies scanned during the flight were used. Calibration coefficients were specified for each flight line separately. The values of the final image data are given in radiometric units [μW cm^{-2} sr^{-1} nm^{-1}]. In cases where two calibration black bodies could not be used for radiometric corrections, one black body was used and calibration coefficients were determined in the laboratory. Utilization of one black body was the standard procedure before the TASI upgrade to the dual black body system.

Georeferencing

Georeferencing was carried out by means of a parametric geocoding method using data acquired by the GNSS/IMU unit and the digital terrain model in the GeoCor program (ITRES Ltd.). In one step, geometric corrections, orthorectification and data georeferencing were performed. For resampling of the data into the coordinate system, the nearest neighbor method was used. Hyperthermal data was georeferenced into the UTM coordinate system (zone 32/33N, WGS-84, depending on locality).

Atmospheric corrections and calculations of temperature characteristics

Radiometric calibrations deliver image data containing radiation from the surface $\varepsilon\, B(T)$, attenuated by atmosphere plus radiation from the atmosphere along the line of sight. Thus, the measured radiance at sensor level L consists mainly of radiance emitted from the land surface $\varepsilon\, B(T)$, downwelling atmospheric radiance $L_{\downarrow atm}$ reflected by the surface, and the atmospheric upwelling radiance $L_{\uparrow atm}$. The sum of all these components is expressed by an RTE as follows:

$$L = \tau\, \varepsilon\, B(T) + \tau\, (1 - \varepsilon)\, L_{\downarrow atm} + L_{\uparrow atm} \qquad \text{eq. 10}$$

$B(T)$ is the radiance of the surface at temperature T according to Planck's law, ε is the surface's emissivity and τ is the atmospheric transmittance. It is important to emphasize that all elements in the equation are wavelength-dependent, but notation for this is omitted for the sake of clarity. Since the sensor is of finite bandwidth, quantities in the RTE equation are replaced by band-effective equivalents. Kirchhoff's law of thermal radiation implies that reflectivity can be rewritten as ($1 - \varepsilon$) for opaque materials. The RTE can be used assuming a cloud-free atmosphere under local thermodynamic equilibrium.

The quantities $L_{\downarrow atm}$, $L_{\uparrow atm}$ and τ were modeled using the MODTRAN 5.3 RT model, which was parametrized with ERA5 data. ERA5 is a reanalysis model provided by the European Centre for Medium-Range Weather Forecasts (ECMWF) with a temporal resolution of 1 h and a spatial resolution of 0.25 (approx. 25 km). The spatial resolution was improved by linear interpolation to a resolution of 0.01 (approx. 1 km). Data values valid for the center point of each locality in the nearest time interval serve as the input for MODTRAN parametrization. Compensating for atmospheric transmittance and upwelling atmospheric radiance led to LLL:

$$LLL = \varepsilon\, B(T) + (1 - \varepsilon)\, L_{\downarrow atm} \quad \text{eq. 11}$$

LLL is the sum of the radiance emitted by the surface and the reflected radiance. Taking the downwelling atmospheric radiation $L_{\downarrow atm}$ into account is not possible without knowing the emissivity of the surface. Eliminating the influence of downwelling atmospheric radiance was part of the calculation of the temperature T and the emissivity ε of the surface – this was performed by TES. From TES, the noisiest bands (1, 2, 3, 4, 5, 14, 15, and 16) were excluded so that the final products had 24 bands. Using the radiance leaving the surface LLL, it was possible to calculate the brightness temperature that approximates the temperature T. The brightness temperature calculation was based on the inversion of Planck's law assuming emissivity equals one. The brightness temperature was calculated from the average of all the spectral bands and is therefore less affected by noise.

Summary of TASI data processing:

1) Radiometric calibration – RadCorr software delivered by sensor producer
2) Geo-orthorectification – GeoCorr software delivered by sensor producer
3) Parametrization of MODTRAN-5.3
4) TES algorithm and atmospheric corrections (AC)

Outputs:

- Image data showing the kinetic temperature (T); **LST** [K]
- Image data showing emissivity; **LSE** [-]
- Image data showing the radiation leaving the surface; **LLL** [W m^{-2} sr^{-1} m^{-1}]
- Image data showing brightness temperature; (broadband brightness temperature) **BBT** [K], spatial pixel resolution: 3.6 m
- Image data showing the measured radiance at sensor level; **RAD** [µW cm^{-2} sr^{-1} nm^{-1}]

3.3 LiDAR

LMS-Q780 is a long-range airborne laser scanner with the capability of full-waveform echo digitization and analysis designed by Austrian company Riegl. The LMS-Q780 is equipped with a rotating polygon mirror, which leads to straight parallel scan lines and enables an equally dense laser footprint pattern on the ground. The broad FOV of the laser scanner 60° compared to *HyPlant* and TASI has the benefits of a high overlap of parallel LiDAR scan lines and higher point density. The Riegl LMS-Q780 is able to distinguish up to ten simultaneous pulses in the air, which results in a dense laser footprint pattern even in rugged areas without any necessity to follow terrain. This is important with regard to the FLEXSense flight planning, which is determined based on the actual sun azimuth and other objectives.

Figure 12 TASI-600 and laser scanner (LiDAR) Riegl LMS-Q780 mounted in the aircraft together with *HyPlant*.

3.3.1 Processing

Trajectory calculation

To calculate the flight trajectory, the POSPac 7.1 software was used. This is followed by the conversion of trajectories in the Riegl – POFImport 1.7.3 software. The input data are GNSS and IMU data recorded at a frequency of 200 Hz. The output is a flight trajectory in the UTM coordinate system. For further processing in the RiPROCESS software, we had to convert the trajectory in the POF Import program to the .pof format.

Georeferencing

The following software from the company Riegl Laser Measurement Systems GmbH was used to adjust the laser data:

RiPROCESS 1.8.4 – software for the computation of adjustments of laser scanner data

RiANALYZE 6.2.2 – full waveform data analysis software

RiWORLD 5.1.3 – software for georeferencing of laser scanner data

GeoSysManager 2.0.8 – management software for coordinate systems and projections database

Export

The resulting laser data were usually exported in the form of a point cloud in the LAZ format (UTM coordinate system, zone 32/33N, WGS-84), including the so-called Riegl extra bytes that assign information from full-waveform analysis (amplitude and pulse width) to each of the points. Orthometric heights were exported. Conversion from ellipsoidal heights (WGS-84) to orthometric heights was based on Earth Gravitational Model 1996 (EGM96).

Digital Elevation Model (DEM)

The point clouds exported from RiPROCESS were used as input data for DEMs calculations in LAS Tools software from rapidlasso GmbH. The process of the DEM calculation was as follows:

1) LiDAR flight lines were merged together for one locality.

2) The merged point cloud was divided into tiles.
3) Noise filtering was performed for each tile.
4) Classification to ground and non-ground points was performed.
5) The digital terrain model (DTM) was calculated by means of the TIN of ground points.
6) The digital surface model (DSM) was calculated by means of the TIN of ground and non-ground points.
7) The normalized DSM (nDSM), also called the canopy height model, was calculated as the difference between the DSM and DTM.

Table 4 Flights used for calculating the DEMs of each area.

Area		Altitude [m]	Date
Italy	Fire experiment	1200	June 24, 2019
	Nursery	1500	June 19, 2019
	S3P	4500	June 16, 2019
	Drought Stress	1500	June 16, 2019
Germany	CKA	680	June 26, 2019
	SEL	680	June 26, 2019
	TR32	1800	June 27, 2019

4 GROUND-BASED INSTRUMENTATION

Different measurements on the ground were performed to complement the airborne data. First of all, an eddy tower stationed at Selhausen during the 2019 campaign provided surface fluxes (section 4.1). Furthermore, FloX systems were employed at both study sites in Germany and in Italy (section 4.2). Special care was taken to characterize the active and passive reference targets, which may play a role in a future Cal/Val strategy for FLEX (section 4.3). Finally, structural and functional plant traits were determined from selected vegetation types in synchrony with the *HyPlant* flyover (sections 4.4 and 4.5).

4.1 EDDY COVARIANCE

One eddy tower was installed at the Selhausen study site, providing surface flux data during the 2019 campaign. Located in a potato field (50.865°N, 6.447°O), this eddy tower is part of the Integrated Carbon Observation System (ICOS), consisting of several eddy covariance (EC) towers positioned across Germany. This is the German contribution to the European network infrastructure of the ICOS monitoring system. In Germany, the EC tower is meant for atmospheric measurements of CO_2, CH_4 and N_2O. The EC tower was equipped with a three-dimensional sonic anemometer (model CSAT-3, Campbell Scientific Inc., Logan, Utah, USA) and an open-path infrared gas analyzer (model LI-7500, LI-COR Biosciences Inc., Lincoln, Nebraska, USA). The analyzer was calibrated every three months in the lab. Both instruments were mounted 2.5 m above the surface. EC measurements of turbulent fluxes were calculated as 30-min averages using the software package TK3.11 (Foken et al. 2004). Data from the EC tower were processed to produce half-hourly values of GPP estimated from the Net Ecosystem Exchange (NEE) measurements using a daytime data-based flux-partitioning algorithm following Lasslop et al. (2010), implemented with the gap-filling and source partitioning software REddyProc (REddyProc Team, 2014). Data gaps in the time series of the meteorological driver variables (taken from the climate station of the Selhausen site) required for modeling GPP were filled before partitioning with a variant of the data interpolating empirical orthogonal functions method (Beckers and Rixen 2003, Graf et al. 2017). The day-time partitioning is provided by the REddyProc package and the approach models GPP with a rectangular hyperbolic light-response curve with additional consideration of the vapor pressure deficit limitation of photosynthesis. GPP day-time partitioning (GPP_{DT}) should correlate better with SIF and vegetation indices because in a way some remote sensing information is already embedded in the modeled GPP.

4.2 FLOX SYSTEMS

JB Hyperspectral Devices UG designed a FloX system for high temporal frequency acquisition of continuous TOC radiometric measurements with a focus on SIF. The system is equipped with two spectrometers: i) Ocean Optics FLAME S covering the full range of visible and near-infrared (VNIR); and ii) Ocean Optics QEPro with high-spectral resolution (FWHM of 0.3 nm) in the range of the fluorescence emission 650–800 nm. Each spectrometer's optical input is split into two fiber optics that lead to i) a cosine receptor measuring the solar irradiance; and ii) a bare fiber measuring the target reflected radiance. Spectrometers are housed in a Peltier thermally regulated box keeping the internal temperature lower than 25°C in order to reduce dark current drift. Moreover, the thermoelectric cooler (TEC) of QEPro is set to 20°C in order to always provide stable measurements. The signal is automatically optimized for each channel at the beginning of each measurement cycle and two associated dark spectra are collected as well. Metadata such as spectrometer temperature, detector temperature and humidity are also stored in the SD memory of the system. The measurements are fully automated and after setup and activation, no further user input is required. The FloX system is optimized for low power consumption and remote installation with multiple interfaces for data storage and transmission. The basic FloX routines are based on SPECY (Forschungszentrum Jülich, IBG-2: Plant Sciences).

4.2.1 FloX Systems in Jülich/Selhausen and CKA, Germany

During the 2019 campaign activities, two FloX systems were deployed during the flyovers from June 25 to June 27, 2019. A stationary FloX system was installed on an ICOS eddy flux tower to record SIF throughout the campaign window (with measurement starting on May 13, 2019) (Figure 13). Unfortunately, automated data storage of this FloX system failed from June 17 on several occasions up to June 25, when there were no measurements at all. That means there are no data on days of the

HyPlant flyover. One dedicated FloX system was deployed at Forschungszentrum Jülich during the flight campaign to measure reflectance and SIF of the active and passive reference targets on June 26 and 27, 2019. At least on the second day of the German campaign (June 27, 2019) there were some technical problems with this particular FloX system. Table 5 shows an overview of all the measurements with the FloX systems in Germany.

Table 5 Overview of FloX system measurements at the German sites during the 2019 flight campaign.

Location	**Instrument**	**Date**
Selhausen	Stationary FloX on the ICOS Tower	May 13 – June 17, June 25, 2019
Forschungszentrum Jülich	Stationary FloX	June 26 + 27, 2019

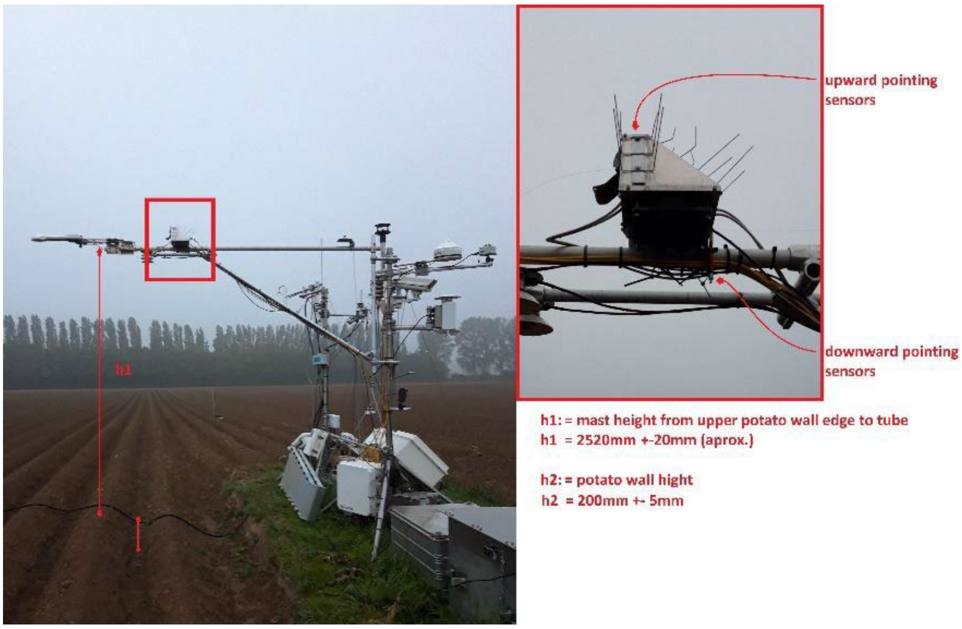

Figure 13 Example FloX installation in Germany. A FloX was installed on an ICOS eddy tower close to Selhausen. This box faces the footprint of the eddy tower and is approximately 4 km away from the atmospheric measurement site.

4.2.2 FloX system stationed in Grosseto, Italy

Three FloX systems were installed at the Le Rogaie site at ground level during the 2019 campaign. One FloX system measured the fluorescence of the DYE panels (Figure 14), which were laid on flat terrain, from June 16 until June 19, 2019. Another FloX system was used to characterize the emission of the large fluorescence reference panels (LFRPs) on June 17, 2019. Furthermore, another FloX system was stationed in the drought stress experiment and measured the water-stressed crop plants from June 11 to June 25, 2019. All measurements also took place on the day of the flyover in synchrony with the *HyPlant* measurements. Table 6 shows an overview over the measurements with the FloX systems in Italy.

Table 6 Overview of the FloX system measurements during the 2019 campaign in Italy.

Location	Instrument	Date
Drought experiment	Stationary FloX	June 11–25, 2019
Reference targets - Dye - LFRP	 Stationary FloX Stationary FloX	 June 16–19, 2019 June 17–19, 2019

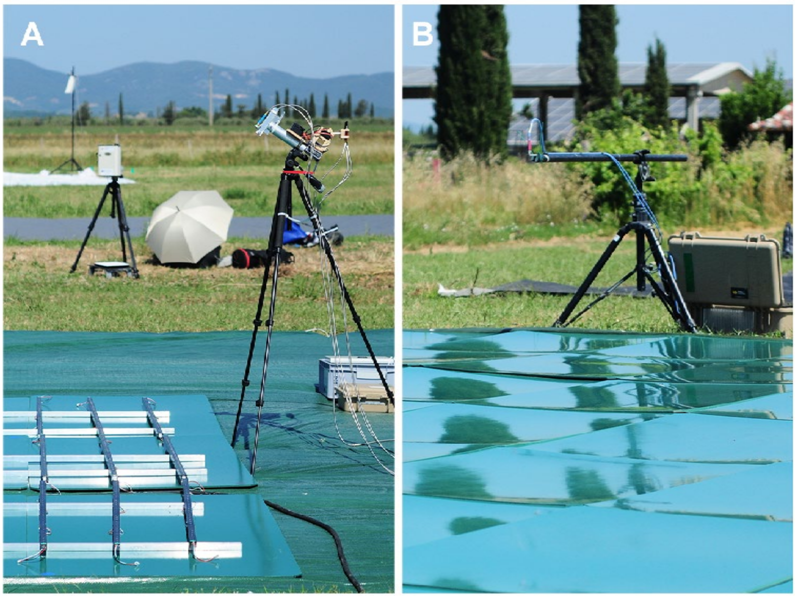

Figure 14 Ground measurement setup of FloX spectroscopy system monitoring the LFRP (A) and passive dye panel (B).

4.2.3 Processing of the data from the FloX system

FloX data processing is entirely based on the open source R software (R Core Team 2017). The core functions of the data processing are contained in two R packages (FieldSpectroscopyCC and FieldSpectroscopyDP) openly available on the GitHub platform at https://github.com/tommasojulitta and released under the license GNU v3.0 (Julitta et al. 2017). The graphical user interface is provided to FloX customers as an R script to facilitate the analysis of the data collected, although the source code is available to JB customers and potentially adaptable to users' needs.

The concept behind the processing was specifically adapted to ESA requirements in the context of the ESA ATMOFLEX project. The processing of the data follows a specific workflow:

1. Reading of input files (i.e. raw data)
2. Conversion of raw data to radiance data (using the calibration files provided by JB)
3. Calculation of apparent reflectance factors
4. Calculation of reflectance-based spectral vegetation indices (SVIs)
5. SIF retrieval according to the SFM (Cogliati et al. 2019)
6. Calculation of QA/QC routines

The data processing procedure is illustrated in the following diagram (from raw to level 2 product) ([RD-05]).

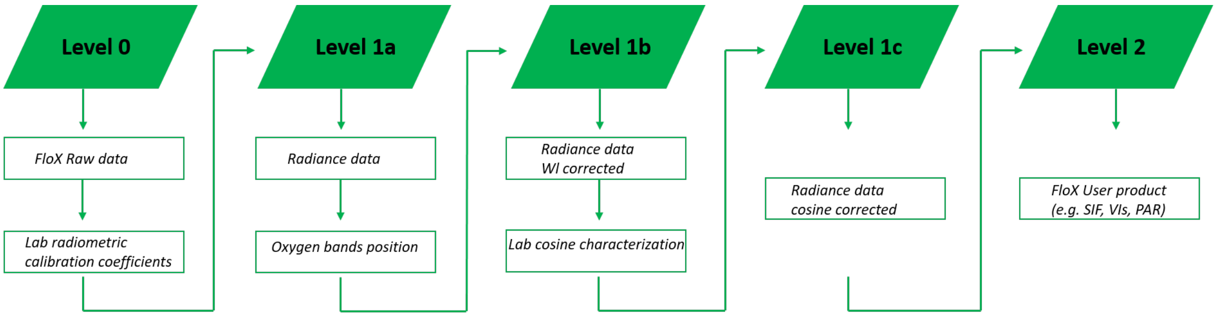

Figure 15 Structure of data processing for the FloX system.

4.3 Reference targets for Cal/Val

One of the objectives of the 2019 campaign was the employment of active and passive reference panels. These fluorescence targets are to be used in the future Cal/Val concept for the FLEX satellite mission. Within this activity, we tested two different concepts for such reference targets: active panels, which use light emitting diodes, and passive panels, which make use of a dedicated fluorescence dye.

4.3.1 Passive reference target

The passive fluorescence targets were developed by Fondazione per il Clima e la Sostenibilità (FCS) in Florence, Italy, to be deployed in the field for the calibration and validation of SIF measurements. They are referred to as dye panels in this study. The multi-layered panel consists of a substrate (wooden panel) and two coatings to reproduce the reflectance and fluorescence of vegetated surfaces (Figure 16). The first coating is referred to as the camouflage layer and is made up of a green camouflage pigment produced by the company Renner (Italy), which is dissolved in a commercial acrylic transparent coating. This coating reproduces the reflectance pattern of vegetation. The fluorescent layer is superimposed onto the existing coating by dissolving the fluorescence dye in a transparent polyurethane resin produced by the company Renner in Italy. The two-component resin is made up of 50% base resin (bisphenol A, epichlorhydrin e oxyrane, mono[(C10-16-alchyloxy) metyl]-derived) and 50% catalyzer (3-Aminometyil-3,5,5-trymetyl-diclo-esilamin and benzyl alcohol). Zinc phthalocyanine, which is the fluorescing component, is initially solubilized within the catalyzer component at a ratio of 0.05% before the base resin is added. The fluorescence coating is then added to the camouflage layer at a thickness <1 mm. To achieve an accurate reproduction of the vegetation reflectance and fluorescence signal, the target underwent extensive laboratory testing before being deployed in the 2019 FLEXSense campaign. A patent request for the device has since been filed at the Italian Patent and Trademark Office (UIBM) under the reference number 102019000020174. During the campaign, 90 of the 0.8 x 1.2m single panels were set up over an area of approximately 9 x 9 m.

Figure 16 Structure of the multi-layered DYE reference panel, consisting of the substrate, camouflage layer and fluorescent layer (FCS 2020, unpublished).

The coating was homogeneously applied, and such homogeneity was tested using an active fluorometer (Hansatech WMA2, UK). Therefore, it was possible to constantly monitor the panels' emission at a specific location and it was assumed that these measurements would be representative of the entire panel setup. This allowed for continuous ground data measurements throughout the flight campaign. The fluorescent dye is known to be rapidly degraded by UV radiation under full sunlight. For this reason, the SIF signal that the panel emitted was reduced over time. To minimize such an effect, the panel was covered after two days of the campaign to prevent further degradation of the coating. Subsequently, the panels were only uncovered during flyovers. This resulted in a relatively low number of ground measurements (only before and after the flyovers) and low SIF emissions (≈0.5 mW $m^{-2}sr^{-1}nm^{-1}$) on June 19 (day four of the campaign). Due to these circumstances the data set was reduced to only include data up to this day.

The fluorescent passive reference target was installed in Braccagni from June 14 to 24, 2019. A reference FloX system continuously measured emissions when the panel was exposed to sunlight. In Figure 17, the FloX setup measuring the dye panels' emission is shown.

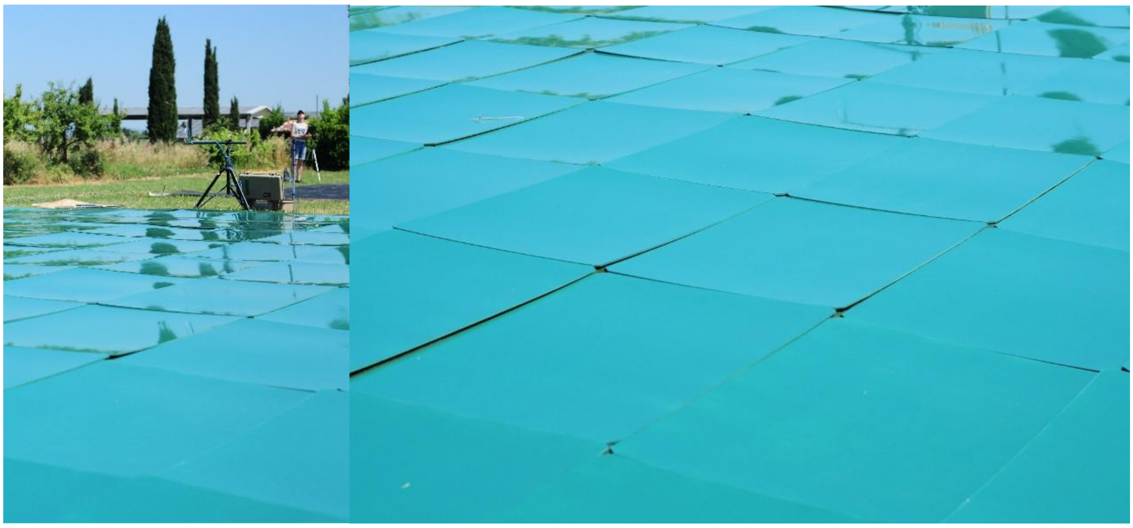

Figure 17 Passive fluorescent dye measured by FloX during the *HyPlant* flyover in Italy.

4.3.2 Active fluorescence reference panels

The active LFRP reference panel was developed by JB Hyperspectral Devices UG (Germany) as a validation tool for ESA's future FLEX satellite mission and its preparatory Cal/Val campaigns. The LFRP is a structure consisting of a maximum of 39 LED strips, each equipped with 36 LEDs, which make up an area of 3 m x 3 m. Two setups were installed (Figure 18b, c): the LP-20 (39 LED strips) and the LP-40 (21 LED strips). The numbers define the distances between the LED strips in cm. The strips are installed on aluminum rods that are painted black to minimize reflection. Each strip emits a signal either at 760 nm or 680 nm. To reduce the effects of underlying vegetation, the ground was covered by a tarp, on top of which wooden panels were placed that mimic the vegetation spectrum (only applied to LP-20). These panels were the same as the ones used for the passive panel setup without the application of the second fluorescent coating.

During the 2019 campaign, the active panels were tested in the Italian field from June 17 until June 20 (Table 7). Additionally, the panels were tested in Germany during the campaign on June 26 and 27, 2019. FloX systems were used to characterize, once in Italy and once in Germany, the emission of the LFRP.

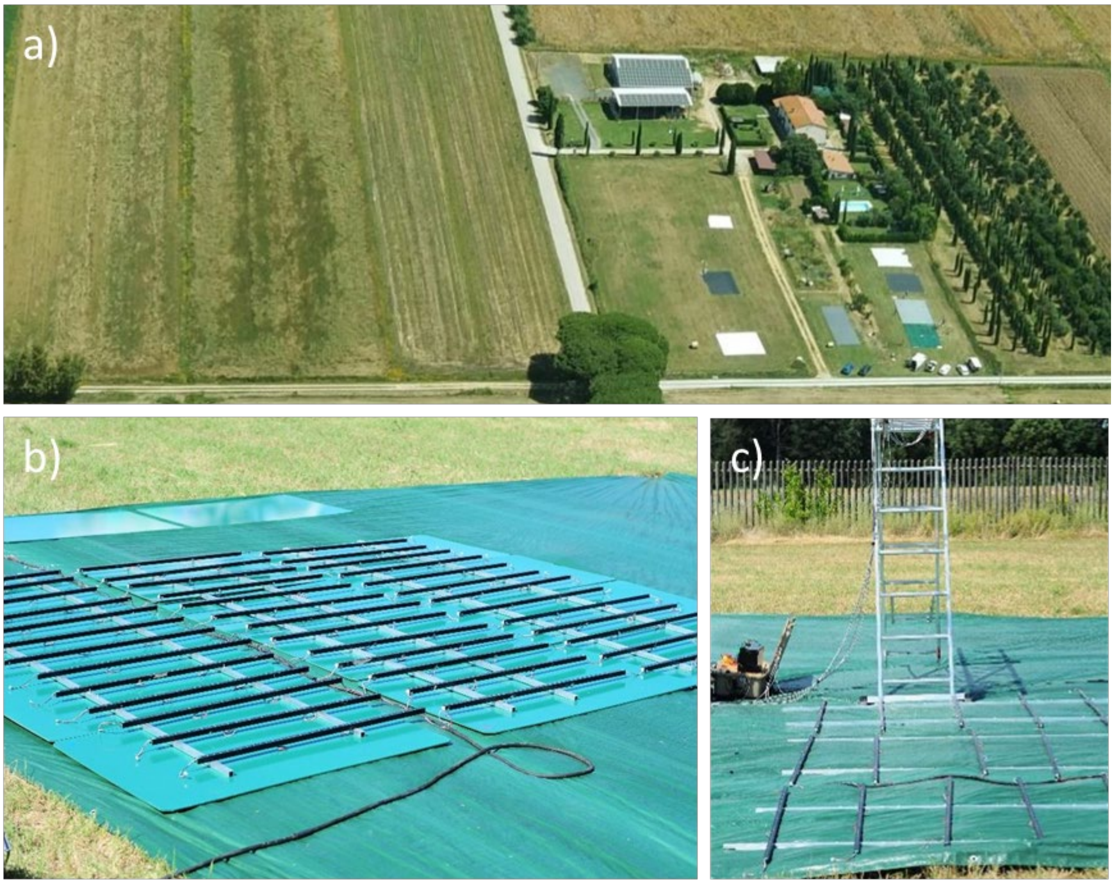

Figure 18 (a) Location of the active reference panels in Italy, LP20 (b) and LP40 panels (c)

Two LFRPs were set during the campaign and the same configuration was maintained both in Italy and in Germany. In particular, as depicted in Figure 18, two 3 m x 3 m panels were deployed, one with a spacing of 40 cm between the rows (LP-40), and one with a spacing of 20 cm (LP-20). In order to reduce the problem with emitted radiance retrieval, the bars were mounted above panels with a reflectance similar to vegetation. In Table 7, the LED power level of the two LFRPs is reported during the *HyPlant* flyovers, i.e. maximum power, minimum power, or (deliberately switched) off.

Table 7 Summary of LFRP power status.

Place	Date	Time	LP20	LP40
Braccagni	June 17, 2019	11.00 local time	ON – max	ON – max
Braccagni	June 18, 2019	11.00 local time	ON – max	ON – max
Braccagni	June 18, 2019	14.00 local time	ON – max	ON – max
Braccagni	June 19, 2019	10.00 local time	ON – max	ON – max
Braccagni	June 19, 2019	13.00 local time	OFF	ON – min
Braccagni	June 19, 2019	16.00 local time	ON – max	ON – max
Daubenrath	June 26, 2019	All day	ON – max	ON – max
Daubenrath	June 27, 2019	All day	OFF	OFF

4.4 Drought stress experiment - Italy

To better understand the link between drought stress and variations in SIF, a dedicated drought stress experiment was undertaken in Grosseto, Italy. This experiment was intensely mapped with the airborne sensor package. To complement airborne measurements, in-situ non-invasive and invasive measurements of plant traits were performed. TOC reflectance and fluorescence were continuously recorded with a FloX system and several measurements were collected during the drought stress experiment (e.g. stomatal conductance, leaf water potential, plant height) to quantitatively describe the impact of drought on structural and functional plant traits and their link to SIF.

Several different measurements were conducted in the field where the drought experiment took place. An overview of the plant parameters that were determined is given in Table 8. During the drought stress experiment, a FloX system was permanently installed in the plot with corn plants exposed to drought stress.

Table 8 Plant/soil parameters that were recorded at the drought stress site.

Parameter	**Start date**	**End date**	**No. of samples**	**Frequency**
Plant biomass	June 11, 2019	June 25, 2019	9 per treatment	2 days
Leaf area				
No. of leaves				
Leaf length				
SPAD				
Height				
Diameter				
Soil water content	June 16, 2019	June 22, 2019	5 per treatment	

Plant growth was monitored by measuring the plant height, stem diameter and leaf length of well-watered and drought-stressed corn plants between June 11 and June 25, 2019. Plants were selected randomly in the field. Stomatal conductance was measured during the drought stress experiment from June 16 to 18, 2019. A porometer was used to capture the dynamics of stomatal conductance four times a day, while measuring nine reference and nine water-stressed corn plants.

Five measurements were taken on the abaxial leaf side per maize plant and the measurements were distributed all around the plant stem to account for different leaf geometry and orientation. Leaf water potential was measured between June 18 and June 22, 2019 from the water-stressed and irrigated plants by means of a pressure chamber according to the method described by Scholander et al. (1965). The upper fully expanded leaves of five plants per plot were removed and stored in a plastic bag before measurement to avoid water losses (Turner and Long 1980).

The LST of the two plots with water-stressed and irrigated plants respectively was monitored by means of Apogee thermal cameras that were installed on a pole. Finally, the spectral reflectance of selected targets in the study area was measured with an ASD FieldSpec4 almost simultaneously with the *HyPlant* flyover on June 16, 2019 ($\pm$ 1 hours). Targets were selected to capture a wide spectral variability, from bright to dark surfaces.

4.5 Characterization of structural and functional plant traits – Germany

To complement the airborne measurements and the ground-based FloX measurements in Germany, in-situ non-invasive and invasive measurements of plant traits (e.g. LAI, biomass, leaf and canopy pigments) were performed.

In-situ plant samples were taken from several fields at Selhausen on June 25, 2019 as part of the SARSense campaign ([RD-07]). The selected crop types were potato, sugar beet, barley, rye, corn and wheat. At CKA samples were taken from different summer wheat varieties on June 25, 2019. On both sites the following parameters were recorded: BBCH scale, plant height, plant biomass, LAI (using the Sun Scan), and leaf chlorophyll content (using a SPAD-502Plus Chlorophyll Meter, Konica Minolta Inc., Japan).

For the SPAD measurements, approximately ten leaf measurements were averaged. The LAI as well as total (fresh and dry) biomass and canopy water content were analyzed from fresh plant tissue samples taken at least within three days of the flyover (Table 9, Figure 19). At the end, leaf disks to determine chlorophyll A, B and carotenoid content were taken and processed according to an established protocol, which is described below.

Table 9 Canopy level parameters that were determined during the flyover. Characterization of all parameters was performed at Selhausen and CKA, Germany.

Canopy parameter	**Measured by**	**Unit**
Total biomass (fresh)	Weighing fresh material	g FW m^{-2} ground area
Total biomass (dry)	Weighing dry material	g DW m^{-2} ground area
LAI	Determining total leaf area	m^2 leaf area m^{-2} ground area
Canopy water content (canopy H_2O)	FW – DW	g H_2O m^{-2} ground area
Chlorophyll content	SPAD502	
	Extraction of chlorophyll according to the protocol (see below)	mg g^{-1} FW
Carotenoid content	Extraction of chlorophyll according to the protocol (see below)	mg g^{-1} FW
Developmental stage	BBCH scale	
Plant height	Measuring size	cm
GPS	Handheld GPS device	Location in field plan

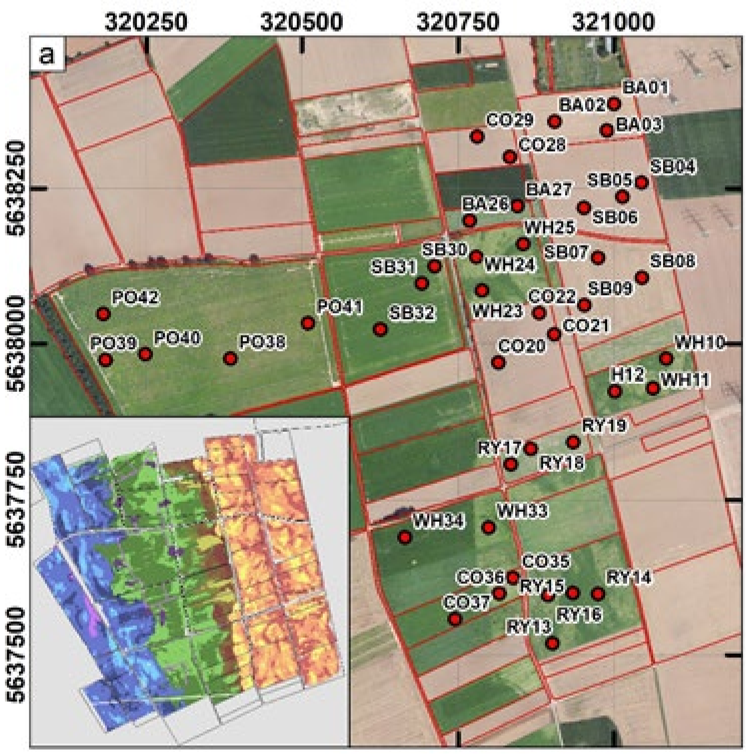

Figure 19 Vegetation sampling locations including code considering crop type and soil heterogeneity and soil characterization of the Selhausen area.

Analysis of leaf pigments

Whole plants covering a 40 cm x 40 cm square were harvested, i.e. for potatoes 2, for wheat 20, for sugar beet 1–2, for barley 30, for maize 2–3, and for rye 20 plants in total.

Then, one whole "representative" plant was taken out of the soil in each field location. It was cut at the roots. Each plant was harvested into a tight plastic bag, which was sealed to prevent water evaporation. In the lab, the fresh weight of the plants was measured while each plant was sealed in the plastic bag. For the determination of the chlorophyll and carotenoid content, fresh green leaves were sampled in the field. Using a leaf tissue puncher, 5–10 leaf disks with a diameter of 9 mm were randomly punched out of the upper green leaves of a plant. The leaf disks were transferred into 2-ml microcentrifuge tubes, immediately frozen in liquid nitrogen, and transported to Forschungszentrum Jülich.

The weight of a bag was determined separately in advance. Then, all plants were taken out of the bags to determine the fresh weight, in order to calculate the LAI of each plant with a LAI meter (Li-3200 Area Meter from LiCor). After leaving the plants in a drying oven at 65 °C for a few days, the dry weight was measured. The canopy water content was determined by subtracting dry weight from fresh weight.

Sample preparation and analysis (chlorophyll and carotenoid)

The leaf disk samples acquired in the field and stored at -80 °C were weighed into 2-mL microcentrifuge tubes with a weight between 10 mg and 20 mg. The extraction of chlorophyll A, chlorophyll B, and carotenoids was performed with 100% acetone buffered with magnesium hydroxide carbonate (~$4MgCO_3$ $Mg(OH)_2$ 5 H2O). 10 g of magnesium hydroxide carbonate were mixed with 500 mL of acetone and stored at 4 °C. 250 µL of the described buffer were added to the previously weighed leaf disk including a metal sphere. Homogenization was performed using the swing mill MM 400 (Retsch, Germany) for 60 s at a frequency of 30 s^{-1}. The metal ball was removed using a magnet and washed three times with 250 µL of acetone buffer that was captured in the microcentrifuge tube. The tubes were then centrifuged at 4 °C at 4100 rpm for 5 min.

250 µL of the supernatant were transferred into a cuvette and mixed with 750 µL of 100% acetone (dilution 1:4). Absorption was measured with a Specord 200 Plus spectrophotometer (Analytik Jena AG, Germany). The measurements were performed at the wavelengths 470 nm, 645 nm, 662 nm, and 710 nm. During all steps, starting at the extraction, the tubes were exposed to as little light as possible and continuously stored on ice until measurement.

For the determination of the chlorophyll and carotenoid content, the absorbance values in the following equations as described in Lichtenthaler and Buschmann (2001) and Lichtenthaler (1987) were substituted with the acquired values:

Chl A= ((11.24*(A_{662} – A_{710}) – 2.04*(A_{645}-A_{710}))*dilution factor)* (extraction vol. / (fresh weight))

Chl B= ((20.13*(A_{645}-A_{710}) – 4.19*(A_{662}-A_{710}))*dilution factor)* (extraction vol. / (fresh weight))

Chl A+B= ((7.05*(A_{662} – A_{710})+18.09*(A_{645}-A_{710}))*dilution factor) * (extraction vol. / (fresh weight))

Bulk Carotenoids= ((((1000*(A_{470}-A_{710})-1.90*ChlA-63.14*Chl B)) /214)*dilution factor)*(extraction vol. / (fresh weight))

The chlorophyll values from this campaign activity showed unusually high values, which were greater than the data from the years before and what we would expect from literature reports. Thus, we have not used these data for further analysis and we will deliver these data with a dedicated label to the ESA data repository. We cannot fully trace back the error as this is not possible with destructive measurements. However, we currently assume that relative differences within the pigment data are correct, while the absolute values are too high.

5 SPECTRAL FITTING METHOD (SFM) FOR FLUORESCENCE RETRIEVAL

5.1 OPERATIONAL SFM RETRIEVAL FOR *HYPLANT* IMAGERY INCLUDING QUALITY FLAGS AND UNCERTAINTY ESTIMATES

The entire data set of *HyPlant*-FLUO flight lines collected during the campaign over the different test sites (n = 158 images) have been processed in a systematic and automatic way. This was possible because the current retrieval algorithm does not require any specific manual input from the user. All the relevant input information requested from the retrieval algorithm are automatically loaded from the instrument ancillary data (i.e., sensor navigation telemetry, latitude/longitude) or derived from them (i.e., SZA, VZA). This allows batch processing of the entire dataset, carried out using a high-performance computer system (Galileo 100, Cineca).

The processing relies on the SFM retrieval developed during the FLEXSense 2018 project. Specifically, a novel concept was introduced to the physics of the algorithm in order to avoid the need for external information to conduct SIF retrieval (sun photometer). The activity developed within FLEXSense 2019 focused on the refinement of overall processing, including the automatic i) calculation of quality flags; ii) SIF retrieval with associated per-pixel uncertainty; and iii) merging of all the several products into a single file. The general scheme of the SIF retrieval chain based on SFM is shown in Figure 20 and a synthetic description is provided in this section.

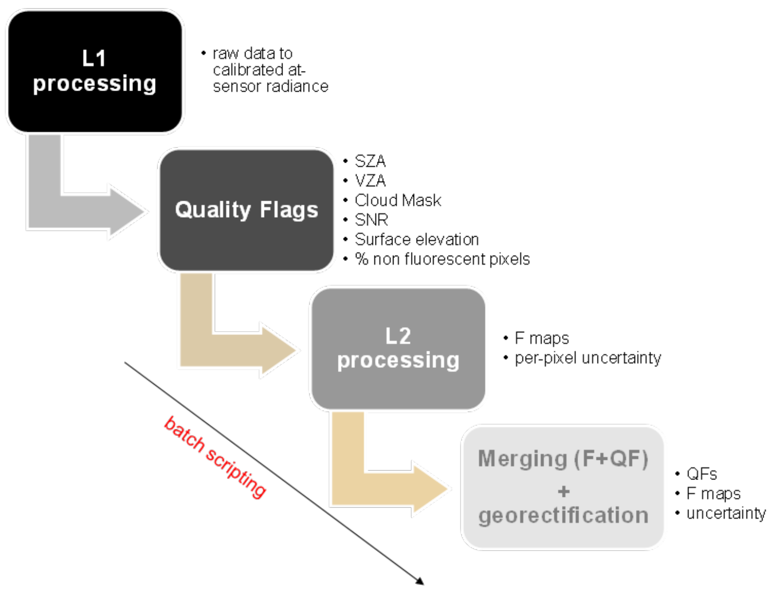

Figure 20 *HyPlant* SFM retrieval processing chain.

5.1.1 Quality Flags

Solar Zenith Angle (SZA)

SZA provides information about the overall irradiance level under clear sky conditions, surface anisotropy, and shadows. Smaller SZA values correspond to higher irradiance and generally determine lower anisotropy effects. SZA is computed by using latitude/longitude and GPS time stored within the header file of each *HyPlant* FLUO at-sensor radiance (L1 product) image. An indication of the overall quality of the imagery in relation to SZA is given in the table as a guide for non-experienced users (optimal = good data quality; suboptimal = medium data quality – data should be used with caution; non-optimal = poor data quality – data can't be used).

SZA (deg)	QUALITY
0-50	Optimal
51-70	Suboptimal
71-90	Non-optimal
Output data format	
SIF map product file	
• SZA[deg] = solar zenith angle in degrees (single value for the entire image)	
Summary pdf file	
SZA value	

View Zenith Angle (VZA)

The VZA provides information about surface anisotropy within the image. Off-nadir pixels are typically strongly affected by surface anisotropy. The VZA maps are not available from the L1 processor (Caligeo, Specim) and therefore a simple script was implemented to derive it for every single pixel. In a first step, VZA is derived from the GPS/IMU navigation file available for each image. The roll angle for every single image line is used to calculate VZA on a pixel basis. At this stage, surface topography is not considered because the SIF retrieval algorithm is limited to the processing of imagery from flat areas only. An indication of the overall quality of the imagery in relation to VZA is given in table as a guide.

VZA (deg)	QUALITY
0-10	optimal
10-20	suboptimal
Output data format	
SIF map product	
• VZA [deg] = view zenith angle in degrees (image)	
Summary pdf file	
Max VZA value	

Cloud mask

Clouds represent one of the most problematic distorting effects during SIF retrieval because they severely affect SIF map quality in multiple ways: i) a direct effect occurs in the 'atmospheric correction' algorithm when clouds could be confused with non-fluorescent targets in the nadir pixels; ii) a second order effect caused by complex radiative effect from clouds that affects the irradiance of surrounding areas.

A dedicated algorithm was prototyped and implemented within the *HyPlant* processor. A binary mask [0, 1] delimitating the area covered by clouds was thus obtained. The algorithm was newly developed and tested since there are no algorithms available that can be adapted to the narrow spectral configuration of the *HyPlant* FLUO sensor. Complexity arises because the FLUO instrument covers a limited spectral range (650–800 nm) and some of the key wavelengths typically used in operational satellite cloud mask processors (i.e., cirrus band) are not available. This limitation could be overcome by using *HyPlant* DUAL data in cloud-mask processing. However, this would require substantial geometric co-registration of FLUO and DUAL data because of the two image geometries.

Therefore, a new algorithm was prototyped that uses the high-resolution observations of the O_2-A band in the FLUO data. The algorithm is mainly inspired by the cloud mask and cloud fraction algorithm fast retrieval scheme for clouds from the oxygen A band (FRESCO and FRESCO+) widely used by atmospheric chemistry satellites (Desmons et al. 2019, Wang et al. 2008). Since FRESCO was designed for satellite data to derive the cloud fraction, it cannot directly be used for high-resolution airborne imagery. For this reason, it was adapted to detect clouds from *HyPlant* FLUO image data.

In practice, the algorithm relies on the analysis of the O_2-A band (i.e., band depth) to gain information about the radiation path length (i.e., sun-target-sensor distance or objects height). The O_2-A band depth of cloudy pixels is lower because of the shorter sun–cloud–sensor path length, while the band depth of a lower elevated surface is higher because the optical path is longer. In practice, the algorithm was implemented as follows: i) O_2-A band depth is calculated from *HyPlant* FLUO at-sensor radiance; ii) K means unsupervised classification is applied to identify the two classes: clouds and surfaces not covered by clouds.

Currently, the cloud mask is not performing correctly for images collected in clear-sky conditions because the algorithm confounds bright surfaces (i.e., metallic roof tops, bright soils, etc.) with clouds. This effect is not very important for the usability of the SIF maps produced, but it introduces a salt-and-pepper artifact in the quality flag products. Further developments are suggested to refine this algorithm for better and more robust results without these cosmetic issues. Since the flight lines are mainly collected in clear-sky conditions, this quality flag can be disabled to process most of the flight lines.

Value	**QUALITY**
0	Cloudy
1	Clear
Output data format	
SIF map product	
• CLOUD_MASK = binary mask with float values [0, 1] (image)	
Summary pdf file	
Cloud cover %	

Signal to Noise Ratio (SNR)

The actual SNR of the at-sensor radiance affects the overall quality of the maps produced by the SIF retrieval algorithm. The SNR is evaluated by means of algorithms based on the analysis of the signal considering the intrinsic spatial variability of natural surfaces and the spectral-spatial correlation between nearby wavelengths and adjacent pixels. The method relies on multiple linear regressions (MLR) in which inter-band (spectral) and intra-band (spatial) correlations are exploited to de-correlate the image data. The Homogeneous Regions Division and Spectral De-Correlation (HRDSDC) method (Fu et al. 2014) is used. This algorithm was adapted to successfully estimate the SNR of PRISMA images by Cogliati et al. (2021); the results obtained closely match the pre-flight characterization performed by Leonardo Aerospace. In particular, the methodology consists of preliminary image segmentation for homogeneous areas (based on a NDVI map); a kernel of limited size is considered around the barycenter of each segmented area. The MLR coefficients (representing spectral-spatial correlation of the adjacent pixels within the kernel) are estimated for each individual area and residuals are used to obtain the noise variance. Afterwards, the SNR for the individual segment and for each waveband of the FLUO spectrometer is determined. All the technical details of the algorithm are described in Cogliati et al. (2021).

The SNR for each individual segmented area (e.g., crop field) is estimated from the pixels around the barycenter of the area and the values assumed equal for all the pixels that belong to this segment. The SNR processing is available and integrated in the *HyPlant* 'operational' processor. The spectral SNR for each segmented area is computed for all wavelengths, while SNR values at 680 nm, 687 nm, 750 nm and 760 nm are stored as image maps within the SFM SIF product maps (representatives of the O_2-A and O_2-B bands).

SNR	**QUALITY**
100-300	optimal
50-100	suboptimal
20-50	non-optimal
Output data format	
SIF map product	
• SNR-680 = signal-to-noise ratio at 680 nm (image) • SNR-687 = signal-to-noise ratio at 687 nm (image) • SNR-750 = signal-to-noise ratio at 750 nm (image) • SNR-760 = signal-to-noise ratio at 760 nm (image)	
Summary pdf file	
SNR mean value and peak SNR (90-98 percentiles) wavelengths 680, 687, 750, 760 nm	

Non-fluorescent reference surface

The SFM method mainly relies on non-fluorescent pixels to constrain the atmospheric correction at the O_2 bands. The existence of non-fluorescent pixels (e.g., bare soil) within the flight line affects the overall possibility and accuracy of the SIF retrievals. This quality flag reports the overall amount of non-fluorescent pixels (%) at nadir (± 30 pixels) that are used in the SIF retrieval.

Value	**QUALITY**
< 1%	doubtful SIF retrieval
> 1%	meaningful SIF retrieval
Output data format	
SIF map product	
• %NON_FLUO_PIXELS = % of non-fluorescent pixels at nadir (single value for the entire image)	
Summary pdf file	
Total % of non-fluorescent pixels	

Surface topography

Topographic effects (elevation/slope/aspect) are not considered or corrected within the current SFM retrieval algorithm. Hence, errors can affect SIF maps calculated on rugged terrain or even areas with subtle elevation changes. Further developments in SIF retrieval should aim at including topographic effects, but for the moment we defined only a quality flag to provide a systematic/automatic flag. The flag is defined as the standard deviation value of the image pixel elevations extracted from the DEM. Larger standard deviation values indicate varying topography and therefore the expected quality of SIF retrievals could be poorer.

Operationally, the global digital elevation model product from ASTER available at a spatial resolution of 1 arc second (approximately 30 m horizontal posting at the equator) is used (https://doi.org/10.5067/ASTER/ASTGTM.003). The implemented routine enables the automatic download of tiles (https://lpdaac.earthdata.nasa.gov) corresponding to the *HyPlant* image and the extraction of values from the area covered by *HyPlant*. The mode and standard deviation values are calculated and stored in the quality flag outputs.

Value	**QUALITY**
> 15 m	suboptimal (rugged terrain)
< 15 m	optimal (flat terrain)
Output data format	
SIF map product	
• SURF_ELEVATION_MODE = mode of the elevation values (single value for the entire image) • SURF_ELEVATION_Q10 = 10th percentiles of the image surface elevation • SURF_ELEVATION_Q90 = 90th percentiles of the image surface elevation	
Summary pdf file	
Mode and standard deviation value	

All the quality flags computed for every pixel of the image are than stored in an ENVI image file; an example is reported in Figure 21.

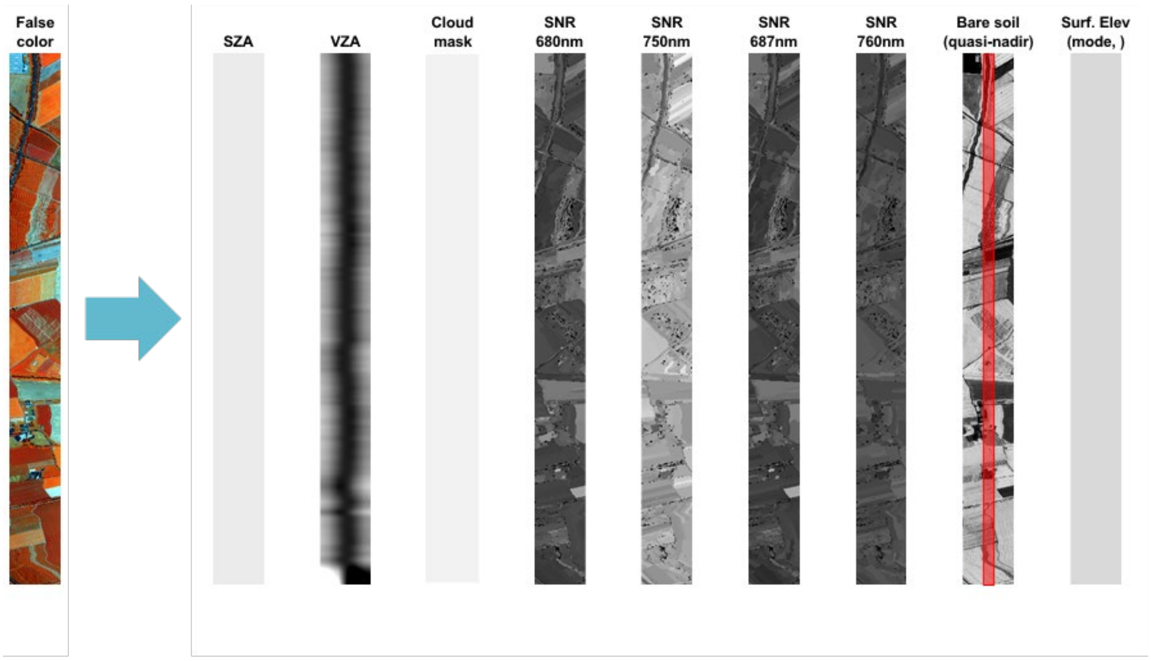

Figure 21 Quality flags derived from *HyPlant* FLUO at-sensor radiance (example from image 20190626-CKA-1313-600-L2-S-FLUO_radiance). For a bigger image, see the appendix.

5.1.2 L2 Processing

Fluorescence retrieval

The red and far-red fluorescence peaks are retrieved from *HyPlant* data by analyzing narrow spectral windows centered on the two O_2-B and O_2-A bands. The airborne fluorescence retrieval consists of three main processing blocks: 1) in-flight characterization of the instrument spectral response functions (SPECCAL); 2) modeling of the atmospheric transfer functions; and 3) decoupling of the canopy fluorescence and reflectance (Spectral Fitting Method, SFM).

The novelty in the fluorescence retrieval resides in the modeling of the atmospheric transfer functions by means of an internal estimation of the 'effective' surface/sensor distance, with the aim of limiting uncertainty about the effect of atmospheric vertical profile on the O_2 bands. The 'effective' distance is not equivalent to the geometric distance, but rather interpreted as the geometric distance that produces an effect on the radiative transfer variables (i.e., O_2 absorption) equivalent to a defined change in atmospheric pressure. On a practical level, this fluorescence retrieval offers a few advances: i) to obtain more robust and accurate fluorescence estimations for the entire variety of atmospheric and environmental conditions; and ii) to provide airborne fluorescence products without a strict need for accurate external auxiliary information (i.e., sun photometer, as required by the previous versions of the algorithm). Operatively, this concept was implemented within the novel *HyPlant* fluorescence retrieval code in the following main processing steps:

<u>Identifying non-vegetated pixels:</u> The NDVI map is exploited to obtain a 'binary classification' of the imagery between two classes: vegetated and non-vegetated pixels. This is done by using a threshold corresponding to a value between $0 < NDVI < 0.15$. Only non-vegetated pixels that are in the central columns of the image are considered (±30 pixels that correspond to a viewing angle of ±1.2°). This is required to prevent any changes in O_2 absorption depth caused by different sensor viewing angles (between 0 and ±16°). In fact, different viewing angles correspond to slightly different surface sensor

path lengths and, consequently, a different amount of O_2 absorption. Finally, the average at sensor radiance spectrum of non-vegetated pixels is computed. An example of the implemented procedure is reported in Figure 22.

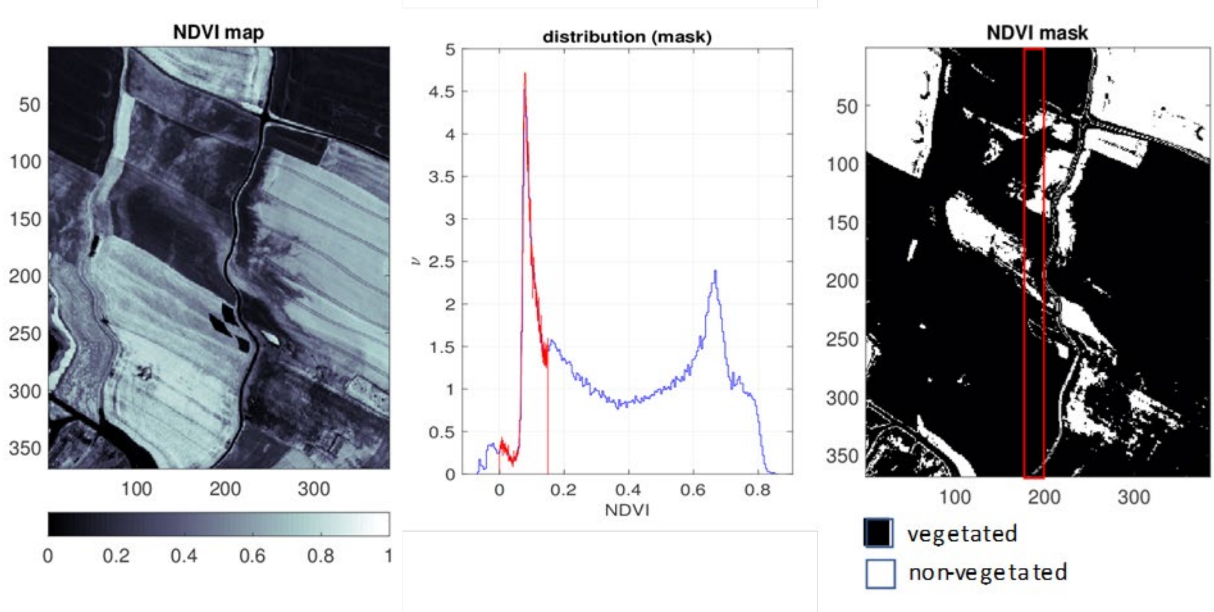

Figure 22 (left) NDVI map; (middle) frequency distribution of NDVI values for the entire image (blue line) and distribution of pixels in the range 0 < NDVI < 0.15 (red line) and (right) NDVI binary mask considering a threshold value of 0.15.

Estimation of 'effective' surface/sensor distance at the O_2 bands: The effect caused by different values of atmospheric pressure can be simulated by changing the geometric surface/sensor distance. Since the parameter H1 of the MODTRAN code (MODerate resolution atmospheric TRANsmission) defines the sensor altitude, it is considered in particular. The MODTRAN simulations are performed considering different values of sensor altitudes for every flight line (Figure 23). Three values are considered: i) nominal flight altitude; ii) ½ nominal flight altitude; and iii) 2x nominal flight altitude. The MODTRAN simulations are stored in an internal Look-up-Table (LUT) (Figure 23) and fluorescence is computed from the average at-sensor distance (estimated in the previous point) considering different sensor altitudes. Thereafter, the 'effective' H1 is derived under the assumption that F = 0 (null fluorescence) for non-vegetated pixels. In practice, the linear regression model between fluorescence and H1 values is estimated, and the 'effective' H1 value, which corresponds to F=0, is computed (Figure 24).

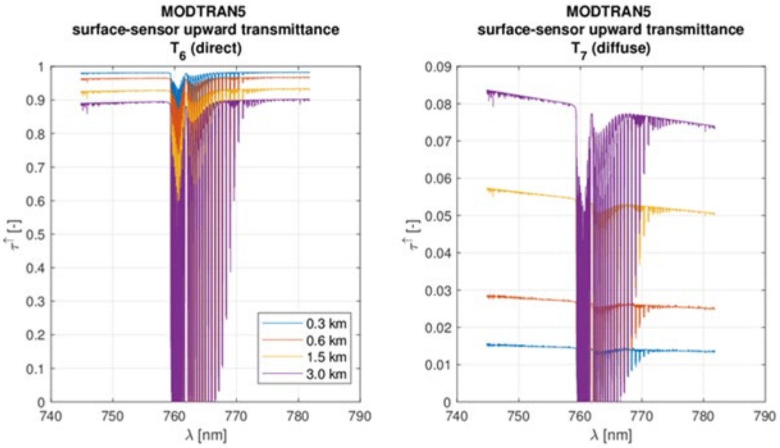

Figure 23 Example of surface to sensor direct (left) and diffuse (right) transmittance spectra computed by MODTRAN5 (spectral resolution of 0.1 cm^{-1}) considering different H1 values.

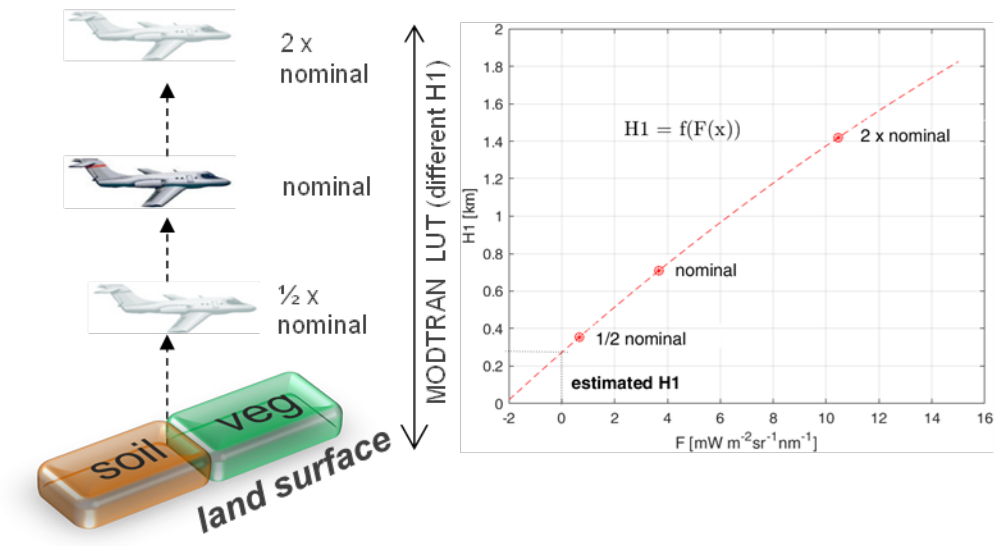

Figure 24 Procedure for atmospheric correction: fluorescence values are computed over non-fluorescent pixels considering different sensor heights. The H1 value that provides fluorescence equal to zero is later on used over the entire image.

<u>Atmospheric RT calculations with different viewing angles:</u> The atmospheric transfer functions are computed with MODTRAN considering the 'effective' H1 value estimated in the previous step. The atmospheric RT calculations are performed twice considering nadir and off-nadir view angles (i.e., 0° and 16°, respectively). This expedient allows a better retrieval of fluorescence at the edges of the image (off nadir), because atmospheric function results are more accurate, even in this part of the imagery. Technically, the off-nadir viewing angle value of 16° is considered sufficiently accurate for the purposes of the RT calculations because the roll angles registered from the IMU is typically lower than 1° in most of the flight lines. Finally, the atmospheric transfer functions for each column of the image are computed by means of a linear interpolation, considering nadir and off-nadir MODTRAN simulations as boundary conditions. The assumption of a linear variation between nadir and off-nadir

might be not very accurate, but for the moment, it is considered a good compromise between complexity and retrieval accuracy.

Fluorescence retrieval: The SFM algorithm relies on forward simulation of at-sensor radiance spectra at the O_2 bands by means of coupled surface/atmosphere RT calculations. The forward simulation assumes that the surface is characterized by a spectrally smooth behavior that can be modeled with simple parametric functions (i.e., polynomials for reflectance; peak-like functions for fluorescence). The propagation of radiation through the atmosphere is performed by using the MODTRAN® computer code. The atmospheric spectra calculated with MODTRAN are further combined according to the T18 system proposed by Verhoef et al. (2018). Afterwards, they are employed to simulate the *HyPlant* at-sensor radiance (*L*). The forward model relies on the four-stream radiative transfer theory (Verhoef and Bach 2012), which represents an accurate and efficient approach for describing the radiative transfer interactions between surface and atmosphere (eq. 12).

$$L = \rho_{so} \frac{E_s^0 \cos\theta_s}{\pi} + \left[\frac{\tau_{ss} r_{so} E_s^0 \cos\theta_s}{\pi} + F_{so} + \frac{(\tau_{sd} + \tau_{ss} \overline{r_{sd}} \rho_{dd}) E_s^0 \cos\theta_s / \pi + \overline{F_{hem}} \rho_{dd}}{1 - \overline{r_{dd}} \rho_{dd}} r_{do} \right] \tau_{oo} + \left[\frac{(\tau_{sd} \overline{r_{dd}} + \tau_{ss} \overline{r_{sd}}) E_s^0 \cos\theta_s / \pi + \overline{F_{hem}}}{1 - \overline{r_{dd}} \rho_{dd}} \right] \tau_{do} \quad \text{eq. 12}$$

The L spectrum is composed by three additive terms that are referred to as atmospheric path radiance, target's surface radiance and adjacency contributions, respectively. The surface reflectance is modeled by four-terms: r_{so} is the target bi-directional reflectance factor, r_{do} the target directional reflectance for diffuse incidence, $\overline{r_{sd}}$ the average surroundings diffuse reflectance for solar irradiance, and $\overline{r_{dd}}$ the average surroundings diffuse reflectance for diffuse incidence. The ρ_{so} is the atmospheric bi-directional reflectance and the ρ_{dd} the spherical albedo of the atmosphere. The τ_{ss} is the direct atmospheric transmission in the direction of the sun, τ_{oo} the direct atmospheric transmittance in the viewing direction, τ_{sd} diffuse atmospheric transmittance for solar incidence and τ_{do} directional atmospheric transmittance for diffuse incidence. E_S^0 is the extra-terrestrial solar spectral irradiance on a plan perpendicular to the sunrays, and θ_s is the local solar zenith angle. F_{so} is the SIF radiance of the target in the observer's direction and $\overline{F_{hem}}$ the hemispherical fluorescence flux of the surrounding. The over bar indicates the spatial filtering of the terms related to the infinitely extended surrounding area. Currently, eq. 12 is employed under the Lambertian assumption for both reflectance and fluorescence, which means that the different reflectance r_{so},r_{do}, r_{sd}, r_{dd} and fluorescence F_{so}, F_{hem} terms are considered equal. To process *HyPlant* imagery, the spectral fitting approach uses the 750 nm–780 nm and 684 nm–697 nm spectral windows for O_2-A and O_2-B bands, respectively. The fluorescence spectral behavior is modeled as a computationally fast pseudo-Voigt, implemented as a linear combination of Lorentzian and Gaussian peak functions. The reflectance spectrum is instead represented by a third order polynomial function at the O_2-A band or a piecewise cubic spline for the O_2-B. The fluorescence/reflectance parameter are thus estimated by means of inverse method, based on an iterative non-linear least square minimization. Least square problems typically formalize the cost function in term of squared difference between simulated (L_{sim}) and observed (L_{obs}) spectra around the O_2 bands.

$$\min \sum_{\lambda} (L_{sim}(\lambda) - L_{obs}(\lambda))^2 \qquad \text{eq. 13}$$

In practice, fluorescence/reflectance parameters are changed in the direction to reduce the cost function, until the best match between simulated and observed spectra is not reached. The minimization algorithm exploits the efficient Trust-Reflective Region algorithm.

Fluorescence uncertainty

SIF retrieval uncertainty is generated by various factors, such as instrument measurement, raw data processing (L0), at-sensor radiance (L1), and SIF retrieval (L2). In this section, we distinguish between the concept of error (difference between the retrieved vs. true value, caused from a bias) and uncertainty (distribution around retrieved value, i.e. caused from random processes in the retrieval). Please see section 6.1 for more details, or Povey and Grainger (2015).

Per-pixel uncertainty is evaluated within the L2 processing during the SIF retrieval, which is the last critical step of the processing chain. Particularly, SFM retrieval is based on the inversion of at-sensor radiance by means of iterative numerical minimization. This operation is prone to introduce uncertainty in the final retrieved values. Since the true value for every pixel is unknown, the uncertainty is estimated (ex-ante uncertainty) based on the standard Gaussian error propagation of non-linear regression methods. The estimation is based on the Jacobian (K) matrix at the solution (final iteration) and the corresponding residuals. The uncertainty of the model free parameters (i.e., fluorescence and reflectance coefficients) is converted to uncertainty on the fluorescence spectrum and finally stored in the output file. The uncertainty is intended as a confidence interval defined at the 1σ statistical level.

The uncertainty estimation is implemented and its interpretation is strictly related to the assumptions and specificities of the retrieval algorithm's physical assumptions. In case of the SFM, the value estimated implicitly in the total budget includes several sources of uncertainty from measurements, pre-processing and the inversion method. For example, random instrument noise in the observed at-sensor radiance (*HyPlant*) inevitably affects the final SIF retrieval because noise propagates through the successive data processing steps. Other sources are explicitly (or implicitly) compensated for by the SFM algorithm, as in the case, for example, of instrument spectral calibration (SPECCAL). Nevertheless, this compensation is not perfect, and the residuals affect SIF uncertainty. Table 10 provides a first systematic summary with the aim of offering insight into this complex topic, in order to explain:

i) different uncertainty sources;

ii) compensation strategies undertaken in the SFM to limit/cancel impact on SIF;

iii) contribution to the total uncertainty budget

Table 10 Uncertainty sources of the SIF retrieval based on SFM.

Source of uncertainty		**Algorithm compensation**	**SFM uncertainty budget**
Instrument measurement and L1 processing **(L1 data)**	Random radiometric noise	Yes from SFM (least square fit)	Yes
	Radiometric calibration	Yes atmospheric correction tuned on non-fluorescent pixels (data driven) from SFM	Limited impact
	Radiometric nonlinearity	Yes from L1 processor	Yes
	Spectral calibration	Yes from SFM (speccal)	Limited impact
	Spatial PSF	Yes deconvolution algorithm	No
	Auxiliary data (nav file)	NA	No
Retrieval model: **- atmospheric correction** **- SIF retrieval** **(L2 data)**	Incomplete model: - spectrally dependent aerosol properties (not retrieved) - water vapor (not retrieved)	No	Yes
	Parametric model (SIF/R forward model)	NA	Yes (characterized with theoretical studies and RT simulations)
	Numerical issue	NA	Yes
	Model constants	NA	NA
	A priori information	NA	NA
Unknown error components		NA	Yes
Natural variability		NA	Yes

For the first time, per-pixel uncertainty (at a 1σ confidence level) has been calculated with the fluorescence maps produced from *HyPlant* and computed systematically over the entire dataset. An example of the SIF uncertainty maps produced is shown in Figure 25.

In summary, as a rule of thumb, the absolute uncertainty observed was roughly on the order of 0.15–0.25 mW $m^{-2}sr^{-1}nm^{-1}$ on average, with relative uncertainty of 10–20% for the vegetated pixels. A diurnal trend was observed, and, as expected, the absolute uncertainty is larger around noon since the absolute fluorescence value is larger (absolute uncertainty depends on signal intensity). Also, the trend observed for the relative uncertainty shows an expected pattern characterized by a lower value at noon. This agrees with the fact that measurement/retrieval conditions are better at noon (higher fluorescence signal, better SNR, lower BRDF, etc.). A detailed and quantitative analysis and discussion is reported in section 8.3.

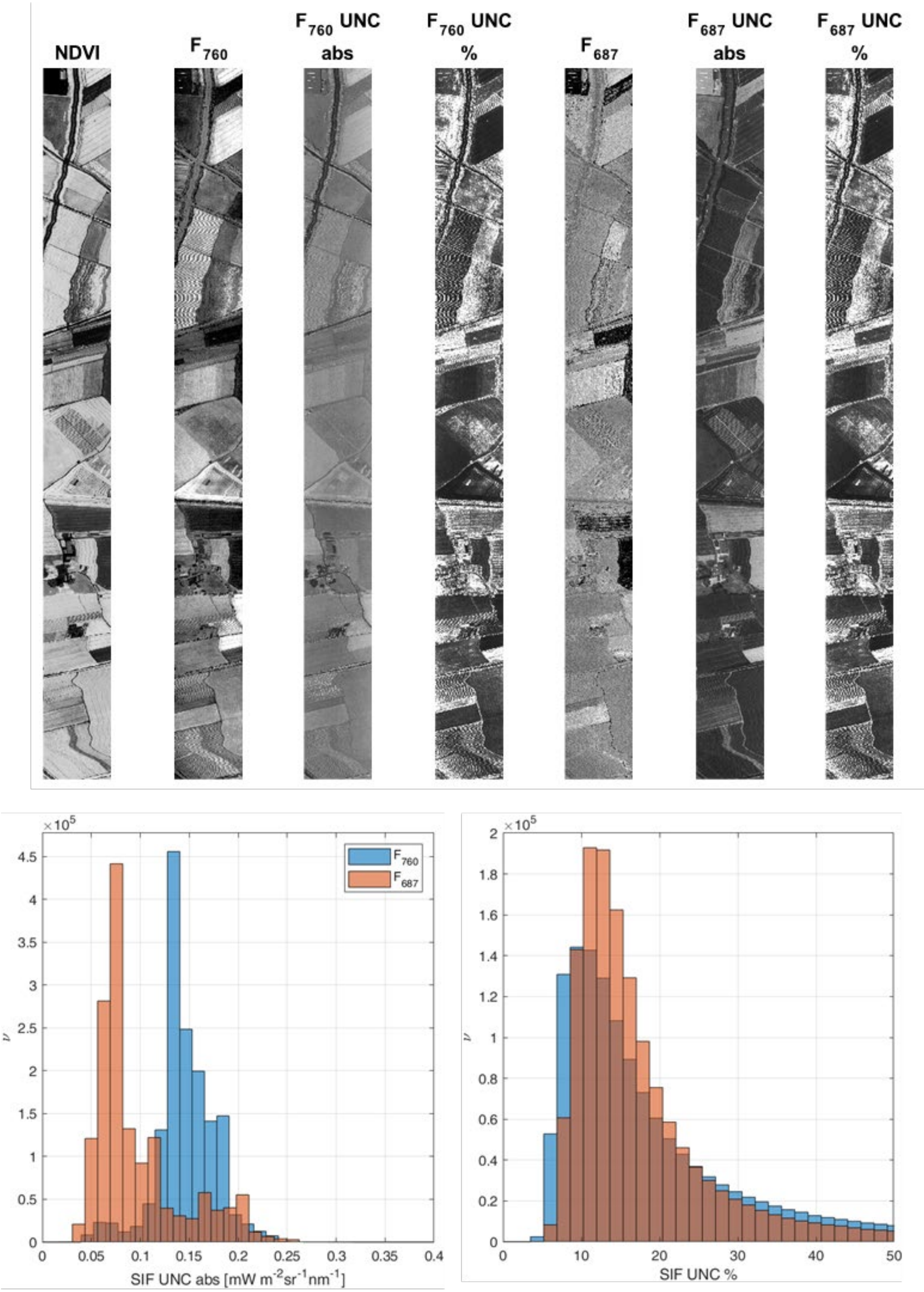

Figure 25 Fluorescence (F) and uncertainty (UNC) estimated at 760 nm and 687 nm in absolute (abs) and relative (%) units.

5.2 Data Product File Format

A new file format for data products was defined to better organize the different products produced from the retrieval algorithm (data layers) within the output data (ENVI file format). The quality flags are stored within the data files produced by the *HyPlant* processing chain as pixel-level values stored within *HyPlant* product files. The intent is to offer numeric values for quantitative and automated selection/filtering of the image data for downstream analysis. A data product quality report file (.pdf file) is produced along with each flight line that summarizes overall quality flags, uncertainties and image statistics. Compared to the past, the fluorescence spectrum at the retrieval spectral window (i.e, corresponding to the O_2 bands) is not provided any longer, because the different wavelengths are extremely correlated and they do not contain additional information compared to the O_2 bands. The fluorescence scalar values at the center of the O_2 bands are stored (i.e., 760 nm and 687 nm for the O_2-A and O_2-B bands respectively) with the quality indices as well.

The ensemble of data product layers including quality flags, SIF maps and uncertainty is depicted in Figure 25 and Figure 26, and detailed in Table 10.

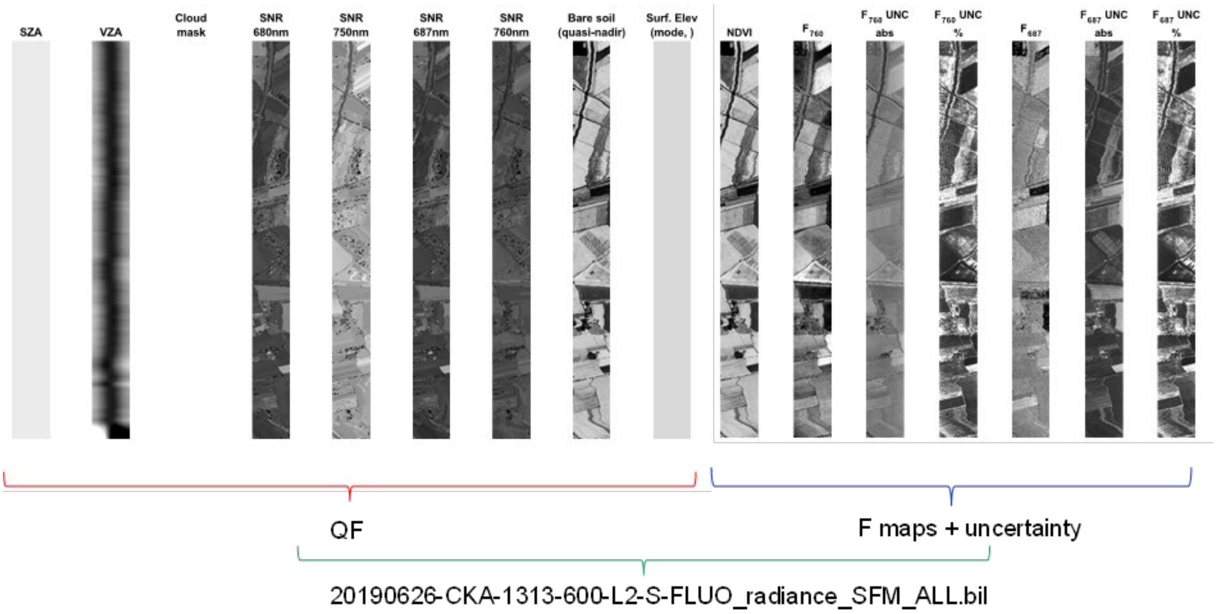

Figure 26 Quality flags, SIF maps and estimated per-pixel uncertainty are stored in the file product obtained from the SFM algorithm (example image 20190626-CKA-1313-600-L2-S-FLUO_radiance_SFM_ALL.bil).

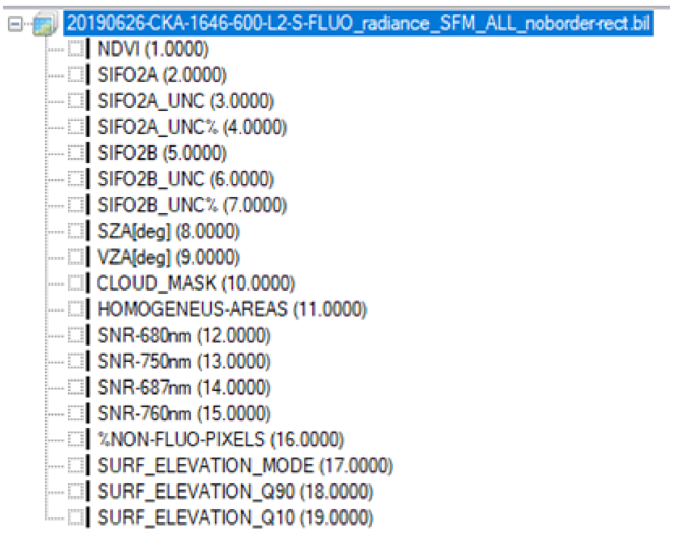

Figure 27 Example of the data layers stored in the output file after quality flags and SFM processing, as visualized in the ENVI software.

Table 11 Description of the data layers in the output file.

LAYER NAME	DESCRIPTION
NDVI	Normalized Difference Vegetation Index
SIFO_2-A	Fluorescence at the O_2-A band
SIFO_2-A_UNC	Uncertainty of the fluorescence at the O_2-A band
SIFO_2-A_UNC%	Relative uncertainty of the fluorescence at the O2-A band
SIFO_2-B	Fluorescence at the O_2-B band
SIFO_2-B_UNC	Uncertainty of the fluorescence at the O_2-B band
SIFO_2-B_UNC%	Relative uncertainty of the fluorescence at the O_2-B band
SZA	Solar zenith angle
VZA	View zenith angle
CLOUD_MASK	Cloud mask
SNR-680	Signal to noise ratio at 680 nm
SNR-750	Signal to noise ratio at 750 nm
SNR-687	Signal to noise ratio at 687 nm
SNR-760	Signal to noise ratio at 760 nm
%NON-FLUO-PIXELS	Percentage of non-fluorescence pixels (+/- 30 pixels from nadir)
SURF_ELEVATION_MODE	Statistical mode of the image surface elevation
SURF_ELEVATION_Q90	90^{th} percentiles of the image surface elevation
SURF_ELEVATION_Q10	10^{th} percentiles of the image surface elevation

The fluorescence retrieval code is implemented in MATLAB using a parallel computing technique (OpenMP). The code can run on Windows desktops or on high-performance Linux-based IT infrastructure. The latter was used to process the entire data set collected during the 2019 FLEXSense campaign, in order to support the project with high-performance infrastructure and simplify the processing activity. Several Linux bash scripts were implemented to simplify the following activities: i) preparation of the scheduler submission scripts (Slurm files); and ii) review and reporting of the information stored in the output log files from the scheduler. The fluorescence retrieval algorithm software code project is implemented in MATLAB and is hosted on the GitLab online service (https://gitlab.com/cogliatisergio/HYPLANT-SFM) to provide simple and fast access and to track changes in the latest and updated version of the software code between the teams involved in development and testing at University of Milano-Bicocca and Forschungszentrum Jülich.

5.3 Development towards integrating different surface and canopy heights into the SFM

Topographic effects (elevation/slope/aspect) are not yet considered within the current retrieval algorithms. This effect can alter the accuracy of the final fluorescence maps in different ways. Elevation changes (i.e., different surface-sensor distance, GNDALT) strongly affect the depth of the oxygen absorption band used for SIF retrieval. A longer surface/sensor path corresponds to a larger O_2 absorption. Studies focused on tower-based fluorescence measurements indicate that 10–20 m affect the O_2-A band depth and, consequently, could impact SIF retrieval (Sabater et al. 2018). This is the main effect and it is a specific issue related to fluorescence retrieval based on O_2 bands.

The slope/aspect plays an additional role in the radiative transfer because the irradiance reaching the surface (computed from MODTRAN in the atmospheric correction) is affected by the topography and needs to be corrected. The method proposed by Minnaert (Richter et al. 1998), for example, is a simple but effective solution. However, slope/aspect also involves the anisotropic behavior of the surface, since the surface is observed from different viewing angles that in some cases could be extreme for surfaces with elevated slope values.

In the current retrieval algorithm, the topographic effect can have a twofold negative impact: i) compromising the estimation of the atmospheric functions in the case of non-fluorescent pixels at different elevation (pixels used as reference in the atmospheric correction, and; ii) individual pixels may be located at a different elevation with respect to those used to derive the atmospheric correction parameter.

An initial concept for considering the topographic effect was developed with the intention to further evolving airborne fluorescence retrieval. In general, this enhancement will enable the processing of flight lines over rugged terrain. However, it will also improve the accuracy of images collected over moderately rugged terrain (i.e., from tens to one hundred meters of elevation change). Potentially, there are two levels of detail that could be considered as part of fluorescence retrieval from O_2 bands:

1. **Coarse scale**: Correcting Earth’s surface topography: the aim here is to provide a first order topographic correction by means of widely available DEM data (i.e., ASTER 30 m). This enables the exploitation of SFM retrieval without a strict requirement for additional data (i.e., LiDAR or stereophotogrammetry)
2. **Fine scale**: Correcting the individual object height, to account for divergent sensor/surface distance while considering the height of objects (trees, grassland, etc.). This requires fine spatial scale DEM data in which the object’s height is properly resolved and compatible with *HyPlant*’s spatial resolution. LiDAR or stereophotogrammetry data collected consistently with *HyPlant* during the campaign could be considered as inputs.

For the moment, we are limiting our initial efforts to the implementation of a **coarse scale** correction considering the **surface elevation**, while neglecting slope/aspect for the moment, since a minor effect is expected at this stage. Our approach aims to correct the first-order topographic effect related to O_2 band depth.

The assumptions adopted in the definition of the algorithm are:

- Atmospheric properties (H1) affecting the fluorescence retrieval at the O_2 bands are assumed to be constant for the entire image. The elevation of individual pixels (GNDALT) is corrected afterwards,
- Atmospheric properties are estimated only from bare soil pixels at a selected elevation (selected elevation: bare soil pixels located at the most frequent surface elevation value),
- Atmospheric properties are estimated by means of the current approach,
- MODTRAN simulations need to cover the DEM variability over the entire image (10^{th}-90^{th} percentile). Look-up table or ML emulators are two possible alternatives,
- MODTRAN simulations are interpolated considering each specific pixel elevation value,
- fluorescence/reflectance are decoupled by means of SFM.

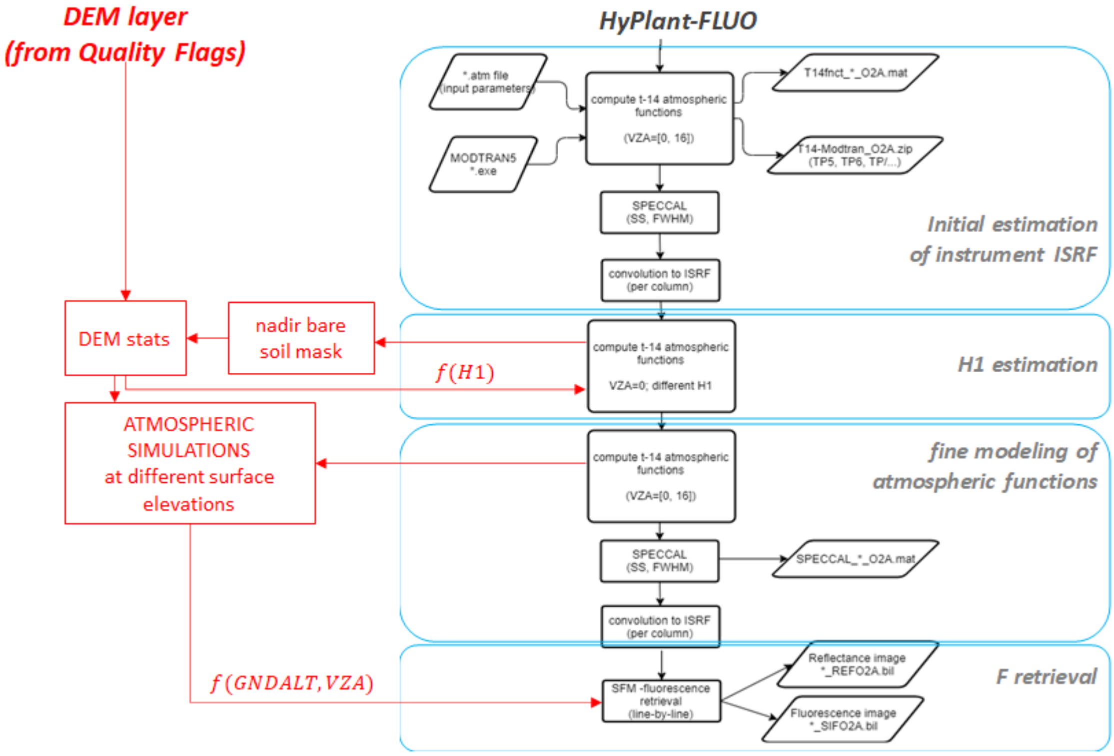

Figure 28 Flowchart of the SFM retrieval algorithm including topographic correction.

6 CHARACTERIZATION OF THE ACTIVE AND PASSIVE REFERENCE TARGETS AND THE EVALUATION FOR THEIR INTEGRATION INTO THE CAL/VAL CONCEPT

6.1 OVERVIEW OF DATA AND CONSIDERATIONS USED TO EVALUATE THE UNCERTAINTY OF SIF PRODUCTS

A thorough evaluation of the accuracy and precision of SIF products is a prerequisite for refining SIF retrieval methods, for developing a Cal/Val scheme for FLEX, and for facilitating SIF-based applications. At least two complementary validation approaches exist: i) a direct evaluation of retrieved SIF, and ii) an evaluation of data used along the entire processing chain, from observations (L0) to calibration (L1) to retrieval (L2) and the representativeness of the observation considering the FLEX satellite footprint (or the footprint of any other core mission). The second approach provides the advantage of attributing bulk SIF retrieval uncertainties obtained from approach (i) to individual methods and assumptions applied in the data processing.

We adopt the approach taken by Povex and Grainier (2015), according to which accuracy contains two components – that is, 'error' and 'uncertainty' (Figure 29). Both can be expressed in absolute (unit values) or relative terms (percent values). We will use the terms 'error' and 'uncertainty' in this report accordingly, i.e. 'error' describes the difference of a measurement from the true or target value, while 'uncertainty' describes the statistical distribution of repeated measurements/retrievals. It should be mentioned that there are different terminologies used in the literature; ISO-5725, for example, uses the terms 'accuracy' or 'trueness' (equivalent to our 'error') and 'precision' (equivalent to our 'uncertainty'). Other terms that are widely used in the remote sensing community are 'systematic error' (also called 'statistical bias') which characterizes the trueness of a measurement or a retrieved value and thus is equivalent to our 'error'. A random error, also called 'statistical variability', characterizes the precision of a measurement or a retrieved value and thus is equivalent to our 'uncertainty' definition.

Thus, 'error' quantifies a possible systematic offset of a value compared to its true representation caused by the observational system (e.g., the instrument is not well aligned) or the processing approach (e.g., the retrieval approach contains an excessively strong assumption). The 'uncertainty' quantifies the variation of a value that was sampled several times compared to its true representation. Uncertainties are often caused by the sensitivity of the observational system (e.g., noise in the observational system) or the natural variation of the observed process/object that cannot be precisely compensated for by the processing approach (e.g., variation within the canopy).

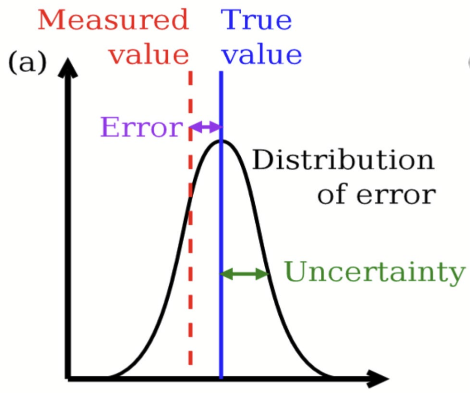

Figure 29 Definition of 'error' and 'uncertainty' based on Povey and Grainger (2015). In this report, we assume a normal distribution of all uncertainties (figure taken from Povey & Grainger 2015).

As part of several campaigns undertaken to support of FLEX, including FLEXSense 2018, FLEXSense 2019, and ATMOFLEX, various field and flight experiments were conducted to collect in situ, airborne and satellite data. This collected data set allows us to move toward a full uncertainty budget for SIF across observational scales. Table 12 provides an overview of available data in support of the quantification of errors and uncertainties in relation to processing level and observational scale.

As part of this activity, we were able to take a step forward in constraining errors and uncertainties associated with *HyPlant* SIF products. We point out the data from ATMOFLEX, which allowed us to consider FloX system uncertainty. From the theoretical considerations (Bumann et al. 2022), *HyPlant* SIF products are influenced by four main sources of uncertainty:

i. **Instrument errors and uncertainty (σ_{inst})**, which includes any instability of the sensor per se and variations that result from errors introduced during the laboratory characterization and calibration. Such calibration uncertainties would be present in the at-sensor-radiance data, which are the input data for SIF retrieval. To better understand these errors and uncertainties related to the instrument itself, we revisited the calibration documents and data from the laboratory calibration in the years 2015–2021. Based on this analysis (see section 3.1.1 for details), we can conclude that the current *HyPlant* system is stable across the years and that there is very low uncertainty in the at-sensor-radiance data (level 1c) of the FLUO module. However, we must assume a considerable error in the absolute at-sensor radiance data, which is related to the error of the SPECIM calibration units. This error in absolute radiance data is in the range of up to 4% and may be relevant when comparing *HyPlant* data across years. This error can be reduced in the future by using an alternative calibration facility that is better suited for the high spectral resolution of the *HyPlant* FLUO module.

ii. **Errors and uncertainty in atmospheric correction** of the data (including the correction for the atmospheric reabsorption of the upwelling SIF signal) ($\boldsymbol{\sigma_{atmo}}$). Here, errors and uncertainty may come from wrong parametrization of the atmospheric transfer modeling or from inaccuracies in the atmospheric correction algorithms. We refer to sections 5, which provides detailed information on this topic. The current SFM atmospheric correction and SIF retrieval are done in one step and thus we cannot give separate figures for the error and uncertainty that are associated with the atmospheric correction per se. See the paragraph below for more details.

iii. **Errors and uncertainty in SIF retrieval (σ_{retr})**, including errors and uncertainty in the iFLD or SFM retrieval code itself. Here, sources of errors and uncertainties may be caused by the selection of non-vegetated reference pixels and the assumptions/parameters used in the retrieval code. With the current SFM retrieval code, atmospheric correction and SIF retrieval are done in one step. Accordingly, we cannot give separate figures for error and uncertainty that are associated with the SIF retrieval per se (see also the paragraph above). With this report, we can present for the first time quantitative error and uncertainty values for the *HyPlant* SFM SIF products (section 5). Additionally, we have performed extensive comparisons between the *HyPlant* SIF products and the known fluorescence emission intensities from the reference targets (sections 4.3 and 6).

iv. **Errors and uncertainties in the representativeness (σ_{rep})** of the SIF image, which includes errors and uncertainties in the pointing accuracy and co-location of the single pixels with ground objects. At the current time, we cannot give a quantitative number for this term. This issue is best addressed in follow-up studies, as it greatly depends on the pointing accuracy of the single sensors. For *HyPlant*, we are currently providing a very high spatial resolution (1–3 m ground sampling distance, or GSD) with a good pointing accuracy (the geometric error of every pixel in *HyPlant* imagery is ≤ 1 pixel). Thus, we greatly oversample a potential 300 x 300 m FLEX pixel, which opens many options to minimize representativeness uncertainties –for example, by using borders around objects.

For now, we assume that these four terms are independent, thus allowing us to calculate a maximum total error and uncertainty of the SIF products (σ_{ges}) according to (eq. 14)

$$\sigma_{ges}^2 = \sigma_{inst}^2 + \sigma_{atmo}^2 + \sigma_{retr}^2 + \sigma_{rep}^2 \qquad \text{eq. 14}$$

By comparing the final *HyPlant* SIF products with the active reference targets (which, however, produced an unrealistically high fluorescence intensity), we can conclude that the error of the final *HyPlant* SIF products is in the range of 0.15–0.7 mW m^{-2} $sr^{-1}nm^{-1}$. The uncertainty of a single pixel in a *HyPlant* map was in the range of 0.6–3 mW $m^{-2}sr^{-1}nm^{-1}$ (Table 19). It should be noted that these errors and uncertainties also contain the errors and uncertainties from instrument calibration and may also contain partially unaccounted for errors and uncertainties from the reference targets. Additionally, the uncertainty values are derived from the active reference targets, which emitted a very intense fluorescence signal, which was higher than the average SIF of natural vegetation by a factor of 5–10. Thus, it is fair to assume that the pixel uncertainty of the *HyPlant* SIF products is more in the range of 0.1–0.5 mW $m^{-2}sr^{-1}nm^{-1}$. Thus, the determined figures for the errors and uncertainties are most likely conservative, i.e. high estimates. We were also able to pin-point factors, such as the calibration facility, that represent easy options for reducing error and uncertainty. In addition, the entire analysis was done on single (un-binned) *HyPlant* pixels. As *HyPlant* maps provide a high spatial resolution of 1 x 1 m GSD, spatial binning may provide a powerful option for increasing the SNR of the sensors, thus reducing uncertainty in future Cal/Val concepts (see section 7).

Table 12 Overview of experiments and data that we collected within the scope of the past years' campaigns, i.e. the ATMOFLEX activity (AF), the two-year FLEXSense campaign (FS18 & FS19) and the PhotoProxy study (PP). Data from the different campaigns shed light on the various components of SIF instrument error and uncertainty. Despite this extensive data set, we also identified some gaps that still need to be addressed before a full and quantitative error and uncertainty budget of ground and airborne SIF products can be achieved. Indicated section numbers refer to data, experiments and analysis documented in the respective ATMOFLEX (AF), FLEXSense 2018 (SF18), FLEXSense2019 (FS19) or PhotoProxy (PP) report.

	Instrument and calibration (at-sensor radiance – L1)	**SIF retrieval (SIF products – L2)**		**Representativeness**
		Atmospheric correction	**SIF inversion**	
In situ: Passive dye and active LED panels	FS19 – section 6.2 (page 69ff) and section 6.3 (page 76ff)	FS19 – section 6.2 and 6.3		FS19 – section 4.3 (page 41ff)[4]
In situ: FloX	DEFLOX final report – section 2.2, AF – WP3, Buman et al. 2022	n.a.		FS18 – section 7.2.2, Buman et. al. 2022, further considerations in PP – section 3.1.2 (page 64ff)
Airborne: *HyPlant*	FS19 – section 3.1.1 (page 15ff)	FS19 – section 5 (page 48ff) and section 6 (page 64ff), AF – WP8 (pages 85–88)		AF – WP8 (qualitative), further considerations in PP – section 3.3 (page 86ff)

Below, we provide a more detailed list of activities carried out to evaluate SIF retrieval error/uncertainty from airborne (1) and ground (2) instruments including the individual uncertainty components: i) instrument characterization; ii) SIF/reflectance inversion. References are provided to the relevant campaign reports for the purpose of reader orientation.

***HyPlant* FLUO – at-sensor radiance (L1)**

- Laboratory uncertainty characterization, including considerations on radiometrical and spectral calibration (FS19, section 3.1.1). Additional material on some aspects is available
    - Influence of the point spread function (PSF) on L1 data and SIF products (HYPER D-2 report [RD-10] & Scharr et al. 2021)
    - Characterization of radiometric non-linearity of *HyPlant* (HYPER D-2 report [RD-10])

- Quality flags for *HyPlant* FLUO data
    - Description and methodology (FS18, section 6)
    - Application to extensive dataset (FS19, section 5.1)

- In-flight vicarious characterization
    - spectral calibration (spectral module) (FS18, section 4.2.1.3)
    - actual image SNR (FS18, section 6.1.6)

[4] Technical failure in LP-40 may have caused some local errors during field measurements and some LED areas may have produced false emissions (see, e.g., the high variability in FL-3 over LP-40).

***HyPlant* – SIF retrieval (L2)**

- Per-pixel SIF retrieval uncertainty
  - Method to estimate uncertainty in the SFM inversion (FS19, section 3.1.2)
  - Uncertainty behaviour across different radiance levels (FS19, section 8.3.1)

- Direct validation of airborne SIF retrievals (*HyPlant* vs. FloX)
  - Natural vegetated targets
    - Selhausen (FS18, section 5.3, section 7.2.2)
    - Grosseto (FS18, section 5.3)
    - Grosseto (AF, WP8, pages 85–88)
    - Majadas (FS18, section 7.4.1)
  - Artificial reference targets
    - Passive targets – DYE (FS19, section 6.2)
    - Active targets – LED (FS19, section 6.3)
  - Indirect validation of airborne SIF retrievals through comparison with RTM simulations based on Grosseto data (AF, WP8, page 89ff)
  - Comparing different SIF retrieval methods (iFLD, SFM, SVD) (FS18, section 5.2)
  - SIF retrieval at different flight altitudes based on Selhausen data (FS18, section 5.4)
  - SIF retrieval in the temporal domain (diurnal cycle at Campus Klein-Altendorf) (FS18, section 7.3.2 & Siegmann et al. 2021)

- SIF retrieval in the spatial domain (land cover)
  - Campus Klein-Altendorf (FS18, section 7.3.2; Siegmann et al. 2021)
  - Selhausen (FS18, section 7.3.2)

- SIF retrieval in the angular domain
  - only a few/sparse ground multi-angular measurements (goniometer) are available in 2018 Grosseto data

FloX – instrument characterization (L1)

- Laboratory spectral characterization and calibration, non-linearity characterization, radiometric calibration, SNR assessment, relative radiometric accuracy between adjacent channels assessment (DEFLOX final report, paragraph 2.2).
- Spectral/radiometric stability in field conditions (AF WP7, page 68ff & Buman et. al. 2022)

FloX – SIF retrieval (L2)

- SFM inversion accuracy (AF, WP3, Cogliati et al. 2019)
- Scaling and spatial representativeness of point measurements
  - Stationary vs. mobile FloX (Selhausen, FS18, section 7.2)
  - FloX representativeness vs. FLEX pixel (Buman et. al. 2022)
  - Selhausen geostatistical analysis (AF, WP8, page 97)

6.2 CHARACTERIZATION OF THE PASSIVE REFERENCE TARGETS

The passive reference targets were characterized initially in the field and, following the campaign, in the laboratory in order to estimate the directionality, spectral signature and amount of emission degradation that became apparent during the first days of the 2019 campaign in Grosseto, Italy.

Figure 30 LRFP and fluorescent dye panels installed in the field in Braccagni, Italy.

To characterize the ground reference targets in the field, three FloX systems were used, namely: JB-001-MM, JB-005-UR and JB-013-ESA. These FloX systems were used to characterize, once in Italy and once in Germany, the emission of the LFRP according to the specific installation configuration (space bar distance and panel size). Furthermore, since the fluorescent dye emission depends on the solar radiance and the dye degrades over time, one FloX was always monitoring the emission during the *Hyplant* overpasses. A preliminary cross calibration of the FloX systems used as a reference in the field was made in Italy to avoid problems related to instrumental differences. In Figure 31, the calibration results for the three systems are reported in terms of downwelling and upwelling radiance, as measured simultaneously by the three systems.

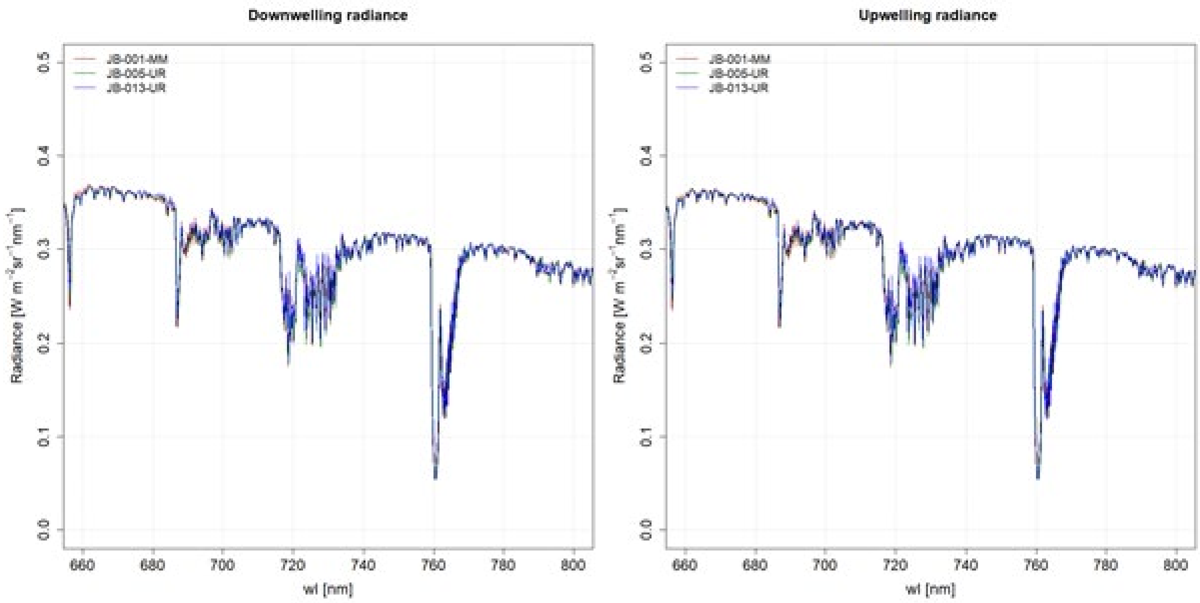

Figure 31 Agreement between the three FloX systems in terms of downwelling and upwelling radiance, as measured above a white spectral panel.

Emission characteristics of the apparent reflectance are shown in Figure 32. Apparent reflectance is plotted as the ratio of irradiance and reflected radiance plus the emitted SIF signal. Peaks in the oxygen absorption bands are visible at 687 and 760 nm (Figure 32 A, B). Although a comparison to natural vegetation measured in the field is missing, the distinct features of the spectral signature such as the red edge starting at 650 nm and the plateauing at 780 nm clearly show the spectral similarity of the dye panel and green vegetation. The measurement was conducted on June 16, the first day of the 2019 FLEXSense campaign in order to minimize the possible effects of dye panel degradation. This measurement might not be the maximum of the emitted SIF of the dye pigments, as there was no information on if and how long the panels were exposed during transport and setup. However, it is an adequate representation of the spectral behavior of a panel that was only briefly exposed to sunlight.

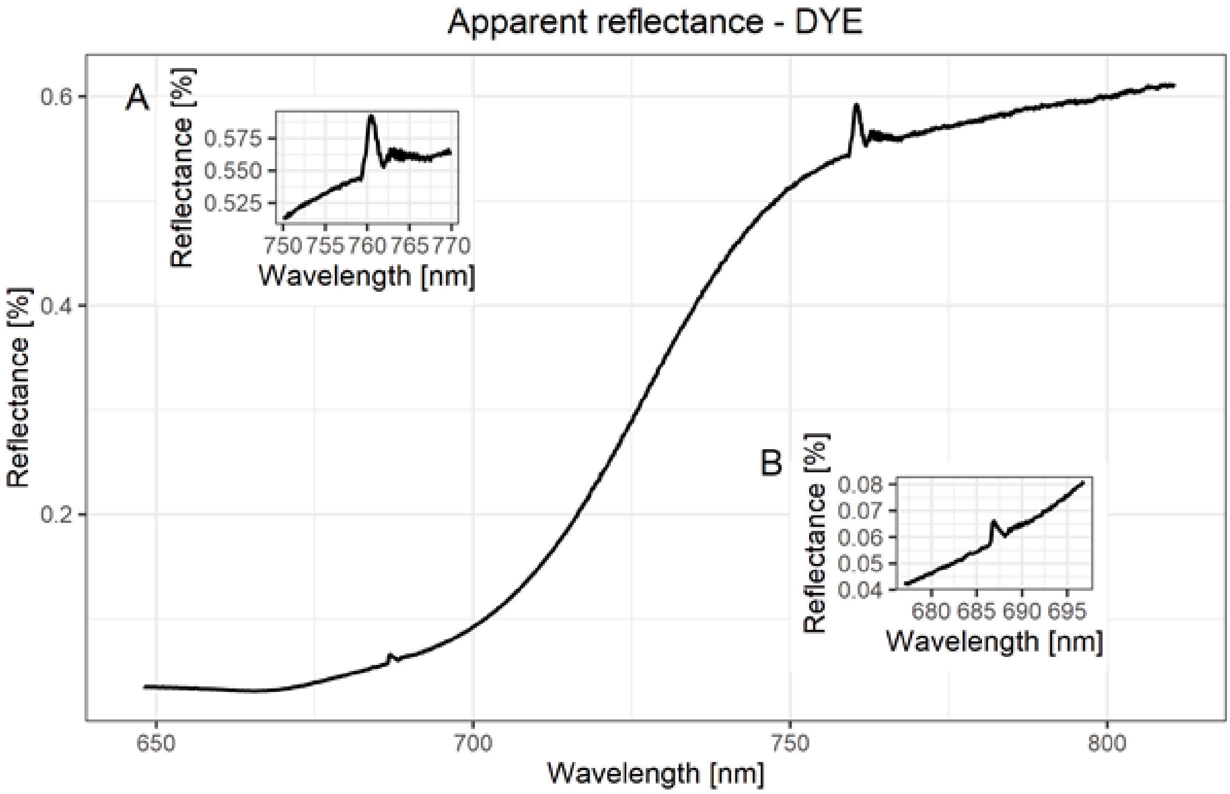

Figure 32 Apparent reflectance of the dye panel as measured in-field by the FLUO spectrometer of the FloX on the first day of the campaign (June 16, 2019). The sub-plots A and B highlight the wavelength ranges of the oxygen absorption features at 760 and 687 nm where the SIF emission is clearly visible.

As mentioned above, signal degradation became apparent during the first measurement days. The exact amount of time that the dye panels were exposed to direct sunlight is difficult to estimate since the ground measurement data set only provides information on the time of the measurement but not if and how long the panels remained uncovered. Continuous measurements from the first day of the campaign showed that the dye panel was uncovered for at least 45 minutes per flyover, during which degradation was already apparent. Though the panel was covered more rapidly after the initial exposure on the first days, the exact amount of exposure cannot be estimated. Therefore, degradation was investigated in relation to the first measurements of the panel.

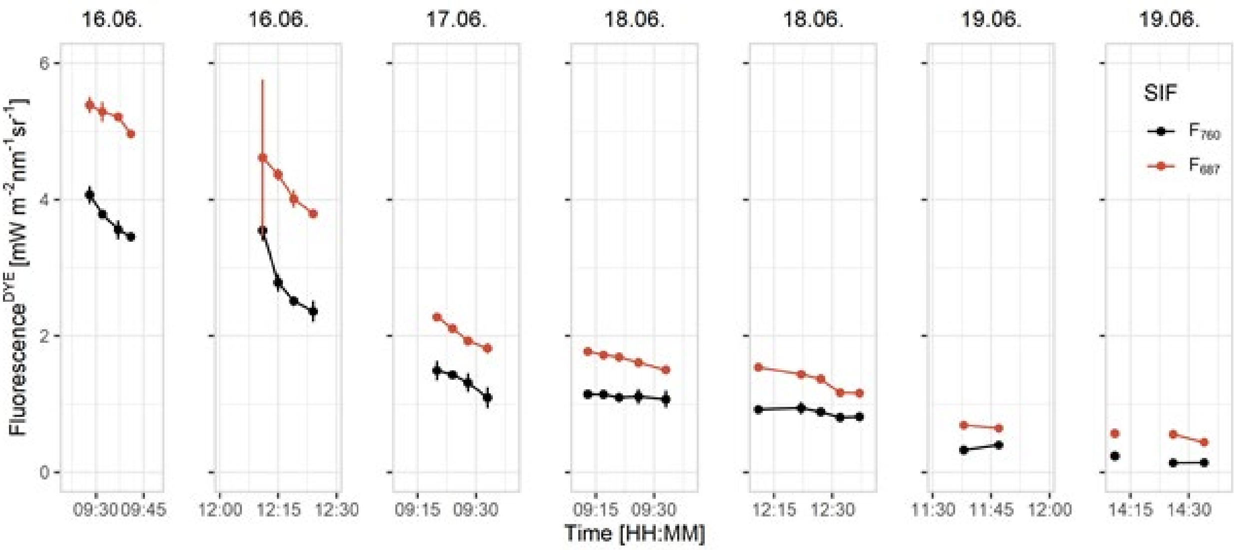

Figure 33 Dye emission of red and far-red fluorescence retrieved with the SFM method from ground measurements using the FloX clustered into *HyPlant* overpass cycles. Each observation correlates to a simultaneous airborne overpass.

Figure 33 shows SIF retrieved from all available ground measurements (processed with the SFM method) that were matched to the respective airborne overpasses used in this study. The observations were clustered into overpass cycles to provide a better understanding of the amount of time involved in the degradation of SIF emission. A general trend of declined emission is visible for both the far-red and red fluorescence, with a low standard deviation throughout, with the exception of the first measurements of the second overpass cycle on day one (June 16, 2019). Unfortunately, the reason for the high standard deviation within the red fluorescence in the specific case of June 16 could not be determined. On the first day of panel deployment (June 16), the panel was left uncovered for 2 hours in direct sunlight after the overpasses in the morning and midday. This explains the strong drop-off in emissions from the second overpass cycle to the third one. From the second day on, the dye panel was only uncovered during the airborne overpasses, as visible in the slower degradation in the following overpass cycles. On the second day of deployment, clouds appeared during midday and afternoon. Therefore, there were only overpasses in the morning. During the third and fourth days, airborne data were recorded again several times during the morning and afternoon. On both days, the panel was covered more rapidly, and therefore a lower number of measurements could be collected. This also explains the lack of standard deviation for most of the observations from June 18 and 19. The higher red emission in comparison to far-red SIF is also visible in the field measurements in Figure 33, which was also observed in the laboratory measurements (Figure 34).

6.2.1 Laboratory characterization

In order to estimate the directional emission characteristics, a laboratory experiment was conducted (Figure 34). A dye panel that was assumed to be unexposed to sunlight was set up horizontally in a laboratory at Forschungszentrum Jülich in Germany. The objective was to get an insight into the angular reflection characteristics through changing illumination angles. The panels radiance was measured at-nadir using an ASD Fieldspec 4 spectroradiometer (ASD Inc., USA) and a Schott KL 2500 LCD halogen lamp (SCHOTT AG Lighting and Imaging, Germany), which was equipped with a 650 nm short-pass filter (Edmund Optics, Germany). The ASD Fieldspec 4 spectroradiometer covers the spectral range of 350–2500 nm and has a FWHM of 1.4 nm in the 350–1000 nm range (ASD Inc., 2010), which is required for this experiment. Before the measurements were conducted, the ASD was warmed up for 90 min. To ensure stable lighting conditions, the Schott cold light lamp was also warmed up, as measurement variation was visible in previous tests. Figure 34 D shows the irradiance spectrum of the Schott cold light lamp measured at different angles reflected by a 95% white Zenith Lite reflectance standard (SphereOptics GmbH, Germany).

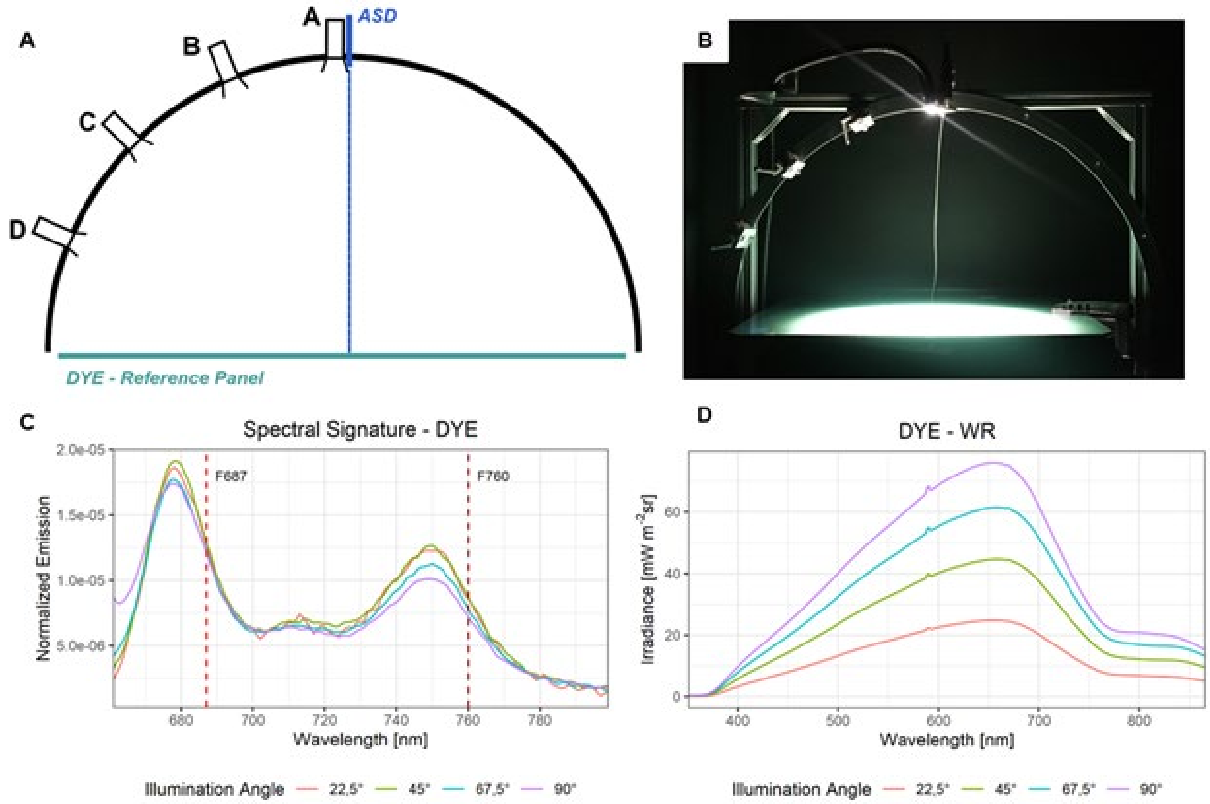

Figure 34 Lab characterization of the dye panel, experiment design (A) and execution (B). Panel C illustrates the normalized emission and spectral signature measured with changing illumination angles showing emission peaks at 678 and 750 nm. Panel D shows the measured irradiance of the Schott cold light lamp for the different illumination angles.

To estimate SIF, radiance and reflectance under the different illumination angles in the developed setup, a measurement protocol consisting of three measurements for each illumination angle was used. A first measurement of a white reference panel (Zenith Lite target, SphereOptics with 95% reflection) was carried out to estimate the irradiance (Figure 34 D), followed by a measurement with the filter disabled to measure the radiance of the dye reference panel. Lastly, the filter was applied and a third measurement was conducted. When the filter is applied, all incoming radiation within the range from 650 to 900 nm is suppressed. Therefore, all light within this spectral region is contributing to the emission of the panel, which is induced by shorter wavelength light that is not suppressed (350–650 nm). Measuring the entire SIF spectrum with the described experimental setup by suppressing specific ranges of incoming radiation is only possible under laboratory conditions. In order to better understand the directional reflectance properties of the panel measurements were collected for four different illumination angles (90°, 67.5°, 45°, 22.5°).

6.2.2 Comparability to field measurements

The comparability of the results from the laboratory experiment and field measurements needed to be addressed, since illumination conditions between the light source used in the experiment and solar illumination in the real world are vastly different. A comparison was established by normalizing the measured upwelling radiance (L↑) with the incoming downwelling radiance (E↓) in the photosynthetic active radiation (PAR) range of the electromagnetic spectrum (400–700 nm). To create a PAR-like value, the integral of the irradiance within this part of the spectrum for each illumination angle setting of the experiment was calculated. Measured radiance was then divided by the calculated values of total irradiance (eq. 15).

$$nEmission_{\lambda} = \frac{1}{L_{\lambda}^{\uparrow}} \int \int_{400\ nm}^{700\ nm} E^{\downarrow} d\lambda \qquad \text{eq. 15}$$

The normalization process for the field measurements was easier, as PAR measurements were already available from FloX data processing. The retrieved SIF for the O_2-A and O_2-B absorption feature was divided by PAR and then compared to laboratory retrieved SIF at 760 and 687 nm (eq. 15).

6.2.3 Spectral signature

The emission characteristics of the dye panel reveal clear differences depending on changes in the illumination angle (Figure 34 C). The general characteristics of all illumination angles of the normalized emission within the SIF spectrum differ from the natural SIF of vegetation. The expected peaks at 685 and 740 nm occur at 678 and 750 nm, respectively. Another difference between the artificial and natural SIF is the stronger expression of the red over the far-red SIF. The emission signature of the dye panel differs from that of vegetation, while the wavelengths of the retrieved SIF are at the same locations. For this reason, F_{687} and F_{760} are derived from the right declining part of the respective emission peaks.

Angular influence on SIF emission

Changing illumination angles led to different spectral signatures for the artificial SIF emission. The relative emission increased when the illumination angle was reduced, with a clear distinction between the peak emissions at 678 nm for the lower two (22.5° and 45°) and higher two illumination angles (67.5° and 90°) in the red fluorescence. In the range of far-red fluorescence (peak emission at 750 nm), the clustering of the two lower illumination angles is still apparent, but differences in emissions at the two higher illumination angles (67.5° and 90°) also become more pronounced. These angular differences are reduced at the 687 nm wavelength and are more pronounced at the 760 nm wavelength. While this setup offered a first analysis of the BRDF, further measurements are needed to determine a robust BRDF of the dye panel.

Degradation

The degradation of emissions is also apparent in the results of the conducted lab experiment. Degradation was characterized in the field and laboratory measurements over a period of 20 min (Field) and 60 min (Lab), respectively (Figure 35). While linearly declining values for the laboratory measurements are clearly visible, the in-field degradation cannot be clearly defined by a linear function. Differences in degradation are linked to incoming radiation, which differ significantly when comparing lab and field measurements. Although normalization mitigates this factor, it cannot mitigate the degrading effect caused by solar radiation in comparison to the light source used in the laboratory experiment. The main reason for this discrepancy between the lab and field data is the molar absorptivity of the fluorescence dye.

Radiation is not only absorbed in the red/far red regions of the spectrum but also in the UV range (<380 nm), a region which is not covered by the light source used in the lab experiment. Much of the degradation effect can therefore be attributed to that part of the spectrum, which explains the differences in degradation behavior between lab and field. As a result of normalization, it is clearly visible that the panel used in the laboratory experiment has already been exposed to as many photons as the in-field panel after 13–15 min of illumination.

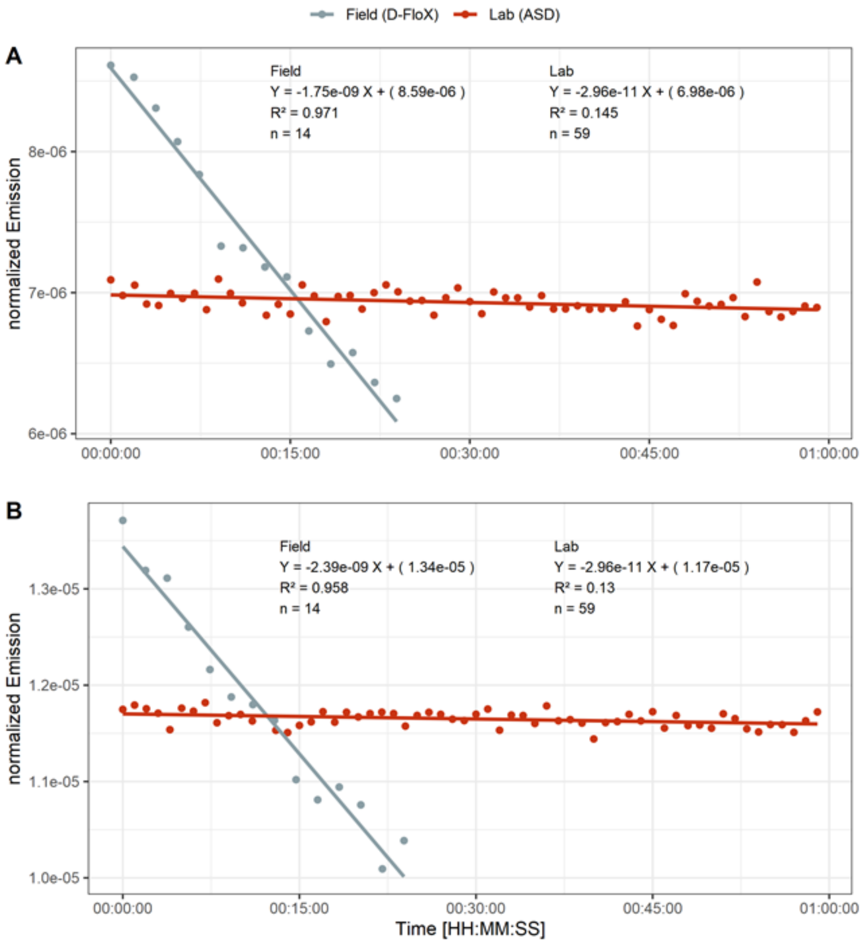

Figure 35 Degradation of normalized emission of the dye panel at 760 (A) and 687 (B) nm over a period of 60 minutes. Radiance was normalized by PAR for the FloX field measurements acquired on June 16 at 12:11 UTC in clear sky conditions. Lab radiance measurements were normalized by the integral of incoming radiance within 400–700 nm, as measured using a 95% white Zenith Lite reflectance standard (SphereOptics, Germany) of the Schott KL 2500 LCD halogen lamp.

6.3 Characterization of the active reference targets (LFRP)

To characterize the emittance of the LFRPs, an in-situ characterization of both models (LP-20, LP-40) was conducted at 10 cm and 20 cm measurement increments respective to the models' spacing between the LED strips. At each measurement step, the power was turned on and off to calculate the upwelling radiance emitted by the LEDs. This allowed the retrieval of the entire spectrum of the panel's SIF emission. The underlying radiation was measured when the panel was turned off, which was then subtracted from the measurement when the panel was turned on. These measurements were used as a constant value for the comparison to airborne retrieved SIF. As this approach was deemed to be the most viable, the narrow FOV of the FloX system in combination with the checkered-pattern setup of the panel (Figure 36) held uncertainties regarding the exact area being observed by the spectrometer. It would only be representative for a specific fraction of the panel that could not be accounted for.

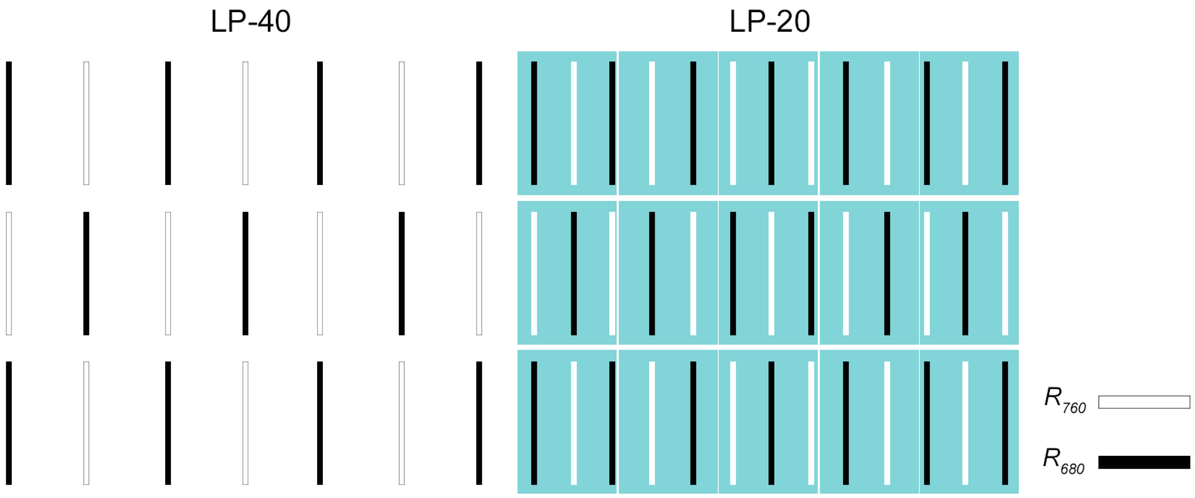

Figure 36 Layout of final installation of LP-40 and LP-20. Green areas represent dye-coated panels. The in-field setup differed in the sense that the panels were installed 3 m apart from each other.

Emission curves of the two LEDs types used to mimic SIF of natural vegetation with the O_2-A LED peak at 750 nm and the O_2-B LED peak at 680 nm are presented in Figure 37. The combination of both emission curves should be similar to the SIF emission curve of natural vegetation.

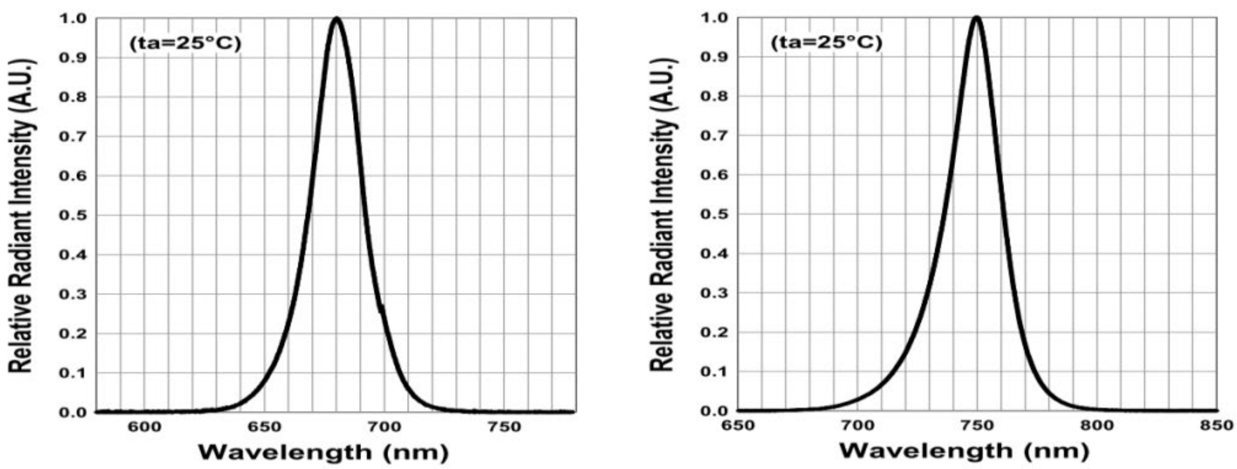

Figure 37 Spectral emission of LEDs installed within the LFRP. Peak emission of the O_2-B LED at 680 nm and 750 nm for the O_2-A, respectively.

6.3.1 Active reference panels (LFRP) – emission characteristics

The emission spectra and intensity of the active panels were characterized in the field with multiple radiance measurements at different positions across the LFRP using a calibrated FloX system. Measurements were done at multiple locations over the LFRP to account for potential spatial heterogeneity in the installation and at different times of the day to account for the potential influence of background reflectance. The emission spectra are derived by subtracting the upwelling radiance measurements with the LFRP turned on from the upwelling radiance measurements with the LFRP turned off. The mean differences of all measurements are shown in Figure 38 and the numerical results are given in Table 13.

The results of the in-field characterization show considerable differences regarding the apparent reflectance spectra of both panels (Figure 38A, LP-20, LP-40). The LP-20 shows a reflectance increase at the red edge, which resembles that of vegetation; furthermore, the two SIF emission peaks at the O_2-A and O_2-B absorption features are visible. The LP-40, in contrast, shows only a slight increase in reflectance towards the red edge. The SIF emission peaks at the O_2-A and O_2-B absorption features are smaller. The differences in the spectral signature of both panels can be explained by the vegetation-mimicking dye panel that was used as a backdrop for the LP-20 (see 4.3.2), while the LP-40 backdrop was a plastic tarp to eliminate background emission from underlying vegetation. Therefore, it can be assumed that the LP-40's apparent reflectance spectrum represents that of the original LFRP setup, as it consists only of aluminum rods, LEDs and the tarp as a background, which should not reflect any vegetation-like features, except the emission of the LEDs.

The SIF emission spectrum of the LP-20 and LP-40 are characterized by peak emissions at 687 nm and 755 nm for LP-20, and 758 nm and 689 nm for LP-40 (Figure 38B). The maximum signal strength of the emission curves is higher than the typical top-of-canopy SIF, but can be considered similar to the fluorescence emission of natural leaves. The far-red SIF peaks of both panels are slightly higher than the red peaks, which also corresponds to natural TOC SIF. The determined mean values for red and far-red fluorescence of both panels (LP-20 and LP-40) were used for the comparison to airborne SIF retrieval from *HyPlant*.

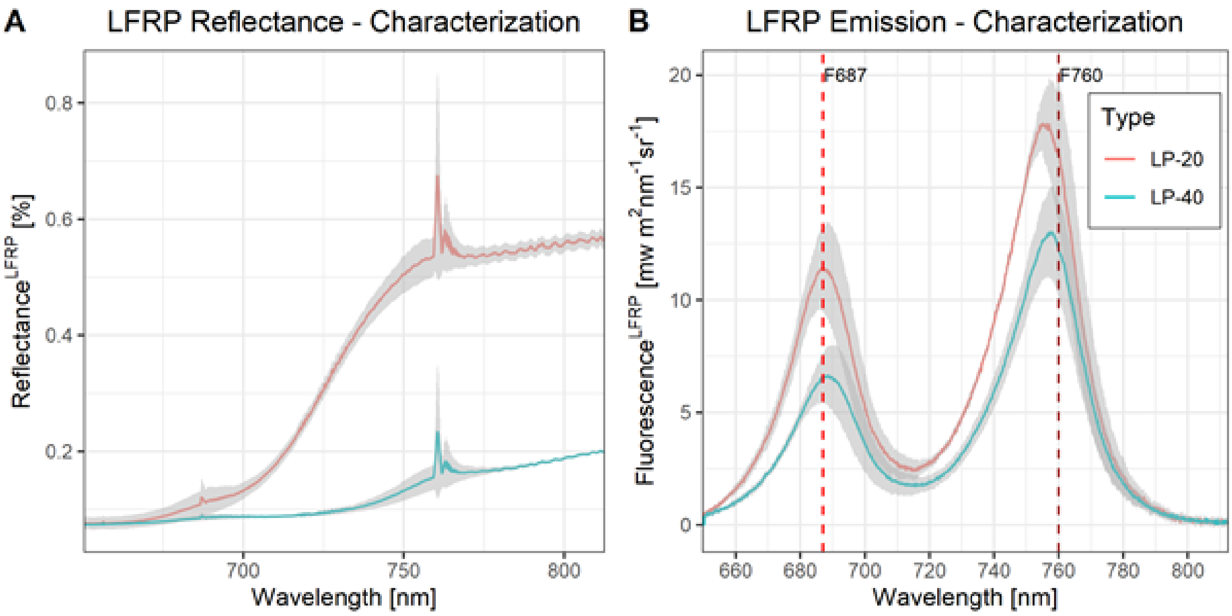

Figure 38 LFRP apparent reflectance (A) and the fluorescence emission spectra (B) of LP-20 and LP-40 panels, as characterized in-field by the FloX measurements. The colored lines represent the mean emission spectra, while the grey areas show the corresponding standard deviations of the collected measurements. Fluorescence emission spectra were calculated by subtracting the panels' radiance when the panel was switched off from measurements when the panel was switched on.

For our considerations on retrieval error and uncertainty estimates, we regard these values to represent the 'true target values', to which we compare the retrieved values from the FloX and *HyPlant* (Table 13). Here, the active reference targets show their advantage, as we have a target value for our comparison, while with the passive reference target we can only compare *HyPlant* products to the FloX-based ground measurements.

Table 13 Emission intensities of the active reference targets in mW $m^{-2}sr^{-1}nm^{-1}$. These data were collected from the LFRPs in the field in Italy, by subtracting the upwelling irradiance with the LEDs turned off from the upwelling irradiance with the LEDs turned on. The difference gives the intensity of the LED rods. Standard deviations were calculated from several, spatially distributed measurements across the reference panels.

	LP-20	**LP-40**
F_{687}-LFRP	11.37 ± 3.26	6.51 ± 2.16
F_{760}-LFRP	16.50 ± 1.85	12.24 ± 1.11

6.4 Comparison of airborne retrieved SIF to ground measurements

The established emission characteristics of the active and passive reference panels were used to determine the performance of the SFM retrieval algorithm. While this test allows for better judgment of the SFM retrieval results, it also reveals potential issues concerning the respective reference panels in a real-world scenario. In this context, a comparison of the airborne and ground-based SFM SIF retrievals was made. Both ground and airborne data were processed using the newest SFM algorithm (see section 3.1). As the dye panel was constantly monitored by a FloX, exact values for each overpass could be assigned to the respective *HyPlant* pixel values, while only single SIF values measured during the characterization of the LFRP panel could be used for the comparison to the airborne data. To evaluate the algorithm's performance for the LFRP, percentages of deviation were calculated from the determined values on the ground and the retrieved SIF from the pixels covering the panels in the *HyPlant* airborne data.

6.4.1 Airborne retrieved SIF – DYE reference panel

The correlation between SIF retrieved from *HyPlant* and the ground measurements conducted by the FloX are shown in Figure 39. The SFM retrieval algorithm was used for both the ground measurement and the airborne data.

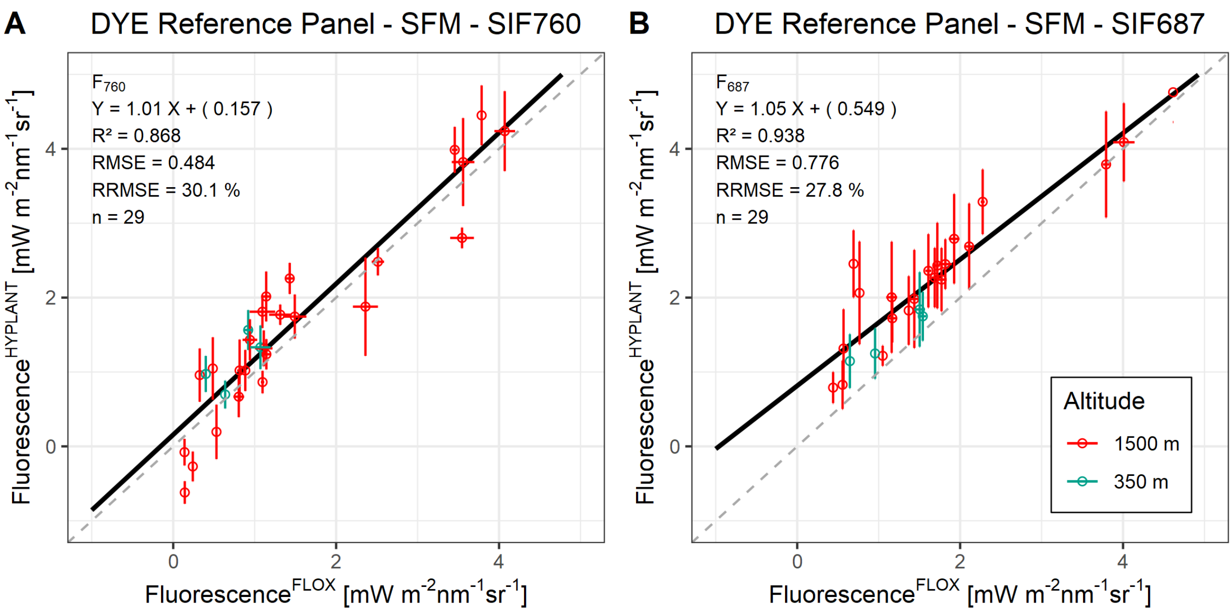

Figure 39 Ground-based FloX measurements in relation to data from *HyPlant*. SIF from both systems was calculated using the SFM approach. All flight lines were included for this correlation analysis. (A) shows the SIF_{760} data and (B) the SIF_{687} data. Error bars (standard deviations) were calculated from the four central pixels within the *HyPlant* data and by averaging 28 subsequent measurements from FloX.

An R^2 of 0.87 can be observed for the comparison of SIF_{760} (Figure 39 A). The determined slope and intercept have values of 1.01 and 0.157, respectively. A slight overestimation for the higher signals can be observed. The standard deviation derived from the airborne measurements in general is higher than that of the ground measurements (rRMSE is 30.1%). While lower values show slight differences, the higher values have a good agreement. Higher values were measured during the early campaign days when the emissions were higher due to lower degradation effects. The linear model for SIF_{687} provided a higher correlation with an R^2 of 0.94 and an rRMSE of 27.8%. The airborne data recorded from 350 m above ground level seem to fit better to the ground measurements of the FloX in comparison to the data recorded from the higher altitude (1500 m). Those observations show a distinct overestimation, especially for lower SIF values (0.5–2.2 $mWm^{-2}sr^{-1}nm^{-1}$), while higher SIF values are only slightly overestimated (Figure 39 B).

6.4.2 Uncertainty of SIF based on passive reference target data

The uncertainty of SIF retrieved from single *HyPlant* pixels and the FloX spectroscopy system are given in Table 14. Since we don't know the true target value of the passive reference targets, we defined the uncertainty as the mean standard deviation of each data point covering the passive DYE panel that was collected and analyzed in the previous sections. While the standard deviation is represented by individual measurements of the same area in the case of the FloX system, the standard deviation calculated for *HyPlant* is based on multiple pixels covering the dye panel. Lower uncertainties were determined for the ground measurements of the DYE panel with the FloX system at 760 and 687 nm (0.089–0.120 mW $m^{-2}sr^{-1}nm^{-1}$). For *HyPlant,* the calculated uncertainties at SIF_{760} and SIF_{687} nm are higher (0.283 and 0.485 mWm^{-2} $sr^{-1}nm^{-1}$). For both systems, the absolute uncertainty for SIF_{687} is higher than for SIF_{760}.

Table 14 Absolute and relative uncertainty of ground (FloX) and airborne (*HyPlant*) measurements, as based on *HyPlant* airborne data of the active and passive reference targets and the corresponding ground data provided by the FloX system. Uncertainties of *HyPlant* SIF products were calculated on single pixels and thus the uncertainty can easily be reduced by spatial binning, which would reduce the uncertainty by the square root of the number of binned pixels.

	Absolute uncertainty [mW $m^{-2}sr^{-1}nm^{-1}$]	**Relative uncertainty [%]**
FloX – SIF_{760}	0.089	6.01
FloX – SIF_{687}	0.120	3.98
***HyPlant* – SIF_{760}**	0.283	11.99
***HyPlant* – SIF_{687}**	0.485	22.31

6.4.3 Airborne retrieved SIF – LFRP

As discussed in sections 4.3.2 and 6.3.1, the emission of the LFRP is used as the reference measure (validation data set) for SIF retrieved from *HyPlant* airborne data. The smaller the difference between the airborne results and the emission of the LFRP, the better the performance of the SFM retrieval applied to *HyPlant* data. To simplify the interpretation of LFRP specific results, flight line names were simplified and changed to FL-1, FL-2, FL-3 and FL-4.

The analysis of the retrieved *HyPlant* SIF values of the LP-20 at 760 nm (Figure 40A, Table 15) shows a some over- and underestimation of the SIF signal in three of the four overflights (FL-1, FL-3 and FL-4, Table 15), while SIF values from one flight is very close to the target (FL-2). The SIF values at 687 nm, by contrast, corresponded very well to the target values for all flight lines (Figure 40B and Table 16).

In the LP-40 setting, the *HyPlant* SIF retrievals for SIF_{760} and SIF_{687} provide a good agreement with the target signals. Only the *HyPlant* SIF products of flight line 3 (FL-3) show a great standard deviation and a great deviation from the expected target value of the panel (Figure 41, Table 17 & Table 18). This strong overestimation observed for FL-3 (+65.9% for F_{687}) is most likely related to a technical malfunction of the active panel at the time of the overpass. Accordingly, we decided to show the data from FL-3, but to exclude these data from future analysis.

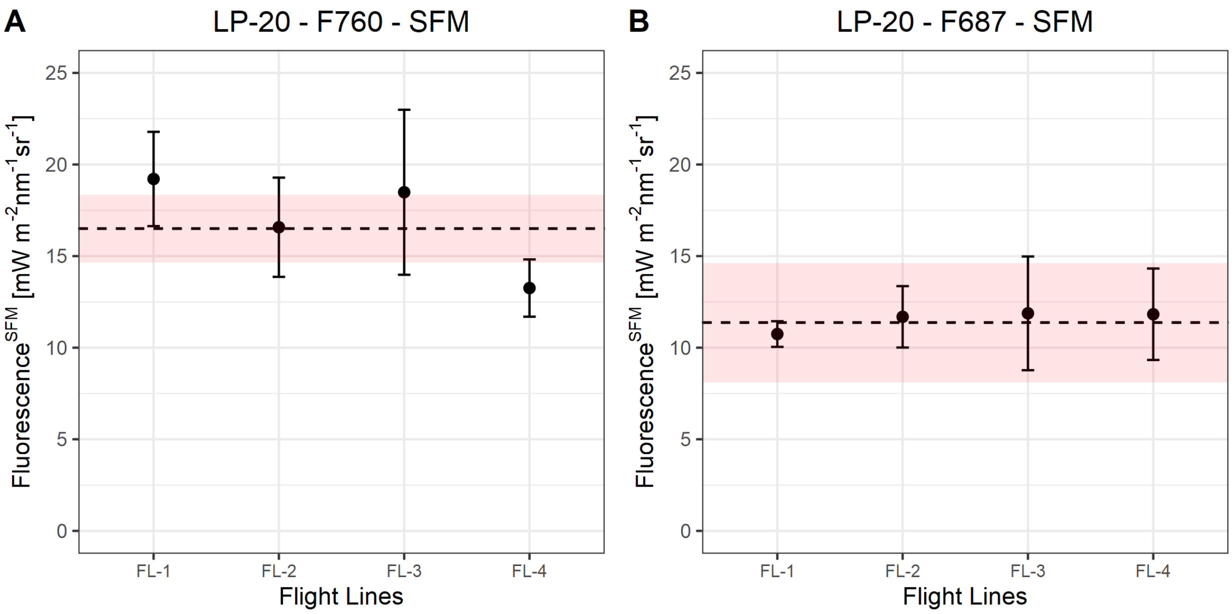

Figure 40 Fluorescence emission of the LP-20 in relation to airborne data retrieved with the SFM-SOIL. The dashed line represents the expected emission, as characterized in-situ for the LFRP panel. The red area marks the standard deviation of the characterization. Far-red fluorescence (760 nm) (A) and red fluorescence (687 nm) (B). Only low altitude (350 m) flight lines were included.

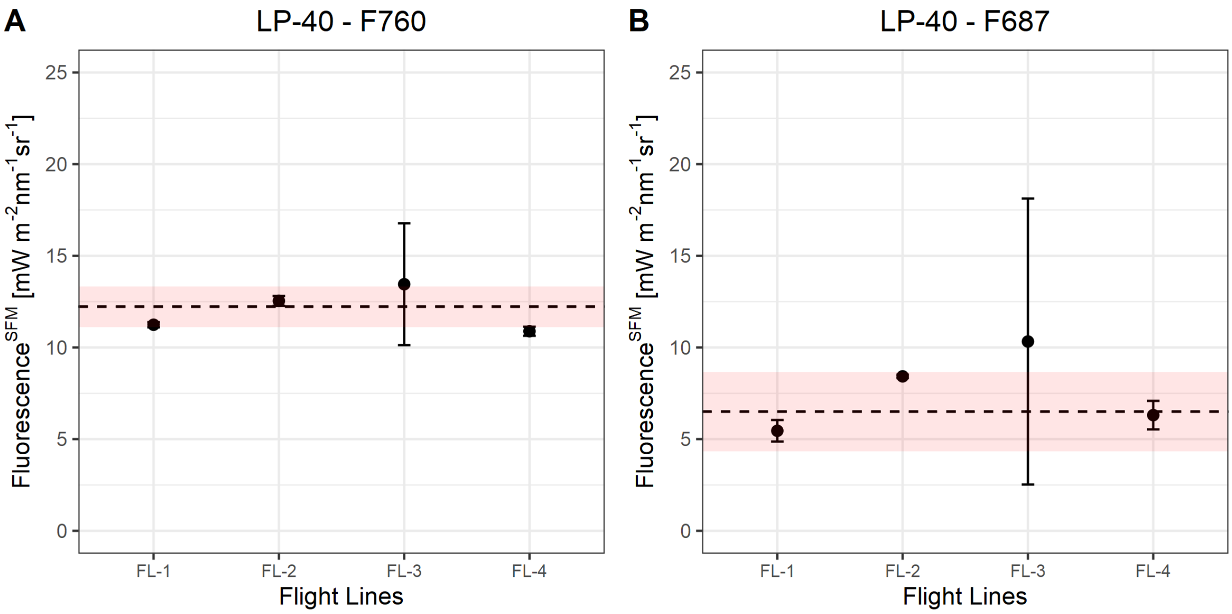

Figure 41 Fluorescence emission of the LP-40 in relation to airborne data retrieved with the SFM-SOIL. The dashed line represents the expected emission, as characterized in-situ for the LFRP panel. The red area marks the standard deviation of the characterization. Far-red fluorescence (760 nm) (A) and red fluorescence (687 nm) (B). Only low altitude (350 m) flight lines were included.

Table 15 Summary table of results for airborne analysis of the LP-20 processed with the SFM-SOIL at 760 nm for *HyPlant* and ground characterization (mean ± SD).

	FL-1	**FL-2**	**FL-3**	**FL-4**
SIF_{760} *HyPlant* [$mW\ m^{-2}sr^{-1}nm^{-1}$]	19.21 ± 2.57	16.58 ± 2.71	18.49 ± 4.50	13.26 ± 1.56
F_{760} LP-20 [$mW\ m^{-2}sr^{-1}nm^{-1}$]	16.50 ± 1.85	16.50 ± 1.85	16.50 ± 1.85	16.50 ± 1.85
rel. Deviation [%]	+ 16.5	+ 0.5	+ 12.1	- 19.7

Table 16 Summary table of results for airborne analysis of the LP-20 processed with the SFM-SOIL at 687 nm for *HyPlant* and ground characterization (mean ± SD).

	FL-1	**FL-2**	**FL-3**	**FL-4**
SIF_{687} *HyPlant* [$mW\ m^{-2}sr^{-1}nm^{-1}$]	10.75 ± 0.7	11.69 ± 1.68	11.88 ± 3.10	11.83 ± 2.50
F_{687} LP-20 [$mW\ m^{-2}sr^{-1}nm^{-1}$]	11.37 ± 3.26	11.37 ± 3.26	11.37 ± 3.26	11.37 ± 3.26
rel. Deviation [%]	- 5.6	+ 2.7	+ 4.4	+ 3.9

Table 17 Summary table of results for airborne analysis of the LP-40 processed with the SFM-SOIL at 760 nm for *HyPlant* and ground characterization (mean ± SD).

	FL-1	**FL-2**	**FL-3**	**FL-4**
SIF_{760} *HyPlant* [$mW\ m^{-2}sr^{-1}nm^{-1}$]	11.24 ± 0.14	12.54 ± 0.27	12.97 ± 4	10.89 ± 0.25
F_{760} LP-40 [$mW\ m^{-2}sr^{-1}nm^{-1}$]	12.24 ± 1.11	12.24 ± 1.11	12.24 ± 1.11	12.24 ± 1.11
rel. Deviation [%]	- 8.1	- 4.3	+ 0.3	- 11.0

Table 18 Summary table of results for airborne analysis of the LP-40 processed with the SFM-SOIL at 687 nm for *HyPlant* and ground characterization (mean ± SD).

	FL-1	FL-2	FL-3	FL-4
SIF_{687} *HyPlant* [mW $m^{-2}sr^{-1}nm^{-1}$]	5.46 ± 0.59	8.43 ± 0.09	11.46 ± 6.2	6.31 ± 0.78
F_{687} LP-40 [mW $m^{-2}sr^{-1}nm^{-1}$]	6.51 ± 2.16	6.51 ± 2.16	6.51 ± 2.16	6.51 ± 2.16
rel. Deviation [%]	- 16.2	+ 14.1	+ 65.9	- 3.1

6.4.4 Error and uncertainty of SIF based on active reference target data

In a next step, we pooled the pixels of all four flight lines (excluding FL-3 for the LP-40).[5] We calculated the error and uncertainty of the *HyPlant* SFM SIF products in relation to the active reference targets and calculated the uncertainties and errors of the *HyPlant* SIF products based on our comparison to the active reference targets (Table 19). Due to the small footprint of the LFRP, the airborne data are made up of two pixels per flight line. Therefore, a total of 8 for the LP-20 and 6 pixels for the LP-40 were used. The uncertainty is highest for the LP-20 at SIF_{760}, while the uncertainty of the LP-20 at SIF_{687} is the lowest. Still, the calculated error of the LP-20 is generally lower than that of the LP-40 within a range of 0.16 to 0.38 mW $m^{-2}sr^{-1}nm^{-1}$.

Table 19 Summary table of target emission of the LFRP (see section 6.3), averaged *HyPlant* SIF pixels (two pixels per flight line), and calculated error of *HyPlant* SIF. LP-20 (n=8), while LP-40 data is based on three observations (n=6).

	Target emission of LFRP	***HyPlant* SIF (mean +- uncertainty)**	**Error of *HyPlant* SIF**
F_{760}-LP-20 [mW $m^{-2}sr^{-1}nm^{-1}$]	16.50 ± 1.85	16.88 ± 2.97	0.38 ± 3.15
F_{760}-LP-40 [mW $m^{-2}sr^{-1}nm^{-1}$]	12.24 ± 1.11	11.55 ± 0.68	- 0.68 ± 0.73
F_{687}-LP-20 [mW $m^{-2}sr^{-1}nm^{-1}$]	11.37 ± 3.26	11.53 ± 1.52	0.16 ± 1.62
F_{687}-LP-40 [mW $m^{-2}sr^{-1}nm^{-1}$]	6.51 ± 2.16	6.73 ± 1.21	0.22 ± 1.31

[5] Closer inspection of the FL-3 data revealed a great difference in SIF values of neighboring pixels. This high difference is the reason behind the large standard deviation values shown in Figure 29B. We experienced some technical instability in the LP-40 panels at the times of this *HyPlant* overpass, and thus we assume that just at the time of the measurements, the LED may have been flickering or affected by another technical error. We thus exclude the LP-40 figures from FL-3 in the overall error budget calculation.

6.5 Further considerations on technical requirements and limitations to the use and scaling of reference panels

Optical remote sensing reference panels have been developed as a central element in the overall Cal/Val concept and one dominant paradigm of field spectroscopy is based on measurements, in which the radiance of the target is compared with that of a reference panel (Milton et al. 2009, Hueni et al. 2017). Such reference panels often provide the crucial element to enable fiducial reference measurement in radiance values. These concepts for radiance measurements can be used for fluorescence measurements and such dedicated fluorescence reference targets are crucial for satellite-based SIF products. Thus, future reference targets for SIF Cal/Val should fulfill the following three criteria, while the third criterium is specific for SIF Cal/Val.

1. Scalability to large areas: Reference targets should be large enough to be visible by the relevant sensor and should be spatially homogeneous.
2. Reference targets should be temporally stable and provide a constant or known radiance emission intensity.
3. Reference targets should have similar reflectance characteristics in the range of SIF retrieval as the retrieval algorithm is optimized for vegetation monitoring.

In the following, we provide some considerations on the usability of the two reference targets (active and passive) and we discuss along the three criteria mentioned above.

Scalability to large areas:
The ***passive DYE panel*** intuitively seems easier to be scaled to large areas than the active LFRP. The dye, the camouflage paint and the coatings used in the passive panels are rather cheap and there are no limitations to paint larger areas and materials such as tarps that can be deployed more easily than rigid wooden panels. Increasing the reference panel's area would, at some point, raise the question of spatial homogeneity, but would reduce e.g. mixed pixel effects and we expect that larger passive panels would generally deliver more robust results.

Upscaling the ***active reference panels*** seems to be more challenging, as power consumption and overheating are issues that are not yet entirely overcome. These issues though could become less prominent by decreasing the intensity of the panels LEDs. Currently, the artificial SIF that is emitted is about 5 to 10-times higher than that of natural SIF, so a signal decrease should solve some of the power issues. This allow the entire structure to be upscaled and could reduce the uncertainty associated with higher signal strength. We, however, think that panel sizes of up to 20 x 20 meters would be technically feasible. This would be clearly large enough to be seen by UAV and airborne systems but still too small for the FLEX satellite. Thus, the active reference panels can most likely not be scaled for a direct validation of the FLEX satellite products, but the active panels may play an important role in the Cal/Val concept (Figure 42) where ground and UAV-based systems may link smaller reference panels to the satellite scale.

Stability over long time periods:
The caveat of the ***passive reference panel***, in their present configuration, is that the pigments greatly degrade over time, as the laboratory and field data showed that a significant amount of emission is

lost through the relatively short time period of solar exposure. However, a series of tests have shown that the addition of proper UV-protectors in the transparent coating above the fluorescent layer could potentially significantly reduce such a degradation. This would also inevitably diminish the fluorescent emission of the panel, but this is something that can be compensated by increasing the concentration of the dye in the mixture. Nevertheless, the practical application of fluorescent panels based on the dye specifically used in this campaign will require continuous monitoring as well as some automatic shielding from sunlight during periods of inactivity. It is currently unclear if an improved chemical formulation of the fluorescence dye will have sufficient stability to be serve as an adequate reference surface for Cal/Val efforts.

The ***active reference panels***, in contrast, were shown to be very stable in the laboratory and the field. Photon emission of the LED is a constant and stable function of electric power and LED systems have been shown to provide a very good stability over longer time periods. Thus, the design of the active reference panels seems to be very stable and suitable for Cal/Val concepts. Instabilities in the intensity of the emission may be caused by temperature changes, as LEDs are known to be temperature dependent. This physical phenomenon, however, is well known and we anticipate that a stable correction function can be developed and established. Additionally, failure of single LEDs will occur on the longer time frame and overpowering of the LEDs may reduce the nominal lifetime of them. As the lifetime of LEDs, however, is very long (several thousand of operational hours) and as the LEDs are only operated for short time periods, we do not see here a major limitation. A maintenance (and cleaning) of such active reference panels would be needed anyway every few months. This is unavoidable for all reference targets and during such a maintenance, a stability check and replacement of malfunctioning LED elements could be included. Thus, in terms of long-term stability the active reference targets show a clear advantage.

Similarity to natural vegetation:

Both reference targets (the passive and active reference panel) were designed having similar reflectance properties as natural vegetation. Even though the reflectance properties are not identical to natural vegetation, we did not see any problems or artifacts in using the standard SIF retrieval approaches over the reference targets. The general feature of vegetation reflectance and fluorescence (e.g. slope across a spectral window) are mimicked by the used materials and thus according to our evaluation the retrieval algorithms can be applied to the reference targets. In this respect, both concepts worked without any problems and no further refinements are needed.

Instruments for field validation of the panels:

Ground validation of the active reference panels should be achieved by characterizing the panels emission prior to deployment. A prior characterization under controlled conditions should be conducted to determine uncertainties. An option for ground validation to ensure that the emission in field is the same as under laboratory conditions could be the inclusion of a diffusion screen that could be installed above the LED strips as it was already tested by JB Hyperspectral on a smaller scale panel. The diffusion screen has the potential to decrease the number of measurements necessary for an in-situ characterization or could even allow for singular direct measurements during the overpasses.

7 CAL/VAL CONCEPT FOR THE FLEX SATELLITE MISSION – CONSIDERATIONS AND RECOMMENDATIONS FROM THE FLEXSENSE AND ATMOFLEX CAMPAIGN ACTIVITIES

Calibration sites usually span areas of multiple kilometers in order to provide a sufficient number of satellite pixels for calibration and validation purposes (Baret et al. 2006). Thus, for FLEX, we would need either homogeneous and stable natural vegetation sites or artificial SIF reference targets that span a minimum of 1 x 1 km and which emit a natural fluorescence signal of known intensity that is spectrally similar to the SIF signal of natural vegetation. In an ideal case, a reference target should be spectrally homogeneous, stable in time and large enough to cover at least one pixel of the satellite sensor (Li et al. 2015, Gorroño et al. 2017). For the FLEX satellite mission, these conditions are particularly difficult or even impossible to meet, as the SIF of natural vegetation changes dynamically over the course of a single day, during the season and as a reaction to environmental conditions: the nature of SIF, which changes greatly in time and also spatially. Thus, a constant and spatially homogeneous natural vegetation surface that would provide a suitably homogeneous target and, which could be used as a 'natural reference' target, does not exist or will at least be very difficult to find. Additionally, the SIF of all plant ecosystems shows great spatial variability, which is much greater than the spatial variability of radiance or reflectance because of the inherent heterogeneity (functional diversity) of single leaves, individual plants and the dynamic nature of the SIF signal. Thus, a classical large, stable and homogeneous natural reference vegetation area seems out of reach.

However, the individual elements above can be integrated in a conceptual framework (Figure 42) that seeks to strike an optimal balance between accuracy and frequency (singular, very precise vs. frequent and distributed, but less accurate, measurements). The elements can be adjusted considering resources available for FLEX Cal/Val activities.

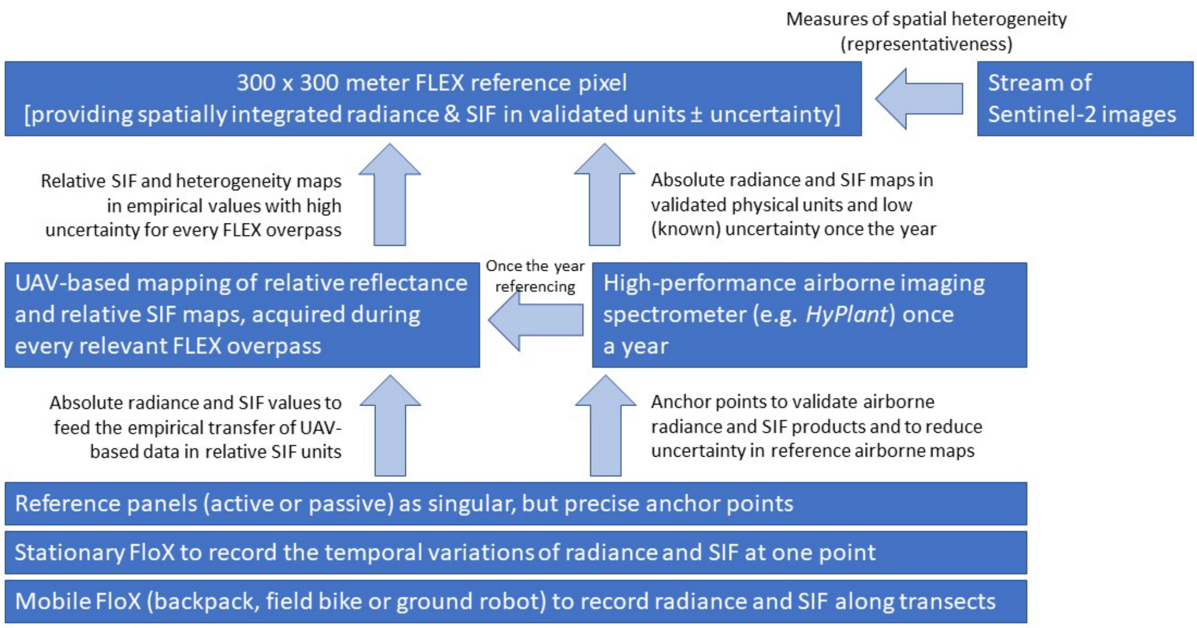

Figure 42 Conceptual framework for integrating the individual components into a Cal/Val scheme for FLEX SIF products.

Based on our internal discussions and considering the current version of the FLEX Cal/Val concept [RD-8], we can present the following recommendations for the selection of appropriate Cal/Val sites.

Agricultural Cal/Val site, with low within field heterogeneity and large fields (field size larger than 300 x 300 m): Here, a stationary FloX system over a representative patch in the field and a basic heterogeneity mapping may already provide reasonably good estimates of a FLEX reference pixel. However, we want to stress that such homogeneous vegetation areas will be hard to find and homogeneity can most likely only be assumed at very limited periods during the year (at times of closed canopy and no environmental stress). The accuracy of the stationary FloX system needs to be regularly checked by using reference targets [-> easy to implement on-site as only a FloX system will be needed; no further investment required; low running costs; but limited usability for FLEX Cal/Val].

Agricultural Cal/Val site, with some field heterogeneity and normal sized fields: We expect that this will be the nominal Cal/Val site for FLEX. Such sites exist across Europe and we can develop a quantitative Cal/Val concept for such sites. We propose to install (i) a stationary FloX system in a selected field to record the temporal dynamics of SIF and to map the impact of potential stress events. To cover spatial heterogeneity, we recommend the use of (ii) a mobile FloX either as a backpack solution or on a field bike to cover the spatial heterogeneity of SIF in absolute units and (iii) a UAV-based SIF camera system to cover the spatial heterogeneity of SIF in relative units. In this concept, reference targets (active or passive) need to be included at the times of FLEX overpasses to quantitatively reference the measurements of different systems [-> slightly higher investment costs: the manual measurements (backpack, field bike, UAV) are only needed during FLEX overpass. Once a year or even bi-/tri-yearly, a mapping with a high-performance airborne sensor is recommended.]

Forest Cal/Val site: Here, FloX systems will be difficult to use and we know that a single stationary FloX system is not sufficient because of the intrinsic heterogeneity of the forest ecosystem. Thus, we recommend using UAV-based point spectrometers (absolute SIF values at selected areas) in combination with a SIF camera system (relative SIF over the whole reference area). Additionally, airborne mapping may be needed to reduce the uncertainty that emerges from the heterogeneity of forest sites. In this concept, active reference targets are mandatory to quantitatively register the SIF and radiance values from the different systems; the reference targets can be placed at any accessible opening within the scene. [-> challenging site because of inaccessibility: thus, several FloX systems and more frequent airborne mapping will be needed.] In this section, we share our considerations on how to include the reference targets that were tested during this campaign activity, into the Cal/Val concept of the FLEX satellite mission ([RD-08]). In the following, we present a concept of how the combination of an artificial reference target, ground-based high-resolution TOC point spectrometer, UAVs and aircraft can be used for FLEX reference sites, thus allowing the quantitative validation of FLEX SIF data products.

7.1 Components of the proposed Cal/Val measurements for FLEX

Component 1: Active or passive reference targets as absolute reference points for SIF intensity

The active and passive reference targets are both promising developments to be used as absolute reference targets for SIF intensity. As outlined above, the active reference targets may be even better suited as reference targets that provide traceable values of SIF emission in physical units. The active reference targets have the advantage of being stable over time and it can be assumed that they will emit known SIF values for a longer time period. These panels can easily be manufactured as 10 x 10 m areas that emit a known SIF-like signal. Even slightly larger targets having a dimension of perhaps 30 x 30 m may still be technically feasible. Much larger areas will have the challenge of power consumption and maintenance. The passive reference targets are cheaper, but have the intrinsic problem of decaying rather quickly. While some current testing with UV-blocking layers is underway to improve the stability of the targets, it remains uncertain as to whether the stability of the passive reference targets can be sufficiently improved. Nevertheless, these reference targets are the main element that can be used as 'absolute anchor points' within the reference FLEX pixel when SIF emission is known numerically.

Component 2a: Stationary and mobile FloX systems to measure irradiance, reflectance and fluorescence

The next components are one or several calibrated FloX systems that will be available at the time of FLEX overpass. The FloX systems have been proven as reliable ground-based point spectrometers having FLEX-like performance. These FloX systems will serve two purposes: (i) they are needed to confirm the SIF emission of the reference targets. (In the case of the active reference targets such a measurement can be done before or after the satellite overpass; perfect time synchrony is not needed.) (ii) During the time of the overpass, the FloX system is to be mounted on a sensor positioning system (see component 2b below) and the FloX is then used to cover the heterogeneity of reflectance and fluorescence of one or more transects of the 300 x 300 m FLEX reference pixel. A blueprint of such a spatial covering was presented during FLEXSense 2018 (see sections 4.5.2 & 7.2.2 in the FLEXSense 2018 report [RD-03]). Based on our experience and considering the need for temporal integration of each measurement (which is needed for sufficient SNR), a full resolution FloX system can maximally record SIF from 300 points during a 2 h measurement window (10 sec integration of measurements; 10 sec moving to next position; measurement window: $\pm$ 1 h of satellite overpass). Additional uncertainty of such mobile FloX measurements mainly comes from the inaccuracy of placing the FloX TOC, which can be reduced by using a dedicated sensor positioning system with which several systems are tested. This will help to reduce the uncertainty of FloX measurements across transects.

Component 2b: Sensor positioning system to record transects and/or numerous points within the FLEX reference pixel

In this section, we return to the concept that to allow highest flexibility, sensors and sensor positioning platforms can be treated independently (Cendrero et al. 2016). Based on the summary that is given above, there are several possibilities to select the most appropriate positioning system for the FloX system. We suggest using the information given here and to come up with a site-specific evaluation of the best tradeoffs between investment costs, running costs and accuracy. This will result in different sensor positioning systems for different types of Cal/Val sites. For the FLEX Cal/Val, we propose the use of a rather stable sensor positioning system that ensures reproducible orientation of the FloX fiber optics and which still is able to cover a large enough number of points within the FLEX reference pixel. Based on the experience of various phenotyping consortia, five different sensor positioning systems (Table 20) were considered and we evaluated their advantages and disadvantages.

Table 20 Evaluation of the advantages and disadvantages of the different sensor positioning systems.

Sensor positioning system	**Reference**	**Advantage**	**Disadvantage**	**Evaluation for reliable positioning a FloX system**	**Comments**
Simple backpack (Mobile FloX)	FlexSense 2018 final report [RD-03] section 4.5.2, Figure 15 & 16	very easy and versatile can also be used in rugged and hilly terrain	some higher uncertainty due to manual pointing of the fiber optics (gimbal can help)	good positioning with some uncertainty because of human pointing	good option for remote sites and to easily include SIF in existing Cal/Val sites
Field bike with FloX	Zendonadi et al. 2021, FLEXSense 2018 final report [RD-03], Figure 122	very easy and versatile, cheap and easy to use, fast	cannot be fully automated	very good and reliable sensor positioning system	good option to be included in existing Cal/Val sites
Automated field bridge or pivot system (e.g FieldSnake)	Figure 82	automated and reproducible measurements possible also	initial investment needed	excellent and automated pointing (depending on quality of the system)	recommended and good option to be included in core FLEX Cal/Val sites
Cable bridge	Kirchgessner et al. 2016	fast transect measurements possible	instability and inaccurate pointing relatively large investment	Instability and inaccuracy in pointing	relatively high investment costs and uncertainty in pointing
UAV/unmanned aircraft	Quiros et al. 2020, Kneer et al. *in preparation*	fast and versatile	reduced quality of light-weight spectrometer/design	FloX system needs to be reduced in weight and thus higher instability	see next section

Component 3: UAV-based mapping of heterogeneity of whole FLEX reference pixel

To correctly account for spatial heterogeneity in the full FLEX reference pixel, a full mapping of the relative SIF heterogeneity is needed. A full spatial mapping of SIF across the 300 x 300 m reference pixel in absolute SIF values is only possible with a calibrated airborne sensor, such as *HyPlant*. The employment of an airborne sensor is rather expensive and seems out of reach for regular Cal/Val activities. Thus, we suggest using the airborne sensor only once per year (see next section) and to map the heterogeneity of this year's vegetation in absolute values. For the regular Cal/Val activities taking place several times during the year (ideally using every clear sky FLEX satellite overpass), we suggest using a UAV system with a SIF sensor, which allows heterogeneity mapping in relative terms. Such imaging sensors are currently being developed (Kneer et al. *in preparation*) and implementation of a UAV-based SIF camera seems technically feasible by the launch date for the FLEX satellite mission.

We suggest that such a 'relative' SIF mapping is the linking element to quantitatively connect the (i) absolute measures of SIF on the reference panels along the transects and from a high-performance airborne sensor with (ii) the actual spatial heterogeneity of relative SIF intensities that need to be recorded at the time of the FLEX satellite overpass.

Component 4: High-performance airborne SIF sensor (e.g. *HyPlant*)

The airborne spectrometer *HyPlant* is currently the most widely used imaging spectrometer for SIF measurements and, to date, 24 publications that use data from this airborne sensor have been released (Rascher et al. 2015, Rossini et al. 2015, Simmer et al. 2015, Wieneke et al. 2016, Drusch et al. 2017, Middleton et al. 2017, Colombo et al. 2018, Gerhards et al. 2018, von Hebel et al. 2018, Bandopadhyay et al. 2019, Gamon et al. 2019, Liu et al. 2019, Siegmann et al. 2019, Tagliabue et al. 2019, Yang et al. 2019, Pinto et al. 2020, Tagliabue et al. 2020, Vila-Guerau de Arellan et al. 2020, Hornero et al. 2021, Bandopadhyay et al. 2021, Porcar-Castell et al. 2021, Scharr et al. 2021, Siegmann et al. 2021, and Zeng et al. 2021). In recent years, however, alternative airborne SIF imaging systems have been developed. These instruments include:

- the *HyPlant*-like instrument from the University of Nebraska–Lincoln, USA. This airborne sensor consists of a spectrally high-resolution module (named IBIS), which is very comparable to the FLUO module of *HyPlant*. As a second module a VIS/NIR spectrometer (covering 400–1050 nm) is attached. This system was first employed in 2018 within the scope of the PhotoProxy project [RD-09]. This system was shown to also provide SIF products, which are, however, only available in relative units, as the system is not radiometrically calibrated and the preprocessing and SIF retrieval is still in an early stage of development. According to the manufacturer, two *HyPlant* systems were sold to China, but according to our knowledge there are no publications or other references available on the whereabouts or use of these systems. Another *HyPlant* systems were sold to Italy and other research institutions are currently in contact with the manufacturer for a *HyPlant* purchase.
- The US company Headwall has released an airborne SIF sensor[6] that was bought and tested by NASA's Goddard Center. According to our knowledge, additional instruments have been purchased by other groups. This sensor is cheaper than a *HyPlant* system and is comparably compact, having only a very small aperture, which greatly limits the photon flux in the system. As a consequence, this system has a substantially lower SNR ratio, and SIF retrieval may greatly be hindered by this technical bottleneck. To date, one scientific publication has characterized the optical performance of this system (Paynter et al. 2020), but no in-flight SIF data are available from this system, yet.

8 SITE SPECIFIC RESULTS

8.1 CAMPAIGN OVERVIEW

The overall schedule (Table 21) was driven by the need to monitor the vegetation during the growing season. The activities were conducted on June 10 to 27, 2019. The airborne measurements were carried out according to weather conditions. The plant sampling was carried out one or two days within the *HyPlant* flyovers.

[6] https://www.headwallphotonics.com/products/application-specific-sensors-sif-imaging

In Germany, the flight campaign was conducted on June 26 and 27, 2019. In proximity to the *HyPlant* flyovers and within the SARSense 2019 campaign, non-destructive and destructive plant measurements were conducted on June 25, 2019.

In Italy, the airborne campaign lasted from June 16 to June 24, 2019 with no flights on June 20 or 22, 2019. Moreover, the ground sampling was carried out from June 11 to 25, 2019. The preparatory activities started in May 2019.

Table 21 Overview of the acquired measurements during the 2019 campaign.

Site		**Instrument**	**Date**
Germany June 26 and 27, 2019 77 lines in total	CKA 35 lines on one day	*HyPlant*/LiDAR/TASI including Reference Tarps, bore sight and diurnal course	June 26, 2019
		Ground sampling (destructive and non-destructive)	June 25, 2019
	Selhausen/Jülich 24 lines on two days	*HyPlant*/LiDAR/TASI including Reference Tarps	June 26 + 27, 2019
		FloX System (Reference Tarps + ICOS Tower)	June 25–27, 2019
		Ground sampling (destructive and non-destructive)	June 25, 2019
	TR32 18 lines on one day	*HyPlant*/LiDAR/TASI	June 27, 2019
Italy June 16–19, 23–24, 2019 75 lines in total	Grosseto 4 lines Sent-3 pattern, 47 lines drought stress experiment, 12 lines tree nursery, 12 lines fire experiment	*HyPlant*/LiDAR/TASI including active and passive reference panels	June 17 + 18 + 19 + 23 + 24, 2019
		FloX system	June 11–25, 2019
		Ground sampling	June 11–25, 2019

8.2 GROSSETO, ITALY

This experimental site is located in central Italy, 20 km from the coastline in central Tuscany. The site is part of a milk production farm. It mainly consists of a large irrigated flat area extending over 72 ha (Figure 43), most of which is irrigated. Within this experimental farm, we have provided two manipulative experiments, one dedicated to the objective of detecting early drought stress and the second field providing the possibility of a controlled fire to test the potential of the high spectral resolution measurements for fire monitoring. Moreover, the nursery that is also part of the experimental site provided many plant varieties for which SIF measurements could be used to study functional diversity.

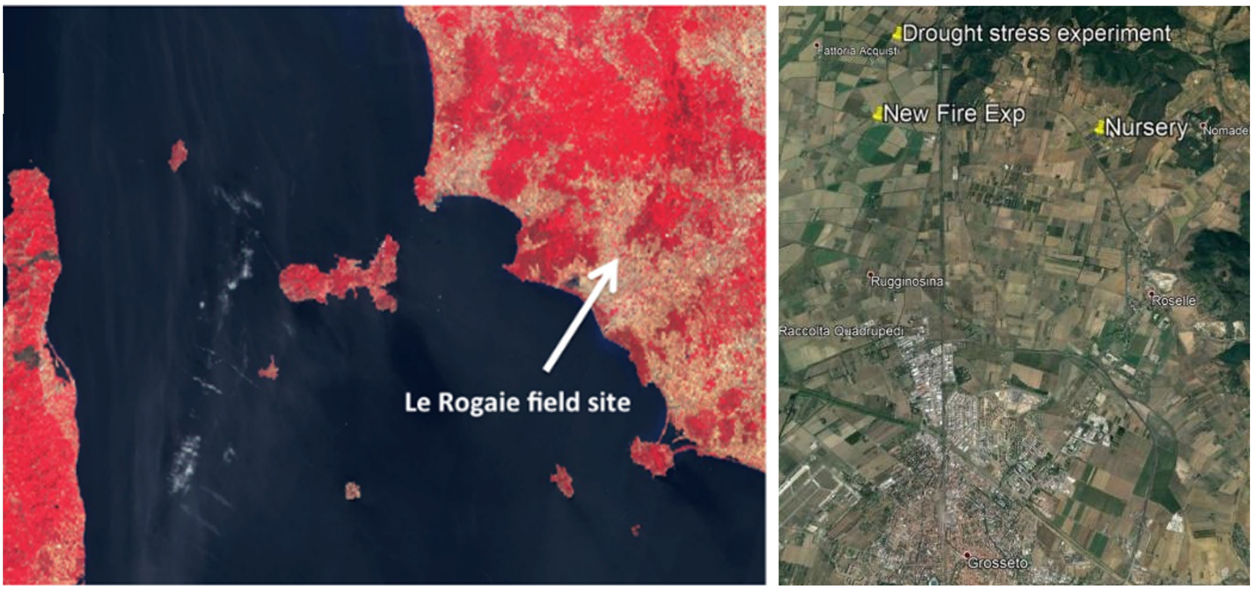

Figure 43 (a) Location of the Le Rogaie field site in Italy and (b) actual study site north of Grosseto with the nursery and the location of the fire/drought stress experiment during the 2019 campaign (picture was taken in 2020).

Flight patterns

Due to the very broad interest for the Grosseto study site, a total of four different flight patterns were flown during the 2019 campaign (Figure 44 and Figure 45). The flight pattern over a lit fire was specifically planned to evaluate if fire can be detected via spectral measurements.

- **PRISMA Pattern [42.83, 11.07]**: Mapping of the area around the irrigation pivot near Braccagni in parallel to a PRISMA overpass, four lines with 4.5-m spatial resolution flown alternating either in northwest or southeast direction. Data acquisition was performed under clear sky conditions around 12.00 h local time
- **Tree nursery [42.50, 11.07]**: Mapping of the nursery area, one line in 1-m resolution flown in a north-south orientation, clear sky conditions and as close to solar noon as possible
- **Drought stress experiment [42.51, 11.03]**: Repeated mapping of the drought experiment at solar noon: one line in 1-m resolution, fluorescent panels were placed in the north of the flight lines
- **Fire experiment [42.50, 11.04]**: Flight lines in 1-m resolution, clear sky conditions, between 10 am and 11 am on the morning on the day the fire was lit; the flight direction was chosen according to actual direction of the fire plume.

Figure 44 Flight lines for the Grosseto study site during the 2019 campaign: a) flight lines for the “nursery” experimental site near Grosseto, Italy; a north–south flight line was flown; b) position of the fire experiment; the flight direction was determined by wind direction; c) flight line for the drought stress experiment; and d) same flight line; the active and passive fluorescent panels were placed the north of the drought stress experiment (see yellow marker).

PRISMA pattern

PRISMA (Hyperspectral Precursor of the Application Mission) is an earth observation satellite with a hyperspectral payload developed and launched by the Italian Space Agency (ASI). *HyPlant* can serve to validate PRISMA data. Figure 45 shows PRISMA flight patterns, which were flown to continue and extend the data set that was started during the 2018 FLEXSense campaign. They are currently being used to optimize the atmospheric correction of FLEX satellite products. No further analysis was performed with these data within the framework of this campaign activity.

Figure 45 PRISMA flight pattern in Grosseto, Italy, during the 2019 campaign.

Tree nursery

HyPlant flyovers also covered a tree nursery near the Le Rogaie farm (LAT 42.837, LON 11.120). The nursery is north of Grosseto and east of the drought and fire experiments, respectively (Figure 44a). A comprehensive classification of the Mediterranean crop species was made before the airborne flyover. In total, there were approximately 365 plots with plants in the nursery, comprising 77 plant species. For most of the species, approximately five replicates were identified, while for some species over 20 replicates were grown in the nursery (Figure 46). During the 2019 campaign, the nursery near Grosseto was overflown 12 times at 1500 agl on June 19, 2019.

Figure 46 Distribution of plant species (land cover) in the “Terra Antica” nursery in June 2019.

Drought stress experiment

A drought stress experiment on corn was made in Grosseto in 2019 (Figure 47). The total study site was a 220 m x 230 m corn field, which was watered by drip irrigation. Two contiguous patterns of the corn field in this study site were treated with different watering regimes. The area was large enough to provide a representative area for airborne acquisitions (30 m x 60 m). In one of the two plots, the irrigation was suspended from June 13, 2019 until June 25, 2019 (red box). Furthermore, a reference area, where the drip irrigation stayed undisturbed, was selected (white box). In-situ measurements took place from June 10 to June 24. Data from the experiment, including measurements of the passive (DYE) and active (LED) fluorescence reference panels, were recorded several times from two flight altitudes (350 and 1500 m agl) from June 16 to 24, 2019. After the experiment, irrigation was resumed and the plants recovered.

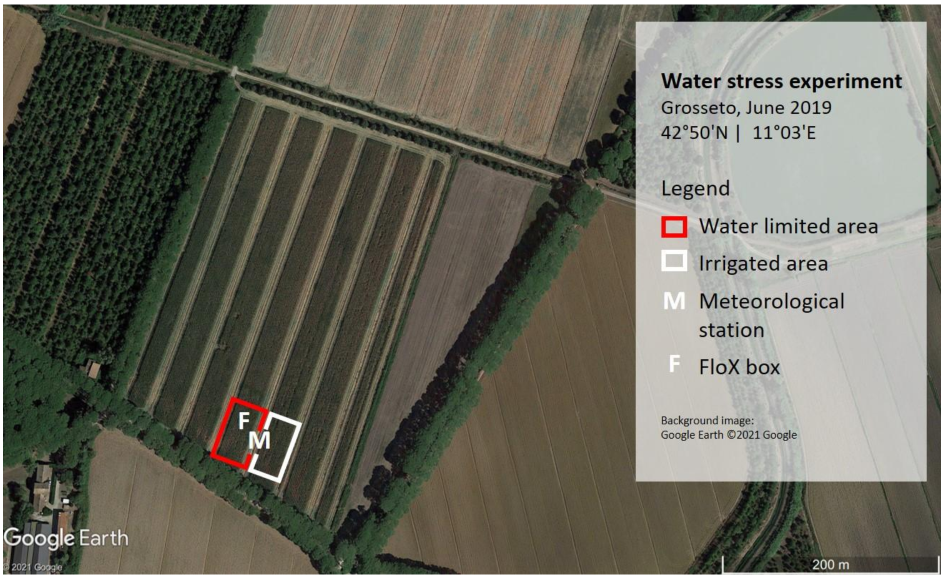

Figure 47 Setting of the water stress experiment with the well-watered maize canopy (white box), the water-limited maize canopy (red box), and the location of the meteorological station and FloX system.

Fire experiment

With this campaign activity, we reacted to the request that we evaluate the potential for detecting and quantifying the intensity of potassium emission lines in high-resolution *HyPlant* data. This would provide further synergies to use the FLEX satellite mission for the global mapping of wildfires, as the extent and density of such fires can be mapped through potassium lines. For a first conceptual experiment, we aimed to use *HyPlant* imagery over a controlled burn, where we could produce an experimental plume of varying extent and density. The controlled burn was initiated in agreement with the local authorities west of the nursery, approximately 5 km north of Grosseto (Figure 48a). To ensure a dense plume, several cubic meters of plant material were gathered in a bare field and lit on June 24 at 9:58 h. The fire developed quickly and produced a dense smoke plume, which was visible for approximately 1 hour. The plume reached its maximum extent 10–15 min after ignition and then gradually declined until the fire ceased at 11:06 h. During the burning, we recorded 12 flyovers with *HyPlant*. The direction of the actual flight line was chosen according to momentary fume direction. The flight altitude was 1000 m above ground level (agl).

Figure 48 Position of the fire experiment north of Grosseto. Picture of the lit fire on June 24, 2019.

8.2.1 Analysis of plant functional heterogeneity in a tree nursery

The analysis of *HyPlant* images over the nursery area had the objective to identify species-specific fluorescence signatures. The retrieved SIF_{760} and SIF_{687} over the study area is shown in Figure 49.

Figure 49 Fluorescence emissions in the A (left) and B (right) O_2-bands as retrieved by the SFM method over the study area of the nursery in Grosseto, Italy. The study area is outlined in Figure 46.

The DUAL image from *HyPlant* was processed to calculate the NDVI of the entire surface of the nursery (Figure 50).

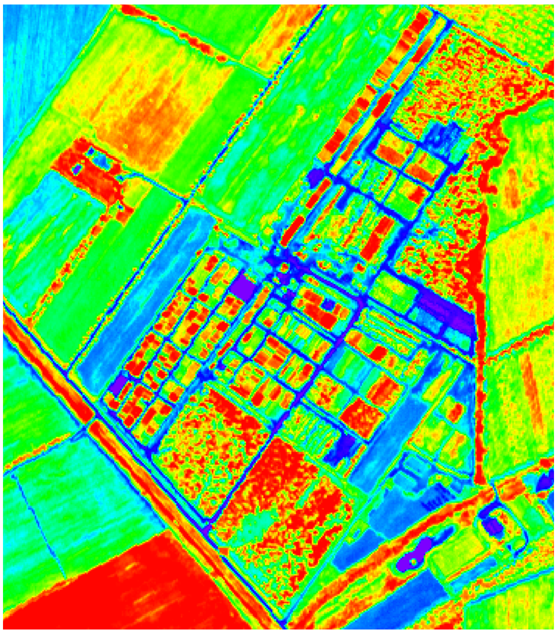

Figure 50 NDVI of the tree nursery area during the 2019 campaign.

The data clearly showed quite some variability between the different plots and species inside the nursery area. Some plots have high NDVI values while others have low NDVI. This is both a consequence of the large biodiversity and of the limited, but often detectable, difference in the density of the plants (in pots) that were arranged inside each plot. It is also rather fortunate, in this case, that there were other non-*HyPlant* images available. A Very High Resolution (VHR) image of the area was obtained from a regional-scale airborne acquisition (Tuscany region, July 2, 2019) and a VHR satellite image is freely available from Google Earth taken on June 21, 2019 (Figure 51).

Figure 51 Snapshot of the airborne images of the tree nursery taken in the first days of July 2019. The image on the left is a panchromatic RGB image while the image on the right is a false color image. The third image (second row) in the figure is available from Google Earth PRO and is dated June 26, 2019.

The following images (Figure 52 and Figure 53) provide some interesting detailed comparison between different plots of the nursery as seen from the airborne images in false color, the *HyPlant* image (narrow-band NDVI) as well as the retrieved SIF_{760} and SIF_{687}. In particular, Figure 52 outlines a well detectable plot of *Eucalyptus grandis* while a plot of *Oleander nerium* is outlined in Figure 53.

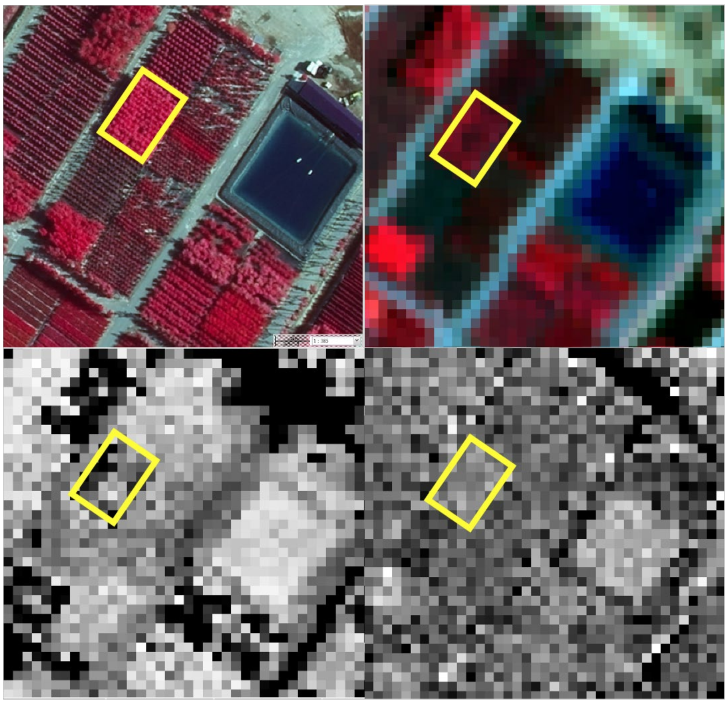

Figure 52 Outline (yellow rectangle) of a plot of *Eucalyptus grandis* inside the nursery area in Grosseto. The images follow this sequence (clockwise): false-color VHR image, *HyPlant* NDVI, *HyPlant* SIF_{760} and SIF_{687}.

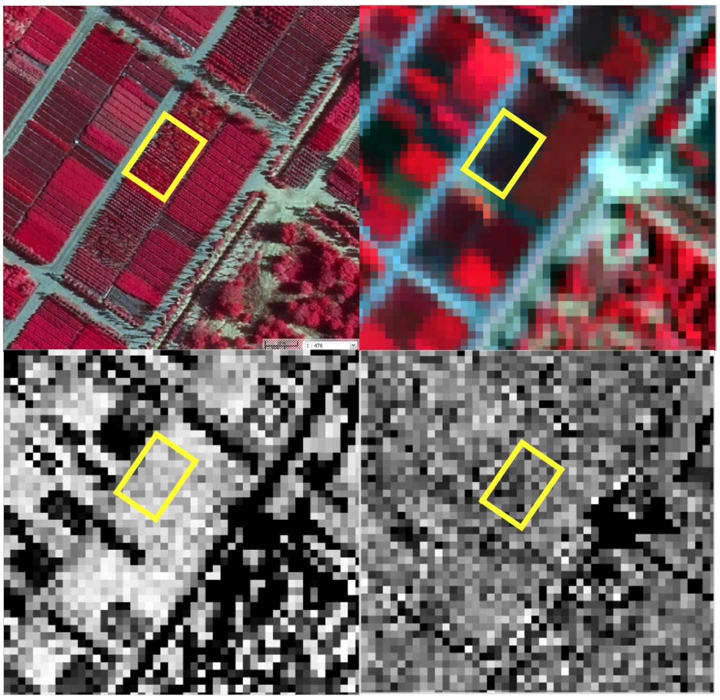

Figure 53 Outline (yellow rectangle) of a plot of *Oleander nerium* inside the nursery area in Grosseto. The images follow this sequence (clockwise): false-color VHR image, *HyPlant* NDVI, *HyPlant* SIF_{760} and SIF_{687}.

The images clearly show some interesting but rather contrasting responses of the two species identified. The Eucalyptus plot appears bright in the false color image and shows a high NDVI value. SIF_{760} fluorescence is lower compared to the neighboring plots, while the SIF_{687} appears to be higher. More plots were then analyzed in the same way by isolating them in the *HyPlant* scene (on the basis of the land use assessment that was made on-site on the date of the flight). This enabled further preliminary analysis of the complex relationship between canopy structure, greenness (NDVI), and the retrieved fluorescence signal in the O_2-A and O_2-B bands.

Figure 54 shows the comparison of SIF_{760} and NDVI in a substantial number of isolated plots (n=39). The data point distribution depicts an interesting reversed relationship between the two variables, which suggests that the fluorescence signal is in fact adding critical information to the solely reflectance-based NDVI. Indeed, species showing the highest NDVI values have the lowest SIF_{760} response and the other way around. Data from same species plots tend to group together, with some exceptions, which is likely associated with the density of the potted plants inside the nursery.

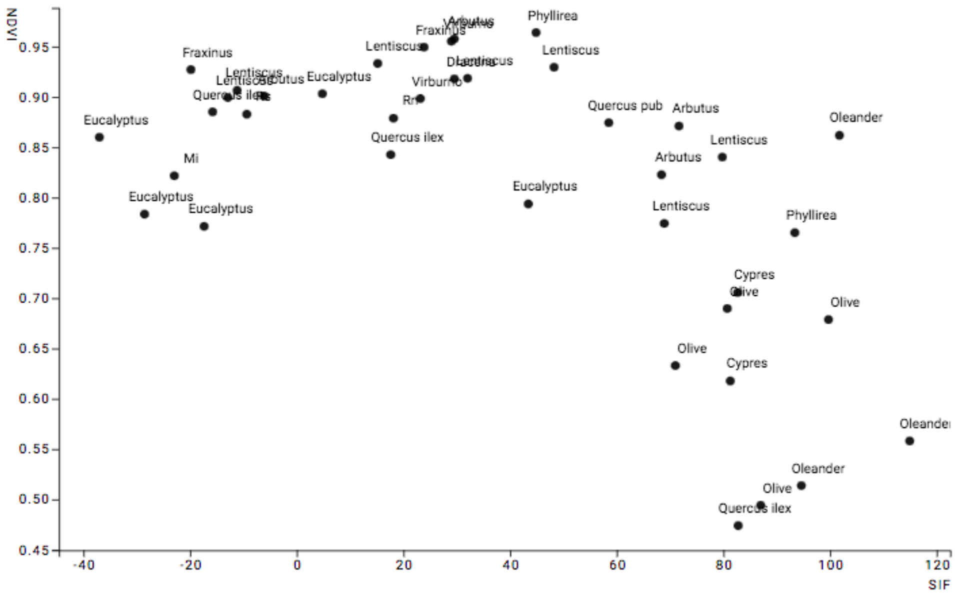

Figure 54 SIF_{760} versus NDVI as measured by *HyPlant* over different plots that were isolated inside the nursery.

These initial results suggested to make a more detailed (even if preliminary) multivariate statistical analysis of the data to tentatively disentangle their complexity and eventually highlight the potentials of using SIF760 and SIF687 in the analysis of biodiversity signatures. A principal component analysis was made using the different plots as sampling units and the three variables (NDVI, SIF_{760} and SIF_{687}) as a source of variance. Not unexpectedly, when the first two components were plotted in a graph (Figure 55), the different species tended to group together in spite of some inter-plot variability likely associated with plant/pot spacing and plant size/status. Some groups, however, tended to overlap and they could not be discriminated on the simple basis of the three selected variables and the resulting eigen-vectors.

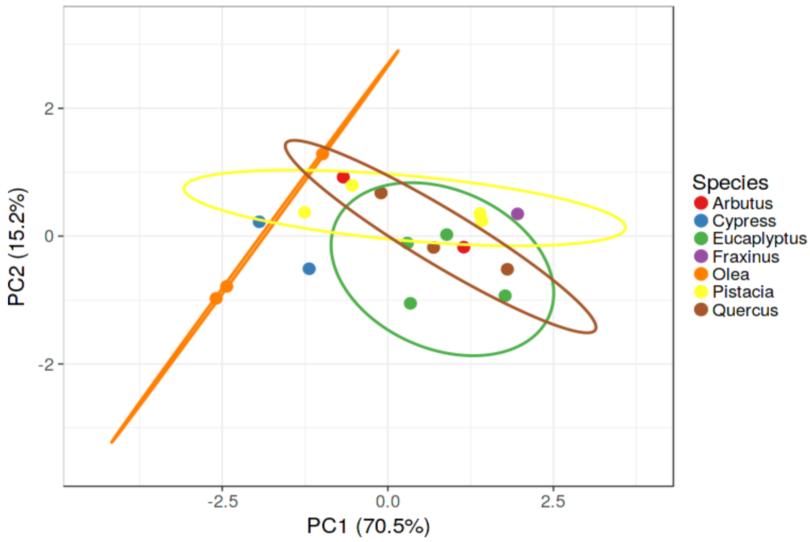

Figure 55 Principal component analysis and the resulting grouping of the species chosen for the analysis. A color legend is provided in the figure. Some of the species with replicated plots tended to group together, but the data show some significant overlap. The observation of opposite trends for some different species is noteworthy.

The heatmap obtained by multivariate analysis (Figure 56) basically confirmed the observation made above for individual plots. The species grouping, although rather imperfect, followed the differential and somewhat opposite behavior that was illustrated above for *Eucalyptus grandis* and *Oleander nerium*. Species ranked in a “high NDVI/low SIF_{760}/high SIF_{687}” group that was clearly separated from the “low NDVI/high SIF_{760}/low SIF_{687}” group.

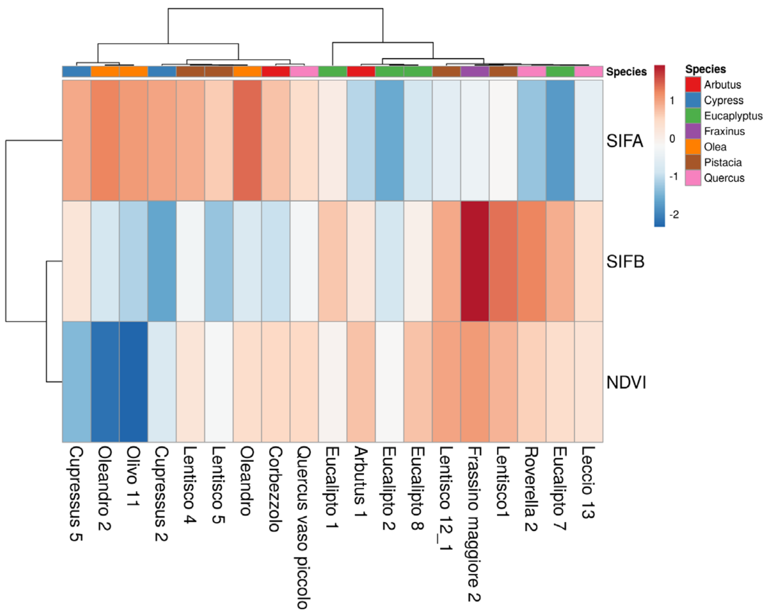

Figure 56 Heatmap obtained from multivariate analysis. SIFA: SIF_{760}, SIFB: SIF_{687}.

As a concluding remark, we must emphasize the preliminary nature of our investigation and subsequent analysis. It is rather obvious, however, that the fluorescence signal can carry important biodiversity-associated information, especially when this is combined with other optical reflectance-based indices. This is a rather novel issue for SIF applications, certainly deserving much more attention, given the potential for further insights. The implications for the future FLEX mission are not negligible, as the relatively low spatial resolution of FLEX may be differentially affected by biodiversity, especially if such biodiversity will actually show diverging responses or anti-correlation between reflectance indices and SIF. This confirms that accurate and possibly detailed information on plant biodiversity will actually be needed for a careful interpretation of the fluorescence signal of FLEX.

8.2.2 Understanding the potential of solar-induced fluorescence to detect early signs of drought

The drought experiment was carefully analyzed during the course of this campaign and our data and results have been used to author a scientific publication. Thus, all of our results and an extended scientific discussion can be found in this publication and are not repeated here (Damm et al. 2022, section 13.1). This publication investigates the sensitivity of SIF_{687}, SIF_{760}, LST, photochemical reflectance index (PRI), Meris terrestrial chlorophyll index (MTCI), and the water band index (WBI) for increasing water limitation. The publication also provides a summary of the most relevant in-situ measurements acquired to validate and interpret airborne data, including abiotic factors (soil water content, meteorological variables), biotic factors (LAI, plant height), and physiological variables (SAP flow, leaf water potential, growth rates). We could clearly demonstrate that SIF greatly changed during just a few days and we could show that the non-irrigated area showed an obvious reduction of SIF_{760} (Figure 57).

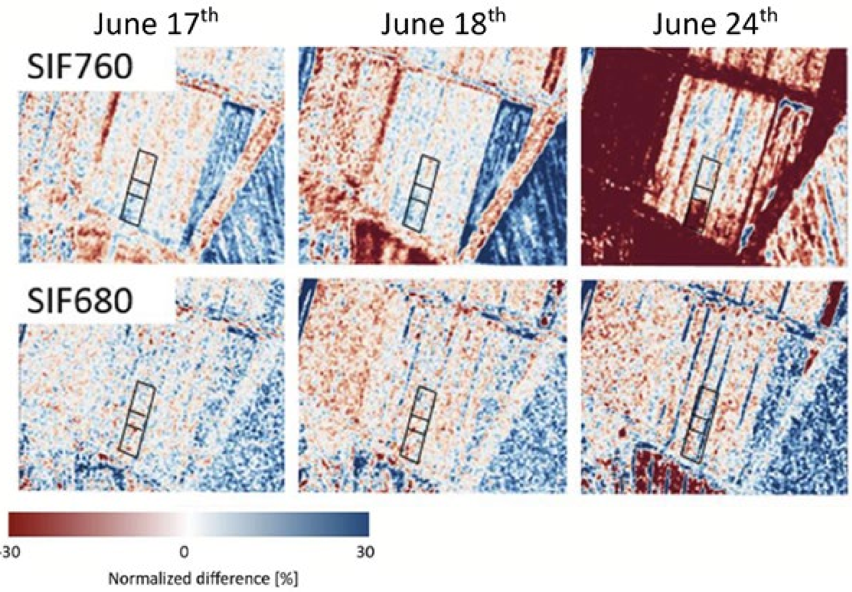

Figure 57 Time series of SIF_{687} and SIF_{760} retrieved from *HyPlant* data by SFM during the drought stress experiment. Measurements were taken on June 17 (left), June 18 (middle) and June 24, 2019 (right) of non-irrigated (lower rectangle), control (highest rectangle) and well-watered corn plants (middle rectangle).

These relative changes were, however, overlaid by three other components – namely, the normal seasonal growth of the crops, varied intensity of incoming PAR, and some discrepancies between the ground and airborne SIF products. These components required a more careful analysis, including the need for data normalization, which was carried out (see Damm et al. 2022 & section 13.1 for details). In the end, we could show that far-red SIF responded fastest with a short-term increase after manifestation of soil water limitation, which was already detectable three days after irrigation was withheld. During the following days, SIF_{760} decreased again, indicating the subsequent degradation of leaf and canopy pigments. We additionally identified different response times in the different remote sensing parameters, representing different plant traits, including short term responses (e.g. stomatal conductance, downregulation of photosynthesis) and medium-term changes (e.g. pigment decomposition, changing leaf water content). Our study demonstrates the complementarity of optical and thermal remote sensing parameters to mechanistically assess the complex cascade of functional, biochemical and structural plant responses to evolving soil water limitation.

8.2.3 Analysis of the fire experiment to evaluate the potential to detect and quantify the depth of the potassium absorption line in the high-resolution *HyPlant* data

LST characterization before and after the burn experiment

The fire event was carefully recorded by thermal infrared measurements (TASI and HYTES) as shown in Figure 58. The burning area is outlined by the black circle and the brightness temperature was greater than 330K.

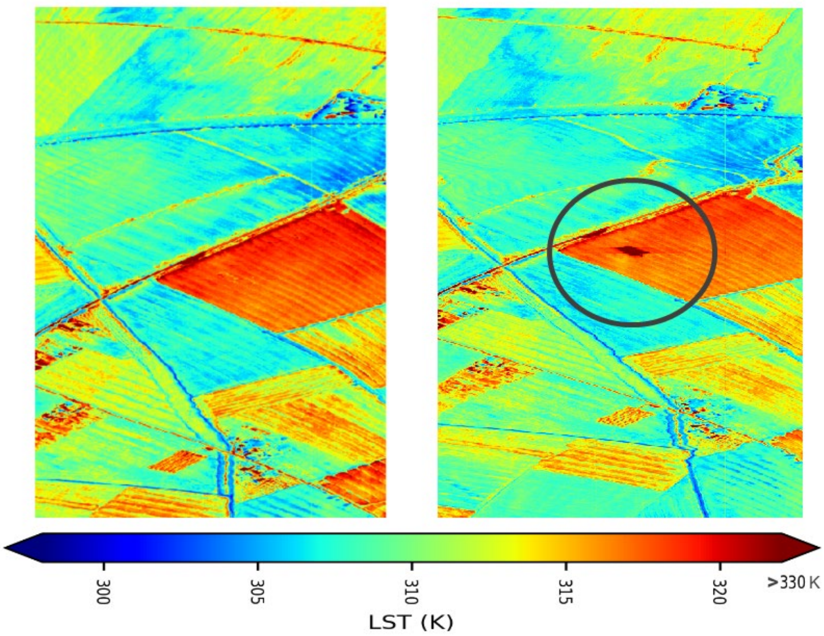

Figure 58 LST characterization before (left) and during (right) the burn experiment. Surface temperature is expressed in Kelvin (K) and a clear difference is detectable between green and bare soils as well as between the background and the burning area (circle).

Potassium emission lines as observed by *HyPlant*

When the flames of the fire event were observed by the *HyPlant* sensor, the two K emission lines at 766.4 nm and 769.8 nm were clearly detectable (Figure 59). This is not surprising, as the resolution of the FLUO spectrometer is sufficient to enable detection. The amplitude of the lines is large, being about 10-fold higher than the shoulders.

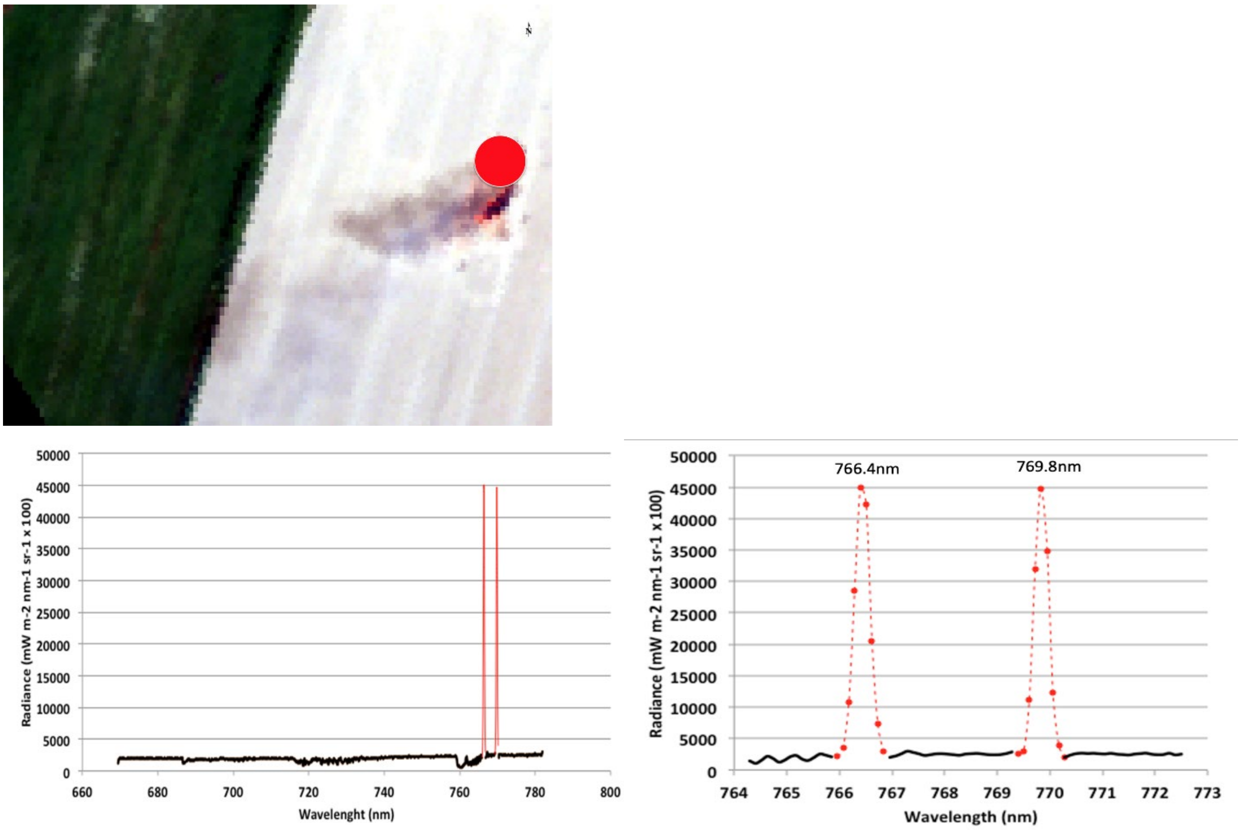

Figure 59 Fire area as seen from *HyPlant* with the region of interest for the extracted spectra (red dot in upper panel). Potassium emission lines as observed by *HyPlant* over the entire FLUO *HyPlant* spectrum (lower left) and zoomed for the K-peaks region (lower right). The amplitude of the K-lines exceeds 10-fold and the FWHM is lower than 1 nm.

This result is very convincing and indicates that *HyPlant* and eventually the future FLEX mission will be capable of detecting surface fire activity. The amplitude of the K-lines suggests that flame detection would be possible even at the low spatial resolution of a FLEX pixel (300 m) in the case of large fires, also potentially enabling the retrieval of critical information on the “flame-front” of wildfires depending on the intensity on the observed K-lines. It is worth noting, here, that wildfires are extremely frequent and cover large forest/bushland areas in some regions of the world (e.g. sub-tropical Africa), and their quantification may provide critical information on the global carbon cycle. For instance, the EU’s Copernicus Atmosphere Monitoring Service found that burning forests released 1.3 gigatons of carbon dioxide in August 2021, mostly in North America and Siberia. In the same year, record high and prolonged heat resulted in devastating fires in Turkey, which were four times more intense than anything previously registered. Greece, Italy, Spain, Portugal, Albania, North Macedonia, Algeria and Tunisia have also battled huge wildfires.

Fluorescence retrieval over the smoke plume

As expected, the *HyPlant* pixels of the smoke plume showed an increased fluorescence signal. Fluorescence emission by the smoke particles themselves can be ruled out. Therefore, the hypothesis might be that such an apparent fluorescence is simply due to the fact that the light reflected by the smoke plume has a shorter path-length across the atmosphere, being the plume at a higher elevation with respect to the soil. This apparent fluorescence was detected on both the O_2-B (Figure 60 and Figure 61) and O_2-A bands (Figure 61).

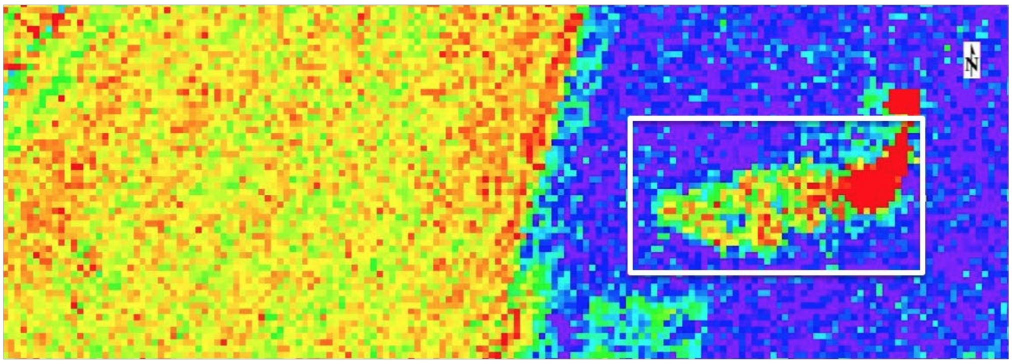

Figure 60 Apparent fluorescence emission in the O_2-B band of the smoke plume area (white box) and of the neighboring vegetated field (left part of the image).

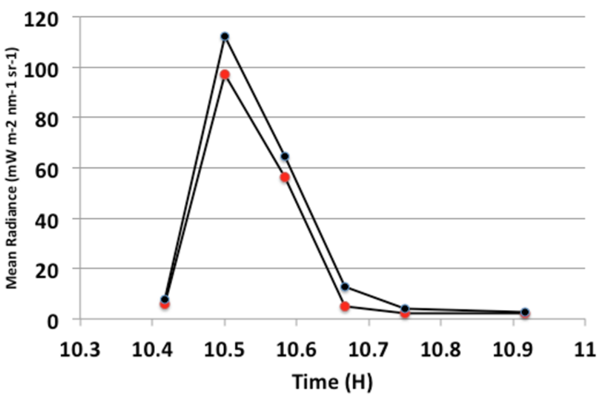

Figure 61 Intensity of the fluorescence signal (SIF_{687} in red, SIF_{760} in back) along six *HyPlant* overpasses.

The fact that changes in height/altitude of the reflecting body affects the fluorescence retrieval (Figure 62) further highlights the importance of a detailed digital terrain model for the appropriate correction of O_2 atmospheric absorbance. On the other hand, it indicates that *HyPlant* (and FLEX) might potentially monitor, on the base of fluorescence retrieval, the height and geographical extent of smoke plumes generated by wildfires.

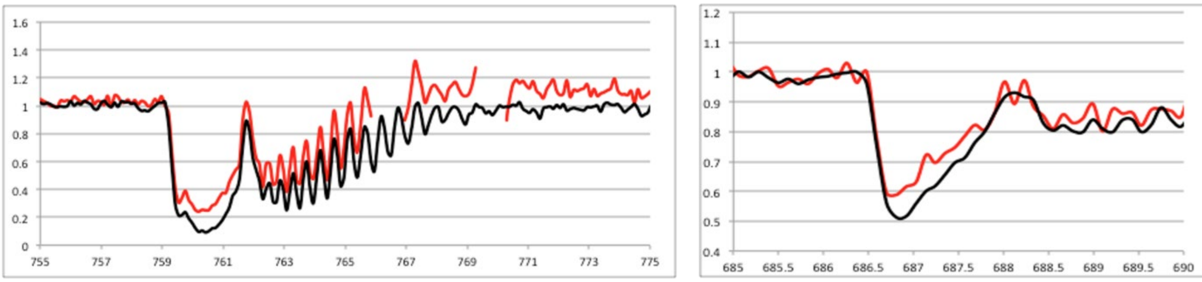

Figure 62 Normalized spectra of smoke plume (red) and of the neighboring vegetated field (black) as measured by the *HyPlant* FLUO module in the O_2-A (left panel) and O_2-B (right panel) regions.

Overall, this confirms the potential of a high-resolution hyperspectral sensor to both detect the wildfires flames using the K-lines and estimate the height of the smoke plume using a combination of “apparent SIF” data and NIR reflectance.

8.2.4 Understanding the diurnal dynamics in solar-induced fluorescence and exploring the associated retrieval uncertainties in the course of the day

On June 19, 2019 the same area of the Grosseto research site was recoded several times by *HyPlant* in the morning, at midday and in the afternoon. This data set was used to investigate the diurnal behavior of the determined SNR, which was introduced as a quality flag of *HyPlant* FLUO at-sensor radiance data (section 5.1), as well as both SIF products (at 760 and 687 nm) and corresponding uncertainty maps. Data sets of the area of interest (Figure 63) were recorded at 10:11 and 10:34 (morning), 13:15 and 13:38 (midday), and 16:11 and 16:34 (afternoon).

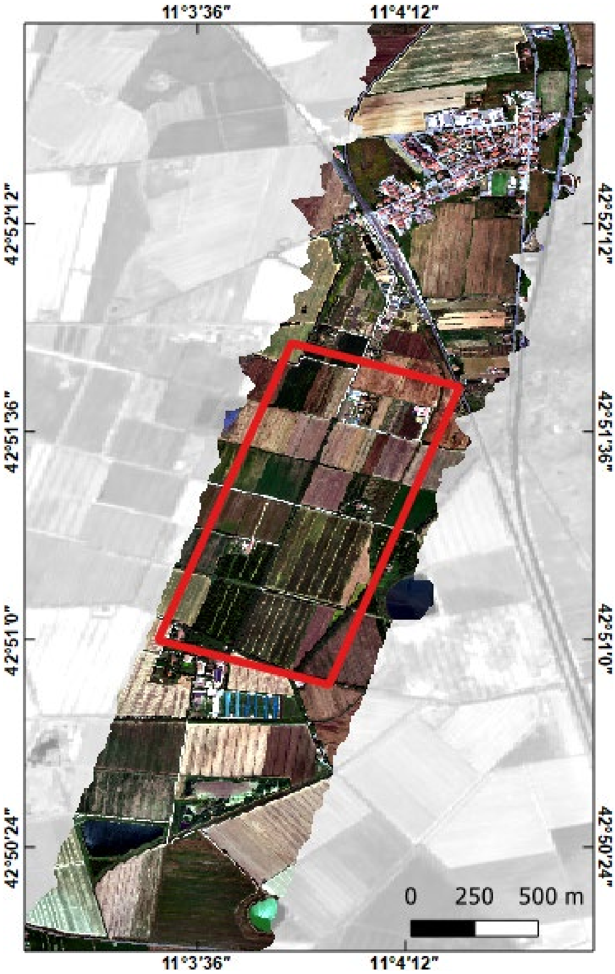

Figure 63 *HyPlant* DUAL true color composite of the flight line recorded at 13:15 on June 19, 2019, with the area of interest (red frame) used for the diurnal analysis.

The SNR within and at the left shoulder outside of both oxygen absorption bands shows a clear diurnal trend, with lower values in the morning and afternoon, and higher values at midday (Figure 64). For both spectral ranges (680–687 and 750–760 nm), the SNR outside the absorption feature is distinctly higher compared to the SNR within the absorption feature. This is expectable, since the signal strength at the left shoulder of both absorption features is much higher. Furthermore, the SNR determined within the absorption features at 687 and 760 nm have comparable values, ranging from 50 in the morning and afternoon to 75 at midday.

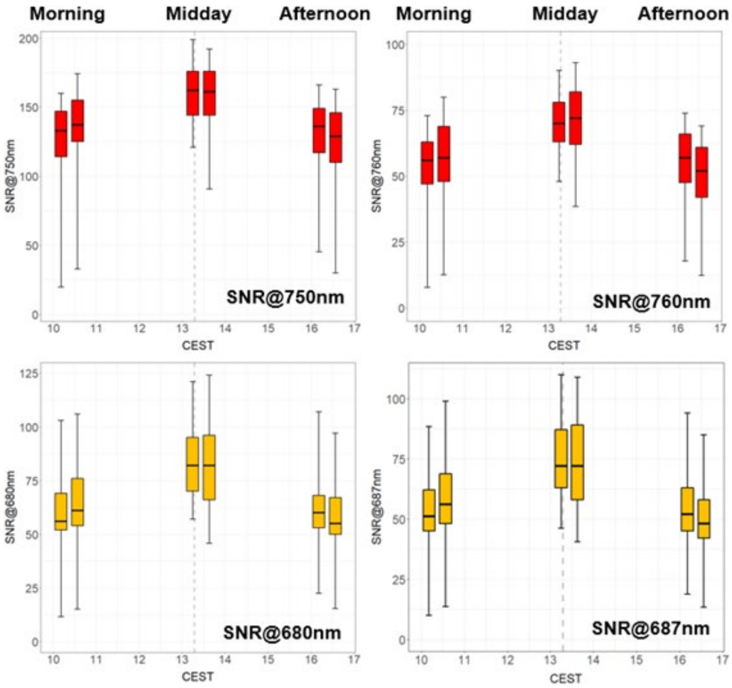

Figure 64 SNR of the *HyPlant* FLUO at-sensor radiance determined outside (750 and 680 nm) and inside (760 and 687 nm) the O_2-A (top) and O_2-B absorption features (bottom), respectively.

Figure 65 illustrates the diurnal course of SIF_{760} in the form of maps and boxplots. While the maps represent the SIF_{760} values of all pixels, the boxplots only include the pixels having an NDVI higher than 0.6, in order to exclude non-vegetation pixels from the analysis. The maps as well as the boxplots clearly show the expected diurnal behavior of SIF_{760} following the intensity of PAR characterized by increasing values in the morning until solar noon followed by decreasing values in the afternoon. The same diurnal trend with similar value ranges was also observed for SIF_{687}, which is illustrated in Figure 66. In the diurnal box plots of both SIF products it is clearly visible that even small changes in sun elevation in the morning and in the afternoon led to detectable changes in the absolute SIF values – for example, the SIF_{760} and SIF_{687} maps and corresponding box plots of the second overflight at 10:34 show slightly higher values compared to the first overflight at 10:11. The same trend in reversed order can be observed for the two afternoon overflights at 16:11 and 16:34, respectively. Both SIF products provide reasonable values for photosynthetically active vegetation, with median values of lower than 1 mW $m^{-2}sr^{-1}nm^{-1}$ in the morning and afternoon, respectively, and median values of around 1.5 mW $m^{-2}sr^{-1}nm^{-1}$ at midday.

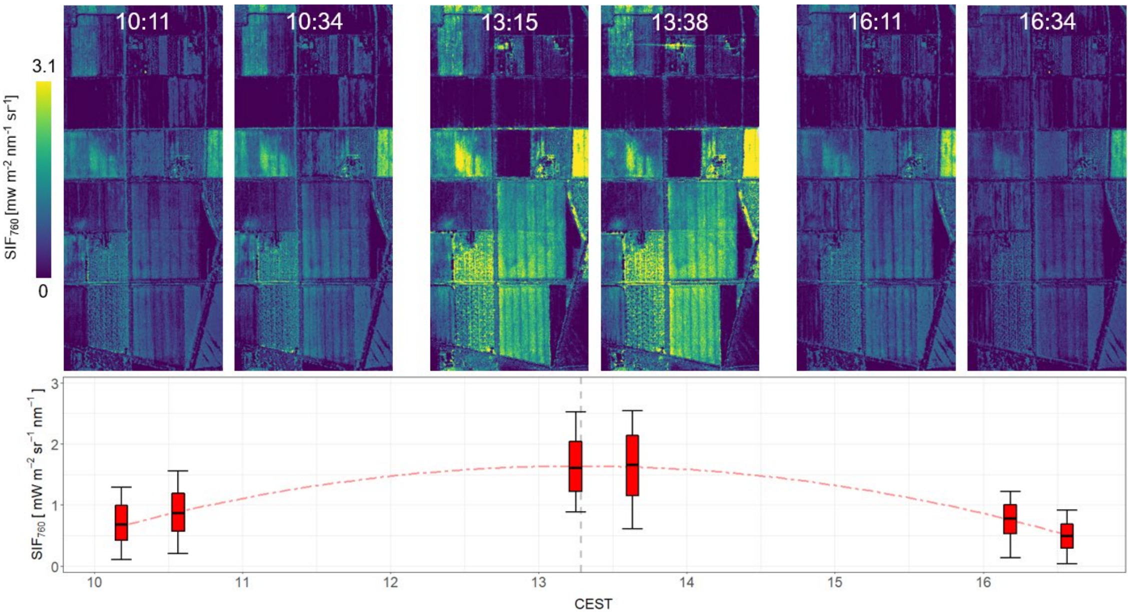

Figure 65 Spatial dynamics of SIF_{760} in the course of the day. SIF_{760} maps of Grosseto acquired on June 19, 2019 (top) and corresponding boxplots showing median, 5th, 25th, 75th and 95th percentiles for the different overflights only considering the pixels having an NDVI higher than 0.6 (bottom). The vertical grey dashed line indicates solar noon.

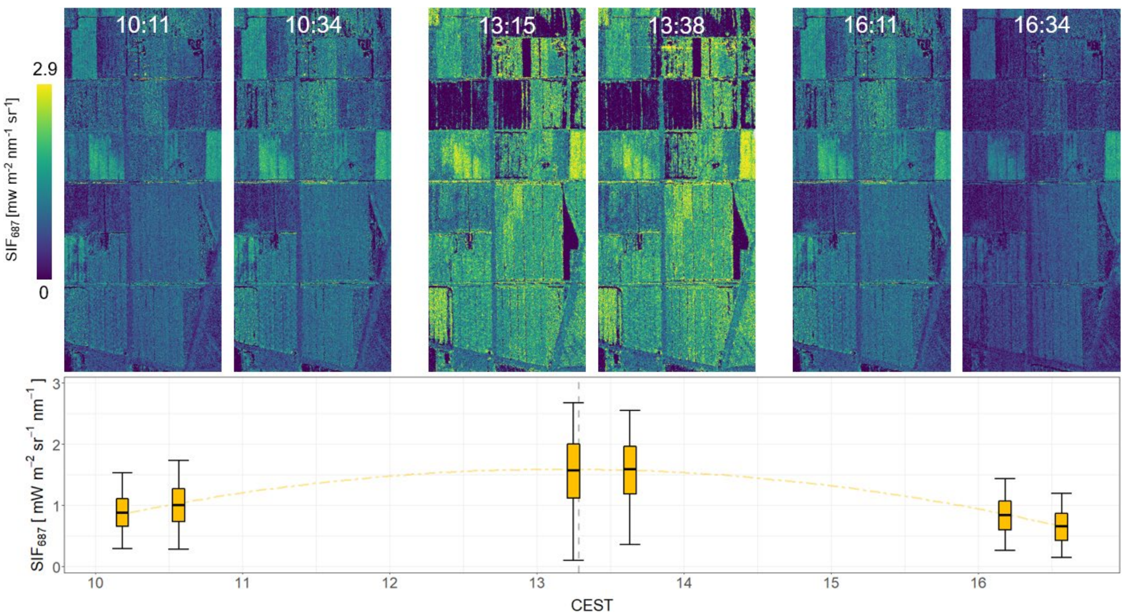

Figure 66 Spatial dynamics of SIF_{687} in the course of the day. SIF_{687} maps of Grosseto acquired on June 19, 2019 (top) and corresponding boxplots showing median, 5th, 25th, 75th and 95th percentiles for the different overflights only considering the pixels having an NDVI higher than 0.6 (bottom). The vertical grey dashed line indicates solar noon.

The absolute SIF uncertainties at the pixel level illustrated in Figure 67 and Figure 68 provide diurnal trends similar to those observed for both SIF maps. This indicates that higher absolute SIF values led to higher absolute uncertainties. Most of the SIF_{760} pixels have an absolute uncertainty between 0.10 and 0.27 mW m^{-2}sr^{-1}nm^{-1}, while for SIF_{687} the values are lower, ranging from 0.05 to 0.22 mW m^{-2}sr^{-1}nm^{-1}.

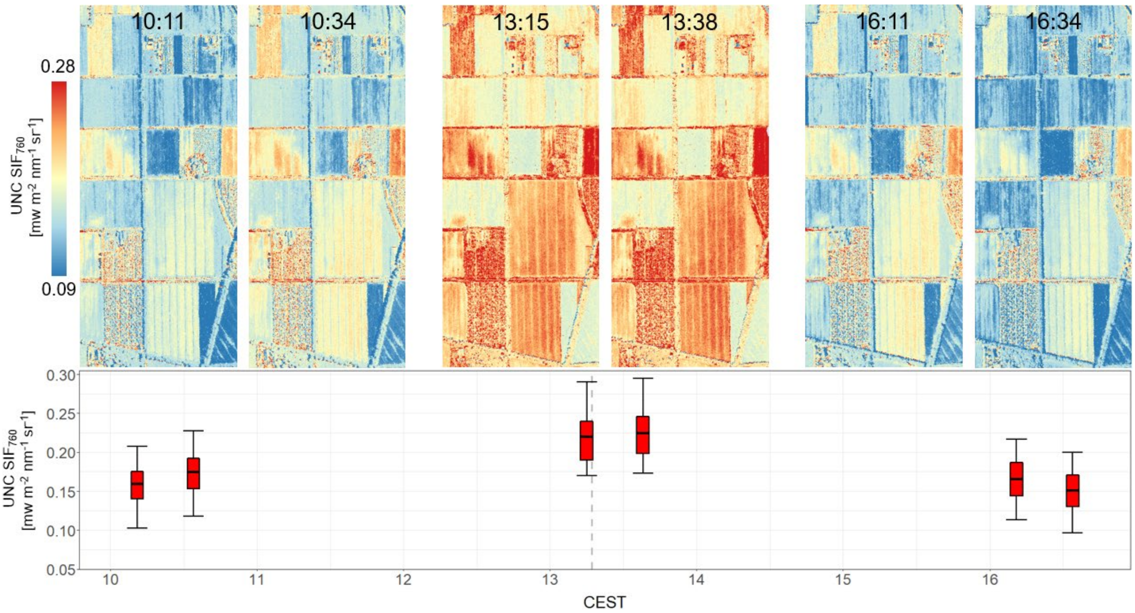

Figure 67 Spatial dynamics of the absolute uncertainty of SIF_{760} in the course of the day. Maps showing the absolute uncertainty of SIF_{760} for Grosseto data acquired on June 19, 2019 (top) and corresponding boxplots showing median, 5th, 25th, 75th and 95th percentiles for the different overflights only considering the pixels having an NDVI higher than 0.6 (bottom). The vertical grey dashed line indicates solar noon.

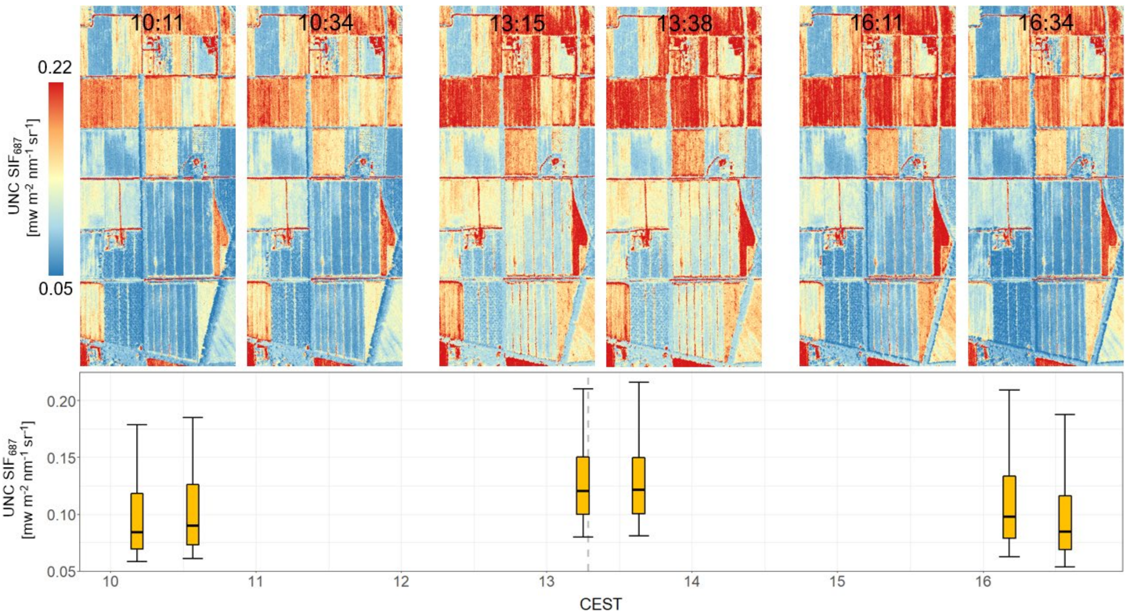

Figure 68 Spatial dynamics of the absolute uncertainty of SIF_{687} in the course of the day. Maps showing the absolute uncertainty of SIF_{687} for Grosseto data acquired on June 19, 2019 (top) and corresponding boxplots showing median, 5th, 25th, 75th and 95th percentiles for the different overflights only considering the pixels having an NDVI higher than 0.6 (bottom). The vertical grey dashed line indicates solar noon.

In contrast, the relative uncertainties shown in Figure 69 and Figure 70 for both SIF products provide an opposite diurnal trend, with lower uncertainties obtained from the midday data sets and higher uncertainties derived for the morning and afternoon overflights. This clearly indicates the benefit of acquiring *HyPlant* data at a time close to solar noon, when irradiance reaches its maximum and BRDF effects are less pronounced, to obtain image data with a high SNR ratio, which is an important prerequisite for retrieving high-quality SIF maps with low uncertainties.

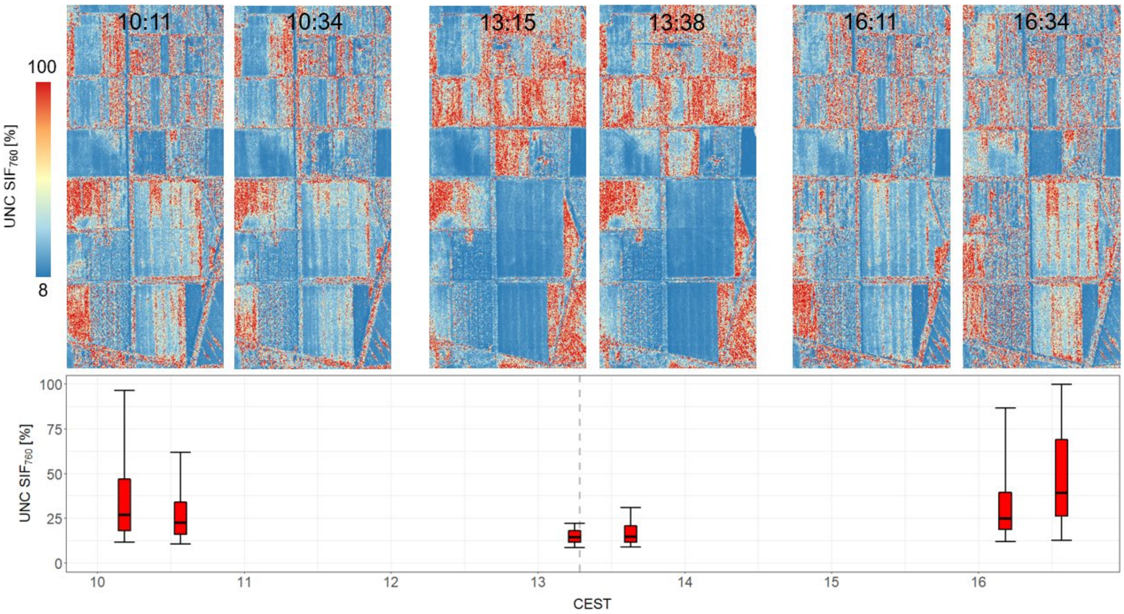

Figure 69 Spatial dynamics of the relative uncertainty of SIF_{760} in the course of the day. Maps showing the relative uncertainty of SIF_{760} for Grosseto data acquired on June 19, 2019 (top) and corresponding boxplots showing median, 5^{th}, 25^{th}, 75^{th} and 95^{th} percentiles for the different overflights only considering the pixels having an NDVI higher than 0.6 (bottom). The vertical grey dashed line indicates solar noon.

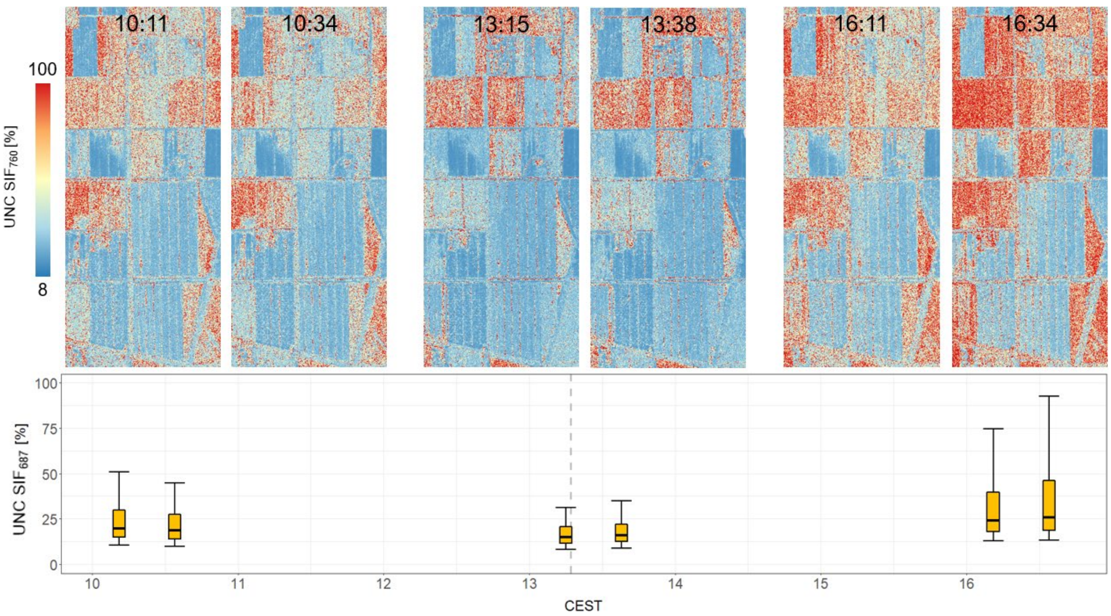

Figure 70 Spatial dynamics of the relative uncertainty of SIF_{687} in the course of the day. Maps showing the relative uncertainty of SIF_{687} for Grosseto data acquired on June 19, 2019 (top) and corresponding boxplots showing median, 5^{th}, 25^{th}, 75^{th} and 95^{th} percentiles for the different overflights only considering the pixels having an NDVI higher than 0.6 (bottom). The vertical grey dashed line indicates solar noon.

For both absolute and relative uncertainty, the derived values for SIF_{687} are lower in comparison to SIF_{760}. This is due to the less pronounced oxygen absorption at 687 nm, resulting in a higher signal measured by *HyPlant*, which consequently lead to a higher SNR ratio in the recorded data. Since the median relative uncertainty values of both SIF products derived from the midday overflights are distinctly lower (10–15%) than those of the morning and afternoon data sets (15–75%), it is recommended that data be acquired close to solar noon (±2 hours) when sun elevation and thus PAR is highest, to ensure the recording of high-quality SIF data.

8.3 Campus Klein-Altendorf, Germany – understanding diurnal dynamics in agricultural systems and the sensitivity of active and passive fluorescence parameters to elevated CO_2

The Campus Klein-Altendorf (CKA) agricultural research site near Bonn comprises 181 ha for field trials and approximately 4,800 m^2 for greenhouse trials. At CKA, research can be conducted with all kinds of plants and crops, ranging from small plants and herbs to large crops like maize, and from annual crops like vegetables to perennial plants like *Miscanthus* and fruit trees (Figure 71 and Figure 72). Plants can be grown for experiments under real-world conditions. Various groups from the University of Bonn and Forschungszentrum Jülich use the site to better understand crop performance and plant traits under natural conditions and to develop new concepts for future agricultural practices.

In recent years, Forschungszentrum Jülich has invested greatly in its measurement capacities at the campus and now operates a network of modern, non-invasive field phenotyping sensors and positioning systems. These include a mini-plot facility and an automated phenotyping system to grow crops in field-like soil conditions in the greenhouse; the motorized multi-use platform FieldSnake; a unique portfolio of imaging sensors for field phenotyping (hyperspectral systems, thermal cameras for active and passive thermography, high-performance imaging spectrometers, stereo cameras, and LiDAR systems); and various established handheld instruments. Additionally, several field plant phenotyping experiments are ongoing at CKA every year. The experiments are under the supervision of IBG-2 at Forschungszentrum Jülich and data from these experiments can be made available.

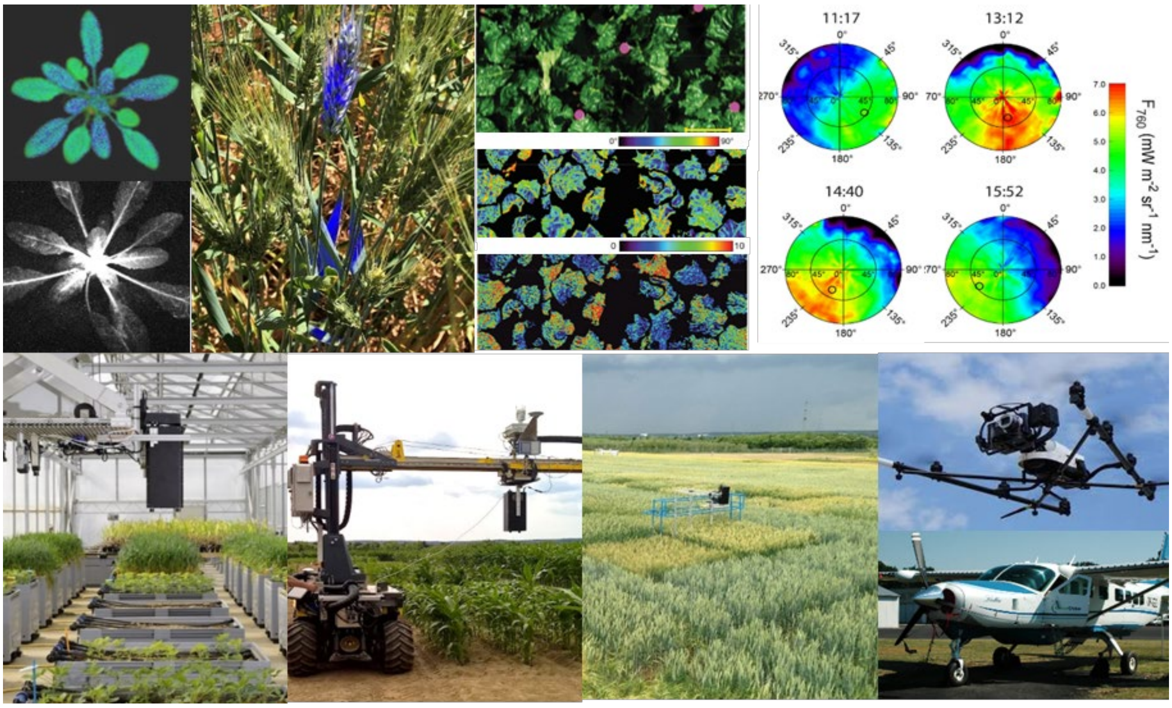

Figure 71 Images from CKA and selected field phenotyping instruments operating within the common experiment at Forschungszentrum Jülich. The plot design of the field traits provides a good test bed to link structural and functional properties of crops with remote sensing observations of SIF.

At CKA, several different experiments were conducted in 2019. The BreedFACE experiment is a new experimental set-up in which plants grow in the field in an environment with elevated CO_2 levels (600ppm). The FACE experiment is composed of a CO_2 supply-tank located approximately 150 m away from the FACE rings (Figure 72b). Two small cabinets are placed close to the ring: one to distribute the CO_2 into the eight pipes through conduction lines, and the second for power supply. The rings are octahedrons consisting of 7.25 m of steel pipe with small openings each 20–30 cm for the ejection of CO_2 in the opposite direction of the wind. An environmental monitoring station equipped with wind speed, wind direction and CO_2 concentration sensors is placed in the center of the ring (Figure 72c). A measurement platform on the FieldSnake contains the active and passive chlorophyll fluorescence sensors (LIFT and FloX) as well as other devices. The whole field is continuously monitored by a PhenoCam system.[7]

The common experiment is a 2.5 ha experimental field where different varieties of rapeseed, wheat, barley, corn and soybean are grown in repeated experimental field plots (Figure 71 and Figure 72). These plots are used for various project activities, including in particular the testing and validation of new plant phenotyping sensors. Thus, the structural and functional traits of the crops are well monitored during the seasonal cycle, with parameters such as LAI, canopy height and photosynthetic capacity routinely measured by different instruments. In previous years, different fluorescence techniques (including active laser-induced techniques and passive sun-induced approaches) were

[7] https://phenocam.sr.unh.edu/webcam/sites/breedfacectr1/,
https://phenocam.sr.unh.edu/webcam/sites/breedfacectr2/,
https://phenocam.sr.unh.edu/webcam/sites/breedfacering1/,
https://phenocam.sr.unh.edu/webcam/sites/breedfacering2/,

used in this central experiment by Forschungszentrum Jülich (e.g. Burkart et al. 2014, 2015, Räsch et al. 2014, Pinto et al. 2016, Quiros et al. 2021). Quiros et al. (2021) has made use of the 2019 data from BreedFACE to study the effect of increased atmospheric CO_2 concentrations on the yield, biomass and chlorophyll fluorescence of three bean genotypes. This study is currently being extended, and there are preparations for a full publication on this topic.

Furthermore, the common experiment consists of core collections of winter rapeseed, maize and barley from the P4P project, which is being undertaken with Bayer Crop Science. The varieties in the reference collection differ in shoot and root traits and provide a test site for various field phenotyping techniques, contributing to the transferability of greenhouse phenotyping to the field.

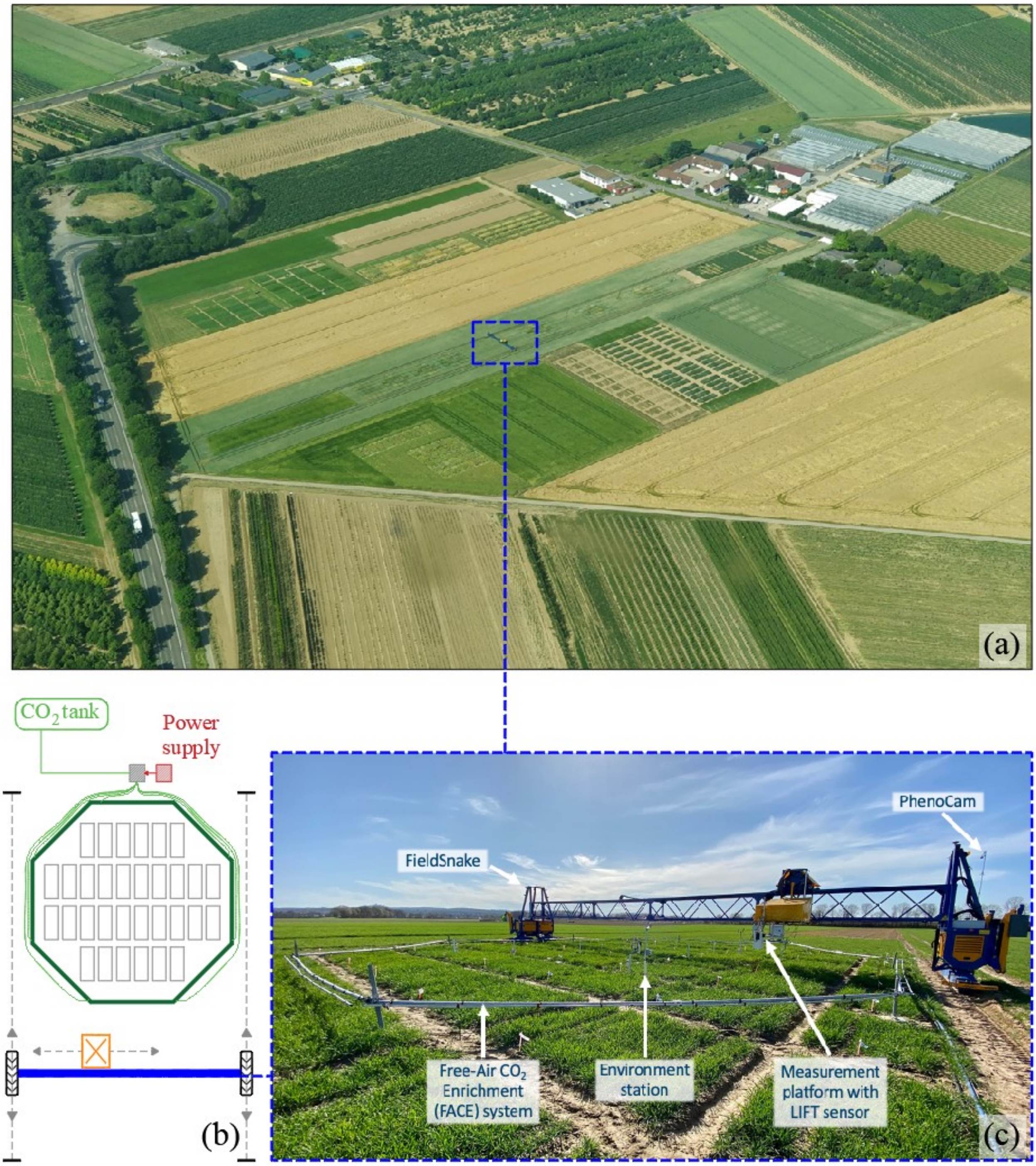

Figure 72 (a) Picture of Campus Klein-Altendorf (CKA) taken during aircraft flyover in June 2019. In the centre, the PhenoRob experiment and BreedFACE facility with the FieldSnake can be seen. (b) and (c) schematic drawing and close-up of the BreedFACE installation and the FieldSnake sensor positioning system.

Flight pattern

Two flight patterns were flown at CKA during the 2019 campaign, which are shown in Figure 73.

- **CKA**: Mapping of all four lines in 1-m resolution, clear sky conditions; a diurnal course was achieved
- **Common experiment at CKA**: Flyover of the PhenoRob and common experiment in 0.5 x 1-m resolution, clear sky conditions and close to solar noon

Figure 73 Flight lines for the mapping of CKA: a) Mapping of CKA, and b) Mapping of the common experiment at CKA that is located in the northern part of the research campus.

8.3.1 Understanding the diurnal dynamics in solar-induced fluorescence and exploring the associated retrieval uncertainties in the course of the day

In previous years, CKA was recorded several times on different days and different times during one day to collect data on an entire diurnal course of SIF. However, on June 26, 2019 for the first time we managed to record the campus five times on the same day. This day, data was recorded at a flight altitude of 680 m above ground level, leading to a GSD of 1 m. During each acquisition, four flight lines were alternately recorded towards either northwest or southeast directions to cover the entire area of CKA. The first two overflights took place in the morning at 10:15 and 11:20 Central European Summer Time (CEST). Data acquisition was continued at midday when CKA was recorded at 13:10 CEST shortly before solar noon (13:34, CEST). The last two data sets were acquired in the afternoon at 15:40 and 16:45 CEST. Using all overflights, the study site was measured five times covering the entire day to track the diurnal dynamics of SIF. Figure 74 shows a true color composite of the *HyPlant* DUAL mosaic of CKA recorded at midday together with a map providing information on the different crops grown in 2019.

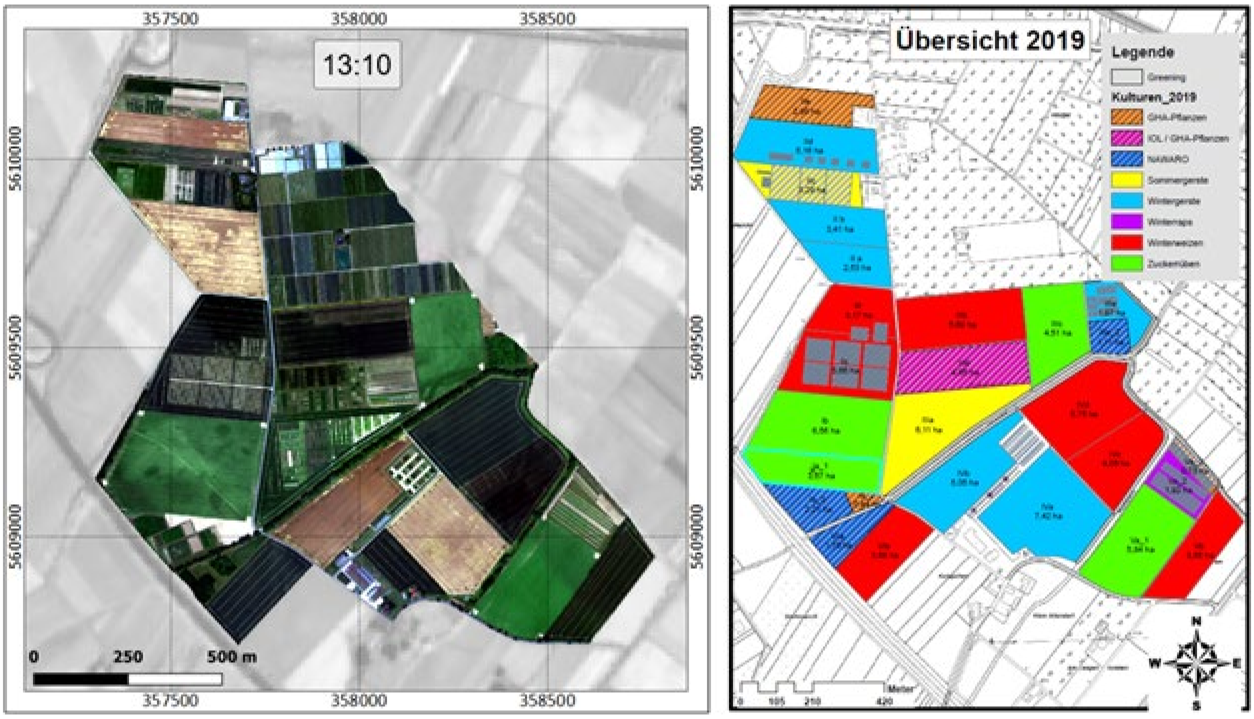

Figure 74 *HyPlant* DUAL true color composite of CKA recorded on June 26, 2019 at 13:10 CEST (left) and a map of CKA providing information on the planted crops in 2019 (right).

Figure 75 illustrates the diurnal course of SIF_{760} in the form of maps and boxplots. While the maps represent the SIF_{760} values of all pixels, the boxplots only include the pixels having an NDVI higher than 0.6 to exclude non-vegetation pixels from the analysis. The maps as well as the boxplots clearly show the expected diurnal behavior of SIF_{760} following the intensity of PAR, characterized by increasing values in the morning until solar noon followed by decreasing values in the afternoon. The sugar beet fields (green highlighted fields in Figure 74 right) provided distinctly higher values in comparison to the cereal fields (blue, purple and red highlighted fields in Figure 74 right), which is consistent with findings presented in Siegmann et al. (2021). Furthermore, the already senescent barley fields (blue highlighted fields in Figure 74 right) were characterized by the lowest SIF_{760} values. This is plausible, since senescent plants are characterized by less photosynthetic activity and thus emit less SIF. The same diurnal trend with slightly lower values was observed for SIF_{687}, which is illustrated in Figure 76. Also, there, the sugar beet fields had the highest values, which is visible especially in the midday overflight. The determined value range of 0 to 3 mW $m^{-2}sr^{-1}nm^{-1}$ and 0 to 2 mW $m^{-2}sr^{-1}nm^{-1}$ for the O_2-A and O_2-B absorption feature, respectively, meets our expectations and is in line with value ranges reported for the same crops in previous studies.

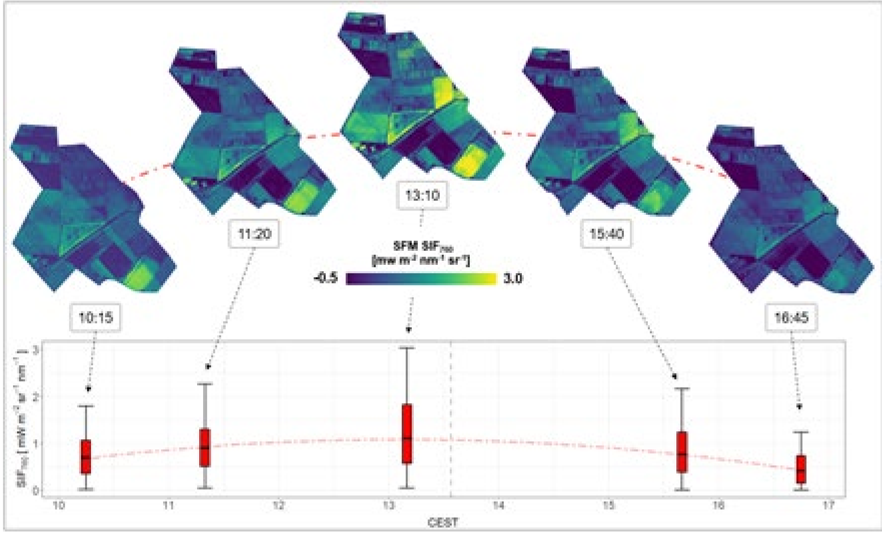

Figure 75 Spatial dynamics of SIF_{760} in the course of the day. SIF_{760} maps of CKA acquired on June 26, 2019 (top) and corresponding boxplots showing median, 5th, 25th, 75th and 95th percentiles for the different overflights while only considering the pixels having an NDVI higher than 0.6 (bottom).

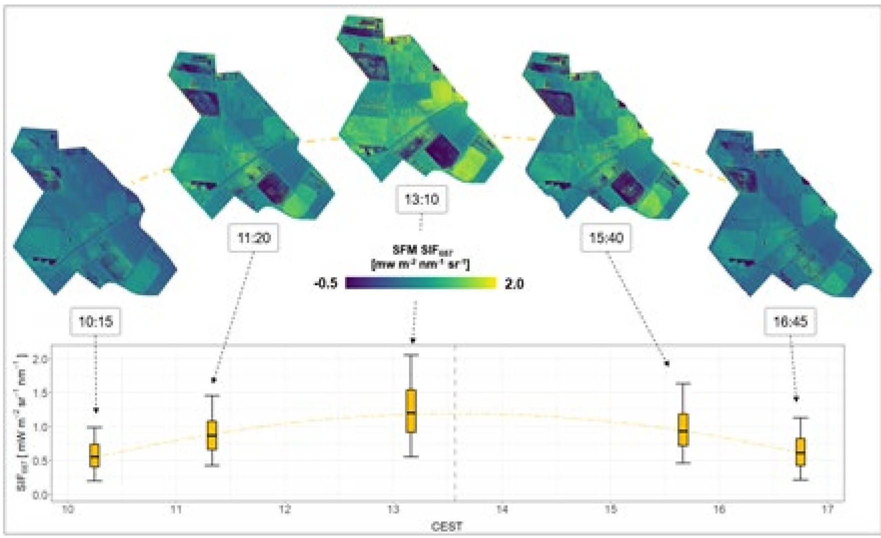

Figure 76 Spatial dynamics of SIF_{687} in the course of the day. SIF_{687} maps of CKA acquired on June 26, 2019 (top) and corresponding boxplots showing median, 5th, 25th, 75th and 95th percentiles for the different overflights while only considering the pixels having an NDVI higher than 0.6 (bottom).

The uncertainty at the pixel level provided with the SIF values is an important information for judging the quality of a SIF map derived from *HyPlant* FLUO at-sensor radiance data. Figure 77 and Figure 78 depict the absolute uncertainties of SIF_{760} and SIF_{687} for the five overflights on June 26. The absolute uncertainties also follow the intensity of PAR throughout the day, characterized by lower values in the morning and afternoon, and higher values at midday. Most of the SIF_{760} pixels have an absolute uncertainty between 0.07 and 0.2 mW $m^{-2}sr^{-1}nm^{-1}$, while for SIF_{687} the values are lower and range from 0.04 to 0.12 mW $m^{-2}sr^{-1}nm^{-1}$. In contrast, the relative uncertainties shown in Figure 79 and Figure 80 for both SIF products provide an opposite diurnal trend with lower uncertainties obtained from the midday data set and higher uncertainties derived for the morning and afternoon overflights.

This clearly indicates the benefit of acquiring *HyPlant* data at a time close to solar noon, when irradiance reaches its maximum and BRDF effects are less pronounced, in order to obtain image data with a high SNR ratio, which is an important prerequisite for retrieving high-quality SIF maps with low uncertainties.

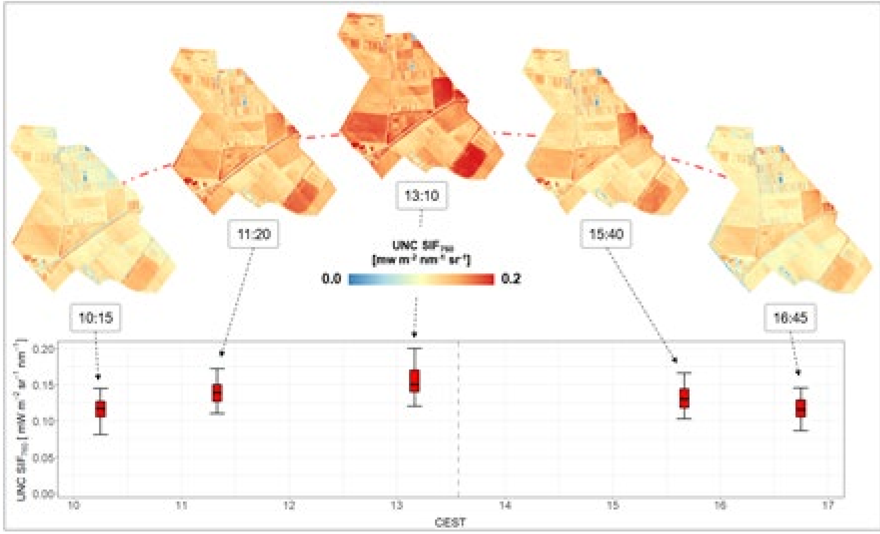

Figure 77 Spatial dynamics of the absolute uncertainty of SIF_{760} in the course of the day. Maps showing the absolute uncertainty of SIF_{760} of CKA acquired on June 26, 2019 (top) and corresponding boxplots showing median, 5th, 25th, 75th and 95th percentiles for the different overflights while only considering the pixels having an NDVI higher than 0.6 (bottom).

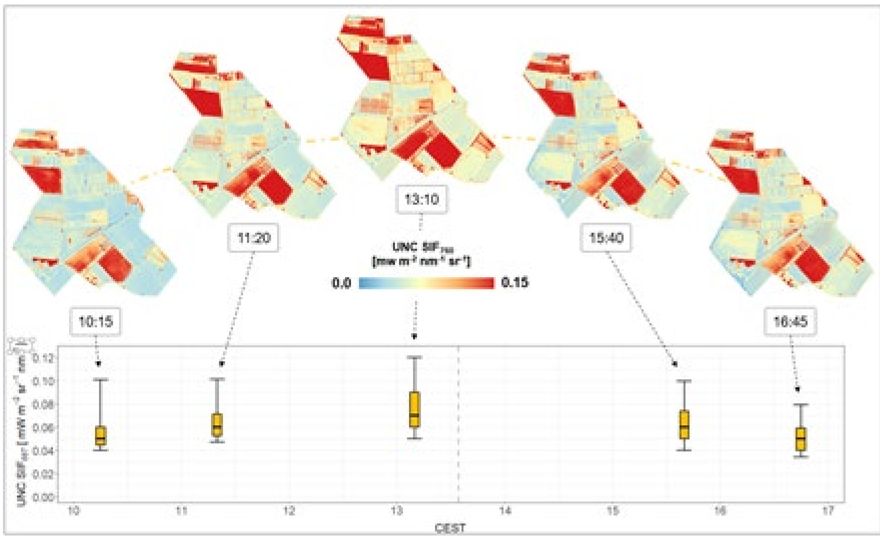

Figure 78 Spatial dynamics of the absolute uncertainty of SIF_{687} in the course of the day. Maps showing the absolute uncertainty of SIF_{687} of CKA acquired on June 26, 2019 (top) and corresponding boxplots showing median, 5th, 25th, 75th and 95th percentiles for the different overflights while only considering the pixels having an NDVI higher than 0.6 (bottom).

For both absolute and relative uncertainty, the derived values for SIF_{687} are lower in comparison to SIF_{760}. This is due to the less pronounced oxygen absorption at 687 nm, resulting in a higher signal measured by *HyPlant*, which consequently leads to a higher SNR ratio in the recorded data. The median relative uncertainty values for both SIF products derived from the overflights at 11:20, 13:10

and 15:40 CEST are in the range of 10 to 15%, which is acceptable for the further use of the SIF maps to analyze the status of the observed crops.

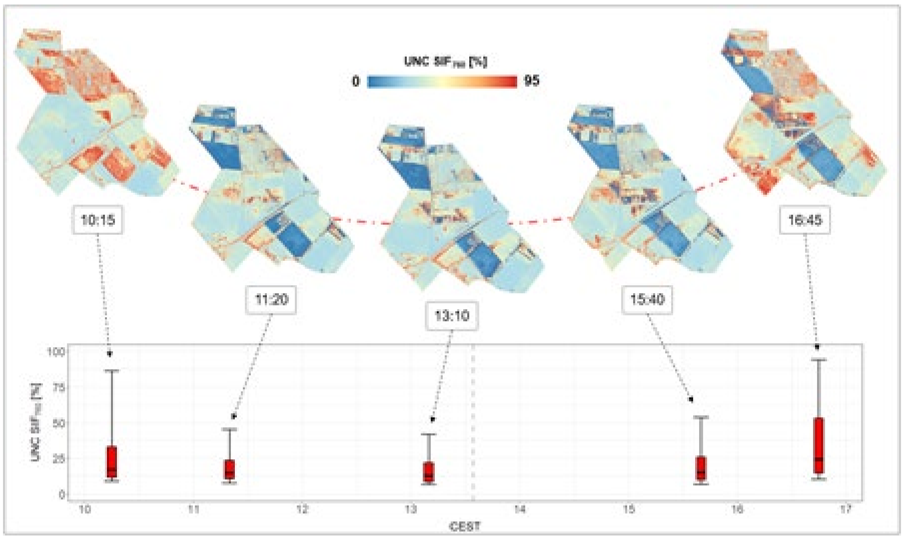

Figure 79 Spatial dynamics of the relative uncertainty of SIF_{760} in the course of the day. Maps showing the relative uncertainty of SIF_{760} of CKA acquired on 26 June 2019 (top) and corresponding boxplots showing median, 5th, 25th, 75th and 95th percentiles for the different overflights while only considering the pixels having an NDVI higher than 0.6 (bottom).

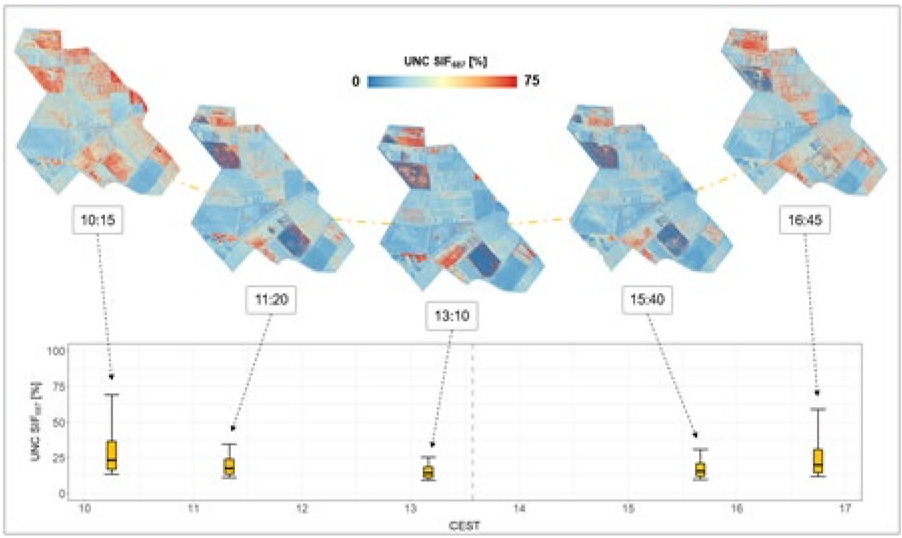

Figure 80 Spatial dynamics of the relative uncertainty of SIF_{687} in the course of the day. Maps showing the relative uncertainty of SIF_{687} of CKA acquired on June 26, 2019 (top) and corresponding boxplots showing median, 5th, 25th, 75th and 95th percentiles for the different overflights while only considering the pixels having an NDVI higher than 0.6 (bottom).

8.3.2 Understanding the influence of elevated atmospheric CO_2 concentrations on active and passive fluorescence

We have further evaluated the impact of elevated atmospheric CO_2 concentrations on the crop photosynthesis and its relation to active and passive fluorescence parameters. We have used the BreedFACE experiment at Campus Klein-Altendorf (Figure 81), which combines the experimental possibility to increase atmospheric CO_2 concentrations to the projected concentrations that we will experience in the year 2040 with the technical possibilities of automated, non-invasive plant phenotyping (Figure 72 and Figure 81)

Figure 81 The BreedFACE installation at Campus Klein-Altendorf. The pipes allow for a controlled release of CO_2 in the down-wind direction. Computer-controlled valves in combination with online CO_2 measurement in the center of each ring facilitates controlled atmospheric CO_2 enrichment over the entire vegetation area. Elevated CO_2 concentrations were controlled at 600 ppm in 2019, simulating future atmospheric CO_2 concentrations during this time of global change.

During the 2019 FlexSense campaign, two different crops were grown within the BreedFACE facility: winter wheat and the common bean. In winter wheat, we measured in parallel active fluorescence parameters with the LIFT instrument and a mobile FloX system, both of which were mounted on the automated sensor positioning platform FieldSnake (Figure 82). The combined use of an active and passive fluorescence measurement system allows for a detailed investigation of the effect of elevated CO_2 concentrations on various functional traits of photosynthetic light reaction. We could show that diurnally changing PAR is the main factor impacting the effective quantum efficiency of photosynthesis. As a second order effect elevated CO_2 concentrations decreased effective quantum efficiency in the wheat varieties, especially during afternoon hours. We currently interpret this as a stomatal related effect, where elevated CO_2 availability allows the plants to limit stomatal resistance. Analysis of the effect of elevated CO_2 on solar-induced fluorescence is still ongoing (Figure 83).

Figure 82 FieldSnake used to position sensors over the experimental plots of the BreedFACE facility at Campus Klein-Altendorf. On the FieldSnake, a FloX system was mounted next to an active analyzer of light-induced fluorescence transients (LIFT) (see Keller et al. 2019a, 2019b, 2021 for the LIFT system)

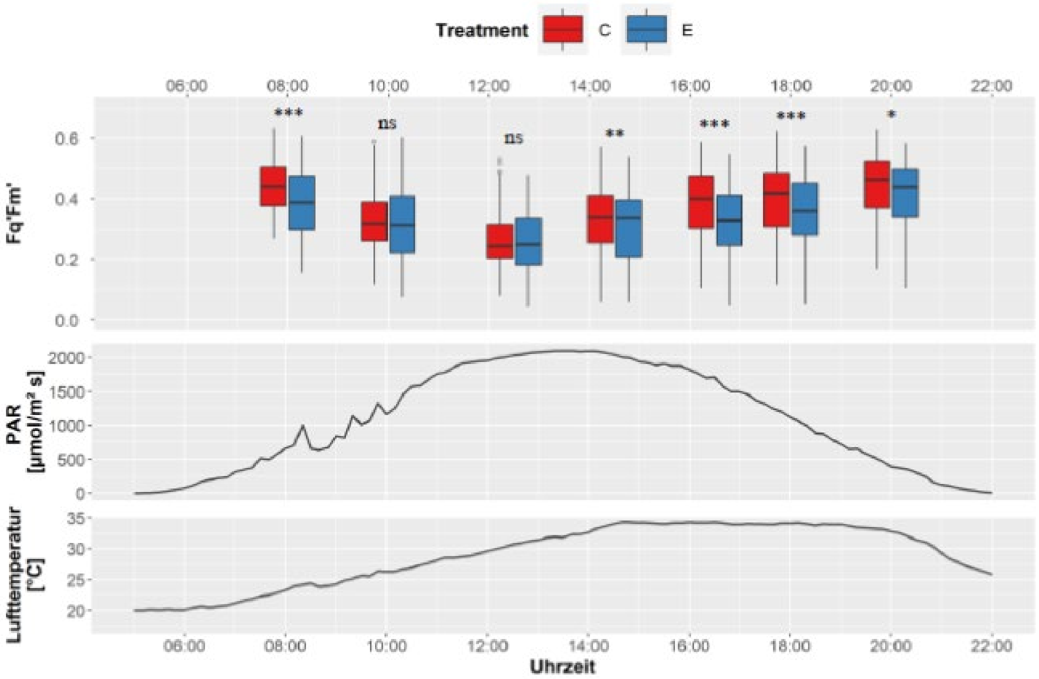

Figure 83[8] Diurnal course of effective quantum efficiency of photosynthesis (Fq'/Fm') in winter wheat measured with the active LIFT instrument and derived from fluorescence parameters. The first order effect of the diurnally changing PAR that reduces effective quantum efficiency is clearly visible. As second order effect, elevated atmospheric CO_2 concentrations resulted in a higher photosynthetic efficiency, especially during afternoon hours.

In the second study, we focused on the effect of different atmospheric CO_2 concentrations on three different bean varieties. We analyzed the response in yield, biomass and mineral content of three bean (*Phaseolus vulgaris* L.) genotypes grown in the BreedFACE experiment during the pod-filling phase. We analyzed diurnal active (quantum efficiency of photosystem II, F_v/F_m) and passive (solar-induced fluorescence) at the beginning and end of pod-filling. Destructive samples were collected for single leaves, stems, grains and pods. We also aimed at the comparison of LIFT, FloX and MoniPAM parameters, as well as the characterization of the FieldSnake, the automated platform used for LIFT and FloX measurements. The results show an overall increase in above ground biomass in the three genotypes (G1=36%, G2=41% and G3=24%). Moreover, the G1 genotype allocated 7% more biomass in the grains under elevated CO_2 concentrations, while the other two genotypes showed the same biomass partitioning observed at the ambient and elevated CO_2. We could also observe an earlier senescence at elevated CO_2, which was associated to plants with less leaf-chlorophyll content; however, leaf photosynthetic activity remained unchanged. We relate the higher biomass and yield at higher atmospheric CO_2 to the interaction of four factors: i) higher stomatal density compared with long term experiments, ii) measured higher photosynthetic efficiency, iii) later CO_2 acclimation, thus avoiding the photosynthesis downregulation effects, and iv) well balanced sink-source interaction, due to the presence of active sinks during the treatment (Quiros et al. 2021).

[8] The data used for this figure are currently being prepared for publication. They can be made available upon request.

8.4 Selhausen, Germany – Complementing a long-term time series of high-resolution data

The TR32 site is a highly instrumented long-term observation site that was established around 2006 by the German Science Foundation (DFG), the University of Cologne, the University of Bonn, and Forschungszentrum Jülich. Further information can be found at http://tr32new.uni-koeln.de/ and in Simmer et al. 2015 (Figure 84).

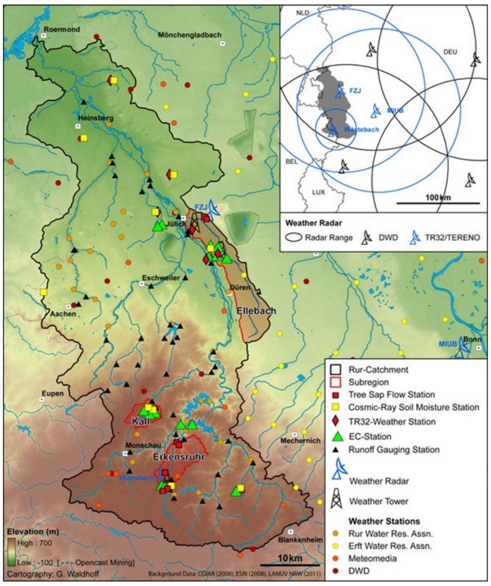

Figure 84 Overview of the Transregional Collaborative Research Centre 32 (TR32) intensive study site, which is equipped with an extraordinarily dense network of ground and atmospheric measurement systems. The site is a catchment and covers several vegetation areas.

The Selhausen agricultural research station is part of this large observation site. It consists of over 50 agricultural fields covering an area of about 1 km by 1 km and is representative in its composition of the heterogeneous rural area of the lower Rhine valley (the main crops are sugar beet, winter wheat, winter barley, maize and rapeseed) (Figure 86). This region belongs to the temperate maritime climate zone, with a mean annual temperature and precipitation of 10°C and 700 mm, respectively (SARSense report [RD-07]). Various ground measurements of SIF, EC and vegetation parameters are collected within numerous fields at this research station. Since 2012, we have used *HyPlant* sensor to map this intensively monitored site (approx. 15 km x 10 km).

We continued this time series in 2019 and recorded airborne data from this site using the established flight patterns (Figure 85). The 2019 data set complements existing data from previous years and these data have been distributed with other groups and are currently being used in various studies, which include:

- An analysis of the correlation between soil Plant Available Water (PAW) and solar-induced fluorescence (Quiros et al. in preparation)
- Use of these data (including 2018 FLEXSense data) to further develop the ARTMO emulator (in partnership with Jochem Verrelst of the University of Valencia)
- Further refinement and validation of SIF downscaling approach as published in Siegmann et al. (2021) using an extended data-set that includes different crop types

Flight patterns

Three flight patterns for data acquisition were flown in Selhausen (Figure 85) to record high-quality reference real-world data and to form the basis for testing and evaluating the level 2 retrievals. Because of the large extent of the TR-32 study site, the measured data can help us to better understand the SIF signal and correlate this signal to the photosynthetic performance of the plants. The flight pattern over Selhausen and the TR32 was particularly useful to expand on existing time series data from selected FLEX core sites in Germany.

- **Boresight calibration**: Four flight lines in 1-m resolution to derive boresight angles, weather conditions unimportant
- **Selhausen**: Four times mapping of all six flight lines in 1-m resolution, clear sky conditions and close to solar noon
- **TR32**: One-time mapping of all 18 flight lines in 3-m resolution, clear sky conditions and close to solar noon

Figure 85 Flight lines for Selhausen area: a) boresight calibration, b) Selhausen, and c) TR32 area.

Evaluation of data quality and qualitative description of the spatial patterns in the study region

Data from the Selhausen area cover an intensively managed agricultural area where several cash crops are grown on nutrient rich soils. A routine field rotation is used by the local farmers, resulting in an annually changing mosaic of different plant types that grow soils which are, in part, highly heterogeneous. Heterogeneity of the soil is caused by an ancient river bed, which still results in different soil types with greatly different water holding capacities in the upper and sub-soil layers.

This pronounced within and between field heterogeneity is used by some study groups to better understand the impact of soil heterogeneity on crop performance and local and regional energy and matter fluxes (Simmer et al. 2015, Brogi et al. 2019) (see also the visible spatial patterns in Figure 86). This natural phenomenon was used in the past to investigate the link of the SIF signal with soil water availability. We previously showed based on 2016 *HyPlant* data that SIF correlates closely with the water holding capacity of the local soils (von Hebel et al. 2018). In another study, we further investigated the 2016 data set of the study site to better understand the scale dependency of reflectance-based vegetation indices and SIF to map this small-scale heterogeneity of vegetation traits (Matveeva et al. submitted).

Figure 86 The agricultural field site Selhausen. 2019 land use map of the study site (left) and picture of the site from the Czech Globe aircraft taken during the campaign in 2019 (right). Note the distinct within field heterogeneity, which is caused by an ancient river bed that modulates local soil properties.

The quality of the 2019 data were tested within this activity and we calculated the full set of SIF products and reflectance-based vegetation indices using the current processing chain and SIF retrievals. Data were then spatially registered to check the pointing accuracy of the adjacent flight lines (Figure 87).

Based on our visual inspection, all data products are of high quality and no radiometric or geometric artifacts were detected in the flight lines. We, however, could see some striping in the SIF mosaics, which are caused by some off-set of the absolute values in the SIF retrievals (see two lower panels in Figure 87). These differences in absolute values between adjacent flight lines are most likely related to the selection of different non-vegetated reference pixels within the SIF retrievals. In the region, various non-vegetated surfaces are visible and the automated algorithm of the iFLD and SFM_{soil} may be sensitive to a biased selection of non-vegetated pixels.

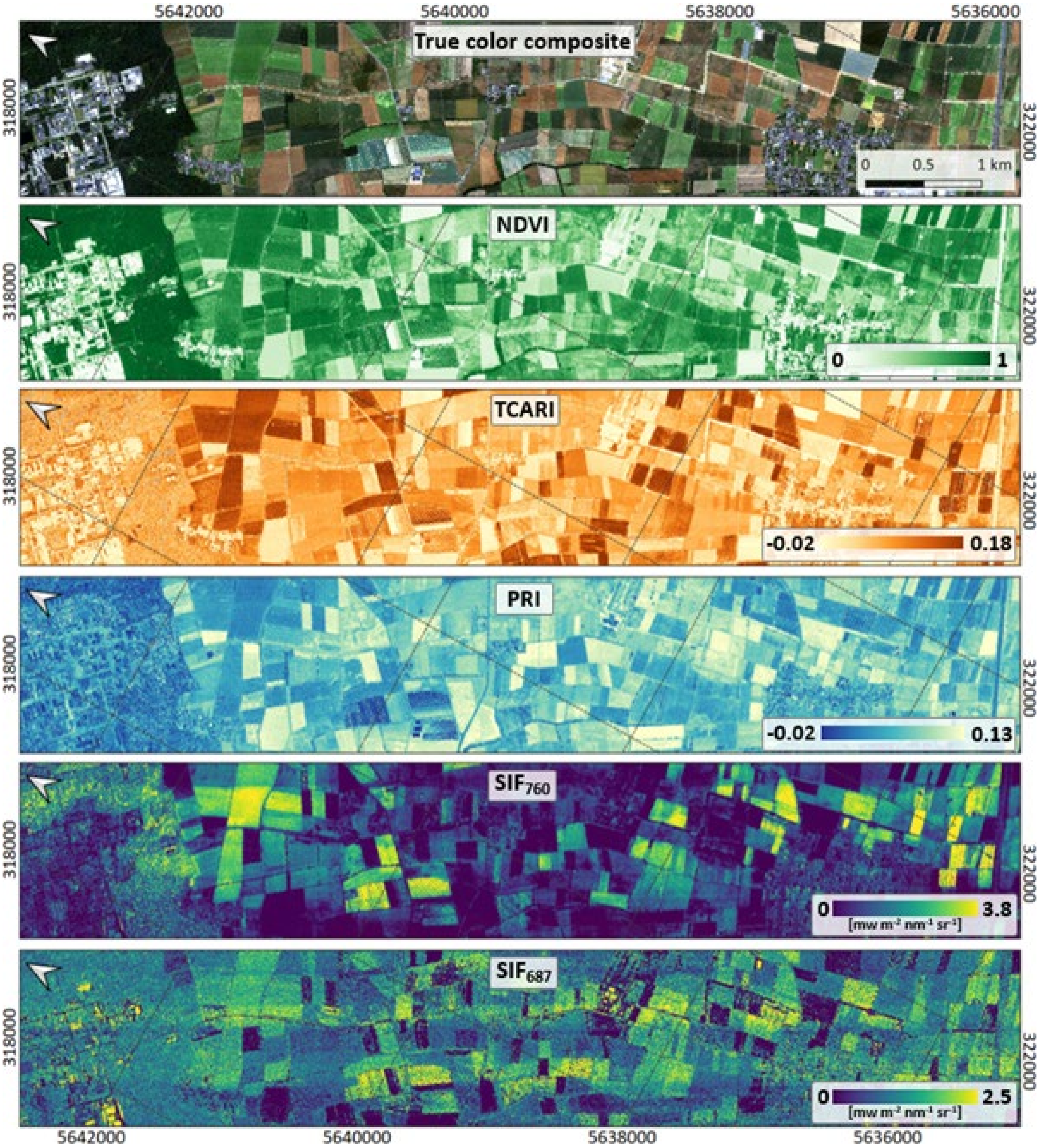

Figure 87 Mosaic of six *HyPlant* flight lines covering the Selhausen area on June 26, 2019 at midday. The different maps (from top to bottom) illustrate a true color composite and different vegetation indices, namely NDVI, TCARI and PRI, derived from *HyPlant* DUAL TOC reflectance data as well as the two SIF maps derived from *HyPlant* FLUO data at 760 and 687 nm using the SFM retrieval.

Analysis of environmental parameters from the EC station in Selhausen during the 2019 campaign activity

During the 2019 campaign, an Eddy Covariance (EC) tower measured carbon and energy fluxes in a potato field near Selhausen (Figure 13). In Figure 88, Latent Heat (LE), Sensible Heat (H) fluxes, Net Ecosystem Exchange (NEE) and Gross Primary Production (GPP) are shown for the growing season from April to September 2019. H and LE show no seasonal patterns. NEE shows a seasonal pattern, but with some outliers that are not visible in the GPP product. GPP shows low values from April to the beginning of June. Then, GPP values increase, reaching a maximum of 35 µmol m^{-2} s^{-1} during the summer from June to August. At the end of July, a distinct decrease in GPP can be seen for several days, followed by another increase, until the values start to continuously decrease from mid-August onwards. NEE values show an opposite trend to GPP values. They decrease until the end of July/beginning of August and then increase until the beginning of September, including a short increase in values at the end of July (Figure 88).

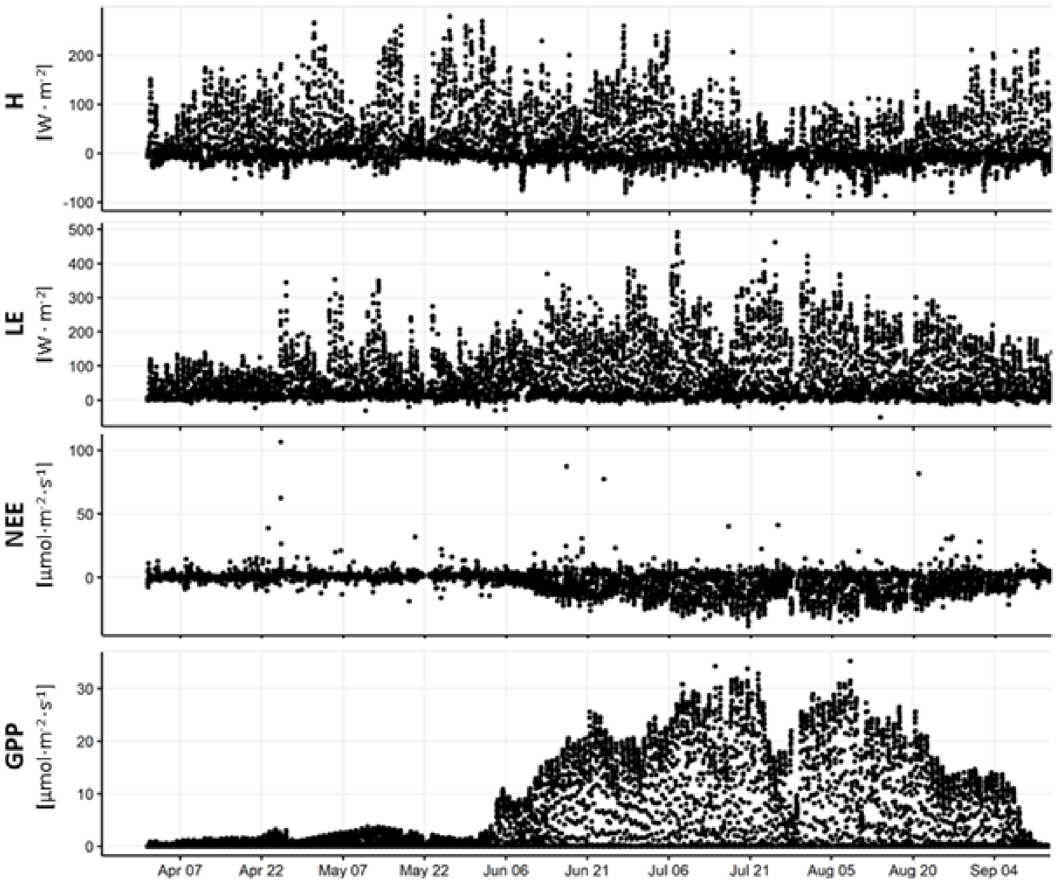

Figure 88 Carbon and energy fluxes from the EC tower which was positioned in 2019 in a potato field near Selhausen. Shown are Latent Heat (LE), Sensible Heat (H), Gross Primary Production (GPP) and Net Ecosystem Exchange (NEE) measured continuously from April to September 2019. GPP was calculated using the daytime method. Gap-filled data are shown if they met the quality standards.

In Figure 89, LE, H, GPP and NEE from potato plants are shown for the days of the *HyPlant* overpasses on June 26 and June 27, 2019 (Figure 89). Basically, all parameters follow a diurnal course. However, H values are higher on June 27 than on June 26, while for LE, the reverse is true. This difference is not visible for NEE or GPP. The sudden drop in GPP after noon on June 26, followed by a plateau, is not so clearly visible in the NEE values and not visible in LE and H at all. This pattern is not repeated on June 27.

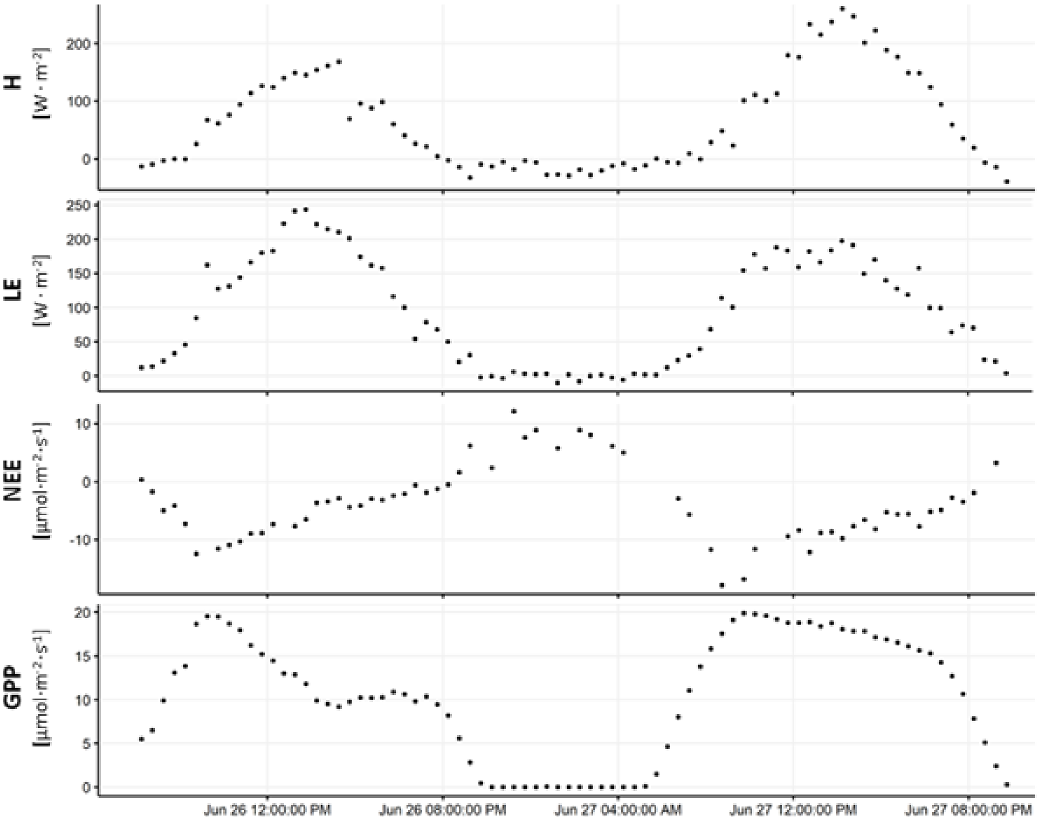

Figure 89 Carbon and energy fluxes from the EC tower which was positioned in 2019 in a potato field near Selhausen. Shown are Latent Heat (LE), Sensible Heat (H), Gross Primary Production (GPP) and Net Ecosystem Exchange (NEE) measured on June 26 and June 27, 2019. Half-hourly values of GPP are shown. GPP was calculated using the daytime method. Gap-filled data are shown if they met the quality standards.

Analysis of SIF and SIF uncertainty of different crops in Selhausen during the 2019 campaign activity

During the SARSense campaign [RD-07], the fields around the EC Tower in Selhausen were mapped to determine which crops were grown in the 2019 vegetation period. In Figure 90, a true colour composite of *HyPlant* DUAL recorded on June 26, 2019 and the corresponding land use map are shown.

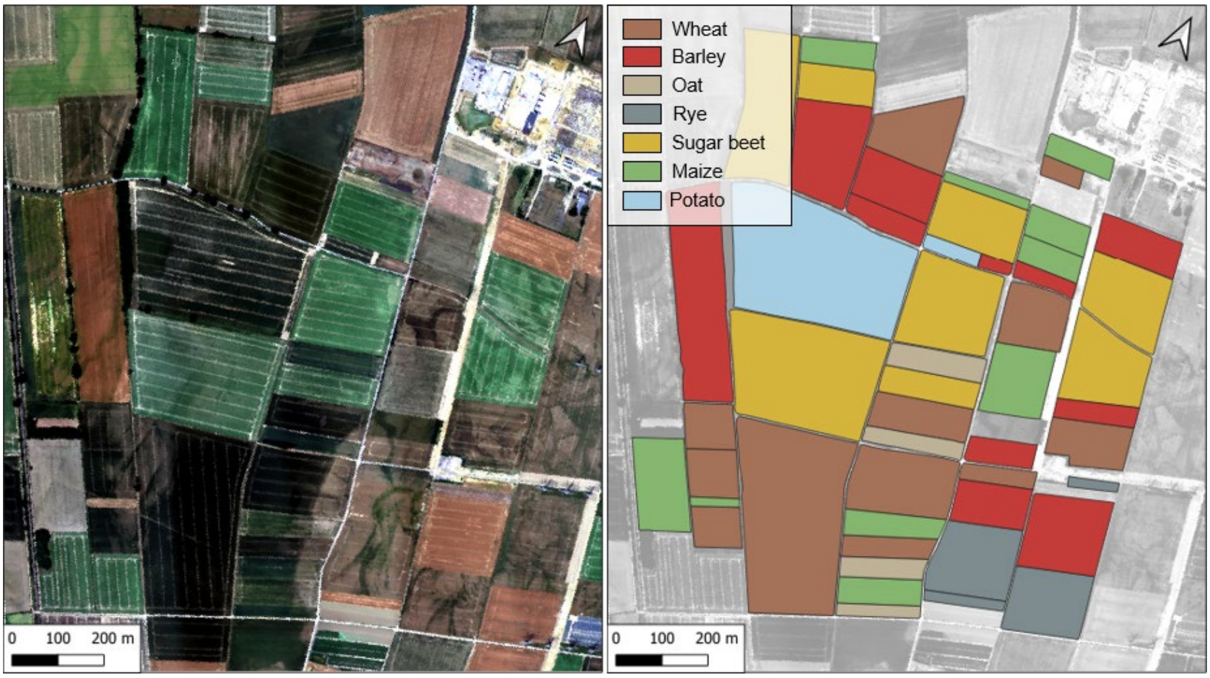

Figure 90 A subset of the agricultural field site Selhausen. *HyPlant* DUAL true colour composite recorded on June 26 (left) and corresponding land use map with the seven crop classes – namely wheat, barley, oat, rye, sugar beet, maize and potato (right).

Figure 91 illustrates the SIF_{760} and SIF_{687} maps and corresponding box plots for the different crop classes derived with the SFM retrieval. For SIF_{760}, the two crops sugar beet and potato provided the highest values, since these two crops are characterized by greenish, photosynthetically active and closed canopies. The cereal crops have distinctly lower values and especially barley and rye provide values close to zero, because they are already senescent and thus their chlorophyll content is very low. One exception is oat, which still seems to be photosynthetically active and therefore has a median value close to 2 mW $m^{-2}nm^{-1}sr^{-1}$. During this time of year, the maize plants are small and the fields have a vegetation cover lower than one. This is the reason why maize also has SIF_{760} values mainly lower than one. The SIF_{687} map looks different in comparison to the SIF_{760} map. Sugar beet and potato again have the highest values but also maize has a similar value (median =1.7 mW $m^{-2}nm^{-1}sr^{-1}$). This is surprising, since the maize canopy was characterized by a fractional cover lower than one, while sugar beet and potato had a closed canopy cover. One reason why SIF_{687} is not higher for sugar beet and potato could be related to the strong reabsorption of red SIF emitted from lower canopy layers by upper canopy layers. Similar to SIF_{760} for the cereal crops, lower SIF_{687} vales were determined, as oat again provided the highest values with a median of 1.2 mW $m^{-2}nm^{-1}sr^{-1}$.

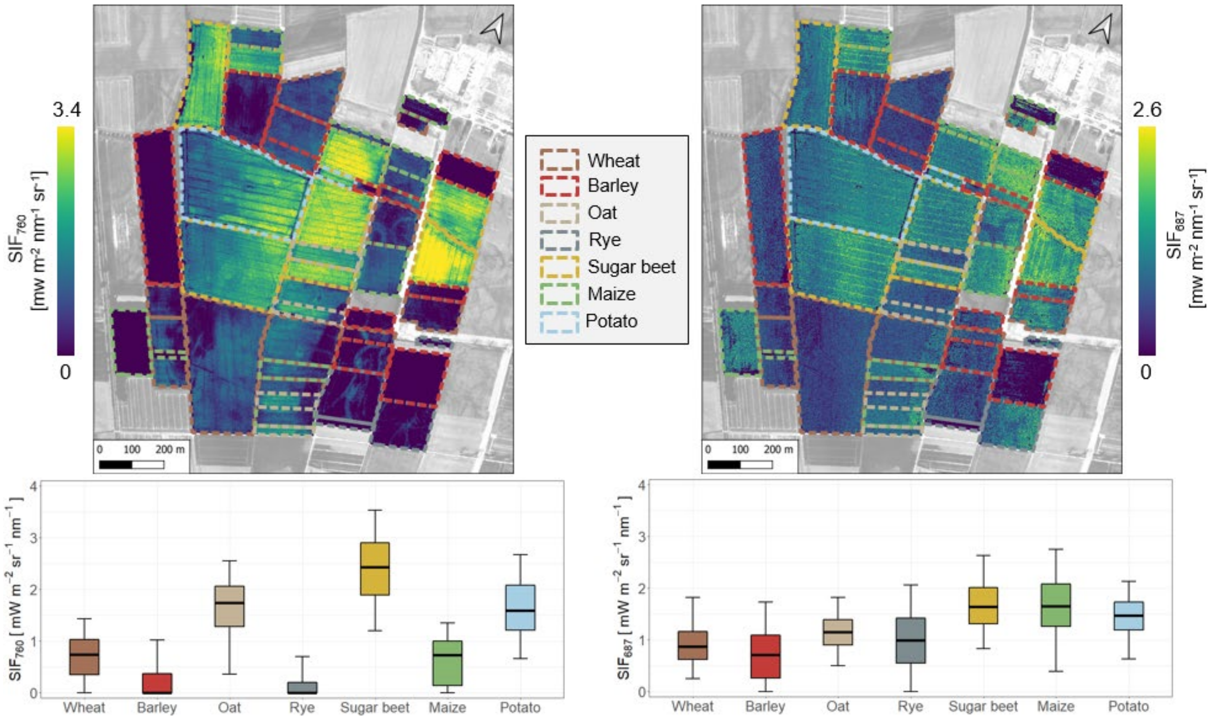

Figure 91 SIF_{760} (left) and SIF_{687} map (right) with corresponding box plots for the individual crop classes.

Figure 92 and Figure 93 show the absolute and relative uncertainties associated to the SIF_{760} and SIF_{687} maps presented in Figure 91. The absolute uncertainties for the different crop classes are in acceptable ranges of 0.1–0.2 mW $m^{-2}nm^{-1}sr^{-1}$ for SIF_{760} and 0.05–0.15 mW $m^{-2}nm^{-1}sr^{-1}$ for SIF_{687}, respectively. A general trend in the absolute uncertainties of both SIF products is that crop classes having higher absolute SIF values also have higher uncertainties. One exception is barley, which had low SIF_{687} values but a relatively high absolute uncertainty that is additionally characterized by a high variance. Once again, the late phenological stage of barley (already senescent) seemed to be problematic in the SIF retrieval. The relative uncertainties also show a similar trend for both SIF products. All crop classes that were greenish and photosynthetically active (oat, sugar beet, maize, potato) had distantly lower relative uncertainties (SIF_{760}: median = 15-20%, SIF_{687}: median = 10-19%). For all other crops that approached or were already senescent (barley, wheat, oat), the determined relative uncertainties were much higher. This underlines once again the difficulty of accurately retrieving SIF from plant canopies characterized by very low chlorophyll content.

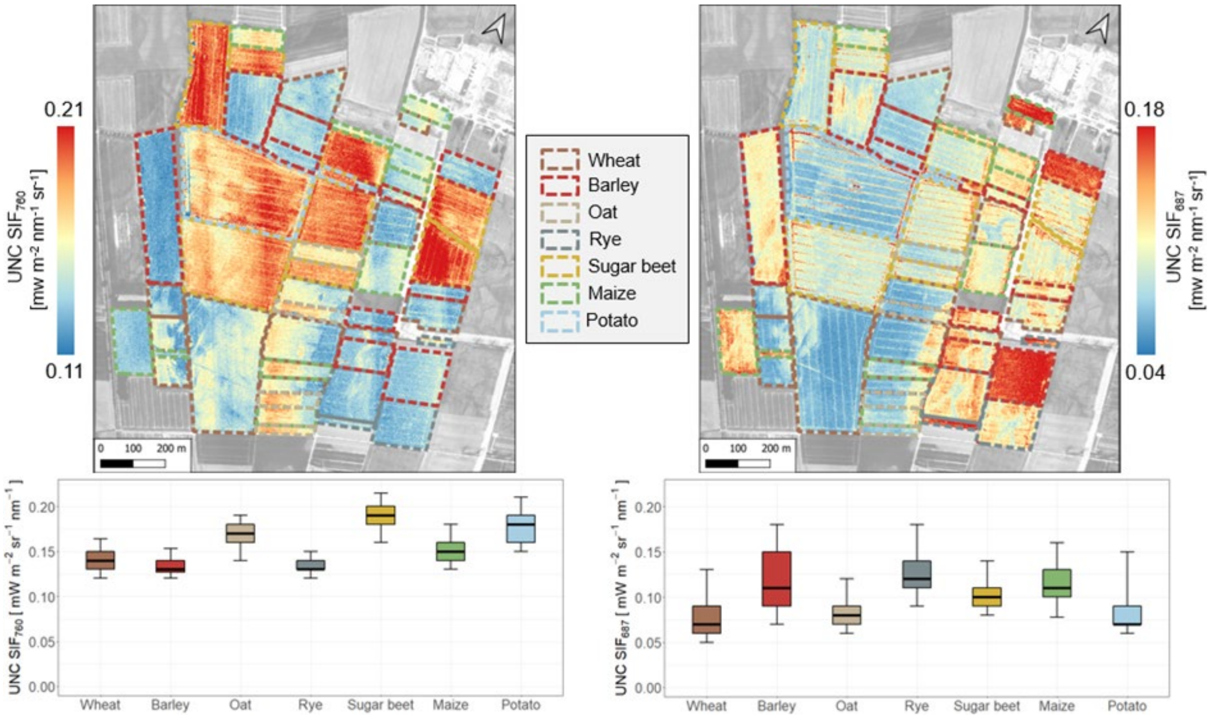

Figure 92 SIF_{760} (left) and SIF_{687} absolute uncertainty map (right) with corresponding box plots for the individual crop classes.

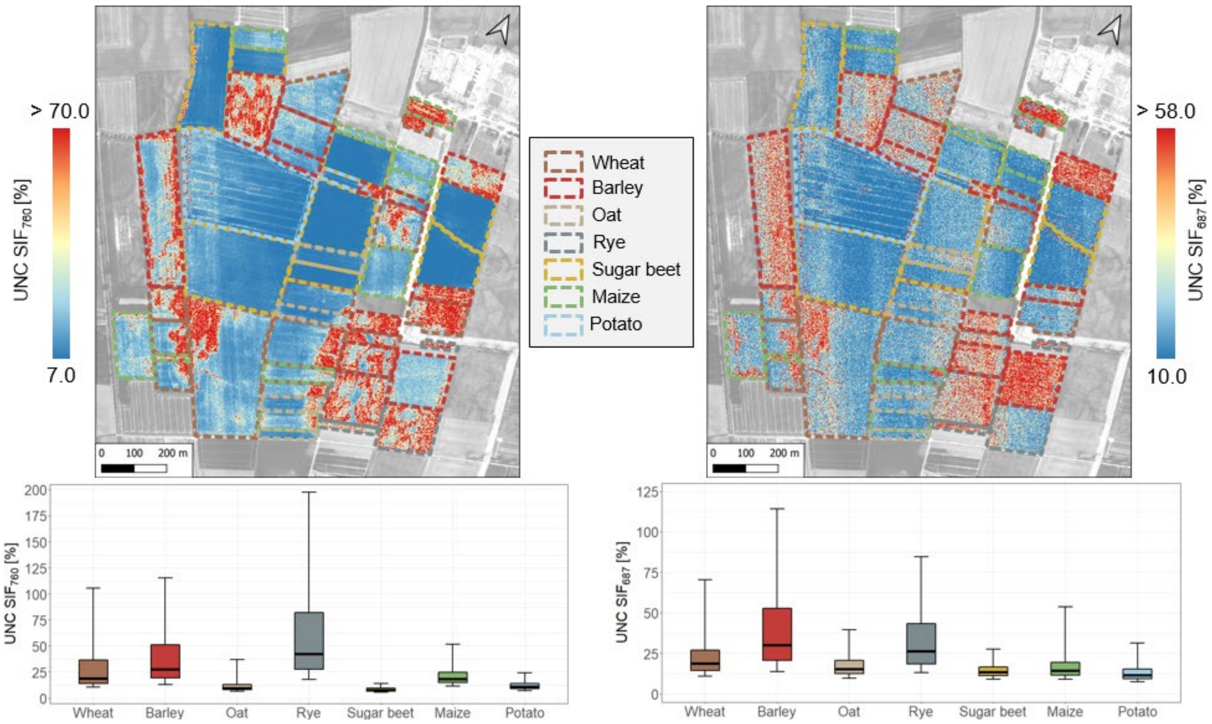

Figure 93 SIF_{760} (left) and SIF_{687} relative uncertainty map (right) with corresponding box plots for the individual crop classes.

9 SYNTHESIS OF 2019 CAMPAIGN DATA AND RECOMMENDATIONS FOR FUTURE ACTIVITIES

In the 2019 Fluorescence Explorer Sense (FLEXSense) campaign, we expanded upon the existing set of field data needed to prepare and implement the FLEX satellite mission. The 2019 data have extended a long-term time series of SIF and hyperspectral reflectance data from the Selhausen and Grosseto areas. They show quantitatively the potential use of SIF and vegetation reflectance for early drought detection, and also spotlight the potential for high-resolution spectral measurements to be used for detection of fire and fire plumes as well as plant biodiversity. Additionally, we are now in a position to deliver SIF values not only in absolute units, but have also made substantial steps towards the estimate of quantitative error and uncertainty in the data produced by the ground and airborne reference instruments FloX and *HyPlant*.

Extended *HyPlant* data with uncertainty layers (sections 5, 8.2.4 & 8.3.1): *HyPlant* data are now routinely delivered with the nominal retrieval methods of the FLEX satellite mission (spectral fitting method, SFM). Furthermore, *HyPlant* data are now produced with new data layers, which give relevant information on data quality. The two diurnal studies from Italy and Germany presented in sections 8.2.4 and 8.3.1 provided consistent results and emphasize the importance of quality flags (e.g., SNR) and uncertainties associated with SIF maps to help with the qualitative assessment of SIF products based on *HyPlant* data. This is an important step and will facilitate the selection of suitable, high-quality *HyPlant* SIF maps for use in further investigations.

We also re-visited *HyPlant's* calibration accuracy and we extensively tested two concepts for the use of SIF reference panels in the field and laboratory. While we were able to provide first estimates of the error and uncertainty associated with *HyPlant* and FloX SIF products, we still cannot provide full error budgets for SIF products along the whole processing chain, because of the complex mathematically non-linear handling of data during atmospheric correction and SIF retrieval. We recommend further evaluation of the existing data set in order to provide a mathematically stringent error and uncertainty budget for *HyPlant*. The calculation of a similar error and uncertainty budget will be attempted for the FloX system, future UAV-based SIF sensors, and other components that may be included in the FLEX Cal/Val concept.

We recommend the use of the new quality layers for HyPlant FLUO at-sensor radiance and the absolute and relative uncertainty associated with the SIF_{687} and SIF_{760} products. These new SIF-product quality metrics include error and uncertainty estimates in the final SIF products.

Evaluation of active and passive reference targets (section 6): The active and passive reference targets have been extensively tested, and both concepts proved valuable for FLEX Cal/Val activities. However, we also identified two technical shortcomings that need to be overcome before SIF reference panels can be used for FLEX Cal/Val activities: (i) the emission intensity and stability of the active LED panels need to be improved, and (ii) the degradation of the DYE passive panels due to light exposure needs to be better handled through improved chemical formulations and UV protectants. The reference panels in combination with ground-based and mobile FloX systems, UAV-based SIF sensors, and *HyPlant*-like airborne reference instruments could be used to develop a concise Cal/Val concept (Figure 42).

We recommend the technical further development of both reference target concepts and the construction of larger panels (20 x 20 meters), including their testing in the field.

Summarizing and integrating *HyPlant* and other uncertainties from the calibration to the fluorescence products (sections 3.1.1, 5.1, 5.3 & 6.4): Based on this activity, we were able to show that the error and uncertainty of *HyPlant* SIF products is in the range of the uncertainty margins for FLEX. The low error of *HyPlant* products is related to the use of non-vegetated reference pixels during SIF retrieval, which is possible with airborne data. We also identified opportunities for substantially improving *HyPlant* data quality – namely, the use of a better laboratory calibration facility, and the better parameterization of the atmospheric correction modules (primarily for the impact of air pressure and surface elevation on SIF retrieval). We could additionally show that an airborne SIF sensor like *HyPlant* plays a vital role in a Cal/Val scheme that contains ground-based FloX systems and mobile mapping of pixel heterogeneity.

We recommend taking advantage of all identified opportunities in a field campaign as part of activities to address the error and uncertainty of every element, including the overall accuracy of FLEX reference products.

Potential of SIF to detect early signs of drought stress (section 8.2.2): The data from the drought stress experiment are complete and can be used in combination with other scientific peer-reviewed studies to develop an 'early drought stress product' for the FLEX satellite mission. In our experimental test case, we demonstrated detection of the physiological effect of drought on photosynthesis several days before it could be derived from vegetation reflectance. This gives hope for a general 'early drought indicator' to be developed based on the existing campaign products.

We recommend the development of an 'early drought stress product' (L2D product) based on this campaign data that combines SIF data, canopy reflectance and canopy temperature (all available from the FLEX/Sentinel-3 tandem mission).

Potential to improve fire detection by exploiting high-resolution FLEX data (section 8.2.3): Spectrally high-resolution FLEX-like data (in this case *HyPlant* data) were shown to be capable of detecting the potassium absorption lines in flames and to monitor the height of smoke plumes on the basis of their 'apparent fluorescence' signal, which varies in line with their height above ground.

We recommend further exploration of the potential for using future FLEX products for fire detection and monitoring.

Potential to obtain novel and relevant information on plant biodiversity (section 8.2.1): SIF data that were collected over a wide range of Mediterranean shrub and tree species in the nursery suggest that fluorescence emission varies to great extent between species, thus presenting a potential additional source of information for biodiversity studies, but also a caveat for future FLEX applications in fragmented and/or highly diverse ecosystems.

We recommend further exploring how biodiversity will final affect fluorescence in FLEX mixed pixels.

10 REFERENCES

Abramowitz M. and Stegun I.A. (1964). Handbook of Mathematical Functions. Dover Publications, New York, 260.

Alonso L., Gómez-Chova L., Vila-Francés J., Amorós-López J., Guanter L., Calpe J., Moreno J. (2008). Improved Fraunhofer Line Discrimination method for vegetation fluorescence quantification. *IEEE Geosci. Remote Sens. Lett*., 5, 620–624.

Bandopadhyay S., Rastogi A., Rascher U., Rademske P., Schickling A., Cogliati S., Julitta T., Mac Arthur A., Hueni A., Tomelleri E., Celesti M., Burkart A., Stróżecki M., Sakowska K., Gąbka M., Rosadziński S., Sojka M., Iordache M.-D., Reusen I., Van Der Tol C., Damm A., Schuettemeyer D., Juszczak R. (2019). Hyplant-Derived Sun-Induced Fluorescence—A New Opportunity to Disentangle Complex Vegetation Signals from Diverse Vegetation Types. *Remote Sensing*, 11(14):1691.

Bandopadhyay S., Rastogi A., Cogliati S., Rascher U., Gabka M. and Juszczak R. (2021). Can spectral vegetation indices serve as proxies for potential Sun-Induced Fluorescence (SIF)? A fuzzy modelling approach on airborne imaging spectroscopy data. *Remote Sensing*, 13, article no. 2545.

Baret F., Morissette J.T., Fernandes R.A., Champeaux J.L., Myneni R.B., Chen J., Plummer S., Weiss M., Bacour C., Garrigues S., Nickeson J.E. (2006). Evaluation of the representativeness of networks of sites for the global validation and intercomparison of land biophysical products: proposition of the CEOS-BELMANIP. in *IEEE Transactions on Geoscience and Remote Sensing*, 44, no. 7, 1794-1803.

Beckers J. M., Rixen M. (2003). EOF calculations and data filling from incomplete oceanographic datasets*. J Atmos Ocean Technol*, 20(12), 1839–1856.

Berk A., Anderson G.P., Acharya P.K., Bernstein L.S., Muratov L., Lee J., Fox M., Adler-Golden S.M., Chetwynd J.H., Hoke M.L. et al. (2005). MODTRAN5: A reformulated atmospheric band model with auxiliary species and practical multiple scattering option. *Proc. Soc. Photo Opt. Instrum. Eng*., 5655, 662–667.

Buman B. Hueni A., Colombo R., Cogliati S., Celesti M., Julitta T., Burkhardt A., Siegmann B., Rascher U., Drusch M. & Damm A. (2022). Towards consistent uncertainty assessments of in situ radiometric measurements for the validation of fluorescence satellite missions. *Remote Sensing of Environment*, 247, 112984.

Burkart A., Cogliati S., Schickling A. & Rascher U. (2014). A novel UAV-based ultra-light weight spectrometer for field spectroscopy. *IEEE Sensor*s, 14, 62-67.

Burkart A., Schickling A., Cendrero Mateo M.P., Wrobel T., Rossini M., Cogliati S., Julitta T., Rascher U. (2015). A method for uncertainty assessment of passive sun-induced chlorophyll fluorescence retrieval by using an infrared reference light. *IEEE Sensors*. 15, 4603-4611.

Cendrero-Mateo M.P., Muller O., Albrecht H., Burkart A., Gatzke S., Janssen B., Keller B., Körber N., Kraska T., Matsubara S., Li J., Müller-Linow M., Pieruschka R., Pinto F., Rischbeck P., Schickling A., Steier A., Watt L.M., Schurr U. & Rascher U. (2016). Field phenotyping – concepts and examples to quantify dynamic plant traits across scales in the field*. Terrestrial ecosystem research infrastructures: challenges, new developments and perspectives*. Chabbi A., Löscher H. (eds.), CRC Press/Taylor & Francis.

Cogliati S., Verhoef W., Kraft S., Sabater N., Alonso L., Vicent J., Moreno J., Drusch M., & Colombo R. (2015). Retrieval of sun-induced fluorescence using advanced spectral fitting methods. *Remote Sensing of Environment*, 169, 344–357.

Cogliati S., Colombo R., Celesti M., Tagliabue G., Rascher U., Schickling A., Rademske P., Alonso L., Sabater N., Schüttemeyer D., Drusch M. (2018). Red and Far-Red Fluorescence Emission Retrieval from Airborne High-Resolution Spectra Collected by the Hyplant-Fluo Sensor." *IGARSS 2018 - 2018 IEEE International Geoscience and Remote Sensing Symposium*, 3935-3938.

Cogliati S., Celesti M., Cesana I., Miglietta F., Genesio L., Julitta T., Schüttemeyer D., Drusch M., Rascher U., Jurado P. and Colombo R. (2019). A spectral fitting algorithm to retrieve the fluorescence spectrum from canopy radiance. *Remote Sensing*, 11, article no. 1840.

Cogliati S., Sarti F., Chiarantini L., Cosi M., Lorusso R., Lopinto E., Miglietta F., Genesio L., Guanter L., Damm A., Pérez-López S, Scheffler D., Tagliabue G., Panigada C., Rascher U., Dowling T.P.F., Giardino C., Colombo R. (2021). The PRISMA imaging spectroscopy mission: overview and first performance analysis. *Remote Sensing of Environment*, 262, 112499, ISSN 0034-4257.

Colombo R., Celesti M., Bianchi R., Campbell P.K.E., Cogliati S., Cook B.D., Corp L.A., Damm A., Domec J.C., Guanter L., Julitta T., Middleton E.M., Noormets A., Panigada C., Pinto F., Rascher U., Rossini M., Schickling A. (2018). Variability of sun-induced chlorophyll fluorescence according to stand age-related processes in a managed loblolly pine forest. *Glob Chang Biol*., 24(7):2980-2996.

Damm A., Guanter L., Laurent V.E., Schaepman M.E., Schickling A., Rascher U. (2014). FLD-based retrieval of sun-induced chlorophyll fluorescence from medium spectral resolution airborne spectroscopy data. *Remote Sensing of Environment*, 147, 256–266.

Damm A., Guanter L., Verhoef W., Schläpfer D., Garbari S., Schaepman M.E. (2015). Impact of varying irradiance on vegetation indices and chlorophyll fluorescence derived from spectroscopy data. *Remote Sensing Environmen*t. 156, 202–215.

Damm A., Cogliati S., Colombo R., Fritsche L., Genangeli A., Genesio L., Hanus J., Peressotti A., Rademske P., Rascher U., Schuettemeyer D., Siegmann B., Sturm J. & Miglietta F. (2022). Response times of remote sensing measured sun-induced chlorophyll fluorescence, surface temperature and vegetation indices to evolving soil water limitation in a crop canopy. *Remote Sensing of Environment*, 273, 112957.

Desmons M., Wang P., Stammes P., and Tilstra L. G. (2019). FRESCO-B: a fast cloud retrieval algorithm using oxygen B-band measurements from GOME-2. *Atmos. Meas. Tech*., 12, 2485–2498.

Drusch M., Moreno J., Del Bello U., Franco R., Goulas Y., Hutz A., Kraft S., Middleton E.M., Miglietta F., Mohammed G., Nedbal L., Rascher U., Schüttemeyer D., Verhoef W. (2017). The FLuorescence EXplorer mission concept - ESA's Earth Explorer 8. *IEEE Transactions on Geoscience and Remote Sensing*, 55, 1273-1284.

Foken T., Göckede M., Mauder M., Mahrt L., Amiro B.D., Munger J.W. (2004). Post-field data quality control. In Handbook of micrometeorology: a guide for surface flux measurement and analysis (eds. X. Lee, W Massman, B Law), 181–208. Dordrecht, the Netherlands: Kluwer Academic Publishers.

Fu P., Li C., Xia Y., Ji Z., Sun Q., Cai W., & Feng D. D. (2014). Adaptive noise estimation from 687 highly textured hyperspectral images. *Applied Optics*, 53(30), 7059.

Gamon J.A., Somers B., Malenovsky Z., Middleton E., Rascher U. and Schaepman M. (2019). Assessing vegetation function with imaging spectroscopy. *Surveys in Geophysics*, 40, 489-513.

Gege P., Fries J., Haschberg P., Schötz P., Schwarzer H., Strobl P., Suhr B. Ulbrich G., Vreeling W.J. (2009). Calibration facility for airborne imaging spectrometers. *ISPRS Journal of Photogrammetry and Remote Sensing*, 64, 387-397.

Gerhards M., Schlerf M., Rascher U., Udelhoven T., Juszczak R., Alberti G., Miglietta F., and Inoue Y. (2018). Remote sensing of water stress symptoms based on airborne optical and thermal images. *Remote Sensing*, 10, article no. 1139.

Gillespie A. R., Rokugawa S., Matsunaga T., Cothern J.S., Hook S. and Kahle A.B. (1998). A Temperature and Emissivity Separation algorithm for Advanced Spaceborne Thermal Emission and Reflection radiometer ASTER images. *IEEE Transactions on Geoscience and Remote Sensing*, 36, 1113–1126.

Gorroño J., Banks A.C., Fox N.P., Underwood C. (2017). Radiometric inter-sensor cross-calibration uncertainty using a traceable high accuracy reference hyperspectral imager. *ISPRS Journal of Photogrammetry and Remote Sensing*, 130, 393-417.

Graf A. (2017). Gap-filling meteorological variables with Empirical Orthogonal Functions. EGU 2017 General Assembly, Vienna (Austria), 23 Apr 2017 - 28 Apr 2017, URL https://juser.fzjuelich.de/record/829701, [Accessed 25 January 2019].

Guanter L., Frankenberg C., Dudhia A., Lewis P.E., Gómez-Dans J., Kuze A., Suto H., Grainger G. (2012). Retrieval and global assessment of terrestrial chlorophyll fluorescence from GOSAT space measurement. *Remote Sensing Environment*, 121, 236–251.

Hornero A., North P.R.J., Zarco-Tejada P.J., Rascher U., Martíne M.P., Migliavacca M. and Hernández-Clemente R. (2021). Assessing the contribution of understory sun-induced chlorophyll fluorescence through 3-D radiative transfer modelling and field data. *Remote Sensing of Environment*, 253, article no. 112195.

Hueni A., Damm A., Kneubuehler M., Schläpfer D., and Schaepman M.E. (2017). Field and Airborne Spectroscopy Cross Validation—Some Considerations. IEEE JOURNAL OF SELECTED TOPICS IN APPLIED EARTH OBSERVATIONS AND REMOTE SENSING, 3, March 2017, 1117.

Jähne B. (2005). Digital Image Processing, 6th ed., Springer: Berlin/Heidelberg, Germany, 463–500.

Joiner J., Guanter L., Lindstrot C., Voigt M., Vasilkov A.P., Middleton E.M., Huemmrich K.F., Yoshida Y., Frankenberg C. (2013). Global monitoring of terrestrial chlorophyll fluorescence from moderate-spectral-resolution near-infrared satellite measurements: Methodology, simulations, and application to GOME-2. *Atmos. Meas. Tech.*, 6, 2803–2823.

Julitta T., Wutzler T., Rossini M., Colombo R., Cogliati S., Meroni M., Burkart A., Migliavacca M. (2017). An R Package for Field Spectroscopy: From System Characterization to Sun-Induced Chlorophyll Fluorescence Retrieval, poster presented on January 17 – 19, 2017 at the ESA workshop in ESRIN, Frascati (Rome), Italy.

Keller B.G., Vass I., Matsubara S., Paul K., Jedmowski C., Pieruschka R., Nedbal L., Rascher U. & Muller O. (2019a) Maximum fluorescence and electron transport kinetics determined by light induced fluorescence transients (LIFT) for photosynthesis phenotyping. *Photosynthesis Research, 140*, 221-233.

Keller B., Matsubara S., Rascher U., Pieruschka R., Steier A., Kraska T. & Muller O. (2019b) Genotype specific photosynthesis × environment interactions captured by automated fluorescence canopy scans over two fluctuating growing seasons. *Frontiers in Plant Science, 10*, article no. 1482.

Keller B., Zimmermann L., Rascher U., Matsubara S., Steier A. & Muller O. (2021). How efficient do crop genotypes convert sunlight into photosynthesis and biomass under fluctuating conditions? *Plant Physiology*, online first.

Kirchgessner N., Liebisch F, Yu K., Pfeifer J., Friedli M., Hund A. and Walter A. (2016). The ETH field phenotyping platform FIP: A cable-suspended multi-sensor system. *Functional Plant Biology, 44*, 154-168.

Kneer C., Burkard A., Bongartz J., Siegmann B. & Rascher U. (*in preparation*) A snapshot imaging system for the measurement of solar-induced chlorophyll fluorescence – addressing the challenges of high-performance spectral imaging for mapping SIF. *IEEE – sensors*.

Lasslop G., Reichstein M., Papale D., Richardson A.D., Arneth A., Barr A., Stoy P. & Wohlfahrt G. (2010). Separation of net ecosystem exchange into assimilation and respiration using a light response curve approach: critical issues and global evaluation. *Global Change Biology*, 16(1), 187–208.

Li C.R., Tang L.L., Ma L.L., Zhou Y.S., Gao C.X., Wang N., Li X.H., Wang X.H., and Zhu X.H. (2015). Comprehensive calibration and validation site for information remote sensing. *ISPRS archives*, XL-7/W3, 1233-1240

Lichtenthaler H. K. (1987). Chlorophylls and carotenoids – pigments of photosynthetic biomembranes. In Methods in Enzymology Eds SP Colowick and NO Kaplan, 350-382. (Academic Press: Sydney).

Lichtenthaler H. K. and Buschmann C. (2001). Current protocols in Food and Analytical Chemistry. F4.3.8-F4.2.4.

Liu X., Guanter L., Liu L., Damm A., Malenovsky Z., Rascher U., Peng. D., Du S., Gastellu-Etchegorry J.-P. (2019). Downscaling of solar-induced chlorophyll fluorescence from canopy level to photosystem level using a random forest model. *Remote Sensing of Environment*, 231, 110772.

Matveeva M., Krieger V., Emin D., Rademske P., Siegmann B., Matveev D., Damm A., Simmer C., van der Tol C., Waldhoff G., Bareth G. & Rascher U. Correlation between solar-induced chlorophyll fluorescence (SIF), NIRv and EVI − a question of scale and plant functional type. *Remote Sensing*, submitted 7. Dec 2021.

Middleton E.M., Rascher U., Corp L.A., Huemmrich K.F., Cook B.D., Noormets A., Schickling A., Pinto F., Alonso L., Damm A., Guanter L., Colombo R., Campbell P.K.E., Landis D.R., Zhang Q., Rossini M., Schuettemeyer D., Bianchi R. (2017). The 2013 FLEX—US Airborne Campaign at the Parker Tract Loblolly Pine Plantation in North Carolina, USA. *Remote Sensing*, 9(6):612.

Mihai L., Mac Arthur A., Hueni A., Robinson I., Sporea D. (2018). Optimized Spectrometers Characterization Procedure for Near Ground Support of ESA FLEX Observations: Part 1 Spectral Calibration and Characterisation. *Remote Sensing, 10*, article no. 289, doi: 10.3390/rs10020289.

Milton E.J., Shaepman M.E., Anderson K., Kneubühler M., Fox N. (2009). Progress in field spectroscopy. *Remote Sensing of Environment*, 113, Supplemenent 1, S92 – S109.

Origo N., Gorroño J., Ryder J., Nightingale J., Bialek A. (2020). Fiducial Reference Measurements for validation of Sentinel-2 and Proba-V surface reflectance products. *Remote Sensing of Environment*, 241, 111690.

Paynter I., Cook B., Corp L., Nagol J., McCorkel J. (2020). Characterization of FIREFLY, an Imaging Spectrometer Designed for Remote Sensing of Solar Induced Fluorescence. *Sensors*, *20*, 4682.

Pinto F., Damm A., Schickling A., Panigada C., Cogliati S., Müller-Linow M., Balvora A. and Rascher U., (2016). Sun-induced chlorophyll fluorescence from high-resolution imaging spectroscopy data to quantify spatio-temporal patterns of photosynthetic function in crop canopies. *Plant, cell & environment*, 39(7), 1500-1512.

Pinto F., Celesti M., Acebron K., Alberti G., Cogliati S., Colombo R., Juszczak R., Matsubara S., Miglietta F., Palombo A., Panigada C, Pignatti S, Rossini M., Sakowska K., Schickling A., Schüttemeyer D., Stróżecki M., Tudoroiu M. & Rascher U. (2020). Dynamics of sun-induced chlorophyll fluorescence and reflectance to detect stress-induced variations in canopy photosynthesis. *Plant, Cell & Environment*, 43, 1637-1654.

Porcar-Castell A., Malenovský Z., Magney T., Van Wittenberghe S., Fernández-Marín B., Maignan F., Zhang Y., Maseyk K., Atherton J., Albert L.P., Robson T.M., Zhao F., Garcia-Plazaola J.-I., Ensminger I., Rajewicz P.A., Grebe S., Tikkanen M., Kellner J.R., Ihalainen J.A., Rascher U. & Logan B. (2021). Chlorophyll a fluorescence illuminates a path connecting plant molecular biology to Earth-system science. *Nature Plants*, 7, 998-1009.

Povey A.C. and Grainger R.G. (2015) Known and unknown unknowns: uncertainty estimation in satellite remote sensing, *Atmos. Meas. Tech*., 8, 4699–4718, https://doi.org/10.5194/amt-8-4699-2015.

Quirós-Vargas J., Bendig J., Mac Arthur A., Burkart A., Julitta T., Maseyk K., Thomas R., Siegmann B., Rossini M., Celesti M., Schüttemeyer D., Kraska T., Muller O. and Rascher U. (2020). Unmanned Aerial Systems (UAS)-based methods for Solar Induced Chlorophyll Fluorescence (SIF) retrieval with non-imaging spectrometers: State of the art. *Remote Sensing*, 12, article no. 1624.

Quirós-Vargas J., Caldeira R.D., dos Santos N.Z., Zimmermann L., Siegmann B., Kraska T., Vasconcelos, M.W., Rascher U. & Muller O. (2021). Response of bean (Phaseolus vulgaris L.) to elevated [CO_2] in yield, biomass and chlorophyll fluorescence. *IGARSS 2021*, 5861-5864.

Raesch A., Muller O., Pieruschka R. & Rascher U. (2014). Field Observations with Laser-Induced Fluorescence Transient (LIFT) Method in Barley and Sugar Beet. *Agriculture*, 4, 159-169.

Rascher U., Alonso L., Burkhart A., Cilia A., Cogliati S., Colombo R., Damm A., Drusch M., Guanter L., Hanus J., et al. (2015). Sun-induced fluorescence—A new probe of photosynthesis: First maps from the imaging spectrometer *HyPlant*. *Global Change Biology*, 21, 4673–4684, doi: 10.1111/gcb.13017.

R Core Team (2017). R: A Language and Environment for Statistical Computing. https://www.R-project.org/

REddyProc Team (2014). REddyProc: Data processing and plotting utilities of (half-) hourly eddy covariance measurements. R package version 1.1.3.

https://www.bgcjena.mpg.de/bgi/index.php/Services/REddyProcWebRPackage [Accessed 25 January 2019].

Richter R. (1998). Correction of satellite imagery over mountainous terrain. *Applied Optics*, 37, Issue 18, 4004-4015.

Rossini M., Nedbal L., Guanter L., Ač A., Alonso L., Burkart A., Cogliati, S., Colombo R., Damm A., Drusch M., Hanus J., Janoutova R., Julitta T., Kokkalis P., Moreno J., Novotny J., Panigada C., Pinto F., Schickling A., Schüttemeyer D., Zemek F., and Rascher U. (2015). Red and far red Sun-induced chlorophyll fluorescence as a measure of plant photosynthesis. *Geophysical Research Letters*, 42, 1632-1639.

Sabater N., Vicent, J., Alonso, L., Verrelst J., Middleton E.M., Porcar-Castell A., Moreno J. (2018). Compensation of Oxygen Transmittance Effects for Proximal Sensing Retrieval of Canopy–Leaving Sun–Induced Chlorophyll Fluorescence. *Remote Sensing*, 10, 1551.

Scharr H., Rademske P., Alonso L., Cogliati S. & Rascher U. (2021). Spatio-spectral deconvolution for high resolution spectral imaging with an application to the estimation of sun-induced fluorescence. *Remote Sensing of Environment*, 267, 112718.

Scholander P.F., Hammel H.T., Bradstreet E.D., & Hemmingsen E.A. (1965). Sap Pressure In Vascular Plants – Negative Hydrostatic Pressure Can Be Measured In Plants. *Science*, 148, 339

Siegmann B., Alonso L., Celesti M., Cogliati S., Colombo R., Damm A., Douglas S., Guanter L., Hanuš J., Kataja K., Kraska T., Matveeva M., Moreno J., Muller O., Pikl M., Pinto F., Quirós Vargas J., Rademsk P., Rodriguez-Morene F., Sabater N., Schickling A., Schüttemeyer D., Zemek F. and Rascher U. (2019). The high-performance airborne imaging spectrometer *HyPlant* – From raw images to top-of-canopy reflectance and fluorescence products: Introduction of an automatized processing chain. *Remote Sensing*, 11, article no. 2760.

Siegmann B., Cendrero-Mateo M.P., Cogliati S., Damm A., Gamon J., Herrera D., Jedmowski C., Junker-Frohn L.V., Kraska T., Muller O., Rademske P., van der Tol C., Quiros-Vargas J., Yang P. and Rascher U. (2021). Downscaling of far-red solar-induced chlorophyll fluorescence of different crops from canopy to leaf level using a diurnal data set acquired by the airborne imaging spectrometer HyPlant. *Remote Sensing of Environment*, 264, 112609.

Simmer C., Thiele-Eich I., Masbou M., Amelung W., Crewell S., Diekkrueger B., Ewert F., Hendricks Franssen H.-J., Huisman A. J., Kemna A., Klitzsch N., Kollet S., Langensiepen M., Loehnert U., Rahman M., Rascher U., Schneider K., Schween J., Shao Y., Shrestha P., Stiebler M., Sulis M., Vanderborght J., Vereecken H., van der Kruk J., Zerenner T., and Waldhoff G. (2015). Monitoring and Modeling the Terrestrial System from Pores to Catchments - the Transregional Collaborative Research Center on Patterns in the Soil-Vegetation-Atmosphere System. *Bulletin of the American Meteorological Society*, 96, 1765–1787.

Tagliabue G., Panigada C., Dechant B., Baret F., Cogliati S., Colombo R., Migliavacca M., Rademske P., Schickling A., Schüttemeyer D., Verrelst J., Rascher U., Ryu Y. and Rossini M. (2019). Exploring the spatial relationship between airborne-derived red and far-red sun-induced fluorescence and process-based GPP estimates in a forest ecosystem. *Remote Sensing of Environment*, 231, article no. 111272.

Tagliabue G., Panigada C., Celesti M., Cogliati S., Colombo R., Migliavacca M., Rascher U., Rocchini D., Schüttemeyer D. and Rossini M. (2020). Sun-induced fluorescence heterogeneity as a measure of functional diversity. *Remote Sensing of Environment*, 247, article no. 111934.

Turner, N.C., and Long, M.J. (1980). Errors arigin from rapid water-loss in the measurement of leaf water potential by the pressure chamber technique. *Australian Journal of Plant Physiology*, 7, 527-537

Verhoef W., Bach H. (2003). Remote sensing data assimilation using coupled radiative transfer model. *Phys. Chem. Earth*, 28, 3–13.

Verhoef W., Bach H. (2003a). Simulation of hyperspectral and directional radiance images using coupled biophysical and atmospheric radiative transfer model. *Remote Sensing of Environment*, 87, 23–41.

Verhoef W., Bach H. (2007). Coupled soil-leaf-canopy and atmosphere radiative transfer modeling to simulate hyperspectral multi-angular surface reflectance and TOA radiance data. *Remote Sensing of Environment*, 109, 166–182.

Verhoef W., Bach H. (2012). Simulation of Sentinel-3 images by four-stream surface–atmosphere radiative transfer modeling in the optical and thermal domains. *Remote Sensing of Environment*, 120, 197-207, ISSN 0034-4257.

Verhoef W., van der Tol C., Middleton E.M. (2018). Hyperspectral radiative transfer modeling to explore the combined retrieval of biophysical parameters and canopy fluorescence from FLEX—Sentinel-3 tandem mission multi-sensor data. *Remote Sensing of Environment*, 204, 942–963.

Vila-Guerau de Arellan J., Ney P., Hartogensis O., deBoer H., van Diepen K., Emin D., de Groot G., Klosterhalfen A., Langensiepen M., Matveeva M., Miranda-García G., Moene A.F., Rascher U., Röckmann T., Adnew G., Brüggemann N., Rothfuss Y., Graf A. (2020). CloudRoots: integration of advanced instrumental techniques and process modelling of sub-hourly and sub-kilometre land-atmosphere interactions. *Biogeosciences*, 17, 4375-4404.

von Hebel C., Matveeva M., Verweij E., Rademske P., Kaufmann M.S., Brogi C., Vereecken H., Rascher U., van der Kruk J. (2018). Understanding soil and plant interaction by combining ground-based quantitative electromagnetic induction and airborne hyperspectral data. *Geophysical Research Letters*, 45, 7571 – 7579.

Wang P., Stammes P., van der A R., Pinardi G., and van Roozendael M. (2008). FRESCO+: an improved O2 Aband cloud retrieval algorithm for tropospheric trace gas retrievals, *Atmos. Chem. Phys.*, 8, 6565–6576.

Wieneke S., Ahrends H., Damm A., Pinto F., Stadler A., Rossini M. and Rascher U. (2016). Airborne based spectroscopy of red and far-red sun-induced chlorophyll fluorescence: Implications for improved estimates of gross primary productivity. *Remote Sensing of Environment*, 184, 654-667.

Yang P., van der Tol C., Verhoef W., Damm A., Schickling A., Kraska T., Muller O. and Rascher U. (2019). Response of crops to a heat wave: Insights from airborne based reflectance and chlorophyll fluorescence measurement. *Remote Sensing of Environment*, 231, article no. 110996.

Zendonadi dos Santos, N., Piepho, H.-P., Condorelli, G. E., Licieri Groli, E., Newcomb, M., Ward, R., Tuberosa, R., Maccaferri, M., Fiorani, F., Rascher, U., & Muller, O. (2021). High-throughput field phenotyping reveals genetic variation in photosynthetic traits in durum wheat under drought. *Plant, Cell & Environment*, 44(9), 2858– 2878.

Zeng Y, Hao D., Badgley G., Damm A., Rascher U., Ryu Y., Johnson J., Krieger V., Wu S., Qiu H., Liu Y., Berry J.A. and Chen M. (2021) Estimating near-infrared reflectance of vegetation from hyperspectral data. *Remote Sensing of Environment*, 267, article no. 112723.

11 DATA STORAGE

Since a large number of measurements and datasets were collected at the different test sites within the campaign period, we set up a hierarchical data structure consisting of different levels to organize the information in a clearly arranged manner. This makes it possible to get an overview of the entire data collected during the campaign and helps to quickly find specific data sets of interest.

In the following, the data storage structure is explained in detail.

The entire data storage structure consists of six levels:

- Level 1 – Campaign
- Level 2 – Country/test site
- Level 3 – Type of data (scale)
- Level 4 – Acquisition date
- Level 5 – Type of device
- Level 6 – Acquired data

Level 1 only consist of the campaign name “2019_FLEXSense”. This allows the data storage structure to be expanded for future campaigns. In Level 2, the different test sites/countries where data was recorded during the campaign are introduced. Moreover, two folders containing the finalized reports and the details on each campaign meeting are created.

- 01_Italy_Grosseto
- 02_Germany_CKA
- 03_Germany_Selhausen
- 98_Reports
- 99_Meetings

In Level 3, each test site is further subdivided into the type of data. In this case, this refers to the different spatial scales of data recording.

- 01_Field_data
- 02_Airborne_data

Field data includes all data acquired directly on the ground (e.g. measured plant traits and measurements of soil moisture) or acquired in closer proximity to the ground (e.g. tower measurements). Airborne data includes all acquired data taken by sensors on the airplane.

In Level 4, the measurements dates on which data were collected with a specific device are listed. Furthermore, in Level 5, the different measurement devices that were used to collect data from the different scales are listed. Subsequently, in Level 6 the measurement devices from Level 5 are further subdivided into products (the location of real data products). Figure 94 provides an overview of the measurement dates and the measurement devices that were used in Germany at the Selhausen test site.

Level 4	Level 5	Level 6
Acquisition date	Type of device	Acquired data
• **20190626** • 20190627	• **01_HyPlant_DUAL** • 02_HyPlant_FLUO • 03_TASI • 04_LIDAR	• 01_TOC_Reflectance • 02_Indices

Figure 94 Levels 4 to 6 of the 2019_FLEXSense data storage for the Selhausen test site based on the example of the *HyPlant* Dual device.

12 APPENDIX

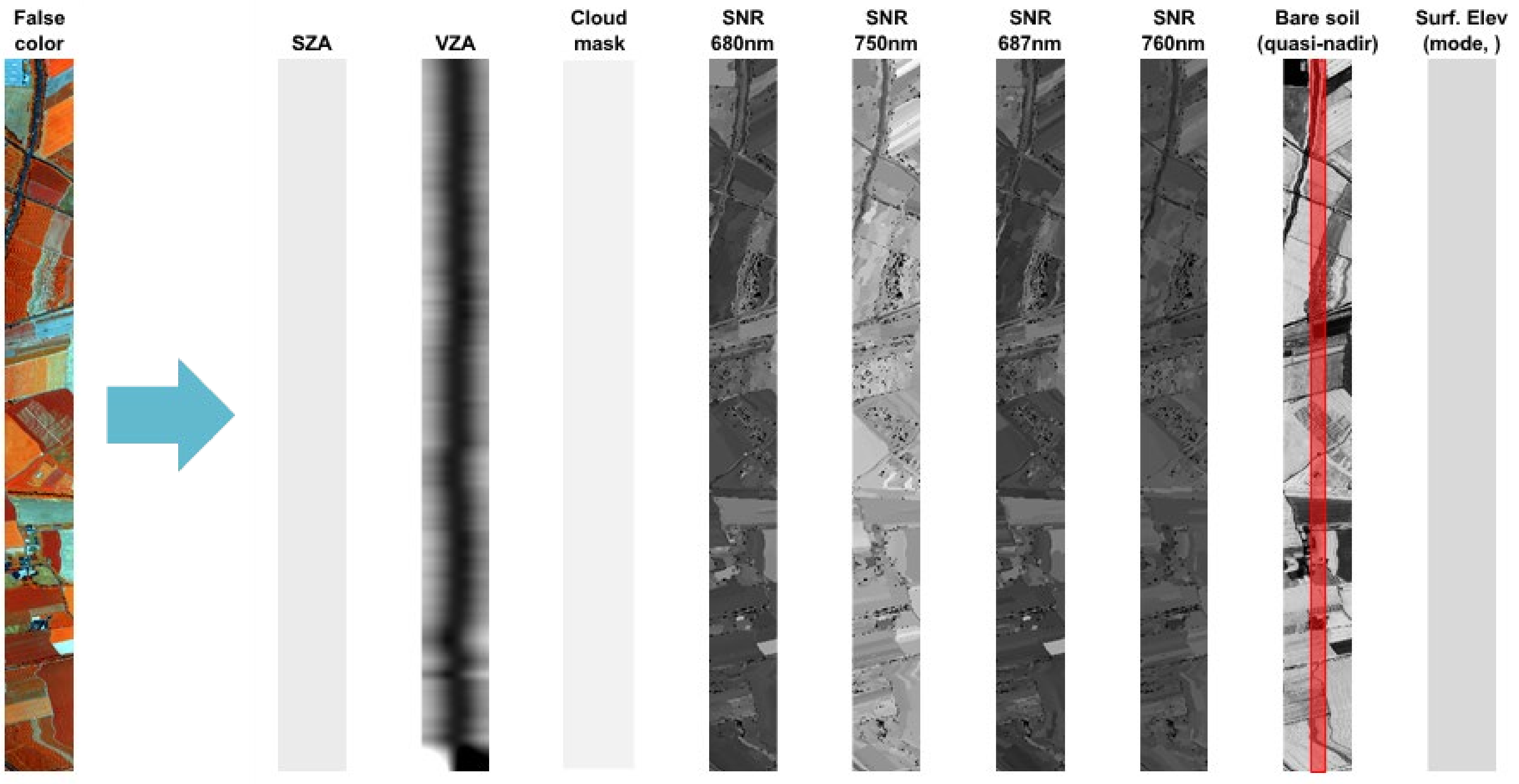

Figure 95 Quality flags derived from *HyPlant* FLUO at-sensor radiance (example from image 20190626-CKA-1313-600-L2-S-FLUO_radiance).

13 SCIENTIFIC PUBLICATIONS THAT RESULTED FROM THIS CAMPAIGN

13.1 PUBLICATION I: DAMM ET AL. (2022) - RESPONSE TIMES OF REMOTE SENSING INDICES

Citation of this publication

Damm A., Cogliati S., Colombo R., Fritsche L., Genangeli A., Genesio L., Hanus J., Peressotti A., Rademske P., Rascher U., Schuettemeyer D., Siegman B., Sturm J., Miglietta F. (2022). Response times of remote sensing measured sun-induced chlorophyll fluorescence, surface temperature and vegetation indices to evolving soil water limitation in a crop canopy. *Remote Sensing of Environment*, 273, 11957.

Link to this campaign activities

Data from this publication were acquired and analysed during this FlexSense campaign and integrated in this report in chapter 8.2.2. The drought experiment was carefully analyzed in the course of this campaign and all of our results and an extended scientific discussion can be found in this publication. This publication investigates the sensitivity of SIF_{687}, SIF_{760}, LST, photochemical reflectance index (PRI), Meris terrestrial chlorophyll index (MTCI), and the water band index (WBI) for increasing water limitation and shows that the combination of different measurement modes (including SIF) is a promising approach to quantify the dynamic early responses of vegetation drought response.

Remote Sensing of Environment 273 (2022) 112957

Contents lists available at ScienceDirect

Remote Sensing of Environment

journal homepage: www.elsevier.com/locate/rse

Response times of remote sensing measured sun-induced chlorophyll fluorescence, surface temperature and vegetation indices to evolving soil water limitation in a crop canopy

A. Damm [a,b,*], S. Cogliati [c], R. Colombo [c], L. Fritsche [a], A. Genangeli [d], L. Genesio [d], J. Hanus [e], A. Peressotti [f], P. Rademske [g], U. Rascher [g], D. Schuettemeyer [h], B. Siegmann [g], J. Sturm [a], F. Miglietta [d,i]

[a] Department of Geography, University of Zurich, Winterthurerstrasse 190, 8057 Zurich, Switzerland
[b] Eawag, Swiss Federal Institute of Aquatic Science and Technology, 8600 Dübendorf, Switzerland
[c] Remote Sensing of Environmental Dynamics Lab., DISAT, University of Milano-Bicocca, P.zza della Scienza 1, 20126 Milano, Italy
[d] Institute of Bioeconomy – IBE, National Research Council – CNR, Via Caproni 8, 50145 Florence, Italy
[e] Global Change Research Institute – CzechGlobe, Czech Academy of Sciences, Bělidla 986/4a, 60300 Brno, Czech Republic
[f] Department of Agricultural, Food, Environmental and Animal Sciences, University of Udine, Via delle Scienze 206, 33100 Udine, Italy
[g] Institute of Bio- and Geosciences, Plant Sciences (IBG-2), Forschungszentrum Jülich GmbH, 52428 Jülich, Germany
[h] European Space Agency, ESTEC, 2201, AZ, Noordwijk, the Netherlands
[i] Fondazione per il Clima e la Sostenibilità, Via Caproni, 8 50145 Florence, Italy

ARTICLE INFO

Jing M. Chen

Keywords:
Soil water limitation
Agricultural ecosystems
Multi-sensor remote sensing
Photochemical reflectance index
MERIS terrestrial chlorophyll index
Water band index

ABSTRACT

Vegetation responds at varying temporal scales to changing soil water availability. These process dynamics complicate assessments of plant-water relations but also offer various access points to advance understanding of vegetation responses to environmental change. Remote sensing (RS) provides large capacity to quantify sensitive and robust information of vegetation responses and underlying abiotic change driver across observational scales. Retrieved RS based vegetation parameters are often sensitive to various environmental and plant specific factors in addition to the targeted plant response. Further, individual plant responses to water limitation act at different temporal and spatial scales, while RS sampling schemes are often not optimized to assess these dynamics. The combination of these aspects complicates the interpretation of RS parameter when assessing plant-water relations. We consequently aim to advance insight on the sensitivity of physiological, biochemical and structural RS parameter for plant adaptation in response to emerging soil water limitation. We made a field experiment in maize in Tuscany (Central Italy), while irrigation was stopped in some areas of the drip-irrigated field. Within a period of two weeks, we measured the hydraulic and physiological state of maize plants in situ and complemented these detailed measurements with extensive airborne observations (e.g. sun-induced chlorophyll fluorescence (SIF), vegetation indices sensitive for photosynthesis, pigment and water content, land surface temperature). We observe a double response of far-red SIF with a short-term increase after manifestation of soil water limitation and a decrease afterwards. We identify different response times of RS parameter representing different plant adaptation mechanisms ranging from short term responses (e.g. stomatal conductance, photosynthesis) to medium term changes (e.g. pigment decomposition, changing leaf water content). Our study demonstrates complementarity of common and new RS parameter to mechanistically assess the complex cascade of functional, biochemical and structural plant responses to evolving soil water limitation.

1. Introduction

Anthropogenic caused global climate change continuously affects our ecosystems and releases a daily fingerprint in weather since 2012 (Sippel et al., 2020). Extreme events, i.e. heat waves, droughts, flooding, become more frequent and additionally impact ecosystem integrity and

* Corresponding author.
E-mail address: alexander.damm@geo.uzh.ch (A. Damm).

https://doi.org/10.1016/j.rse.2022.112957
Received 11 August 2021; Received in revised form 10 January 2022; Accepted 11 February 2022
Available online 28 February 2022

functioning in complex and manifold ways (Reichstein et al., 2013; Schuldt et al., 2020; Sippel et al., 2018; von Buttlar et al., 2018). Increasing evidence suggests that our capacity to unravel underlying interactions and feedbacks between climate dynamics, weather conditions and ecosystem functioning requires to go beyond pure climatological considerations and include impact perspectives in terms of alterations of carbon and water cycling (Reichstein et al., 2013; Smith, 2011). At the same time, sensitive concurrent observations of ecosystem functioning (e.g. carbon and water cycle dynamics) and abiotic environmental drivers for impactful events are pivotal to advance understanding but are still rare.

Remote sensing (RS) increasingly allows assessing valuable direct or indirect indicators of ecosystem functions and environmental driver across observational scales. Recent studies demonstrate suitability of RS to inform, for example, assessments of ecosystem carbon (Ciais et al., 2014; Ryu et al., 2019) and water exchange processes (Talsma et al., 2018; Wang and Dickinson, 2012). Besides the success of existing approaches under normal environmental conditions, biases were recently reported for RS based carbon exchange assessments under extreme climatic conditions (Miralles et al., 2019; Stocker et al., 2019). Furthermore, water exchange estimates work well for evapotranspiration, while assessment of its component fluxes (i.e. transpiration, evaporation) are still error prone (Talsma et al., 2018).

In particular simplifications in assessment schemes combined with insensitivity of RS proxies for complex water related mechanisms in the soil-plant-atmosphere system can partly explain observed biases and uncertainties in estimates of ecosystem functions (Dolman et al., 2014; Miralles et al., 2019). So-called plant-water relations act at different time scales and are highly sensitive to abiotic factors (e.g. soil water availability, atmospheric demand for water) and biotic factors (e.g. photosynthetic rates, stomatal conductance, plant structure). Knowledge of plant-water relations is, thus, critical to constrain estimates of ecosystem functioning under extreme conditions. A review by Damm et al. (2018) on the state of RS to assess plant-water relations indicates that this area is still dominated by empirical approaches to assess components of the complex water exchange between soil, plants and the atmosphere. Although mechanistic models exist (Bonan et al., 2014; Garcia-Tejera et al., 2017), they are rarely combined with RS data due to the complexity of required model parameters and missing sensitive observations.

Increasing maturity of RS technologies including measurements of sun-induced chlorophyll fluorescence (SIF) (Mohammed et al., 2019; Porcar-Castell et al., 2021) and multi-sensor concepts (Gerhards et al., 2016; Zarco-Tejada et al., 2012) opens additional opportunities to derive sensitive information and mechanistically assess plant-water relations (Jonard et al., 2020). SIF observations complement existing RS parameters and expand the range of RS accessible plant physiological processes towards ones acting at short temporal scales. In fact, it was recently found that SIF is sensitive to short term stomatal responses induced by water stress (Shan et al., 2019). Such developments complement traditional methods based on surface temperature, biochemical changes (i.e. decomposition of pigments, leaf water loss), mid-term acting structural adaptation, phenological responses, and ecosystem species composition (cf. Damm et al. (2018) for a review on this topic). However, the retrieval of SIF is delicate since superimposed by several other factors including counteracting physiological processes (i.e. non-photochemical quenching, NPQ) (Cendrero-Mateo et al., 2016), structural interferences (Li et al., 2019; Yang et al., 2019) and illumination effects (Damm et al., 2015; Yang et al., 2019). Besides SIF, the retrieval of common vegetation traits is also affected by illumination, structural and other effects (Barton and North, 2001; Damm et al., 2015; Myneni et al., 1995), which challenges their interpretation. Further, knowledge on causal relations between dynamics in plant response to water stress and required sensitivity of RS data are not fully exploited yet.

We hypothesize that retrieval uncertainties due to the complexity of common and new observations partly hide the inherent sensitivity of these observations for plant-water relations under water limited conditions. It is essential to disentangle unwanted sensitivities from targeted sensitivity of available RS parameter to finally provide mechanistic approaches for RS based assessments of plant-water relations. Further, it is important to understand specific temporal responses of RS indicators to soil water limitation. We therefore designed a soil water manipulation experiment in a maize field in Tuscany, Italy, with a particular focus on the sensitivity of physiological proxies (SIF and the photochemical reflectance index (PRI)), surface temperature (T_s), biochemical proxies (canopy water and chlorophyll content) for the early detection of water limitation. The field was equipped with several instruments to measure soil and plant water relations and environmental parameters, and we complemented these data with extensive biometric measurements and airborne RS observations. We assess diverse impacts of soil water limitation on plant hydraulic and growth parameters using in situ measurements. We then apply time series analysis to unravel the temporal sensitivity of various RS observations for increasing water limitation. We discuss and consolidate our results to suggest essential observations for robust assessments of the complex cascade of functional, biochemical and structural plant responses that evolve under increasing soil water limitation.

2. Methods

2.1. Test site and experimental design

The core experimental area of this study is a 220 × 320 m maize field (42°51′01.8"N 11°03′49.4″E, 10 m a.s.l.), located in a large agricultural region close to the city of Grosseto, Tuscany, Italy. The test site has a typical Mediterranean climate with hot and dry summers and mild winters. The maize field is equipped with a drip irrigation system, where the tubes are filled with water every two to three days for around 3 h. On average, a total amount of 6 mm of water per day is delivered independently of the natural precipitation regime, resulting in a soil moisture content of 20% per volume. On 13th June 2019, the irrigation tubes were removed from one sub-plot of 50x35m in the south of the field (orange box in Fig. 1). In situ measurements took place from 10 June to 24 June in the water-limited area and a well-watered area next to the treated canopy (orange and blue box in Fig. 1). Since canopy structure and observation/illumination geometry can influence the retrieval of RS parameters and cause differences between both investigated plant rows, we identified two other plots in the same plant rows to quantify the effect of these superimposing factors and facilitate the interpretation of our results (dark and light grey box in Fig. 1). Airborne data acquisition started on 16 June and lasted until 24 June. After the experiment, the irrigation was re-established in the water-limited canopy area.

2.2. In situ environmental and plant measurements

2.2.1. Environmental data

Canopy temperature and relative humidity were continuously measured above the canopy with a portable weather station. Soil water content in the first 25 cm of the soil was determined on 13, 16, 18, 20 and 22 of June using a portable Time Domain Reflectometry (TDR) probe. A FloX spectrometer system (jb-hyperspectral.com) was installed 3 m above the water-limited canopy area to measure irradiance and canopy reflected radiance every two minutes in high spectral resolution (i.e. 0.17 nm between 650 and 800 nm, 1.5 nm between 400 and 950 nm). We derived photosynthetic active radiation (PAR) by calculating the integral of the irradiance measurements between 400 and 700 nm.

2.2.2. Plant growth

Plant growth parameter were non-destructively collected in situ every two days on 11 marked plants per treatment. Plant height and steam diameter were measured on 11 June before the irrigation was stopped and from 16 to 28 of June. We calculated growth rates from

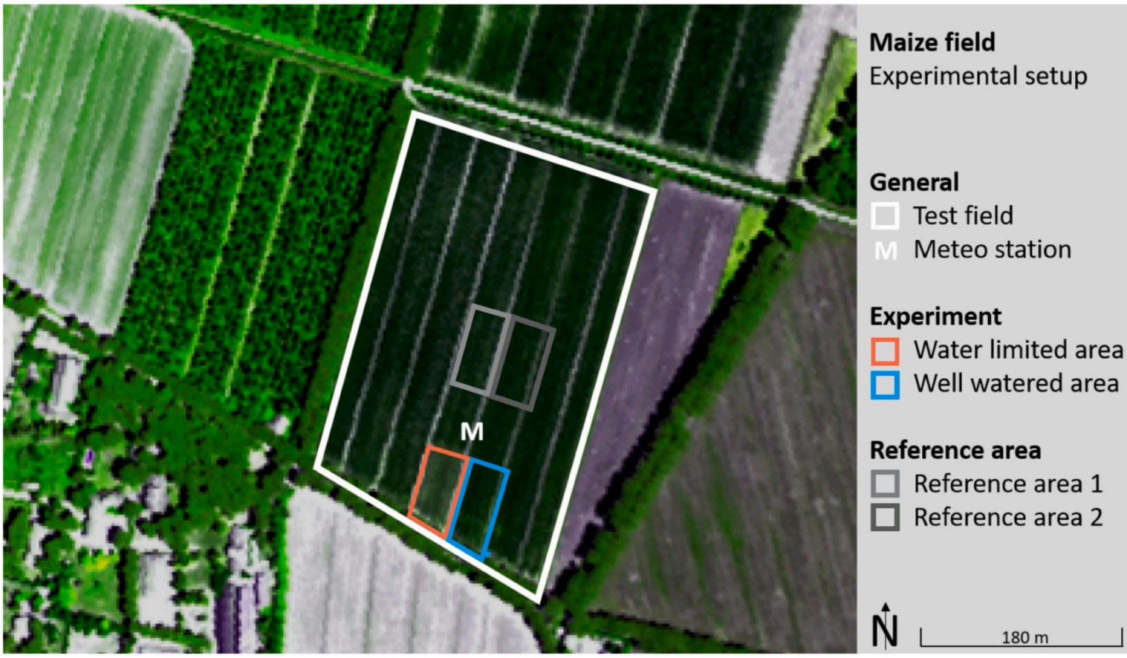

Fig. 1. Test site (white box) and experimental setup with the water-limited canopy (orange box) and the well-watered canopy (blue box), both equipped with in situ measurements. The grey marked areas are used to evaluate the temporal difference between plant rows due to superimposing structural and illumination / observational effects. The background image shows a false colour composite of HyPlant on 24 June 2019. (For interpretation of the references to colour in this figure legend, the reader is referred to the web version of this article.)

height measurements as difference between two adjacent observations per treatment.

2.2.3. *Chlorophyll content*

Variation in chlorophyll content was determined indirectly via measurements with a SPAD-502 chlorophyll meter (Konica-Minolta) on 11 marked plants per treatment. The SPAD instrument measures the difference of light transmission at two contrasting wavelengths differently affected by chlorophyll absorption. The resulting SPAD value requires an empirical conversion to effective chlorophyll content but in absence of such a function, we did not convert SPAD readings in units of chlorophyll content. Measurements started on 11 June before the irrigation was stopped and was continued every second day between 16 and 22 June.

2.2.4. *Leaf water potential*

Leaf water potential (ψ_l) was measured from 18 to 22 June on five individual maize plants that were randomly chosen in both the water-limited and well-watered canopy area. The upper fully expanded leaves were removed, stored in a plastic bag to avoid water losses (Turner and Long, 1980) and immediately measured. Leaf water potential was determined by means of a pressure chamber (PMS, Instrumentation Co. Corvallis, OR, USA) according to the Scholander et al. (1965) method. Leaves were measured between 10:00 and 15:30 on 18, 19, 20, and 21 June (mid-day measurements) and between 6:30 and 7:45 on 22 June (pre-dawn measurement).

2.2.5. *Stomatal conductance*

From 16 to 19 June, we measured leaf stomatal conductance (g_s) in mmol m^{-2} s^{-1} with a SC-1 Leaf Porometer (Decagon Devices, Inc., Pullman, WA, United States) during the day between 7:30 and 17:00. We obtained g_s for nine maize plants in both the water-limited area and the well-watered area. We took five measurements on the abaxial leaf side per maize plant and the measurements were distributed all around the plant stem to account for different leaf geometry and orientation.

2.2.6. *Sap flow measurements*

Canopy transpiration was measured by means of heat-balance sap-flow gauges (Peressotti and Ham, 1996), where heat is applied to the entire circumference of the stem encircled by a heating tape and the sap flow is obtained by measuring the difference in the fluxes of heat into and out of the heated section of the stem (Sakuratani, 1981). Ten gauges were installed on an equivalent number of plants in the irrigated and the non-irrigated plot and the fluxes were calculated at half-hour intervals from 8 June to 25 of June to obtain reliable estimates of the amount of water transpired.

2.3. *Airborne spectroscopy in the optical domain*

The main analysis of this paper is based on 42 flight lines acquired with the airborne imaging spectrometer HyPlant between 16 and 24 June (Table 1).

The HyPlant system consists of three pushbroom line scanners. Two of them share the same fore optic and form the DUAL module. This module quasi continuously samples the visible/near infrared (VNIR) and shortwave infrared (SWIR) spectral range (380–2500 nm) with a spectral resolution of 3.65 nm (VNIR) and 10.55 nm (SWIR). The third pushbroom line scanner, called FLUO, is able to record data in the spectral range between 670 and 780 nm with a spectral resolution of 0.28 nm (Rascher et al., 2015; Siegmann et al., 2019). While the DUAL

Table 1
Time of HyPlant flights during the experimental period in central European summer time (CEST).

Date	Morning (CEST)	Afternoon (CEST)
16 June	11:28, 11:32, 11:37, 11:41	14:11, 14:15, 14:19, 14:24
17 June	11:20, 11:24, 11:28, 11:33	
18 June	11:13, 11:17, 11:21, 11:26	14:22, 14:27, 14:32, 14:37
19 June	10:11, 10:19, 10:27, 10:34	13:15, 13:22, 13:30, 13:38
		16:11, 16:18, 16:26, 16:34
20 June		14:12, 14:16, 14:21, 14:25
23 June	11:09, 11:14, 11:18, 11:28	
24 June	11:13, 11:17	

module enables the retrieval of common vegetation parameter, i.e., canopy structure, pigment composition and other biochemical traits, the FLUO module facilitates the retrieval of SIF in both, the O_2-A and O_2-B absorption band. The flight height of 350 m resulted in a pixel size of 1 m. After a rigorous data pre-processing following the procedure described in Siegmann et al. (2019), we retrieved SIF and other remote sensing proxies indicative for the vegetation state.

2.3.1. SIF retrieval

Red and far-red SIF were quantified by exploiting the O_2-B and O_2-A absorption bands using and adapted Spectral Fitting technique (Meroni et al., 2010; Cogliati et al., 2015). The algorithm relies on forward simulations of at-sensor radiance spectra at the O_2 bands by means of coupled surface-atmosphere radiative transfer equations (Cogliati et al., 2019; Verhoef et al., 2018). The surface reflectance and fluorescence are modeled with simple parametric equations characterized by a spectrally smooth behaviour (i.e. polynomials for reflectance, peak-like functions for fluorescence). The physically based code *MODerate resolution atmospheric TRANsmission* 5 (MODTRAN-5) (Berk et al., 2005) is instead employed to calculate the atmospheric radiative transfer within the narrow windows corresponding to the O_2 bands. The exact atmospheric state is often unknown, causing slight uncertainties in the description of the atmospheric state and finally SIF retrieval uncertainties. We therefore used an image-based approach to optimize the parameterization of the atmospheric radiative model. In practice, the surface-sensor path length (i.e. determining the amount of oxygen absorption) was varied in MODTRAN-5 to analytically retrieved the effective path length that satisfies the condition of zero SIF for non-fluorescent targets. Instrument center wavelength and bandwidth were characterized with the SpecCal algorithm originally proposed by Meroni et al. (2010) and adapted for airborne data analysis. Resulting sensor characteristics are essential to convolve MODTRAN-5 based atmospheric transfer function. The retrieval of SIF within both O_2 bands is based on an iterative optimization algorithm that matches at-sensor radiance spectra measured with HyPlant and forward modeled using the coupled surface-atmosphere radiative transfer equations.

2.3.2. Other vegetation parameter

Based on the top-of-canopy reflectance derived from HyPlant DUAL data after atmospheric correction (Siegmann et al., 2019), the MERIS terrestrial chlorophyll index (MTCI) (Dash and Curran, 2004), Water Band Index (WBI) (Penuelas et al., 1993) and Photochemical Reflectance Index (PRI) (Gamon et al., 1992) were calculated to approximate canopy chlorophyll content, canopy water content, and non-photochemical quenching, respectively. The three reflectance indices were calculated as:

$$\mathrm{MTCI} = \frac{\mathrm{R}_{754\pm4} - \mathrm{R}_{709\pm5}}{\mathrm{R}_{709\pm5} + \mathrm{R}_{754\pm4}} \tag{1}$$

$$\mathrm{WBI} = \frac{\mathrm{R}_{955-970}}{\mathrm{R}_{890-905}} \tag{2}$$

$$\mathrm{PRI} = \frac{\mathrm{R}_{570\pm2.5} - \mathrm{R}_{531\pm2.5}}{\mathrm{R}_{570\pm2.5} + \mathrm{R}_{530\pm2.5}} \tag{3}$$

where R_λ correspond to the average reflectance of the HyPlant DUAL spectral bands. We used the average over the wavelength interval specified by the subscripts in Eqs. 1–3 to compensate for data noise.

2.4. Airborne thermal remote sensing

Along with the collection of HyPlant data, we acquired thermal data using the TASI-600 spectroradiometer. TASI is a pushbroom line scanner measuring in the longwave infrared (LWIR) spectral region between 8′000 to 11′500 nm in 32 spectral bands (Itres Research Ltd). The flight height of 350 m resulted in a spatial resolution of 1.8 m. Acquired data were processed by a standard processing chain described in Hanus et al. (2016), further details can be also found under (http://olc.czechglobe.cz/en/processing/tasi-data-processing/). The standard processing includes a radiometric correction using the RadCor software (Itres Research Ltd) and, in absence of calibrated black body scans, laboratory determined calibration coefficients. Afterwards, an atmospheric correction was applied to compensate atmospheric up and downwelling radiance and atmospheric transmissivity and finally retrieve land surface temperature (T_S).

2.5. Data normalization at airborne level

We applied two data normalization strategies to compensate canopy structural and illumination effects that often superimpose dynamics in retrieved SIF and other vegetation parameters. A first data normalization only acted in the temporal domain. We calculated the difference between investigated RS parameter (P) at a certain point in time and the mean of the RS parameter obtained from the first four airborne data acquisitions of the campaign in the morning of 16 June (e.g. P^{16}) as:

$$\Delta P = P - P^{16} \tag{4}$$

The resulting time series of ΔP represents the increment of individual RS parameter considering the first four observations (16 June) in physical units. It must be noted that the first flight took place three days after the irrigation was stopped (13 June) but both the water-limited and the well watered canopy areas were still in the same state with no signs of soil water limitation.

The second data normalization acted in the spatial and temporal domain. We calculated the normalized difference of a RS parameter for the water-limited canopy (P_{EXP}) considering the well-watered canopy as reference (P_{REF}) (orange and blue area in Fig. 1) for a given point in time ($P_{EXP\text{-}REF}$). Further, we calculated the same normalized difference considering two reference areas in the same rows but not affected by the experiment, while the canopy in sam row as the water-limited canopy was used as (P_{EXP}) and the other one as (P_{REF}) (bright grey and grey area in Fig. 1).

$$P_{EXP-REF} = \frac{P_{EXP} - P_{REF}}{P_{REF}} \bullet 100 \tag{5}$$

Resulting spatially normalized $P_{EXP\text{-}REF}$ values were then related to the mean of the first four observations of 16 June (${P_{EXP-REF}}^{16}$) to calculate a time series of increments of spatially normalized differences ($\Delta P_{EXP\text{-}REF}$) considering the first observation (16 June) as:

$$\Delta P_{EXP-REF} = P_{EXP-REF} - P^{16}_{EXP-REF} \tag{6}$$

Resulting $\Delta P_{EXP\text{-}REF}$ values for SIF, MTCI, PRI, WBI, T_S are supposed to normalize structural and related illumination effects caused by different observation times and view angles.

2.6. Statistics

We used two statistical measures to evaluate the effect and reliability of the applied water limitation on the response of plants as approximated by the various RS parameters, including the 95% confidence intervals assuming a z-distribution and the effect size using *Cohen's d* by taking the standard deviation of the well-watered canopy into account. Since the maize field was covered with many observations (pixels), we selected every tenth pixel per region of interest (cf. Fig. 1) to minimize the problem of spatial (e.g. environmental factors) and technical autocorrelation (e.g. pixel-cross talk), and to reduce the number of observations.

3. Results

3.1. Environmental parameter

During the observational period, weather conditions were good with five almost cloud free days, six days with scattered clouds and one day with overcast conditions (22 June), while PAR reached up to 400 W m^{-2} on partly scattered days (Fig. 2*A*). Air temperature ranged between 11.7 and 37.1 °C with a mean of 24.3 °C (Fig. 2*B*). Relative humidity ranged between 21.7% and 93.9% with a mean value of 60.5% (Fig. 2*C*). The induced irrigation-stop caused an immediate drop of soil water content, reaching a reduction of 65% at the end of the experiment (Fig. 2*D*).

3.2. Impact of soil water limitation on plant-water relations from an in situ perspective

3.2.1. Plant growth

We found a reduced growth rate between the water-limited and the well-watered canopy. Both canopies had similar stem diameters at the beginning of the experiment (26.5–26.8 mm), while plants in the water limited canopy showed a significantly reduced increase of the stem diameter compared to plants in the well-watered canopy. Already on 16 June, notable differences were observed that reached 10% at the end of the experiment (31.8 mm for the well-watered canopy, 28.9 mm for the water-limited canopy) (Fig. 3*A*). Concerning canopy height, plants in both canopies started with different heights (i.e. 82 cm for the well-watered canopy, 75 cm for the water limited canopy, Fig. 3*B*). Both canopies showed a height increase, with plants of the water-limited area lagging behind and reaching a 22% difference at the end of the experiment (i.e. 1.7 m of the well-watered canopy and 1.3 m of the water-limited canopy (Fig. 3*B*). The growth rates for the well-watered canopy continuously increased from 2 cm/day to 8.3 cm/day on 28 June (Fig. 3*D*). Growth rates for the watered-limited plants increased from 1 cm/day to and 4.5 cm/day on 22 June and even decreased until 25 June (2 cm/day) but showed a substantial increase towards the end of the experiment (7 cm/day) when the water-limited canopy was again irrigated.

3.2.2. Leaf chlorophyll content

SPAD based estimates of the leaf chlorophyll content indicate that both treatments started at a comparable level (i.e. 50.7 and 51.1 SPAD values) and showed a notable difference already on 16 June. The SPAD value slightly decreased for the water-limited plants (reaching 49.7 on 22 June), while SPAD values increased for the well-watered canopy (52.5 on 22 June) (Fig. 3*C*).

3.2.3. Leaf water potential

ψ_l measurements were started on 18 June, 5 days after the irrigation was stopped and soil water content already droped by 52%, and were lower in water-limited canopy (−12.13 MPa to −13.83 MPa) compared to the well-watered canopy (−9.27 MPa to −10.48 MPa) (Fig. A1*A*). Predawn measurements made on 22 June, 9 days after the experiment started, indicate manifested water limitation in terms of reduced ψ_l (i.e. -9.17 MPa), while the well-watered canopy has a higher ψ_l (−5.2 MPa) (grey marked area in Fig. A1*A*).

3.2.4. SAP flow

SAP flow shows a large dynamic at a diurnal time scale and across the experiment (Fig. A1*B*). A typical diurnal pattern with highest values around noon-time (0.5–0.8 mm h^{-1}) is overlaid with some scatter caused by environmental factors (e.g. varying net radiation, wind, temperature). Diurnal differences between the water-limited and the well-watered canopy are particularly visible before noon with a reduced SAP flow of the water limited canopy from 13 June until 23 June. After the irrigation was re-established, SAP flow rates of the water-limited canopy substantially increased and even exceeded the rated of the well-watered canopy, reaching maximum values of 0.8 mm h^{-1}. Daily aggregated SAP flow started at a similar level on 10 June (3.5 mm day^{-1}), while the daily rates for the well-watered canopy were constantly larger compared to the water-limited canopy with an increasing difference until 22 June. After the cloudy day on 22 June with some rainfall and re-establishing the irrigation afterwards, daily rates of the water-limited canopy even exceeded the one of the well-watered canopy and reached values of 6 mm day^{-1}. (Fig. A1*B*).

3.2.5. Stomatal conductance

g_s measurements started on 16 June, three days after irrigation was stopped. Acquired data are scattered and less conclusive (Fig. A2). In general for both, the water-limited and the well-watered canopy, we observe an increase of g_s from the morning (50–90 mmol m^{-2} s^{-1}) to noon time (80–140 mmol m^{-2} s^{-1}). Concerning diurnal changes between both treatments, our measurements tend to show that the slope of a fitted linear model representing diurnal dynamics stays relatively constant for all days in the well-watered canopy (i.e. slope between 1.3 and 6.2), and declines from 5.6 (16 June) to −0.2-1.7 (18 and 19 June) in the water-limited canopy (Fig. A2). The water-limited canopy shows a

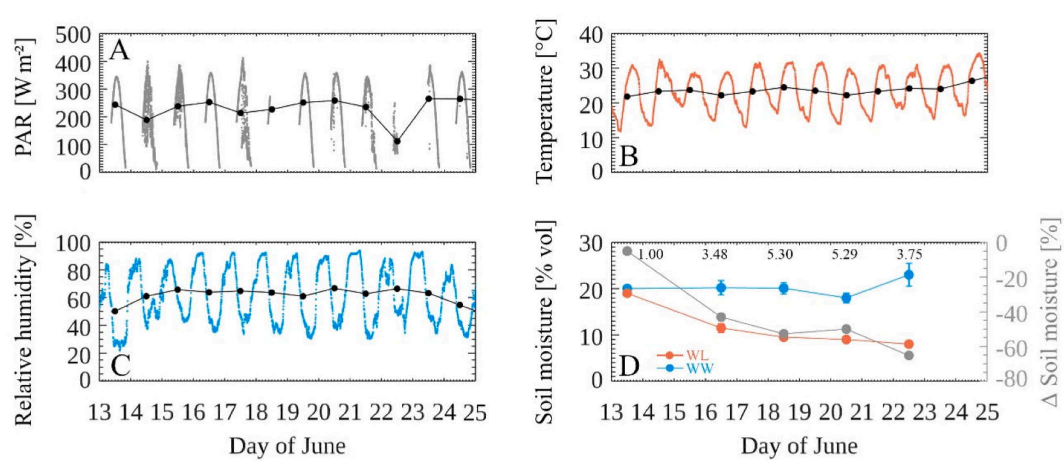

Fig. 2. Overview of environmental factors during the duration of the experiment from 13 to 25 June 2019. A: Photosynthetic active radiation (PAR). B: Air temperature at 2 m height. C: Relative humidity at 2 m height. D: Volumetric soil water content in the upper 25 cm of the water-limited (WL) area (orange), the well-watered (WW) area (blue) and the percent difference between both curves (grey). The black dots in A-C represent the mean value per day. Error bars indicate the 95% confidence interval and numbers the effect size (Cohen's d). (For interpretation of the references to colour in this figure legend, the reader is referred to the web version of this article.)

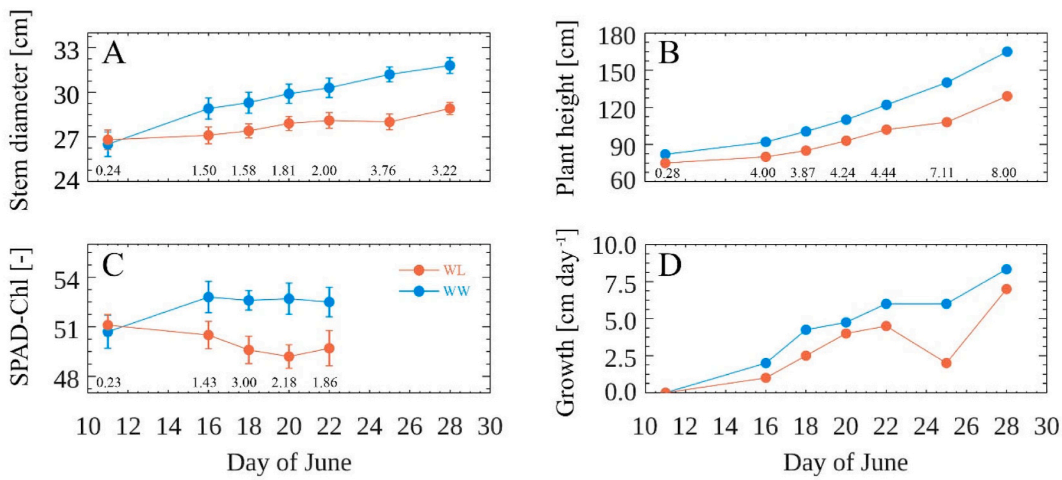

Fig. 3. Development of structural, biochemical and growth parameters of the water-limited (WL) area (orange) and the well-watered (WW) area (blue). A: Stem diameter. B: Plant height. C: SPAD based leaf chlorophyll content. D: Growth rate representing the height difference between two adjacent days. Error bars indicate the 95% confidence interval and numbers the effect size (Cohen's d). (For interpretation of the references to colour in this figure legend, the reader is referred to the web version of this article.)

decline of g_s in the late afternoon (mean g_s decreases from 140 to 70 mmol m^{-2} s^{-1} between 16 to 19 June), while the well-watered canopy shows a less varying mean g_s ranging between 95 and 125 mmol m^{-2} s^{-1} from 16 to 19 June (Fig. A2).

3.3. Temporal dynamics of plant-water relations from an airborne RS perspective

Investigated RS parameter red and far-red SIF, vegetation indices (i.e. PRI, MTCI, WBI) and Ts show diverse temporal responses in accordance to evolving soil water limitation (Fig. 4).

3.3.1. Fast changing remote sensing parameters: SIF_{760} and SIF_{685}

Compared to the first day of airborne measurements on 16 June, ΔSIF_{685} for the well-watered and the water-limited area at 11:00 continuously decrease and are lowered by around 0.32 and 0.18 mW m^{-2} nm^{-1} sr^{-1} on 24 June respectively (Fig. 4*A*). On 19 June, ΔSIF_{685} shows a local minima of around −0.45 mW m^{-2} nm^{-1} sr^{-1} for both areas since observations took place around one hour earlier compared to the other days. The normalized $\Delta SIF_{EXP-REF}{}^{685}$ values indicate a rapid increase of SIF_{685} of around 5.6–9.8% in the water-limited canopy compared to the well-watered canopy in the morning which stays at this level until 24 June (Fig. 4*B*). $\Delta SIF_{EXP-REF}{}^{685}$ of the reference plots indicate in average smaller SIF_{685} values for the plant row of the water-limited canopy compared to the other row but differences fluctuate around zero.

ΔSIF_{760} of the well-watered canopy increases in the morning by 0.43 mW m^{-2} nm^{-1} sr^{-1} from 16 to 24 June. ΔSIF_{760} of the water-limited canopy varies at the end of the experiment with increased values between 0.09 and 0.25 mW m^{-2} nm^{-1} sr^{-1} (Fig. 4*C*). Normalized $\Delta SIF_{EXP-REF}{}^{760}$ values show a highly interesting pattern. $\Delta SIF_{EXP-REF}{}^{760}$ of the water-limited canopy first increases compared to the well-watered canopy from 16 June to 18 June (11.9%) and then starts decreasing until 24 June (−7.7%) (Fig. 4*D*). The first increase is not visible for the reference canopies that exhibit in the first four days around 5% smaller SIF_{760} values in the plant row of the water-limited canopy compared to the plant row with the well-watered canopy, followed by a 7.9% increase of $\Delta SIF_{EXP-REF}{}^{760}$ towards 24 June.

3.3.2. Moderately changing remote sensing parameters: T_S, PRI, MTCI, WBI

ΔT_S values also show a slight but continuous increase in the morning for both treatments on the first two days (between 0.45 and 0.9 °C). On 19 June, ΔT_S declines (−0.76 to −1.0 °C) due to earlier data acquisition. The water-limited canopy eventually reaches an increased temperature of 3.5 °C on 24 June, while the well-watered one shows a temperature increase on 24 June of 1.2 °C (Fig. 4*E*). The normalized time series $\Delta Ts_{EXP\text{-}REF}$ indicates continuously increasing temperatures in the water-limited canopy, reaching 7.1% higher values compared to the well-watered canopy at the end of the experiment (Fig. 4*F*). $\Delta Ts_{EXP\text{-}REF}$ for the reference canopies is slightly decreasing until June 24 (−2.2%).

ΔPRI, indicative for NPQ, shows a decreasing trend between 16 and 24 June in the morning, while PRI values for the well-watered canopy show a larger decline compared to the water-limited canopy. The ΔPRI time series also shows discontinuity for both treatments (e.g. increasing values on 23 June, Fig. 4*G*). Normalized $\Delta PRI_{EXP\text{-}REF}$ values indicate a continuous increase of PRI for the water-limited canopy compared to the well-watered canopy, reaching 20.4% higher values on 24 June (Fig. 4*H*). The $\Delta PRI_{EXP\text{-}REF}$ values of the reference canopies indicate that PRI of both plant rows does not largely change from 16 to 24 June (−3.4 to 2.7%).

MTCI represents the canopy chlorophyll content. Retrieved ΔMTCI values show a continuous increase for both the water-limited and the well-watered and canopy until 19 June, followed by continuous increase of MTCI for the well-watered canopy until 24 June and a slight decline of MTCI for the water-limited canopy until 24 June (Fig. 4*I*). The normalized $\Delta MTCI_{EXP\text{-}REF}$ time series clearly shows that the water-limited canopy is affected by growth limitation. MTCI values stay constant until 19 June (change <1.5%) and then decline towards 24 June (−13.8%) (Fig. 4*J*). The $\Delta MTCI_{EXP\text{-}REF}$ values of the reference canopies indicate that MTCI of both plant rows does not notably change from 16 to 24 June (−0.02 to 3.0%).

ΔWBI values, indicative for the inverse of canopy water content, constantly decrease between 16 and 24 June for both canopies. The time series shows some discontinuity for both treatments (e.g. slight intermediate increases on 18 and 23 June) (Fig. 4*K*). Normalized $\Delta WBI_{EXP\text{-}REF}$ values confirm that the canopy water content does not notably change between the water-limited and the well-watered canopies (−0.57 to 0.69%). The $\Delta WBI_{EXP\text{-}REF}$ values of the reference canopies indicate also almost no WBI differences between both plant rows from 16 to 24 June (up to −1.5%, Fig. 4*L*).

3.4. Spatio-temporal dynamics of plant-water relations

The spatial representation of changes in normalized airborne RS parameters (i.e. $\Delta P_{EXP\text{-}REF}$) provides an additional and confirming

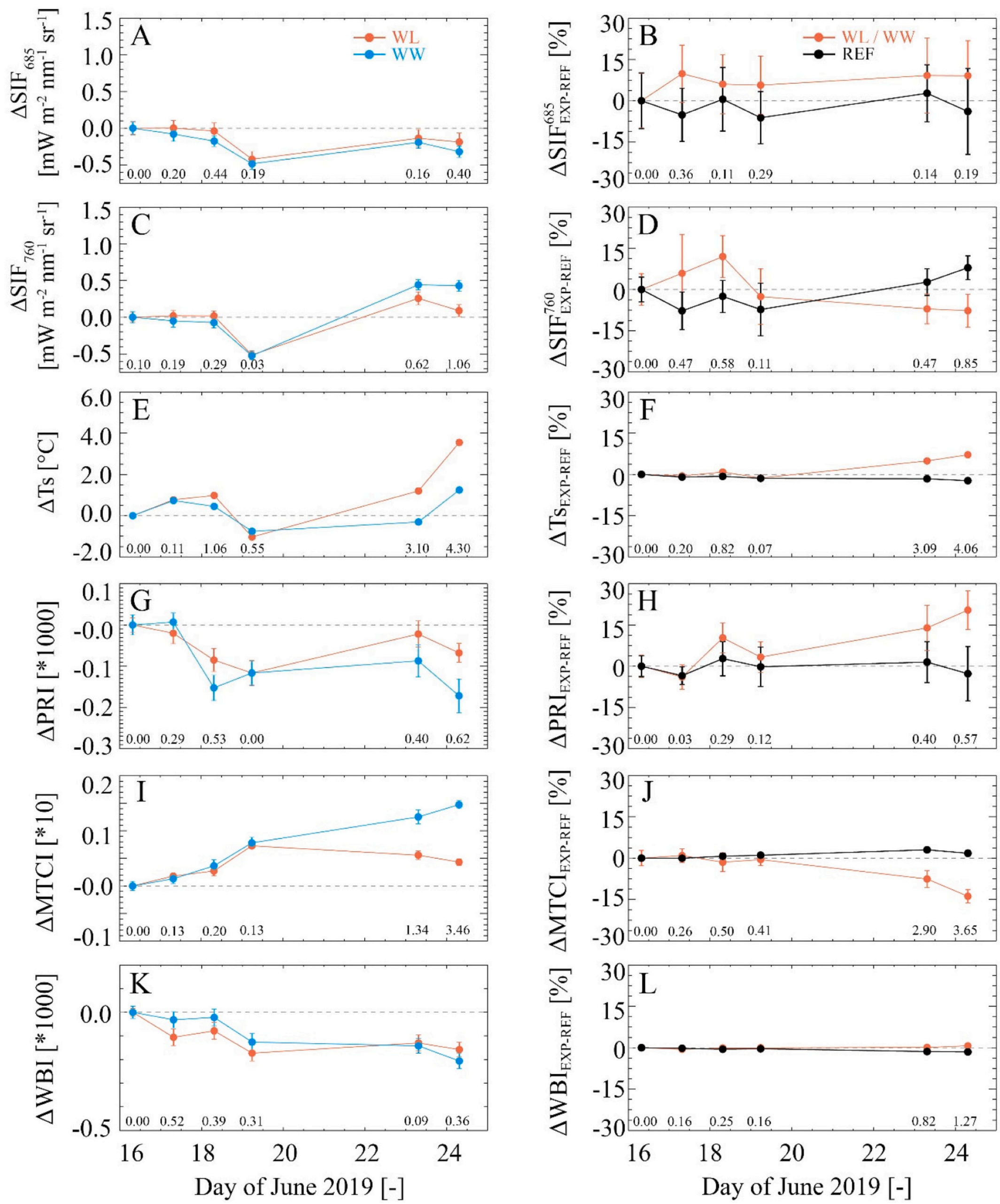

Fig. 4. Changes of remote sensing (RS) parameter during the water manipulation experiment in a maize canopy between 16 and 24 June 2019 acquired in the morning (10–11:30 CEST). Left column: Shown changes represented the difference of a certain RS parameter (P) compared to the first observation (16 June) in parameter units (ΔP) for the water-limited field (orange) and well-watered field (blue). From top to bottom: red sun-induced chlorophyll fluorescence (SIF685), far-red SIF (SIF760), surface temperature (Ts), photochemical reflectance index (PRI), MERIS terrestrial chlorophyll index (MTCI), and water band index (WBI). Right column: percentage changes representing the relative difference between the water-limited and the well-watered area (orange), normalized considering the percentage change of the first day (16 June) ($\Delta P_{EXP\text{-}REF}$). The black line shows the normalized percent changes of two reference areas in the same plant rows not affected by the water-limitation experiment. Error bars indicate the 95% confidence interval and numbers the effect size (Cohen's d). (For interpretation of the references to colour in this figure legend, the reader is referred to the web version of this article.)

perspective on trends explained in the previous section 3.3. Fig. 5 shows the maize field under investigation and highlights the relevant canopy areas.

$\Delta SIF_{EXP-REF}{}^{760}$ is rather noisy but one can recognize increased $\Delta SIF_{EXP-REF}{}^{760}$ values in the water-limited area, showing higher values on June 17 and 18 compared to the well-watered area. At the end of the campaign, $\Delta SIF_{EXP-REF}{}^{760}$ substantially decreases in the water-limited area but remains constant for the other regions. $\Delta SIF_{EXP-REF}{}^{685}$ is also rather noisy but no differences between both treatments are visible. $\Delta PRI_{EXP\text{-}REF}$ and $\Delta Ts_{EXP\text{-}REF}$ show an increasing contrast between well-limited and well-watered canopy starting on 18 June, while a notable difference between the water-limited and the well-watered canopy appears on 24 June. For $\Delta MTCI_{EXP\text{-}REF}$ and $\Delta WBI_{EXP\text{-}REF}$ a reduction of values in the water-limited area appears later than 18 June but is well visible on 24 June.

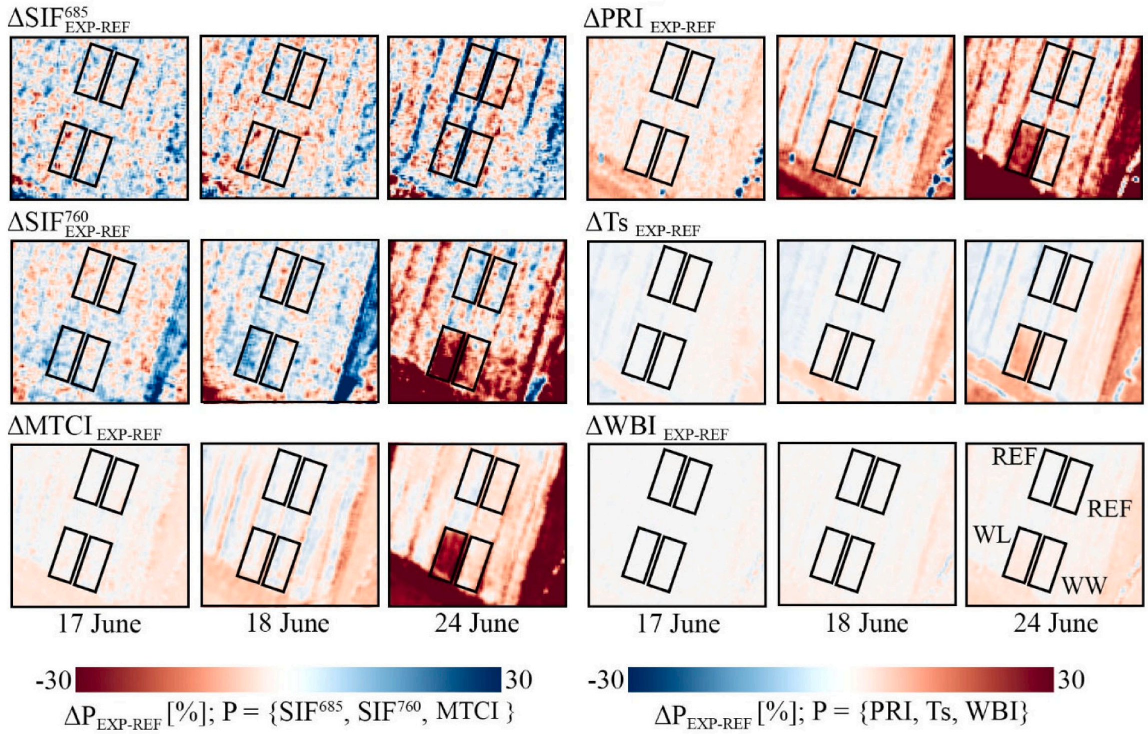

Fig. 5. Response of remote sensing (RS) parameter to evolving water-limitation in a corn canopy one day (17 June), two days (18 June) and eight days after start of flight experiment (24 June). The boxes indicate the locations of the differently treated areas of the experiment, i.e. water-limited (WL), well-watered (WW) and the two reference areas (REF). Please note that the colour scheme changes between RS parameters to enable an intuitive colour representation with red indicating a negative effect and blue a positive effect. (For interpretation of the references to colour in this figure legend, the reader is referred to the web version of this article.)

4. Discussion

4.1. Sensitivity of normalized remote sensing parameters for evolving soil water-limitation

We observed specific responses of normalized RS parameter to water-limitation that differ in their temporal dynamics and amplitude. This expected behaviour is caused by the sensitivity of individual RS parameters for specific plant adaptation mechanisms, including functional and biochemical/structural changes to water limitation (cf. Damm et al. (2018) for a review on this topic). Highly interesting is the observed morning double response of normalized SIF_{760} ($\Delta SIF_{EXP-REF}{}^{760}$) with first a short-term increase with increasing water-limitation, followed by a longer-term decrease under sustained water-limitation (cf. Figs. 4-5). Further, SIF_{685} ($\Delta SIF_{EXP-REF}{}^{685}$) showed an immediate increase but no reduction over time.

In fact, three to five days after the experiment started (16–18 June), soil moisture content was already reduced by 43% and 52% (Fig. 2*D*) and first signs of reduced SAP flow in the water-limited canopy in the morning hours were visible (Fig. A1*B*). In situ growth parameters already indicate a slight separation of the water-limited and well-watered canopy with even slightly reduced SPAD based leaf chlorophyll and growth rates for the water-limited canopy. An increase of SIF_{760} and SIF_{685} in the water-limited canopy compared to the well-watered canopy under these conditions where already a slight reduction of SIF due to the lower chlorophyll content could be expected is likely driven by physiology. We also calculated the NIRv that was introduced as RS proxy sensitive for structural variation of SIF (Badgley et al., 2017; Zeng et al., 2022). The $\Delta NIRv_{EXP-REF}$) time series shows only small differences in the first days between the well-watered and water limited canopies and the reference plots (2.8 and 4.0% respectively), indicating no structural difference between both, the well-watered and the water-limited canopy that could explain the shorter dynamics in SIF (Fig. A3*B*, Fig. A5*B*). Dynamics in red and green reflectance was analysed and we found fast and continuous responses of $\Delta R_{GREEN\ EXP-REF}$ and $\Delta R_{RED\ EXP-REF}$ starting on 18 June that cannot explain the fast increase of $\Delta SIF_{EXP-REF}{}^{760}$ on 17 June and the decline after 19 June (Fig. A3*F*, A3*H*). Other RS derived parameters support that plants could have reacted physiologically to the evolving water-limitation. Slightly higher $\Delta Ts_{EXP\text{-}REF}$ in the water-limited field compared to the well-watered field already visible in the morning but even more pronounced in the afternoon (Fig. A4*F*) could indicate a partly stomatal closure that possibly inhibits PS and thus increases chances of SIF emission. $\Delta PRI_{EXP\text{-}REF}$, representing the regulation of NPQ, is similar in the morning for the water-limited and well-watered canopy until 17 June and increases afterwards, indicating that NPQ in water-limited canopy does not reach a critical level to quench notably more electrons from the light reaction compared to the well-watered canopy at least until 17 June.

After eleven days after the experiment started (22 June), soil moisture content of the water-limited field decreased by 65% compared to the well-watered canopy. Growth sensitive RS parameters show a relevant reduction ($\Delta MTCI_{EXP\text{-}REF}$ and $\Delta WBI_{EXP\text{-}REF}$), confirmed by in situ observations of growth parameters. The decline of $\Delta SIF_{EXP-REF}{}^{760}$ (lower SIF_{760} in the water-limited field compared to the well-watered field) after 19 June is possibly determined by structural changes (i.e. lower canopy chlorophyll in the water-limited treatment) and physiological effects. The structural sensitivity is confirmed by the lowered $\Delta NIRv_{EXP-REF}$ for the experimental canopies (−5.0%) and the parallel increase for the reference canopies (5.7%) (Fig. A3*B*). Further, the increasing $\Delta Ts_{EXP\text{-}REF}$ in the morning and afternoon indicates higher stomatal closure in the water-limited canopy, while increasing $\Delta PRI_{EXP\text{-}REF}$ in the water-limited area compared to the well-watered area indicates substantial NPQ that causes a stagnation or even lower SIF_{760} in the water-limited canopy compared to the well-watered canopy.

Earlier studies (van der Tol et al., 2009; Van Wittenberghe et al.,

2021) demonstrate at leaf level that SIF together with NPQ increases with environmental stress. The modelling study by van der Tol et al. (2009) additionally indicates a NPQ threshold causing a stagnation or even decreases of SIF when NPQ becomes the dominant pathway of photons (cf. Fig. 3a in (van der Tol et al., 2009). At coarser canopy level, several studies indicate a decrease of SIF_{760} with environmental stress (Sun et al., 2015; Yoshida et al., 2015). Both results seem contradicting but can be explained by the complex interplay of physiological and structural plant response to drought that act at different time scales. The theoretically known double response of SIF_{760} under evolving stress is, to our knowledge, now for the first time shown in an airborne experiment.

Concerning SIF_{685}, we observed increase of $\Delta SIF_{EXP-REF}{}^{685}$ in the water-limited canopy during the entire period. It is known that red SIF is re-absorbed by chlorophyll and the observed behaviour of $\Delta SIF_{EXP-REF}{}^{685}$ is likely a complex interplay of a longer-term structural response and physiological SIF_{685} changes that seem to keep in balance.

4.2. Limitation of this study and ways forward

Results obtained in this study correspond to theory discussed in literature and findings from airborne level are supported by detailed in situ measurements. Nevertheless, some limitations of our experimental setting must be noted to better judge reliability and representativeness of obtained results.

One limitation is that we present results from a single maize field that was measured once without replicates. This certainly asks for other studies to repeat such an experiment ideally at a variety of different crops and environmental settings. Although a comprehensive set of in situ observations was available, it is not complete. Collected data are sufficient to reveal a clear plant growth response for increasing water-limitation but more supportive measurements would be helpful for data interpretation and transferability of results. Particularly interesting would be eddy flux measurements of evapotranspiration and leaf physiological information including NPQ and g_s obtained from leaf gas chamber measurements. Further, more detailed soil water data such as soil water content, soil water holding capacity and field capacity would be important to quantify plant available water.

Besides SIF, we used simple retrieval approaches to quantify plant parameter from airborne data (i.e. vegetation indices) and RS data were acquired under slightly different observation times in the morning (10:15–11:30) and afternoon (13:30–15:30). It is well known that the retrieval of RS plant parameters must account for various superimposing factors, including illumination effects (Damm et al., 2015; Fawcett et al., 2018; Kückenbrink et al., 2019), atmospheric disturbances (Cendrero-Mateo et al., 2019; Guanter et al., 2010), canopy structure (Feng et al., 2002) with its related reflectance anisotropy (Weyermann et al., 2014), and instrumental effects (Damm et al., 2011; Hueni et al., 2017). Since the compensation of these disturbing effects if often less reliable than required, small artefacts in retrieved RS parameter remain. Furthermore, RS parameter represent highly dynamic traits (e.g. SIF, Ts) that change during the day, while slightly different observation times immediately complicate the interpretation of observed RS parameter dynamics. Our results indicate that revealing subtle canopy responses such as the double SIF_{760} response from original time series is difficult due to imperfections of RS parameter retrieval schemes.

We consequently applied a rigorous spatio-temporal data normalization to compensate RS parameter variation caused by above superimposing effects. Our results successfully demonstrate that most of these superimposing effects can be compensated with such normalization strategies (cf. differences between ΔP and normalized $\Delta P_{EXP\text{-}REF}$ trends in Fig. 4), which is in agreement with other studies (Zarco-Tejada et al., 2012). The implementation of spatio-temporal normalization strategies is not straightforward due to missing references. Our experiment provided important insight on the severity of these superimposing effects and clearly indicates the need for an optimized planning of combined field and airborne experiments. Concerning environmental monitoring at larger scales, temporal normalization and rigorous data filtering would be essential to avoid misinterpretation of data.

Our study provides further evidence that the RS based assessment of plant responses to water-limitation is complex. Approximating plant stress using multiple RS parameter sensitive for involved processes that act at different temporal scales should be preferred over the use of single parameter. Particularly sensitive, independent and complementary proxies including SIF_{760}, Ts, NPQ (via PRI or more sophisticated approaches), and growth sensitive parameter (leaf pigments and water content, LAI) are of high interest as also discussed in previous research (Damm et al., 2018; Gerhards et al., 2016).

5. Conclusions

New RS technology opens various pathways to assess plant-water relation across ecological relevant scales but the complexity of environmental stress related plant responses still poses a substantial challenge. Our experimental findings confirm theoretical knowledge on the variety of physiological plant reactions following evolving soil water-limitation and their respective temporal dynamics (i.e. SIF representing fast changing adaptation, followed by PRI (as proxy for NPQ), Ts, MTCI (as proxy for canopy chlorophyll content) and WBI (as proxy for leaf water content)). We conclude that canopy measured SIF_{760} shows a highly complex response to emerging soil water-limitation, with a mainly physiology caused short-term increase compared to its normal, followed by a decrease due to biochemical and structural effects. This theoretically known behaviour was here for the first time shown at canopy scale using airborne data. We conclude that time series of spectroscopy images, rather than point measurements and a rigorous data normalization is key to compensate for the various factors causing dynamics in observed RS parameter. Particularly effects caused by changing illumination and structure substantially superimpose dynamics in retrieved RS parameter that tend to mask subtle plant responses. We suggest to substantially invest in research to exploit multi-data approaches for a consistent observation of plant information representing first and second order responses of plant-water relations. We consider such approaches to provide most robust and mechanistic insight on environmental change effects on ecosystem functioning.

Credit author statement

A.D., R.C., F.M., U.R., D.S. conceptualized the experiment; A.D. implemented the data analysis; S.C., P.R., B.S. and J.H. processed airborne data and documented them; L.F., J.S., A.G., L.G., A.P., J.S. acquired, processed and described the field data; A.D. prepared an advanced draft of the manuscript with contributions from S.C., R.C., L. F., A.G., L.G., B.S., J.S., and F.M. All co-authors reviewed and edited the manuscript draft.

Data sharing and accessibility

The data that support the findings of this study are available from the corresponding author upon reasonable request and will be soon available via the campaign data site of ESA.

Declaration of Competing Interest

The authors declare that they have no known competing financial interests or personal relationships that could have appeared to influence the work reported in this paper.

Acknowledgements

Airborne data acquisition and parts of the data analysis was financed by the European Space Agency (ESA) in the frame of the FLEXSense campaign (ESA Contract No. 4000125402/18/NL/NA) and the Photoproxy campaign (ESA contract No. 4000125731/19/NL/LF). We are grateful to the anonymous reviewers for providing excellent and highly constructive comments to improve this manuscript.

Appendix A

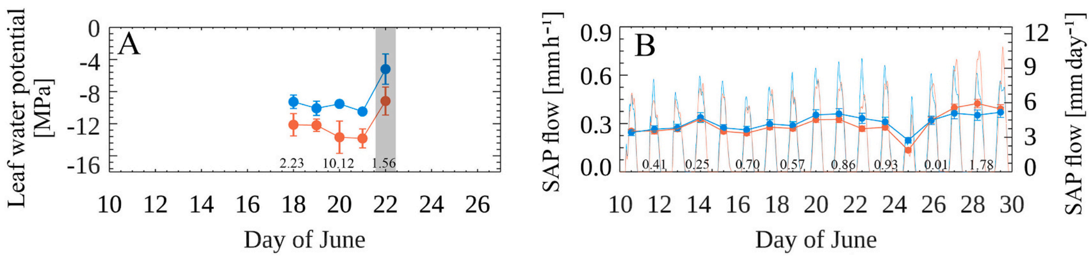

Fig. A1. Left: Mean Leaf water potential (in MPa) of well-watered (blue) and water-limited (orange) corn leaves around noon time. The measurement on 22 June represents pre-dawn conditions. Error bars indicate the 95% confidence interval. Right: Mean diurnal cycles of sap flow measurement of ten corn plants in the well watered canopy (blue) and ten in the the water-limited area (orange). Dots represent daily mean values. Error bars indicate the 95% confidence interval for this period. Numbers in both panels show the effect size (Cohen's d). (For interpretation of the references to colour in this figure legend, the reader is referred to the web version of this article.)

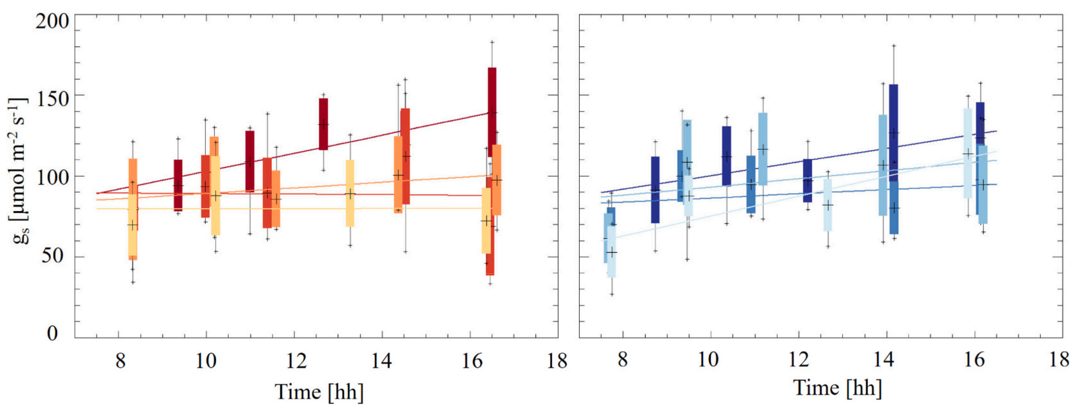

Fig. A2. Stomatal conductance (g_s) between water-limited canopy (left) and well-watered canopy (right). Boxes indicate the mean (black cross), standard deviation (extend of the box) and extreme values (black vertical lines) of 30 measurements on nine plants within 30 min. The lines indicate a linear model fitted to mean g_s values per diurnal cycle. Colours indicate the time of the experiment, ranging from dark red and blue (16 June) to yellow and bright blue (19 June). (For interpretation of the references to colour in this figure legend, the reader is referred to the web version of this article.)

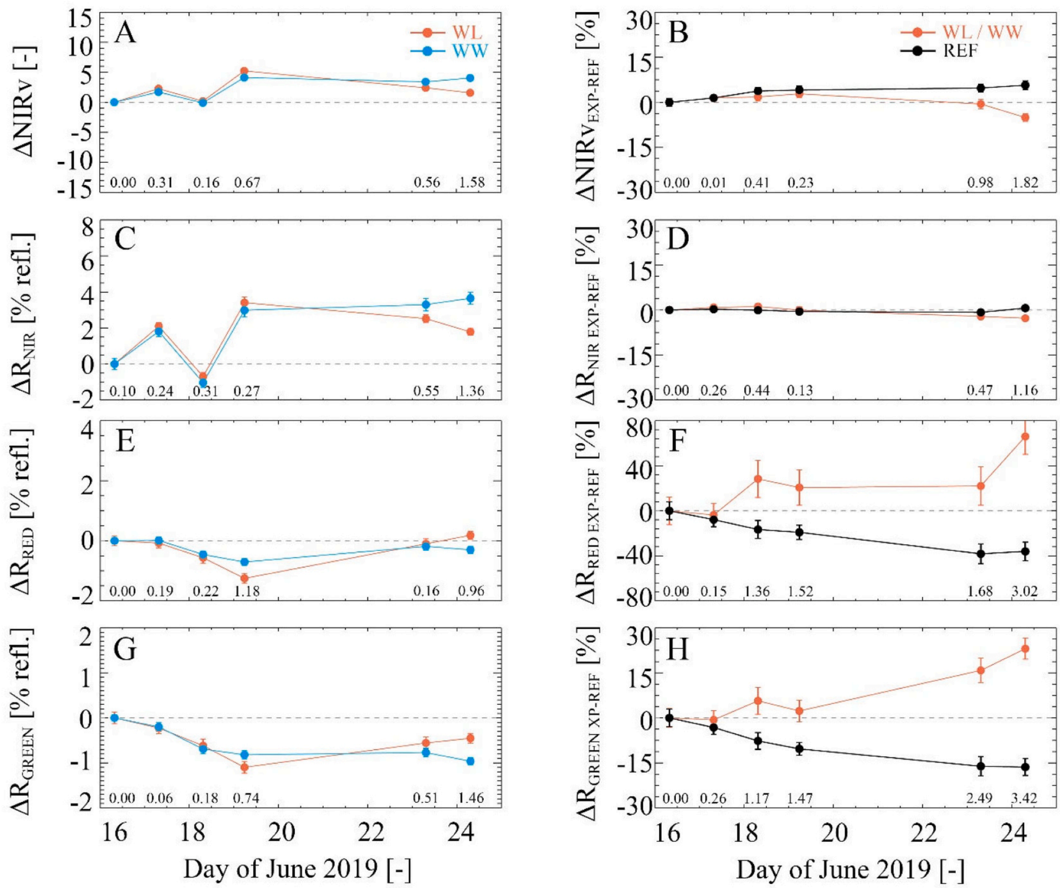

Fig. A3. Changes of the structure sensitive vegetation index NIRv and green, red and NIR reflectance during the water manipulation experiment in a maize canopy between 16 and 24 June 2019 acquired in the morning (10:00–11:30 CEST). Left column: Shown changes represented the difference of a certain RS parameter (P) compared to the first observation (16 June) in parameter units (ΔP) for the water-limited field (orange) and well-watered field (blue). Right column: percentage changes representing the relative difference between the water-limited and the well-watered area (orange), normalized considering the percentage change of the first day (16 June) ($\Delta P_{EXP\text{-}REF}$). The black line shows the normalized percent changes of two reference areas in the same plant rows not affected by the water-limitation experiment. Error bars indicate the 95% confidence interval and numbers the effect size (Cohen's d). (For interpretation of the references to colour in this figure legend, the reader is referred to the web version of this article.)

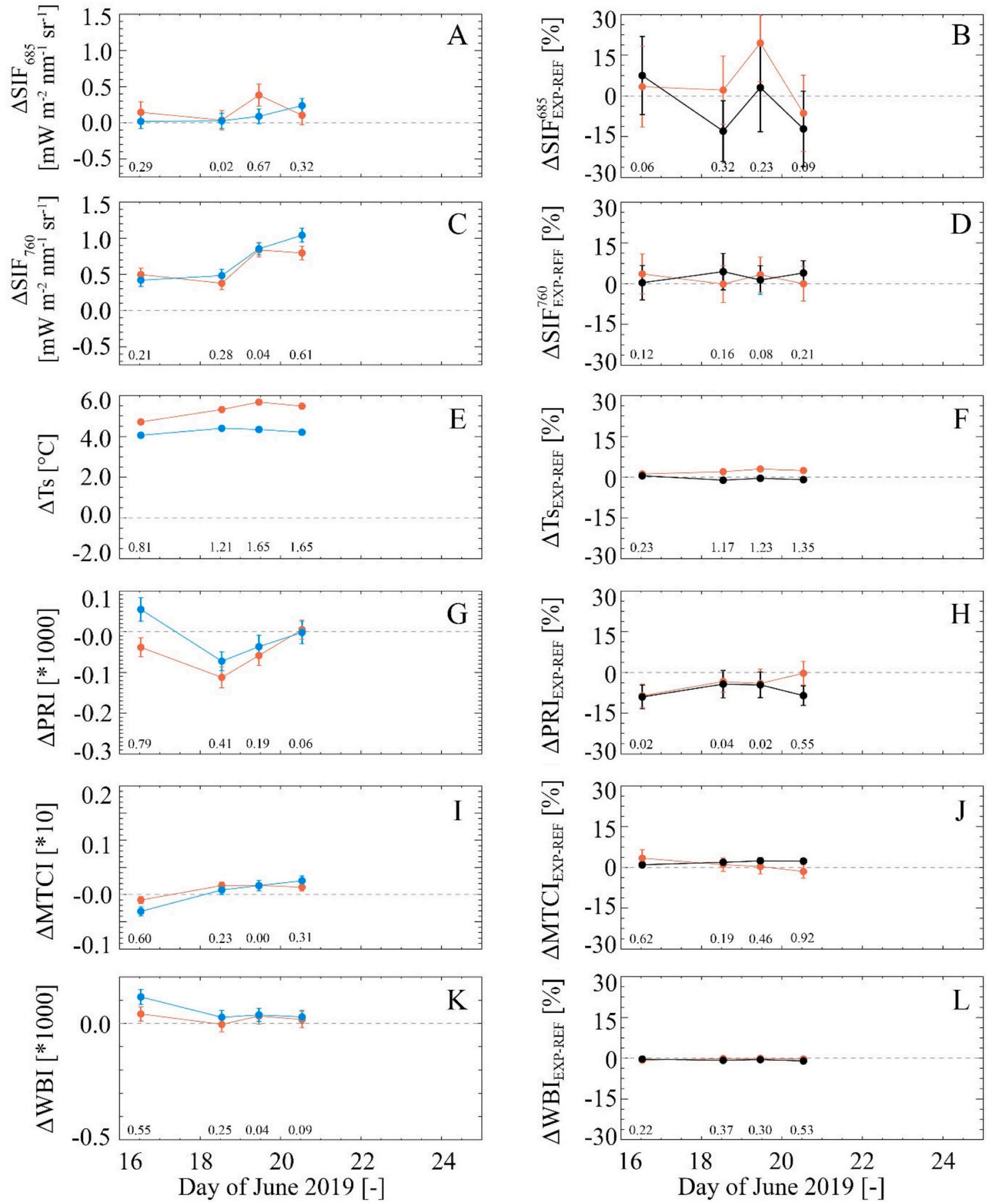

Fig. A4. Changes of remote sensing (RS) parameter during the water manipulation experiment in a maize canopy between 16 and 24 June 2019 acquired in the afternoon (13:30–14:30 CEST). Left column: Shown changes represented the difference of a certain RS parameter (P) compared to the first observation (16 June) in parameter units (ΔP) for the water-limited field (orange) and well-watered field (blue). From top to bottom: red sun-induced chlorophyll fluorescence (SIF685), far-red SIF (SIF760), surface temperature (Ts), photochemical reflectance index (PRI), MERIS terrestrial chlorophyll index (MTCI), and water band index (WBI). Right column: percentage changes representing the relative difference between the water-limited and the well-watered area (orange), normalized considering the percentage change of the first day (16 June) ($\Delta P_{EXP\text{-}REF}$). The black line shows the normalized percent changes of two reference areas in the same plant rows not affected by the water-limitation experiment. Error bars indicate the 95% confidence interval and numbers the effect size (Cohen's d). (For interpretation of the references to colour in this figure legend, the reader is referred to the web version of this article.)

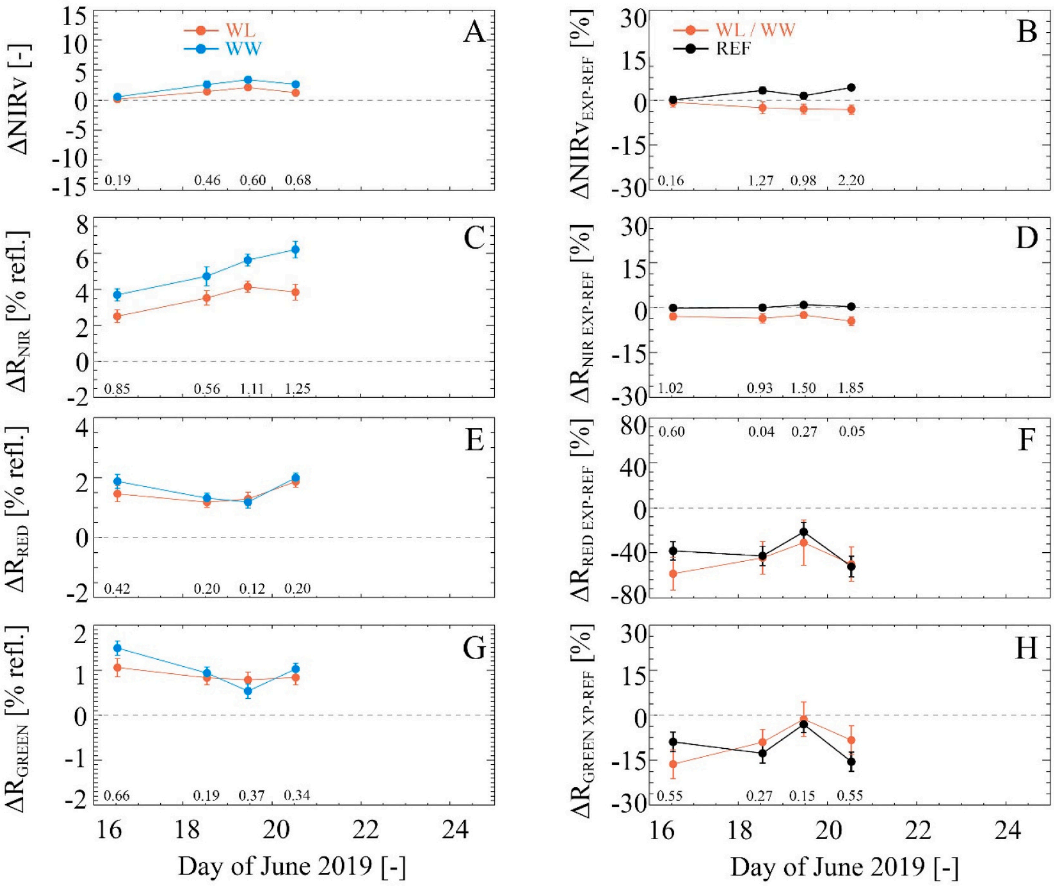

Fig. A5. Changes of remote sensing (RS) parameter during the water manipulation experiment in a maize canopy between 16 and 24 June 2019 acquired in the afternoon (13:30–14:30 CEST). Left column: Shown changes represented the difference of a certain RS parameter (P) compared to the first observation (16 June) in parameter units (ΔP) for the water-limited field (orange) and well-watered field (blue). Right column: percentage changes representing the relative difference between the water-limited and the well-watered area (orange), normalized considering the percentage change of the first day (16 June) ($\Delta P_{EXP\text{-}REF}$). The black line shows the normalized percent changes of two reference areas in the same plant rows not affected by the water-limitation experiment. Error bars indicate the 95% confidence interval and numbers the effect size (Cohen's d). (For interpretation of the references to colour in this figure legend, the reader is referred to the web version of this article.)

References

Badgley, G., Field, C.B., Berry, J.A., 2017. Canopy near-infrared reflectance and terrestrial photosynthesis. Sci. Adv. 3.

Barton, C.V.M., North, P.R.J., 2001. Remote sensing of canopy light use efficiency using the photochemical reflectance index - model and sensitivity analysis. Remote Sens. Environ. 78, 264–273.

Berk, A., Anderson, G.P., Acharya, P.K., Bernstein, L.S., Muratov, L., Lee, J., Fox, M., Adler-Golden, S.M., Chetwynd, J.H., Hoke, M.L., Lockwood, R.B., Gardner, J.A., Cooley, T.W., Borel, C.C., Lewis, P.E., 2005. MODTRAN5: A reformulated atmospheric band model with auxiliary species and practical multiple scattering options. Proc. Soc. Photo-Optical Instrument. Eng. 5655, 662–667.

Bonan, G.B., Williams, M., Fisher, R.A., Oleson, K.W., 2014. Modeling stomatal conductance in the earth system: linking leaf water-use efficiency and water transport along the soil–plant–atmosphere continuum. Geosci. Model Dev. 7, 2193–2222.

Cendrero-Mateo, M.P., Moran, M.S., Papuga, S.A., Thorp, K.R., Alonso, L., Moreno, J., Ponce-Campos, G., Rascher, U., Wang, G., 2016. Plant chlorophyll fluorescence: active and passive measurements at canopy and leaf scales with different nitrogen treatments. J. Exp. Bot. 67, 275–286.

Cendrero-Mateo, M.P., Wieneke, S., Damm, A., Alonso, L., Pinto, F., Moreno, J., Guanter, L., Celesti, M., Rossini, M., Sabater, N., Cogliati, S., Julitta, T., Rascher, U., Goulas, Y., Aasen, H., Pacheco-Labrador, J., Mac Arthur, A., 2019. Sun-induced chlorophyll fluorescence III: benchmarking retrieval methods and sensor characteristics for proximal sensing. Remote Sens. 11.

Ciais, P., Dolman, A.J., Bombelli, A., Duren, R., Peregon, A., Rayner, P.J., Miller, C., Gobron, N., Kinderman, G., Marland, G., Gruber, N., Chevallier, F., Andres, R.J., Balsamo, G., Bopp, L., Breon, F.M., Broquet, G., Dargaville, R., Battin, T.J., Borges, A., Bovensmann, H., Buchwitz, M., Butler, J., Canadell, J.G., Cook, R.B., DeFries, R., Engelen, R., Gurney, K.R., Heinze, C., Heimann, M., Held, A., Henry, M., Law, B., Luyssaert, S., Miller, J., Moriyama, T., Moulin, C., Myneni, R.B., Nussli, C., Obersteiner, M., Ojima, D., Pan, Y., Paris, J.D., Piao, S.L., Poulter, B., Plummer, S., Quegan, S., Raymond, P., Reichstein, M., Rivier, L., Sabine, C., Schimel, D., Tarasova, O., Valentini, R., Wang, R., van der Werf, G., Wickland, D., Williams, M., Zehner, C., 2014. Current systematic carbon-cycle observations and the need for implementing a policy-relevant carbon observing system. Biogeosciences 11, 3547–3602.

Cogliati, S., Celesti,, M., Cesana, I., Miglietta, F., Genesio, L., Julitta, T., Schuettemeyer, D., Drusch, M., Rascher, U., Jurado, P., Colombo, R., 2019. A spectral fitting algorithm to retrieve the fluorescence spectrum from canopy radiance. Remote Sens. 11 (16).

Cogliati, S., Verhoef, W., Kraft, S., Sabater, N., Alonso, L., Vicent, J., Moreno, J., Drusch, M., Colombo, R., 2015. Retrieval of sun-induced fluorescence using advanced spectral fitting methods. Remote Sens. Environ. 169, 344–357.

Damm, A., Erler, A., Hillen, W., Meroni, M., Schaepman, M.E., Verhoef, W., Rascher, U., 2011. Modeling the impact of spectral sensor configurations on the FLD retrieval accuracy of sun-induced chlorophyll fluorescence. Remote Sens. Environ. 115, 1882–1892.

Damm, A., Guanter, L., Verhoef, W., Schläpfer, D., Garbari, S., Schaepman, M.E., 2015. Impact of varying irradiance on vegetation indices and chlorophyll fluorescence derived from spectroscopy data. Remote Sens. Environ. 156, 202–215.

Damm, A., Paul-Limoges, E., Haghighi, E., Simmer, C., Morsdorf, F., Schneider, F.D., Van der Tol, C., Migliavacca, M., Rascher, U., 2018. Remote sensing of plant-water relations: an overview and future perspectives. J. Plant Physiol. 277, 3–19.

Dash, J., Curran, P.J., 2004. The MERIS terrestrial chlorophyll index. Int. J. Remote Sens. 25, 5403–5413.

Dolman, A.J., Miralles, D.G., de Jeu, R.A.M., 2014. Fifty years since Monteith's 1965 seminal paper: the emergence of global ecohydrology. Ecohydrology 7, 897–902.

Fawcett, D., Verhoef, W., Schläpfer, D., Schneider, F.D., Schaepman, M.E., Damm, A., 2018. Advancing retrievals of surface reflectance and vegetation indices over forest ecosystems by combining imaging spectroscopy, digital object models, and 3D canopy modelling. Remote Sens. Environ. 204, 583–595.

Feng, G., Yufang, J., Schaaf, C.B., Strahler, A.H., 2002. Bidirectional NDVI and atmospherically resistant BRDF inversion for vegetation canopy, *- 40*, - 1278.
Gamon, J.A., Penuelas, J., Field, C.B., 1992. A narrow-waveband spectral index that tracks diurnal changes in photosynthetic efficiency. Remote Sens. Environ. 41, 35–44.
Garcia-Tejera, O., Lopez-Bernal, A., Testi, L., Villalobos, F.J., 2017. A soil-plant-atmosphere continuum (SPAC) model for simulating tree transpiration with a soil multi-compartment solution. Plant Soil 412, 215–233.
Gerhards, M., Rock, G., Schlerf, M., Udelhoven, T., 2016. Water stress detection in potato plants using leaf temperature, emissivity, and reflectance. Int. J. Appl. Earth Obs. Geoinf. 53, 27–39.
Guanter, L., Alonso, L., Gomez-Chova, L., Meroni, M., Preusker, R., Fischer, J., Moreno, J., 2010. Developments for vegetation fluorescence retrieval from spaceborne high-resolution spectrometry in the O2-A and O2-B absorption bands. J. Geophys. Res.-Atmos. 115.
Hanus, J., Fabianek, T., Fajmon, L., 2016. Potential of airborne imaging spectroscopy at czechglobe. In: Halounova, L., Safar, V., Toth, C.K., Karas, J., Huadong, G., Haala, N., Habib, A., Reinartz, P., Tang, X., Li, J., Armenakis, C., Grenzdorffer, G., LeRoux, P., Stylianidis, S., Blasi, R., Menard, M., Dufourmount, H., Li, Z. (Eds.), Xxiii Isprs Congress, Commission I, pp. 15–17.
Hueni, A., Damm, A., Kneubuehler, M., Schlapfer, D., Schaepman, M.E., 2017. Field and airborne spectroscopy cross validation-some considerations. IEEE J. Select. Top. Appl. Earth Observ. Remote Sens. 10, 1117–1135.
Jonard, F., de Canniere, S., Brüggemann, N., Gentine, P., Short Gianotti, D.J., Lobet, G., Miralles, D.G., Montzka, C., Pagán, B.R., Rascher, U., Vereecken, H., 2020. Value of sun-induced chlorophyll fluorescence for quantifying hydrologicalstates and fluxes: current status and challenges. Agric. For. Meteorol. 291.
Kückenbrink, D., Hueni, A., Damm, A., Schneider, F.D., Gastellu-Etchegorry, J.P., Schaepman, M.E., Morsdorf, F., 2019. Mapping the irradiance field of a single tree: quantifying vegetation induced adjacency effects. IEEE Trans. Geosci. Remote Sensing 57 (7), 4994–5011. *8645789*.
Li, X., Gentine, P., Lin, C., Zhou, S., Sun, Z., Zheng, Y., Liu, J., Zheng, C., 2019. A simple and objective method to partition evapotranspiration into transpiration and evaporation at eddy-covariance sites. Agric. For. Meteorol. 265, 171–182.
Meroni, M., Busetto, L., Colombo, R., Guanter, L., Moreno, J., Verhoef, W., 2010. Performance of spectral fitting methods for vegetation fluorescence quantification. Remote Sens. Environ. 114, 363–374.
Miralles, D.G., Gentine, P., Seneviratne, S.I., Teuling, A.J., 2019. Land-atmospheric feedbacks during droughts and heatwaves: state of the science and current challenges. Ann. N. Y. Acad. Sci. 1436, 19–35.
Mohammed, G., Colombo, R., Middleton, E., Rascher, U., van der Tol, C., Berry, J.A.L.N., Goulas, Y., Perez-Priego, O., Damm, A., Meroni, M., Joiner, J., Cogliati, S., Verhoef, W., Gastellu-Etchegorry, J.P., Malenovský, Z., Miller, J.R., Guanter, L., Moreno, J., Moya, I., Frankenberg, C., Zarco-Tejada, P.J., 2019. Remote sensing of solar-induced chlorophyll fluorescence (SIF) in vegetation: 50 years of progress. Remote Sens. Environ. 231, 111177.
Myneni, R.B., Maggion, S., Iaquinto, J., Privette, J.L., Gobron, N., Pinty, B., Kimes, D.S., Verstraete, M.M., Williams, D.L., 1995. Optical remote-sensing of vegetation - modeling, caveats, and algorithms. Remote Sens. Environ. 51, 169–188.
Penuelas, J., Filella, I., Biel, C., Serrano, L., Save, R., 1993. The reflectance at the 950-970 nm region as an indicator of plant water status. Int. J. Remote Sens. 14, 1887–1905.
Peressotti, A., Ham, J.M., 1996. A dual-heater gauge for measuring sap flow with an improved heat-balance method. Agron. J. 88, 149–155.
Porcar-Castell, A., Malenovský, Z., Magney, T., Van Wittenberghe, S., Fernández-Marín, B., Maignan, F., Zhang, Y., Maseyk, K., Atherton, J., Albert, L.P., Robson, T. M., Zhao, F., Garcia-Plazaola, J.-I., Ensminger, I., Rajewicz, P.A., Grebe, S., Tikkanen, M., Kellner, J.R., Ihalainen, J.A., Rascher, U., Logan, B., 2021. Chlorophyll a fluorescence illuminates a path connecting plant molecular biology to earth-system science. Nature Plants 7, 998–1009.
Rascher, U., Alonso, L., Burkhart, A., Cilia, C., Cogliati, S., Colombo, R., Damm, A., Drusch, M., Guanter, L., Hanus, J., Hyvärinen, T., Julitta, T., Jussila, J., Katajak, K., Kokkalis, P., Kraft, S., Kraska, T., Matveeva, M., Moreno, J., Muller, O., Panigada, C., Pikl, M., Pinto, F., Prey, L., Pude, R., Rossini, M., Schickling, A., Schurr, U., Schüttemeyer, D., Verrelst, J., Zemek, F., 2015. Sun-induced fluorescence - a new probe of photosynthesis: first maps from the imaging spectrometer HyPlant. Glob. Chang. Biol. 21, 4673–4684.
Reichstein, M., Bahn, M., Ciais, P., Frank, D., Mahecha, M.D., Seneviratne, S.I., Zscheischler, J., Beer, C., Buchmann, N., Frank, D.C., Papale, D., Rammig, A., Smith, P., Thonicke, K., Van Der Velde, M., Vicca, S., Walz, A., Wattenbach, M., 2013. Climate extremes and the carbon cycle. Nature 500, 287–295.
Ryu, Y., Berry, J.A., Baldocchi, D.D., 2019. What is global photosynthesis? History, uncertainties and opportunities. Remote Sens. Environ. 223, 95–114.
Sakuratani, T., 1981. A heat balance method for measuring water flux in the stem of intact plants. J. Agric. Meteorol. 37.
Scholander, P.F., Hammel, H.T., Bradstreet, E.D., Hemmingsen, E.A., 1965. Sap pressure in vascular plants - negative hydrostatic pressure can be measured in plants. Science 148, 339-+.
Schuldt, B., Buras, A., Ahrend, M., Vitasse, Y., Beierkuhnlein, C., Damm, A., Gharun, M., Grams, T., Hauck, M., Hajek, P., Hartmann, H., Hilbrunner, E., Hoch, G., Holloway-Phillips, M., Körner, C., Larysch, E., Lübbe, T., Nelson, D.B., Rammig, A., Rigling, A., Rose, L., Ruehr, N.K., Schumann, K., Weiser, K., Werner, C., Wohlgemuth, T., Zang, C., Kahmen, A., 2020. A first assessment of the impact of the extreme 2018 summer drought on Central European forests. Basic Appl. Ecol. 45, 86–103.
Shan, N., Ju, W., Migliavacca, M., Martini, D., Guanter, L., Chen, J., Goulas, Y., Zhang, Y., 2019. Modeling canopy conductance and transpiration from solar-induced chlorophyll fluorescence. Agric. For. Meteorol. 268, 189–201.
Siegmann, B., Alonso, L., Celesti, M., Cogliati, S., Colombo, R., Damm, A., Douglas, S., Guanter, L., Hanuš, J., Kataja, K., Kraska, T., Matveeva, M., Moreno, J., Muller, O., Pikl, M., Pinto, F., Vargas, J.Q., Rademske, P., Rodriguez-Morene, F., Sabater, N., Schickling, A., Schüttemeyer, D., Zemek, F., Rascher, U., 2019. The high-performance airborne imaging spectrometer HyPlant-from raw images to top-of-canopy reflectance and fluorescence products: introduction of an automatized processing chain. Remote Sens. 11.
Sippel, S., Reichstein, M., Ma, X.L., Mahecha, M.D., Lange, H., Flach, M., Frank, D., 2018. Drought, heat, and the carbon cycle. Curr. Climate Change Rep. 4, 266–286.
Sippel, S., Meinshausen, N., Fischer, E.M., Szekely, E., Knutti, R., 2020. Climate change now detectable from any single day of weather at global scale. Nat. Clim. Chang. 10, 35-+.
Smith, M.D., 2011. An ecological perspective on extreme climatic events: a synthetic definition and framework to guide future research. J. Ecol. 99, 656–663.
Stocker, B.D., Zscheischler, J., Keenan, T.F., Prentice, I.C., Seneviratne, S.I., Peñuelas, J., 2019. Drought impacts on terrestrial primary production underestimated by satellite monitoring. Nat. Geosci. 12, 264–270.
Sun, Y., Fu, R., Dickinson, R., Joiner, J., Frankenberg, C., Gu, L.H., Xia, Y.L., Fernando, N., 2015. Drought onset mechanisms revealed by satellite solar-induced chlorophyll fluorescence: insights from two contrasting extreme events. J. Geophys. Res.-Biogeosci. 120, 2427–2440.
Talsma, C.J., Good, S.P., Jimenez, C., Martens, B., Fisher, J.B., Miralles, D.G., McCabe, M. F., Purdy, A.J., 2018. Partitioning of evapotranspiration in remote sensing-based models. Agric. For. Meteorol. 260-261, 131–143.
Turner, N.C., Long, M.J., 1980. Errors arising from rapid water-loss in the measurement of LEAF water potential by the pressure chamber technique. Aust. J. Plant Physiol. 7, 527–537.
van der Tol, C., Verhoef, W., Rosema, A., 2009. A model for chlorophyll fluorescence and photosynthesis at leaf scale. Agric. For. Meteorol. 149, 96–105.
Van Wittenberghe, S., Laparra, V., Ignacio Garcia-Plazaola, J., Fernandez-Marin, B., Porcar-Castell, A., Moreno, J., 2021. Combined dynamics of the 500–600 nm leaf absorption and chlorophyll fluorescence changes in vivo: Evidence for the multifunctional energy quenching role of xanthophylls. BBA-Bioenergetics 1862.
Verhoef, W., van der Tol, C., Middleton M., E., 2018. Hyperspectral radiative transfer modeling to explore the combined retrieval of biophysical parameters and canopy fluorescence from FLEX - Sentinel-3 tandem mission multi-sensor data. Remote Sens. Environ. 204, 942–963.
von Buttlar, J., Zscheischler, J., Rammig, A., Sippel, S., Reichstein, M., Knohl, A., Jung, M., Menzer, O., Arain, M.A., Buchmann, N., Cescatti, A., Gianelle, D., Kiely, G., Law, B.E., Magliulo, V., Margolis, H., McCaughey, H., Merbold, L., Migliavacca, M., Montagnani, L., Oechel, W., Pavelka, M., Peichl, M., Rambal, S., Raschi, A., Scott, R. L., Vaccari, F.P., van Gorsel, E., Varlagin, A., Wohlfahrt, G., Mahecha, M.D., 2018. Impacts of droughts and extreme-temperature events on gross primary production and ecosystem respiration: a systematic assessment across ecosystems and climate zones. Biogeosciences 15, 1293–1318.
Wang, K.C., Dickinson, R.E., 2012. A review of gobal terrestrial evapotranspiration: observation, modeling, climatology, and climatic variability. Rev. Geophys. 50.
Weyermann, J., Damm, A., Kneubuehler, M., Schaepman, M.E., 2014. Correction of reflectance anisotropy effects of vegetation on airborne spectroscopy data and derived products. IEEE Trans. Geosci. Remote Sens. 52, 616–627.
Yang, P., van der Tol, C., Verhoef, W., Damm, A., Schickling, A., Kraska, T., Muller, O., Rascher, U., 2019. Using reflectance to explain vegetation biochemical and structural effects on sun-induced chlorophyll fluorescence. Remote Sens. Environ. 231, 110996.
Yoshida, Y., Joiner, J., Tucker, C., Berry, J., Lee, J.E., Walker, G., Reichle, R., Koster, R., Lyapustin, A., Wang, Y., 2015. The 2010 Russian drought impact on satellite measurements of solar-induced chlorophyll fluorescence: insights from modeling and comparisons with parameters derived from satellite reflectances. Remote Sens. Environ. 166, 163–177.
Zarco-Tejada, P.J., Gonzalez-Dugo, V., Berni, J.A.J., 2012. Fluorescence, temperature and narrow-band indices acquired from a UAV platform for water stress detection using a micro-hyperspectral imager and a thermal camera. Remote Sens. Environ. 117, 322–337.
Zeng, Y., Chen, M., Hao, D., Damm, A., Badgley, G., Rascher, U., Johnson, J.E., Dechant, B., Siegmann, B., Ryu, Y., Qiu, H., Krieger, V., Panigada, C., Celesti, M., Miglietta, F., Yang, X., Berry, J.A., 2022. Combining near-infrared radiance of vegetation and fluorescence spectroscopy to detect effects of abiotic changes and stresses. Remote Sens. Environ. 270, 112856.